RICE UNIVERSITY

Transport of Components and Phases in a Surfactant/Foam EOR Process for a Giant Carbonate Reservoir.

by

José Luis López-Salinas

A THESIS SUBMITTED
IN PARTIAL FULFILLMENT OF THE
REQUIREMENTS FOR THE DEGREE

Doctor of Philosophy

APPROVED, THESIS COMMITTEE:

G. J. Hirasaki

George J. Hirasaki, A.J. Hartsook Professor in Chemical Engineering, Co-Chair.

Clarence A. Miller

Clarence A. Miller, Louis Calder Professor Emeritus in Chemical Engineering
Research Professor, Co-Chair.

Mason B Tomson

Mason B. Tomson, Professor in Civil and Environmental Engineering

Sibani Lisa Biswal, Assistant Professor in Chemical and Biomolecular Engineering

Maura C. Puerto, Research Scientist

HOUSTON, TEXAS
December, 2012

ABSTRACT

Transport of Components and Phases in a Surfactant/Foam EOR Process for a Giant Carbonate Reservoir

by

José Luis López-Salinas

The transport of components and phases plays a fundamental role in the success of an EOR process. Because many reservoirs have harsh conditions of salinity, temperature and rock heterogeneity, which limit process options, a robust system with flexibility is required.

Systematic experimental study of formulations capable to transport surfactant as foam at 94°C, formulated in sea water, is presented. It includes methodology to conduct core floods in sand packs using foaming surfactants and to develop “surfactant blend ratio- salinity ratio maps” using equilibrium phase behavior to determine favorable conditions for oil recovery in such floods. Mathematical model able to reproduce the foam strength behavior observed in sand packs with the formulations studied is presented.

Visualization of oil recovery mechanism from matrix is realized using a model system of micro-channels surrounded by glass beads to mimic matrix and fractures respectively. The observations illustrate how components may distribute within the matrix, thereby releasing oil into the fractures.

The use of chemicals to minimize adsorption is required when surfactant adsorption is important. The presence of anhydrite may limit the use of sodium

carbonate to reduce adsorption of carbonates. A methodology is presented to estimate the amount, if any, of anhydrite present in the reservoir. The method is based on brine software analysis of produced water compositions and inductively coupled plasma (ICP) analysis of core samples. X-ray powder diffraction (XRD) was used to verify the mineralogy of the rock. X-ray photoelectron spectroscopy (XPS) was used to obtain surface composition for comparison with bulk composition of the rock.

Adsorption of surfactants was measured using dynamic and static adsorption experiments. Determining the flow properties of the rock samples via tracer analysis permitted the simulation of the dynamic adsorption process using a mathematical model that considers the distribution of adsorbed materials in the three different regions of pore space. Using this method allows one to predict adsorption in a reservoir via simulation.

ACKNOWLEDGEMENTS

I would like to express my deepest gratitude to my supervisors, Professor George J Hirasaki and Professor Clarence A Miller, who contributed immensely to my learning process, education and research throughout my studies at Rice University. It was my privilege to be his student and to complete my studies under his supervision.

I thank Professors Mason Tomson and Lisa Biswal for serving in my thesis committee and all their support they gave me using their labs.

I thank Maura Puerto for all the support building and designing the equipment used during experiments, serving in my thesis committee and all her advices, and support.

I thank Roberto Roca Education Program and ITESM for financial support.

I thank all people who help me in my research; Daniel Krishock, Dr. Fernando de la Garza, Dr. Kishore Mohanty, and the people from PEMEX and IMP.

The outstanding staff of the Chemical and Biomolecular Engineering department greatly enhanced my research experience at Rice U. They are too many to name; however, I wish to single out undergrad students Insoo Ro, Dion Hubble, Maggie Menhchen Tang, Tarek Hariz and Kyu Hun Yoo for their support and contributions. The grad students Aarthi Muthuswamy, Neeraj Rohilla, AmirHosein Valiollahzadeh, Kun Ma, Aparna Raju

Sagi, Michael Rauschhuber and Leyu Cui for all the discussions and learning interactions.

I am deeply grateful with all the support and encouragement from my wife Angelica and my daughters Andrea and Esther. Also the amazing people: Alejandro Garcia Cuellar, Rosa E. Rangel Quintanilla and Juana Maria Lopez Cruz, who helped me and my family during this journey.

Special thanks to Darlene and George Hirasaki for their kindness with my family.

TABLE OF CONTENTS

Abstract		I
Acknowledgements		III
Table of Contents		V
List of Tables		XIII
List of Figures		XVII
Chapter 1	Introduction	1
1.1	Enhanced Oil Recovery	1
1.2	Foam for EOR	2
1.3	Thesis Scope and Organization	4
Chapter 2	Technical Background	7
2.1	Amphiphiles and Surfactants	7
2.2	Classification of Surfactants	8
2.3	Fundamentals of Foam Flow in Porous Media	11
2.4	Mechanism of Foam Formation and Decay	14
2.4.1	Foam Formation	15
2.4.1.a	Capillary snap-off	15
2.4.1.b	Lamella Division	16
2.4.1.c	Leave-behind	17
2.4.2	Foam Destruction	18
2.4.2.a	Capillary Suction Coalescence	18
2.4.2.b	Gas Diffusion	21

2.5	Apparent Viscosity in Porous Media	21
2.6	Foam Modeling	25
2.7	Empirical Methods	26
2.8	Mechanistic Methods	27
2.9	Phase behavior	27
2.9.1	Solubilization	27
2.10	Surfactants Phase Behavior	39
Chapter 3	Properties of Material and Phases	41
3.1	Crude Oil IFT	42
3.2	Crude Oil Viscosity	44
3.3	Acid Number	51
3.4	Contact Angle	51
3.5	Surfactant Viscoelasticity	54
3.6	Surfactant Surface Tension	62
Chapter 4	Anhydrite Determination in Carbonate Formations	65
4.1	Introduction	65
4.2	Anhydrite Determination	68
4.3	Information about the Seawater and Formation Brines	69
4.4	Description and validation of software	71
4.5	Methodology	77
4.6	Results	79
4.7	Conclusions about the Chapter 4	89

Chapter 5	Static Adsorption and Analytical Methods to Measure Surfactants	90
5.1	Overview of Chapter 5	90
5.2	Methods to Quantify surfactants	92
5.3	Analytical Techniques to Measure Concentrations During Static Adsorption Experiments	94
5.4	Quantification of both, IOS and Carboxylate surfactants in UT Blends	99
5.5	Colorimetric two-phase titrations, to measure thermal stability of $C_{24}PO_{25}EO_{56}CO_2Na$ in UT_{Old} Blend and addition of polyacrylate to improve aqueous stability.	102
5.5.1	Aqueous Stability	102
5.6	Colorimetric two-phase Titrations Measuring Adsorption of $C_{28}PO_{25}EO_{25}COONa$ and $C_{15\text{-}18}$ IOS in UT_{New} Blend.	109
5.7	Thermal Behavior	111
5.7.1	Thermal Behavior of 1% Individual Surfactants in DI Water at 90°C ($C_{28}PO_{25}EO_{25}COONa$ and $C_{15\text{-}18}$ IOS)	111
5.7.2	Thermal Behavior of 1% Surfactant Blend in Seawater, 90 °C ($C_{28}PO_{25}EO_{25}COONa$ and $C_{15\text{-}18}$ IOS, 1:1)	112
5.7.3	Thermal Behavior of 1% Surfactant Blend in Seawater, Contacted with Dolomite 90°C ($C_{28}PO_{25}EO_{25}COONa$ and $C_{15\text{-}18}$ IOS)	113
5.7.4	Sacrificial Agents to Reduce Adsorption	113
5.8	Remarks	115

5.9	Thermal Stability of Cocamidopropyl Betaine	116
Chapter 6	Dynamic Adsorption Experiments, Modeling and Simulation.	122
6.1	Introduction	122
6.2	Mathematical Model for Dynamic Adsorption	123
6.3	Experimental Dynamic Adsorption (Rock, Brine, Tracer and Surfactant)	138
6.3.1	Measure Permeability	141
6.4	Results of Adsorption	148
6. 4.1	Results of Adsorption for the Silurian Outcrop Dolomite	148
6.4.2	Results of Adsorption for the Composite Zaap Rock.	151
6.5	Mathematical Model Proposed	155
6.6	Simulation of Dynamic Adsorption (Model Parameters Fitting)	157
6.7	Conclusion of Chapter 6	172
Chapter 7	Foam and Oil Experiments	173
7.1	Foam Studies with Oil Recovery using “Surfactants Ratio – Salinity Ratio” Maps to Select Injection Conditions for Oil Recovery	174
7.1.1	Surfactants Used in Oil Recovery Study with Foam	175
7.1.2	Materials and Methods for the Core Flood Experiments, and Foam Experiments in Sand Packs	178
7.1.2.a	Diagram of Equipment for Foam Experiments and Core Floods	183
7.1.2.b	Surfactants	185

7.1.2.c	Brine Composition used During Experiments	185
7.1.3	Foam Study with Oil Recovery using "Surfactants-Ratio Salinity-Ratio" Maps, to Select Injection Conditions for High Recovery (i.e. Phase behavior and core floods in foaming systems**).**	185
7.1.3.a	Oil Recovery with co-injection of Surfactant and Nitrogen	186
7.1.3.b	Particular Observations Related to Some Core Floods.	194
7.1.3.c	Foam During Oil Recovery Experiments.	202
7.2	Screening of Surfactant Blends to Produce Strong Foams	213
7.2.1	Surfactants used in the Foam Screening Process.	215
7.2.1.a	Anionic-Zwitterionic Blends	220
7.2.1.b	Zwitterionic-Cationic Surfactants	220
7.2.2	Foaming Study for C_{16-18}AOS	223
7.2.3	Foaming Study for LB+C_{16-18}AOS	227
7.2.4	Comparison of surfactants as foamers	230
7.2.5	Observations about Foam Studies with Oil Recovery using "Surfactants Ratio – Salinity Ratio" Maps to Select Injection Conditions for Oil Recovery, and the Screening Process of Foaming Surfactant Blends	239
7.3	Mathematical Model, Parameters Fit and Simulation.	240
7.3.1	Algorithm to Fit Parameters of the Model.	244
7.3.2	Fitting process of foam model.	248
7.4	Gravity Drainage - Imbibition Experiments	259
7.4.1	Imbibition in the Special Designed Foaming-Imbibition Cell.	261

7.4.2 Procedure During Imbibition Experiment In Foaming Environment 263
7.4.3 Oil Recovery in the Autoclavable-Imbibition Cell using 300 mD Silurian Dolomite Outcrop Cores 265
7.4.4 Procedure for Imbibitions Experiments 266
7.4.5 Analysis from Imbibition Experiments 271
7.5 Experiments in Capillaries to Visualize Oil Recovery in Gas Cap 280
7.5.1 Preparation of the Capillary Tubes 282
7.5.2 Oil recovery from Oil Filled Micro-Capillaries Immersed in Aqueous Surfactant Solution at 94°C 283
7.5.3 Oil recovery from Oil Filled Micro-Capillaries Immersed in Foaming Stream at Room Temperature. 290
Chapter 8 Conclusions and Recommendations 297
8.1 Adsorption 297
8.2 Foam 299
8.3 Corefloods 301
8.4 Imbibition Experiments 302
8.5 Studies for Visualization of Crude Oil Mobilization within Micro-Channels in an Environment with Foam 304
8.6 Presence of Anhydrite in the Formation 306
Nomenclature 308
Chapter 4 Nomenclature 308

	Chapter 6 Nomenclature	310
	Chapter 7 Nomenclature	315
References		320
Appendices		345
Appendix 3A	Interfacial Tension of Contaminated Oils	345
Appendix 3B	Viscosity of Dead Oil	346
Appendix 3C	Rheology Models to Describe Surfactant Blends	347
Appendix 3D	Prediction of Rheology at 94°C	349
Appendix 3E	Falling Sphere Viscometer	351
Appendix 3F	Contact Angle Determination	352
Appendix 3G	Idealization of Molecular Interactions	353
Appendix 4A	XRD Results	356
Appendix 4B	Analytical Methods	357
Appendix 4C	Water Analysis	358
Appendix 5A	Titration of Blends using Low pH	362
Appendix 5B	Titration at Low pH	363
Appendix 5C	Titration at High pH	364
Appendix 5D	Titration of Blends Containing Zwitterionic, Anionic and Cationic Surfactants.	365
Appendix 5E	Titration for Zwitterionic	367
Appendix 5F	Sacrificial Agents, Titration Reagents and Indicators	369
Appendix 6A	Determination of Adsorption	372
Appendix 6B	Representation of the Porous Structure	375

Appendix 7A	Information about Surfactants	377
Appendix 7B	Foam Equipment	378
Appendix 7C	CDC Parameters and Equations	378
Appendix 7D	Aqueous Stability of UTB Formulations	379
Appendix 7E	Oil in Plateau Borders	380
Appendix 7F	Algorithm	381
Appendix 7G	Brine Comparison	381
Appendix 7H	Analytical Solution of Counter Current Imbibitions for Strong Water	382
Appendix 7I	Material for Experiments in Micro-Channels	383
Appendix 7J	Solutions of Mixtures of the UT Blend	383
Appendix 7K	IMP Transient Foam	385
Appendix 7L	Oil Recovery in Rectangular Capillaries, and Oil Recovery for a Bunndle of Rectandular Capillaries	387
Appendix 7M	Parameters for foam simulation / surfactants of different nature	389

LIST OF TABLES

Table 2-1	Approaches to predict surfactant behavior.	29
Table 2-2	Ways the interaction between portions of surfactant modifies the Winsor R ratio.	33
Table 2-3	Equivalence between *SAD* and Winsor *R*-ratio.	34
Table 2-4	Correlation to estimate the surfactant affinity difference.	35
Table 2-5	Dipole-induce dipole interaction between the surfactant and the oil phase.	36
Table 2-6	Weakening of the hydrogen bonds between water molecules with temperature.	36
Table 2-7	Weakening of the hydrogen bonds between the molecules of water and the oxygen in the ethylene oxide groups with temperature and the salting parameter.	37
Table 3-1	IFT values of dead crude oil measured at 25°C in 5% NaCl	43
Table 3-2	Viscosity of fluids at reservoir temperature (273ºF)	50
Table 3-3	Viscosity of different simulated live crude oil vs. live crude oil and dead oil.	50
Table 3-4	Contribution to critical packing parameter in the scenarios described.	61
Table 3-5	Typical dimensionless number during measurements.	64
Table 4-1	Elemental analysis of the rock after ICP.	84
Table 4-2	Atomic percentage for analyzed samples.	86

Table 5-1	UT formulations in this research	93
Table 5-2	Sample preparation	96
Table 5-3	Composition of components of UT Blend for calibration.	100
Table 5-4	Polyacrylate contacted with dolomite.	105
Table 5-5	Thermal behavior of 1% surfactant in DI Water at 90°C.	112
Table 5-6	1% Surfactant in seawater, contacted with dolomite 90 °C.	113
Table 5-7	Reduction of activity in a 3.89 pH buffer after 2 months of ageing at 100°C.	119
Table 5-8	CAPB Half-life as a function of pH and temperature.	120
Table 6-1	Brines used for surfactant solutions and for tracer analysis.	146
Table 6-2	Silurian Dolomite adsorption/retention.	150
Table 6-3	PEMEX Composite Dolomite adsorption/retention.	153
Table 6-4	Simplified equations for initial guess.	159
Table 6-5	Parameters for simulation after fitting.	163
Table 6-6	Parameters for simulation in case III.	168
Table 6-7	Surface area measured in different dolimites.	170
Table 6-8	Analysis of the surface of the rock.	171
Table 6-9	XPS analysis.	171
Table 7-1	Surfactants blends used in core floods.	175
Table 7-2	Brines composition using stock salts.	185
Table 7-3	Conditions needed to recover residual oil.	192
Table 7-4	Initial condition of the porous media for test “6” and “7”	198
Table 7-5	Comparison of foam strength for surfactant blends.	212

Table 7-6	Surfactants used for screen surfactants blends for foaming in seawater and 94°C.	215
Table 7-7	Hydrotropes.	222
Table 7-8	Combinations of surfactants used in the foaming tests.	230
Table 7-9	Viscosities of foam at quality 70% and 1cm^3/min of liquid flow rate at 94°C. Part I.	231
Table 7-10	Viscosities of foam at quality 70% and 1cm^3/min of liquid flow rate at 94°C. Part II.	234
Table 7-11	Contributions to the mobility reduction factor.	242
Table 7-12	Default parameters for relative permeability and capillary pressure.	249
Table 7-13	Initial and final values during the search process.	250
Table 7-14	Parameters after fitting three different surfactant blends.	256
Table 7-15	Description of steps during imbibition.	264
Table 7-16	Some values of properties for calculations during imbibitions experiments.	273
Table 7-17	Dimensions of capillaries used.	280
Table 7-18	Comparision among permeability ratios for capillaries, glass beads and reservoir rock.	282
Table 3C-1	Parameters for Jeffrey Model for AOS.	348
Table 5F-1	List of sacrificial agents.	369
Table 5F-2	List of titration reagents and indicators.	371
Table 7A-1	Surfactants and salts.	377

Table 7A-2 Information of surfactants. 377

Table 7C-1 Parameters for capillary desaturation curve. 378

Table 7G-1 Composition synthetic brine. 381

Table 7J-1 Parameters for porous media. 384

LIST OF FIGURES

Figure 2-1	Cartoon of surfactants located at the interface. Non-ionic, anionic, zwitterionic and cationic, labeled from left to right	10
Figure 2-2	Foam in poruous media	12
Figure 2-3	Mechanism of capillary snap-off	16
Figure 2-4	Cartoon representing the lamella division	17
Figure 2-5	Cartoon representing the leave-behind mechanism of lamella generation	18
Figure 2-6	Cartoon representing foam destruction	19
Figure 2-7	Interaction between surfactant molecules, and molecules in aqueous and organic phases	31
Figure 2-8	Characteristic curvature of surfactants	38
Figure 3-1	IFT Of crude Oil in 5% NaCl Brine at room temperature	44
Figure 3-2	Viscosity as function of temperature for dead crude oils, and a dead oil filtered at 50°C	45
Figure 3-3	Viscosity of crude oil measured in the Couette flow viscometer.	46
Figure 3-4	Viscosity of Reservoir Fluid at 237°F	47
Figure 3-5	Composition of cyclohexane and dead oil to the live oil viscosity	49
Figure 3-6	Water receding contact angles at room temperature	52
Figure 3-7	Water advancing angle after ageing	53
Figure 3-8	Water advancing angle	54

Figure 3-9.	Viscosity curve for surfactant blends	55
Figure 3-10	The viscoelasticity of the blend CAPB+C_{16-18}AOS+BTC	56
Figure 3-11	Comparison of the viscosity measured at high shear rate.	57
Figure 3-12	Room temperature rheogram for LB+C_{16-18}AOS 1% in seawater	58
Figure 3-13	Cartoon of cross section of worm-like micelle, adapted from Lopez-Diaz and Castillo (2010)	60
Figure 3-14	Surface tension for LB+C_{16-18}AOS 2:1 (w/w) in seawater at 25ºC	63
Figure 4-1	Relationship of the retardation time and mass percentage of $CaSO_4$ in dolomite rock	66
Figure 4-2	Relation of Retardation time and porosity or the rock; the effect worsens for less porous media	67
Figure 4-3	Excess of the main ions respect to typical seawater and ionic strength	69
Figure 4-4	Indicate the composition of the water for the different wells in this study	70
Figure 4-5	Saturation temperature respect to anhydrite for the seawater.	75
Figure 4-6	Prediction of the solubility of calcium sulfate at different temperatures	76
Figure 4-7	Solubility of calcium sulfate in a 20% mass NaCl brine at different temperatures	77
Figure 4-8	Saturation index for anhydrite for different formation brines	79

Figure 4-9	Sample from a carbonate reservoir before and after treated in the shaker box	81
Figure 4-10	Zoom of a section of the response of the intensity for three different samples; anhydrite, sample (F1A) and dolomite	82
Figure 4-11	Sample before trimming, before cleaning after being cut and after the cleaning process	83
Figure 4-12	Samples of rock formation, dolomite used in adsorption experiments, and doped dolomite	84
Figure 4-13	XPS for core sample	87
Figure 4-14	Peaks for quantification of O, C, Ca and Mg	88
Figure 4-15	The Silicon quantification	88
Figure 5-1	High pH titration	97
Figure 5-2	Comparison of different techniques for titrating SDS	98
Figure 5-3	Effect of bromocresol green for titration at high pH	99
Figure 5-4	Verification of titration techniques (1) of (2)	100
Figure 5-5	Verification of titration techniques (2) of (2)	101
Figure 5-6	Appearance of samples after 90°C for a week in seawater	103
Figure 5-7	Test Results of thermal stability UT old, 1-week testing in seawater at 90°C	104
Figure 5-8	Effect of adding polyacrylate to Old UT Blend	104
Figure 5-9	UTold + Polyacrylate 500 ppm 1- week 90°C	106
Figure 5-10	Effect of additives on Static adsorption on dolomite powder of the Old UT Blend	107

Figure 5-11	Total Surface Concentration, aged 2 days at 90ºC	108
Figure 5-12	Static adsorption; UTNew Blend in Seawater at 90°C	109
Figure 5-13	Summary of Static Adsorption Test Results at 90°C	110
Figure 5-14	Aqueous surfactant solutions in DI water after ½ week	111
Figure 5-15	Adsorption estimation	114
Figure 5-16	Surfactant solutions of CAPB	117
Figure 5-17	Chromatogram of CAPB at low pH buffer	117
Figure 5-18	Comparison peaks for the Lauramidopropyl betaine and Myristamidopropyl betaine (peaks) in the CAPB sample	118
Figure 5-19	Dependence of pseudo first order constant.	119
Figure 5-20	Pseudo first order constant rate for hydrolysis of CAPB	121
Figure 6-1	Figure Cartoon to simplify the porous structure of a rock	123
Figure 6-2	Laplace domain response if double porosity model is used	133
Figure 6-3	Double porosity model, using finite core boundary condition	134
Figure 6-4	Different views of a low permeability sample from the formation	142
Figure 6-5	Different views of a high permeability sample from the formation	142
Figure 6-6	Actual cores used during dynamic adsorption experiments	143
Figure 6-7	Core sample preparation	144
Figure 6-8	Experimental setup	145

Figure 6-9 Seawater and formation brine fit well the Nikolsky-Eisenman equation 147

Figure 6-10 Surfactants and tracer response in the effluent from Silurian dolomite 149

Figure 6-11 Surfactants and tracer response in the effluent after contacting composite PEMEX rock at 99°C 151

Figure 6-12 Mass ratio of IOS respect to the total surfactant blend in the effluent 152

Figure 6-13 Parameters used during the fitting in Laplace domain, f=0.3, N_{St12}=1, N_{Pe12}=20 161

Figure 6-14 Comparison of the response of tracer and surfactant using the triple porosity model for the low permeability composed core 162

Figure 6-15 Tracer and surfactant comparison response using the triple porosity model for the high permeability Silurian outcrop core 164

Figure 6-16 Simulated response of a finite slug of Anionic or Amphoteric surfactant respect to a tracer in dolomite rock, assuming adsorption 100% irreversible 165

Figure 6-17 Simulated response of a finite slug of Anionic or Amphoteric surfactant respect to a tracer in dolomite rock, assuming that some desorption may occur 166

Figure 6-18 Simulated response of a finite slug of Anionic or Amphoteric surfactant respect to a tracer in dolomite rock, assuming adsorption is reversible 167

Figure 6-19	Preliminary results of surface area using NMR	172
Figure 7-1	Binary anionic surfactant blends used in the research	176
Figure 7-2	Surfactant blend scan used characterize the surfactants	177
Figure 7-3	Experimental setup	183
Figure 7-4	Phase behavior map, and graphic representation of the dilution path for foam experiments	187
Figure 7-5	Oil recovery for different tests	189
Figure 7-6	Capillary desaturation curves for the three scenarios	190
Figure 7-7	Silica sand sample	194
Figure 7-8	Pictures of the sand pack at the end of the test “6”	195
Figure 7-9	Oil recovery during test “6”	199
Figure 7-10	Flow sequence in test “6”	200
Figure 7-11	Oil recovery during test “6”	201
Figure 7-12	Sequence of injection of phases during test “7” and the history of apparent viscosity	202
Figure 7-13	The plot corresponds to the mixture of Triton X200 (C_9-ϕ-$(EO)_{8.6}$ SO_3Na) and internal olefin sulfonate C_{20-24}IOS in proportion 70:30 (w/w)	204
Figure 7-14	Phase behavior map and snapshots of blend scan for seawater and for 50% seawater-50% formation brine	205
Figure 7-15	Foam apparent viscosity for the $C_{12}(EO)_7SO_3Na$ + C_{20-24} IOS blend (60/40) in seawater	206

Figure 7-16 Transient of starting a foam experiment. System $C_{12}(EO)_7SO_3Na$ + C_{20-24} IOS Blend 60:40 (w/w) in seawater 207

Figure 7-17 Pressure drop response during flow rate perturbation for the aqueous phase 209

Figure 7-18 Transient of starting a foam experiment. System: $C_{28}H_{57}(PO)_{25}(EO)_{25}CO_2Na$ + C_{15-18} IOS in seawater 210

Figure 7-19 Solubility scan at 1% total surfactant concentration in synthetic seawater at 30°C 217

Figure 7-20 Solubility map for 1% total surfactant concentration in synthetic seawater at room temperature 218

Figure 7-21 Solubility map at room temperature for the pseudo ternary surfactant system. 219

Figure 7-22 Solubility scan at 1% total surfactant concentration in synthetic seawater at 30°C 219

Figure 7-23 Viscoelasticity of cationic-zwitterionic blends 221

Figure 7-24 Transient of AOS foam 223

Figure 7-25 Apparent viscosity vs. total flow rate for quality between 0.7 and 0.78 at 94°C, 1% C_{16-18}AOS in NaCl brine at seawater ionic strength 225

Figure 7-26 Foam quality effect on apparent viscosity at a total flow rate of 3 cm^3/min 226

Figure 7-27 The surfactant flow rate was 1 cm^3/min, Nitrogen injection at 10 sccm 227

Figure 7-28 The surfactant flow rate was 1 cm^3/min, Nitrogen injection at 10 sccm. System: 1% LB+C_{16-18}AOS, 2:1 (w/w) in synthetic seawater 228

Figure 7-29 Production of oil, collected during co-injection of simulated live oil and foam 229

Figure 7-30 Apparent viscosities of three different experiments. System: 1% IMP in synthetic sea water 232

Figure 7-31 Effect of quality for IMP formulation at two different flow rates. System: 1% IMP in synthetic sea water 233

Figure 7-32 Comparison of foam strength for different surfactants at 94°C and 1% total surfactant concentration in a sand pack, using qualities between 60 -70% 235

Figure 7-33 Viscosity of 1% surfactant solution in syntheric seawater. 236

Figure 7-34 Effect of foam quality on apparent viscosity for CAPB+C_{16-18}AOS and LB + C_{16-18}AOS at 1% total surfactant concentration in synthetic seawater, 94°C 237

Figure 7-35 Effect of gas quality on foam viscosity for 0.33% Overall blend concentration in synthetic seawater at 94°C for a constant total flow rate of 3 cm^3/min 238

Figure 7-36 Values of "*fmdry*" after the fitting process using a default value of "*epdry*" 250

Figure 7-37 Apparent viscosity comparison, between experimental values and simulated values 252

Figure 7-38 Apparent viscosity comparison, dashed lines obtained after fitting the value of u_{ref} in equation 7-28 255

Figure 7-39 Simulation of the foam viscosity using the mobility reduction factor approach 257

Figure 7-40 Apparent viscosity comparison for IMP formulation, simulation and experiments 259

Figure 7-41 Apparatus to test formulation 262

Figure 7-42 Components of apparatus for imbibition experiment in foaming environment. 263

Figure 7-43 Oil recovery from a 40 mD formation core saturated with simulated live crude oil 265

Figure 7-44 Imbibition test results for 3 similar plugs of Silurian core saturated with synthetic Pemex oil 84/16 wt crude /Cyclo-C6 and seawater 267

Figure 7-45 Appearance overtime of " LB + C_{14}AOS + BTC" solution 269

Figure 7-46 Comparison % OOIP recovery for two systems 270

Figure 7-47 Relationship between inverse of Bond number, and the product of remaining wetting phase saturation by the Bond number 274

Figure 7-48 Analytical vs. experimental oil recovery 275

Figure 7-49 Comparison of analytical solution, empirical solution and experimental for "LB + C_{14}AOS + BTC" 277

Figure 7-50 Remaining non-wetting phase saturation for different permeabilities, data adapted from Schechter *et al*. (1994) 279

Figure 7-51 The matrix has three ranges of permeability. (Adapted from personal communication with Antonio Villavicencio, PEMEX) 281

Figure 7-52 Snapshots during gravity drainage in micro-channels 283

Figure 7-53 IFT calculation by the shape of drops emerging from capillary immersed at 90°C in Rice Formulation for Pemex Gas Cap 284

Figure 7-54 Oil recovery history curves from capillaries immersed in aqueous surfactant solution 289

Figure 7-55 Setup to study distribution of fluids within a system with contrasting permeabilities 291

Figure 7-56 Frames taken during horizontal foam experiment 292

Figure 7-57 Pictures taken after foam test using 100 μm capillary 293

Figure 7-58 Oil recovery history curve from horizontal capillary filled with crude oil, immersed in flowing foam 295

Figure 7-59 Frames of upper section of capillary every 12 s 296

Figure 3A-1 Comparison of IFT for crude oils 345

Figure 3B-1 Viscosity measured using Couette flow viscometer. 346

Figure 3B-2 Evolution of AKAL crude oil viscosity at 60°C exposed to atmosphere 346

Figure 3C-1 $C_{16\text{-}18}$ AOS 1% Effect of divalent ions 347

Figure 3D-1 Prediction of rheology at high temperature using Kuryashov approach 349

Figure 3E-1 High temperature falling sphere viscometer 351

Figure 3F-1 Contact angle measurement 352

Figure 3G-1 Comparison of different surfactants and surfactant blends 353

Figure 3G-2 Precipitate and/or coacervates observed in presence of high concentration of divalent cations in aqueous solutions 355

Figure 4A-1 Intensity response of the powder XRD from a rock sample and a sample of dolomite 356

Figure 4A-2 Intensity response of the powder XRD from a rock sample and a sample of anhydrite 356

Figure 4C-3 Comparison of saturation index for a seawater with different pH 358

Figure 4C-4 Saturation index of a formation brine with high content of silica 359

Figure 4C-5 Incremental solubility of the seawater at low and high pressure. 359

Figure 4C-6 Incremental solubility of the synthetic formation brine used in the experiments during core flooding 360

Figure 4C-7 Most of the formations at low salinities 361

Figure 5B-1 Evolution of the titration at low pH. 364

Figure 5E-1 Evolution of the titration for CAPB 367

Figure 5E-2 Comparison of titration for CAPV and LB 368

Figure 5F-1 Aqueous stability of surfactant solutions 370

Figure 6A-1 Curve during the first stage of cleaning, while injecting aqueous brine with no surfactant 373

Figure 6A-2 The collect effluents after titration are used to estimate the total adsorption after mass balance during the cleaning 374

Figure 6B-1 Representation of a piece of core material with macro pores and dendritic pores 375

Figure 6B-2 The zoom in the micro pore space 376

Figure 7D-1 Aqueous stability in UT blend with LB in seawater 379

Figure 7D-2 Aqueous stability in UT blend with LHS in seawater 379

Figure 7D-3 Aqueous stability in UT blend with LHS in UT brine 380

Figure 7E-1 Crude oil in Plateau Borders 380

Figure 7G-1 Brine comparison 381

Figure 7J-1 Pseudorheology for foam LB + AOS 385

Figure 7K-1 Start up of 1% IMP formulation in sea water . 385

Figure 7K-2 Transient to see the effect of stopping liquid injection. 386

Figure 7K-3 Resume of foam, and transient after stopping gas injection. 386

Figure 7L-1 Oil recovery from a bundle capillaries 387

Figure 7L-2 Comparison of normalized oil recovery by gravity 388

Figure 7L-3 Normalized oil recovery from micro-channels 388

Chapter 1

INTRODUCTION

1.1 Enhanced oil recovery

There exist three classical steps in oil recovery reported by Bavière (1991). Primary recovery when hydrocarbons are extracted from the reservoir by means of wells drilled from the surface into it. If the initial pressure inside the reservoir is high, the oil, gases and even water may be produced. In primary recovery, if the pressure is decreased, a pumping system can be used, but at a point when the proportion of gas and water to oil is high, and the pressure low, its limit is reached (when the production becomes too small). This stage is characterized for its small recovery (around 10% in average). Lake (1989) indicates that oil is recovered by natural drive mechanisms: solution gas, water influx, gas cap drive or gravity drainage. Secondary recovery is when water or gas is injected in order to maintain a high pressure inside, and not only to maintain pressure but push forward the oil contained in the reservoir towards the producing wells. But this can’t last forever; it becomes no longer cost effective when the extracted fluid has a high ratio of injected fluids to oil. Therefore if both primary and secondary processes are used only a fraction from 15% to 60% can be obtained. Tertiary recovery is any technique applied after secondary recovery.

Enhanced oil recovery (**EOR**) is oil recovery by injection of materials not normally present in the reservoir, covering all modes of recovery processes (drive, push-pull, and well treatments), and many oil recovery agents, and is not restrictive of any of the phases of recovery (i.e. primary, secondary or tertiary). Injection of a displacing fluid may begin in early stages, even before depletion in the stage of primary recovery. Techniques for improving displacement and sweep efficiencies may be used from the beginning. Those techniques and processes are called enhanced oil recovery.

1.2 Foam for EOR

The use of surfactant solutions that increase oil recovery has been deeply studied. In the sixties it was proposed to use foams instead of just aqueous surfactant solutions as displacement agents. The first experiments showed that oil from porous structures unrecoverable by conventional water or gas drives could be displaced by foam. The efficiency of the foam was believed to be the result of the high foam viscosity (apparent viscosity) and its penetration in pores of various sizes. Laboratory research has indicated that the foam-drive process can recover a significant proportion of the oil remaining in unconsolidated sand packs subjected to conventional secondary recovery operations. Exerowa and Kruglyakov (1998) reported that researchers experimented with crude oils and unconsolidated porous media, indicating that total recovery increased from 60% (from water flooding) to 90% after foam injection using 36 foaming agents (23 anionic, 6 non-ionic and 7 amphoteric) to establish the effect of foam quality (gas

volume fraction), the surfactant kind and concentration, the mode of the foam injection and the foam bank size on the displacement ability of the foam. The main point of these experiments was that the oil recovery changed with the quality of foam and the permeability.

Yan *et al.* (2006) investigated different factors' effects on sweep efficiency by foam in smooth heterogeneous fractures and applied their theory to that situation assuming the same gas fractional flow in each portion of the fracture and no cross-flow. Their study was based on the fact that foam can reduce viscous fingering and gravity override caused by the low viscosity and density of the gas. They consider foam to improve efficiency of a surfactant process for oil recovery in a reservoir consisting of multiple fractures separating matrix blocks where oil is retained by capillarity and/or wettability. Yan *et al.* (2006) concluded that foam can greatly improve the sweep efficiency in a heterogeneous fracture system. Sweep efficiencies can be affected by gas fractional flow, aperture ratio and bubble size.

The use of foams to improve oil recovery has been used in lab scale and has been tested in real reservoirs, according with Blaker *et al.* (1999), and predictions based on laboratory experiments and simulations seem to match with results of real processes. Opportunities for research to deeply understand all the phenomena in foam processes as stated by Kovscek *et al.* (2002) are numerous.

In this project the study is centered on finding formulations to produce foam applicable at harsh conditions of seawater and formation brine and temperature ca. 94°C, and to understand the limitations of different surfactants proposed to recover oil from a carbonate reservoir for a particular crude oil, though detailed results applicable to that reservoir, many trends and conclusions have wider applicability. The limitations of the surfactants studied are from the point of view of adsorption, aqueous stability, transport, and oil recovery

1.3 Thesis scope and organization

The transport of components and phases plays a fundamental role in the success of an EOR process. Because many reservoirs have harsh conditions of salinity, temperature and rock heterogeneity, which limit process options, a robust system with flexibility is required. This research is focused on the transport of surfactant for EOR applications of foam with the potential to generate strong foam, have aqueous stability, be tolerant to salinity and hardness, and at the same time be able to reduce IFT and/or change wettability. Limitations for any surfactant to be used include: excessive adsorption/retention, thermal degradation, or reaction in the formation. Those limitations were studied in the project. Not only the transport of phases through the pore bodies and throats in porous media, but also transport in a fractured reservoir is of interest. Fractures increase the importance of heterogeneities of the porous media, a matter addressed in this project.

This dissertation is divided in chapters with the following content:

Chapter 2 introduces basic background about surfactants, some principles of foams and its formation in porous media, and ideas that are in the common use to guide the understanding of how surfactant can change its behavior in oil-water systems, by changes in salinity, temperature, hydrocarbon composition and type of surfactant.

Chapter 3 deals with interfacial and transport properties of crude oil and surfactants blends. It includes measurements of interfacial tension, surface tension, contact angle, viscosity, and rheology of fluids used during the research. Some measurements were done only at room temperature, but most of them were done at both room temperature and 94°C or reservoir temperature. Measurements were required to plan experiments in chapter 7, and for the analysis of the results.

Chapter 4 Anhydrite determination in carbonate formations, presents a methodology to estimate the amount, if any, of anhydrite present in the reservoir. This chapter presents results of experimental measurements, and principles of thermodynamics that can be used to infer the potential to find anhydrite in a formation using software to process reports of water analysis and conditions of pressure and temperature in the formation.

Chapter 5 contains the description of techniques to measure: concentration of the surfactants, thermal stability of surfactants, and adsorption of surfactants on

dolomite rocks. It briefly describes as well studies to test if scale inhibitors, chelating agents or sacrificial agents have potential to reduce adsorption of surfactants on rocks.

Chapter 6 presents the methodology to measure adsorption of surfactants, with aid of dynamic experiments, and results are presented. It also describes the study of flow properties of the rock samples via tracer analysis. This chapter includes the simulation of the dynamic adsorption process using a mathematical model proposed that considers the distribution of adsorbed materials in the three different regions of pore space.

Chapter 7 includes results of foam experiments to screen surfactants blends with potential to produce foam. Describe evaluation of surfactants from the point of view of foam strength during oil recovery in core floods experiments, and imbibition experiments. It presents analysis of imbibition experiments done using surfactant blends with potential to produce strong foams. There is discourse about the fitting process of a model to simulate foam in steady state. It discuss the results of experiments for visualization of oil recovery mechanism from matrix using micro-channels surrounded by glass beads to mimic matrix and fractures respectively, to illustrate how components may distribute within the matrix of the rock, thereby releasing oil into the fractures.

Chapter 8 Conclusions and recommendations for future work.

Chapter 2

TECHNICAL BACKGROUND

This chapter will discuss some important aspects about surfactants, foam and phase behavior. The rest of the technical background will be discussed in the following chapters for the particular application.

2.1 Amphiphiles and Surfactants

The word amphiphile comes from two Greek roots, the prefix amphi which means double, and the root philos which means affinity, Salager (2002). An amphiphilic substance exhibits a double affinity, which can be defined from the physico-chemical point of view as a polar-apolar duality. A typical amphiphilic molecule consists of two parts. One part is a polar group which contains heteroatoms such as O, S, P, or N, included in functional groups such as alcohol, thiol, ether, ester, acid, sulfate, sulfonate, phosphate, amine, amide, etc,. The other part is the apolar group which can be a hydrocarbon chain of the alkyl or alkylbenzene type, sometimes with even a few nonionized oxygen atoms as in a propylene oxide or butylene oxide chain. The polar portion exhibits a strong affinity for polar solvents like water, and it is often called hydrophilic part. The apolar portion is called lipophile, from Greek root lipos which means grease.

The word surfactant (i.e., *surface-active-agent*) is a substance which exhibits some superficial o interfacial activity. According to Salager (2002) not all the amhiphiles display activity, only the amphiphiles with more or less equilibrated hydrophilic and lipophilic tendencies are likely to migrate to the surface or interface.

Amphiphiles exhibit other properties than tension lowering and this is why they are often named according to their use such as: antistatic agent, bactericide, biocide, corrosion inhibitor, detergent, dispersant, emulsifier, foaming agent, soap, surfactant, wetting agent, etc.

2.2 Classification of surfactants

A simple classification of surfactants is based on the nature of the hydrophilic group. Several classes may be distinguished like anionic, cationic, amphoteric and non-ionic, Tadros (2005). Typical cartoons of the surfactants are included in fig 2-1

Nonionic surfactants carry no electrical charge, as their water solubility is derived from the presence of polar functionalities capable of significant hydrogen bonding interaction with water (e.g., polyoxyethylenes, sugars, polyglycidols).

Anionic surfactants contain anionic functional groups at their head, such as sulfate, sulfonate, phosphate, and carboxylates, etc.

Zwitterionic (amphoteric) surfactants have both cationic and anionic parts attached to the same molecule. The cationic part is based on primary, secondary, or tertiary amines or quaternary ammonium cations. The anionic part can be more variable and include sulfonates, or carboxylate. Some common surfactants include sultaines, betaines, amidopropyl betaines, sulfo-hydroxy betaines, etc.

There are a wide variety of chemical structures possible of amphoteric, four main classes can be found commercially available. Those classes, and their predominant ionic forms and ionization characteristics are summarized as follows according to Myers (2006):

- **Class 1**. Amine/carboxylic acids containing both free amine (–**NR_2**) and free acid (–**COOH**) functional groups. These will be cationic at low pH (**R–N^+R_2H–R–COOH**), isoelectric near neutral pH (**R–N^+R_2H–COO^-**), and anionic at high pH (**R–NR_2 –COO^-**).
- **Class 2.** Quaternary ammonium/carboxylic acids. These materials contain a permanent cationic site (**–N^+R_3**) as well as the carboxyl group. At low pH they will be cationic. At slightly alkaline pH they will become isoelectric and remain so. They can never become anionic.
- **Class 3**. Amine/sulfonic acids (or sulfate ester). Having the strong acid sulfonic acid group, which is highly ionized even at low pH, these materials will form internal salts and will be isoelectric in very acidic media. As the pH is raised, the protonated amine is neutralized to yield a net

anionic species. These materials are essentially the opposite of the class 2 surfactants.

- **Class 4.** Quaternary ammonium/sulfonic acids (or sulfate esters). Possessing both the permanent cationic charge of the quaternary ammonium group and the highly ionizing strong acid, these materials will be isoelectronic over most of the pH range, except at very low pH under conditions where ionization of the acid may be suppressed.

Cationic surfactants are those in which the hydrophilic portion contains a positively-charged ion, or cation. Typical examples are trimethylalkylammonium chlorides or bromides, and the chlorides or bromides of benzalkonium and alkylpyridinium ions. The examples given are called quaternaries, because they all contain a quaternary ammonium ion.

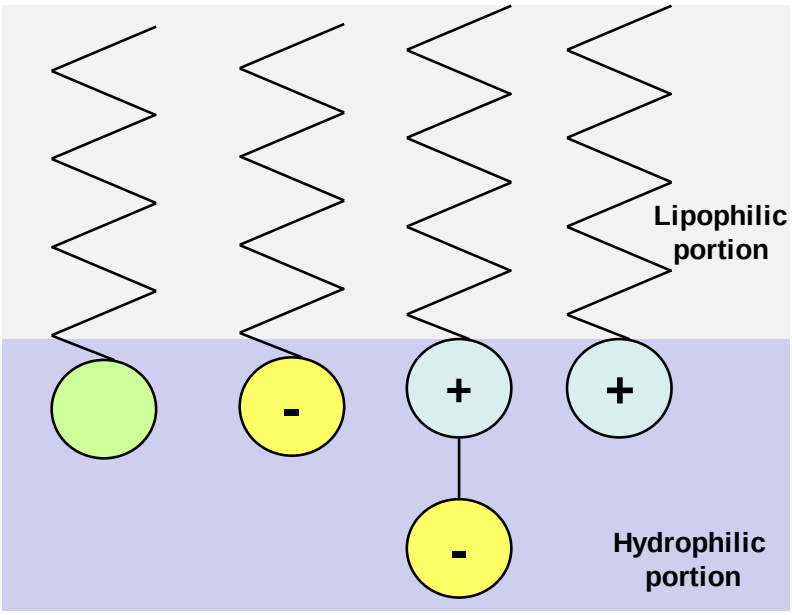

Figure 2-1 Cartoon of surfactants located at the interface. Non-ionic, anionic, zwitterionic and cationic, labeled from left to right.

Most of the types of surfactants described in this section were used during this project. They were used to produce reduction of the interfacial tension, to modify wettability and/or as foaming agents.

2.3 Fundamentals of Foam Flow in Porous Media

The behavior of the foam in porous media is related to the connectivity and geometry of the rock. Porous media have several characteristics that are important to the flow of foam, like the size distribution of the pores and throats. Foam mechanisms for generation and destruction of lamellae depend strongly on the body to size aspect radio. For large pores occupied mainly by the non-wetting fluid, the wetting fluid resides in the corners and in thin wetting films coating the pore walls. The non-wetting phase resides in the central portion of these large pores. Small pores are filled with wetting fluid. Then the wetting phase remains continuous. During two-phase flow, the non-wetting fluid flows in interconnected large pore channels, while wetting fluid flows in interconnected small channels and in corners of non-wetting-phase occupied pores because of pressure gradients in the wetting phase.

Bulk foam is present when the length scale confining the fluids is greater than the length scale of the bubbles, and can be classified as “kugelschaum” (i.e. ball foam) and “polyderchaum” (i.e. polyhedral foam). In the first category, spherical bubbles well separated conform the foam, and in the second category the bubbles are separated by thin films or lamellae. When the foam flows in porous

media, bubbles and lamellae span completely across the porous space and are called confined foam according to Radke and Gillis (1990).

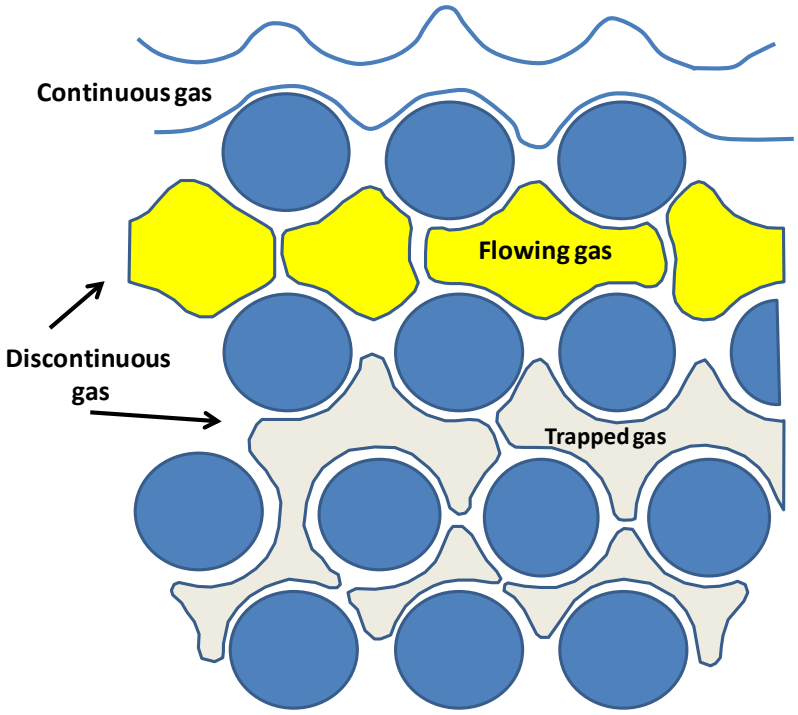

Figure 2-2 Cartoon of three different forms that gas can take in porous media

When the characteristic pore size is comparable to or less than the characteristic size of dispersed gas bubbles, the bubbles and lamellae span pores completely. At low gas fractional flow, the pore spanning bubbles are widely spaced, separated by thick wetting liquid lenses or bridges. At high gas fraction flow, the pore-spanning bubbles are in direct, contact, separated by lamellae. Hirasaki and Lawson (1985) denoted this direct-contact morphology as the individual-lamellea regime.

Although both bulk foam and individual-lamellae foam can exist in principle, effluent bubble sizes equal to or larger than pore dimensions are usually reported. It is generally accepted that single bubbles and lamellae span the pore space of most porous media undergoing foam flow in the absence of fractures.

Fig 2-2 shows the schematic of foam in porous media. The gas can be trapped or flowing as a continuous or discontinuous phase. In discontinuous gas foam, the entire gas phase is made discontinuous by lamellae, and no gas channels are continuous over sample-spanning dimensions. Gas is encapsulated in small packets or bubbles by surfactant-stabilized aqueous films. In continuous gas foam, the media contain some interconnected gas channels that are interrupted by lamellae over macroscopic distances much greater than pore dimensions.

Discontinuous foam forms under co-injection of gas and surfactant solution, provided that the wetting phase saturation and flow rate are high enough for foam generation. When the wetting phase saturation is low enough, the lamellae generation rate may become lower than the rupture rate, and paths of continuous gas flow may result.

Fig 2-2 is also a summary of the pore-level microstructure of foam during flow through porous media. Because of the dominance of capillary forces, wetting surfactant solution flows as a separate phase in the small porespaces. A minimal amount of wetting liquid transports as lamellae. So the wetting-phase relative permeability is unchanged when foam is present. When both flowing and trapped gas exist, flowing foam occurs in large pores because the resistance there is less

than in the smaller pores. Then bubble trapping can happen only in intermediate sized pores.

Thus, foam can be classified into “weak” foam and “strong” foam. For “weak foam” with no moving lamellae, the increase in trapped gas saturation is important to the behavior of foam flow as it results in the blockage of gas pathways, which reduces the relative permeability of gas. The trapped gas reduces mobility, but the rest of gas flows as continuous gas.

“Strong” foam flows by a different mechanism. The lamellae make the flowing gas discontinuous. Then the bubbles trains face much higher resistance than in continuous gas flow. The apparent viscosity of the discontinuous foam is much greater than in continuous foam. The combined effect of the reduction of gas relative permeability and the increase of apparent gas viscosity greatly increases the mobility reduction effect of foam.

The most important factors that affect foam trapping and mobilization are pressure gradient, gas velocity, pore geometry, bubble size, and bubble-train length. Increasing the pressure gradient can open new channels which were occupied by trapped gas.

2.4 Mechanism of Foam Formation and Decay

The identity of a single bubble or train is not conserved over large distances in porous media. Bubble trains usually exist in a time-averaged sense. The bubbles

are continually destroyed and created. It is necessary to understand the mechanism of foam formation and decay.

2.4.1 Foam Formation

Three fundamental pore-level foam generation mechanism are generally accepted: capillary snap off, lamella-division and leave-behind. Capillary snap-off and lamella-division generate strong foam or discontinuous gas foam. while leave-behind generates weak foam or continuous gas foam.

2.4.1.a Capillary snap-off

Capillary snap-off can repeatedly occur during multiphase flow in porous media regardless of the presence or absence of surfactant. It is recognized as a mechanical process. As in Fig 2-3 a, a gas finger first enters a liquid filled pore throat. At that time, the interface curvature and capillary pressure rise to the equilibruim entry value. As bubble passes through the pore throat, the curvature and the capillary pressure at the bubble front fall with the expansion of the interface (see figure 2-3 b). A pressure gradient develops which drives liquid from the pore body toward the pore throat, where it accumulates. As a collar grows, snap-off occurs. Then generated foam bubble has a similar size to that of the pore bodies (see figure 2-3c).

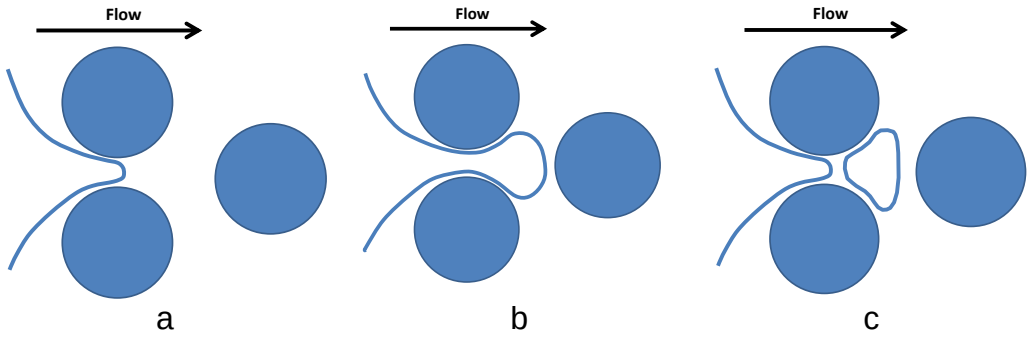

Figure 2-3 Mechanism of capillary snap-off. Adapted from Kovscek and Radke 1993.

Snap-off depends on liquid saturation or, equivalently, on the medium capillary pressure. Except for alteration of solution properties such as surface tension, it is essentially independent of surfactant formulation.

2.4.1.b Lamella division

Lamella division occurs when lamellae already exist, and the pressure gradient must be large enough to mobilize the lamellae. As indicated in Fig 2-4, a moving lamella train encounters a point where flow branches in two. Then the lamella may split into two and enter both flow paths.

The most important factors that govern lamella division are the pressure gradient, pore geometry and the bubble size. The bubble size must be larger than that of the pore body for the lamella to span the pore space. When the flowing lamella train is surrounding by stationary lamella, lamella division does not happen because the stationary lamellae or bubbles can act as pore walls to prevent branching of the flow. Rossen (2003) suggested that lamella division should also

depend on the pressure gradient and be proportional to gas velocity. Lamella division can generate discontinuous gas foam, which is strong foam.

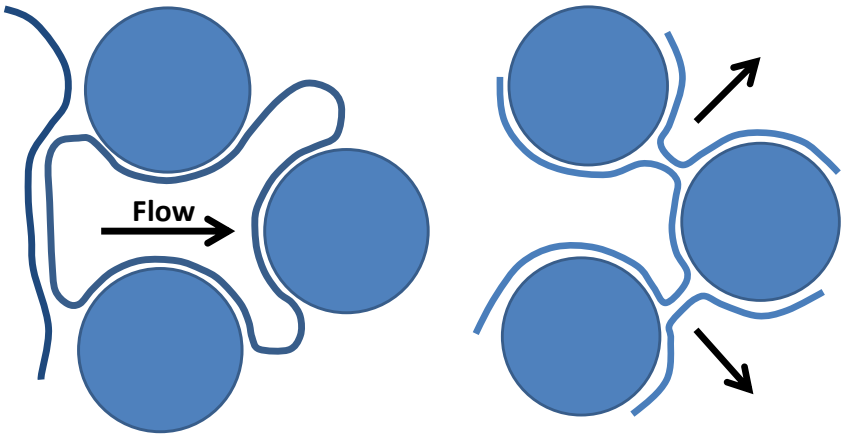

Figure 2-4 Cartoon representing the lamella division

2.4.1.c Leave-behind

When two gas menisci invade adjacent liquid-filled pore bodies, a lamella is left behind (see Fig 2-5) as the two menisci converge downstream. A stationary stable lamella emerges as long as the capillary pressure is not high and the pressure gradient is not large.

The lamellae or lenses from leave-behind are generally oriented parallel to the local direction of flow, and can generate only continuous gas foam, which is weak foam, because a continuous gas foam is produced.

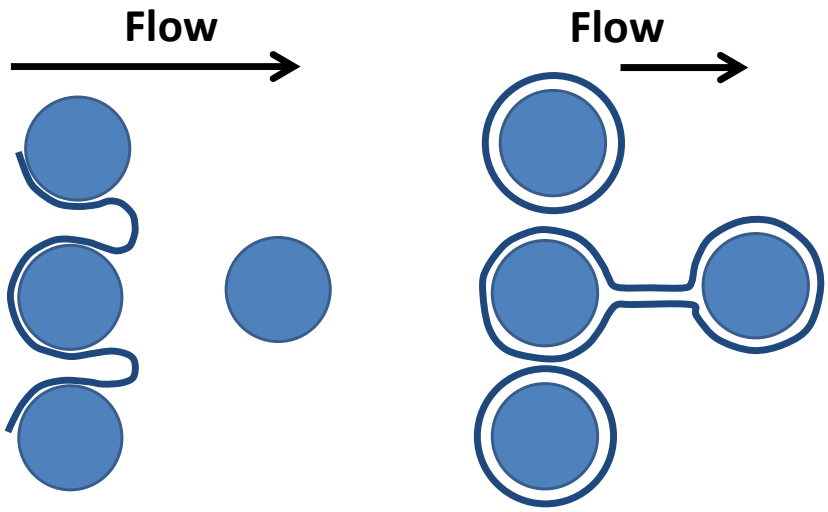

Figure 2-5 Cartoon representing the leave-behind mechanism of lamella generation

2.4.2. Foam destruction

The foam generation is often accompanied by foam destruction. Two basic mechanisms of foam destruction or coalescence have been found. They are capillary suction and gas diffusion. Capillary suction coalescence is the primary mechanism for lamella breakage. The other mechanism is coarsening by gas diffusion.

2.4.2.a Capillary suction coalescence

Coalescence due to capillary suction is strongly affected by surfactant formulation. Thin lamellae are not thermodynamically stable, and their existence is accompanied by excess normal forces within the films originating from long-range concentrated intermolecular interactions. This effect can be described as

the disjoining pressure Π, which is the combined effect of repulsive and attractive forces within a lamella as described by Miller and Neogi (2008). Here Π is a function of film thickness. When Π is positive, repulsive forces dominate. When it is negative, attractive forces are indicated. When surfactant is absent, the disjoining pressure Π is negative, which shows attractive van der Waals forces dominate. Then the lamella will collapse immediately. When a surfactant is adsorbed at the gas/liquid interface, the lamella can be stabilized. The disjoining pressure Π may be positive from the repulsive forces of the electrical double-layer caused by the adsorption of ionic surfactants. The factors determining the stability are the surfactant concentration, surfactant structure, and the ionic content of the aqueous solution.

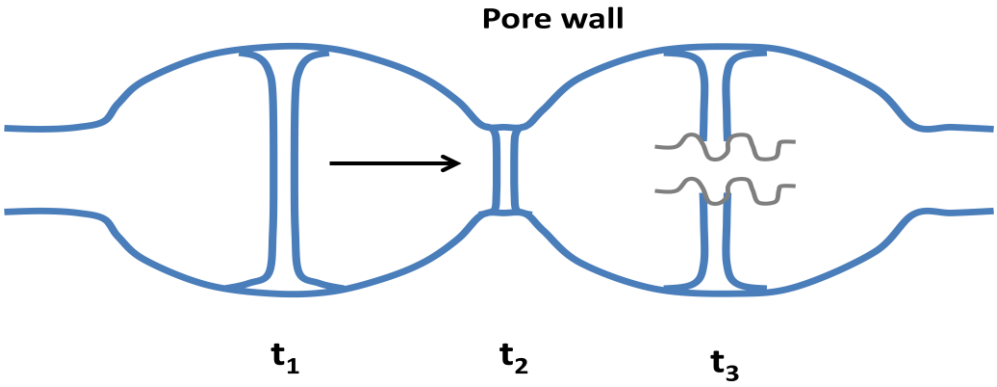

Figure 2-6 Cartoon representing foam destruction

Coalescence behavior of flowing foam bubbles is more complicated than that of static lamella. Fig 2-6, presents a lamella at successive times t_1, t_2 and t_3. As the lamella translates from left to right, it is squeezed upon entering the constriction at time t_2. Film thickness increases to conserve liquid mass, and the disjoining

pressure is corresponding low. When the film moves out of the pore constriction, it is stretched upon expansion into the downstream body. The film thins to conserve mass, and the disjoining pressure is now high. It causes film thickness to oscillate about the equilibrium film thickness established for the static film. A thin film with mobile surface will rupture during stretching if its thickness falls below the critical film thickness h_{cr} according to Jimenez and Radke (1989). Therefore, a moving thin film could rupture at a limiting capillary pressure P_c^*, which is less than the maximum disjoining pressure $\Pi_{max.}$ Thus, moving lamellae can be less stable than static ones.

Marangoni effect (Gibbs-Marangoni) is also a restoring and stabilizing force in a lamella according to Alvarez (1998). When the lamella film is stretched in the pore space, the stretching can cause a local reduction in surfactant concentration and an increase in the local surface tension (Gibbs effect) if the surfactant transports slowly to the lamella surface. Then the liquid can be dragged from locations with low surface tension to the thinner region with high surface tension works against lamella thinning.

Singh *et al*. (1997) found that Jimenez and Radke's previous theory could be applied only to a limited regime. They found that when the film surface is immobilized by surfactants, moving lamellae may be more stable than stationary lamellae according to Singh *et al*. (1997). For this case, moving lamella trains will switch paths as stationary lamellae rupture and new paths of least resistance appear. This may be preferred mode of foam flow when it is desired to contact as

much as of the porous medium as possible with flowing continuous gas foam. When the film is mobile, the stationary lamellae will be more stable than the moving lamellae. This case is in qualitative agreement with Jimenez and Radke's theory. So the choice of a suitable surfactant is important for the stability of foam in porous media.

2.4.2.b Gas diffusion

For trapped foam bubbles, the gas on the concave side of the bubbles has a higher pressure than on the convex side according to the Young-Laplace equation. Higher pressure corresponds to higher chemical potential. Driven by this difference in chemical potential, gas dissolves in the liquid film and escapes by diffusion from the concave to the convex side of the film. The film moves to the pore throat and the lamella curvature diminishes. In the porous media, coalescence takes place when two lamellae reach the same pore throat. It is mainly governed by pore dimensions and the location in the pore space.

2.5 Apparent viscosity in porous media

Hirasaki and Lawson (1985), developed the theory to predict viscosity of foam in porous media, suggesting that a reasonable conceptual model of natural porous medium is a bundle of interconnected capillaries of different sizes and constrictions. Later Falls *et al*. (1989) worked with foams in homogeneous bead packs adding the contribution of the constrictions in the porous unconsolidated media. Then the apparent viscosity can be calculated as the sum of four

contributions: (1) that resulting from slugs of liquid between bubbles or viscosity of liquid slugs between bubbles, (2) the viscous resistance of liquid between the foam bubbles and capillary wall, that manifests as an interface deformation, (3) the surface tension gradient that results from a surface gradient in surfactant concentration, and (4) the effect of pore constriction.

$$\mu_{app} = \mu_{app}^{liq} + \mu_{app}^{shape} + \mu_{app}^{grad} + \mu_{app}^{con} \qquad \textbf{(Equation 2-1)}$$

The viscosity contribution from liquid slugs in capillary tube from Hirasaki and Lawson (1985) is:

$$\mu_{app}^{liq} = \mu L_s n_L \qquad \textbf{(Equation 2-2)}$$

Where L_s is the length of liquid slugs, number of lamellae per unit length of the capillary and μ is the liquid viscosity .

The contribution of the deformation of the foam bubble to apparent viscosity in capillary tube was also reported.

$$\mu_{app}^{shape} = 0.85 \frac{(\mu n_L R)}{(\frac{r_c}{R})} (\frac{3\mu U}{\sigma})^{-1/3} \quad \left[(\frac{r_c}{R})^2 + 1\right] \qquad \textbf{(Equation 2-3)}$$

Where *U* is the velocity of bubble, σ is the surface tension, r_c is the radius of curvature of gas-liquid interface and *R* is the capillary radius.

From Hirasaki and Lawson (1985), the apparent viscosity resulting from surface tension gradient is:

$$\mu_{app}^{grad} = (\mu n_L R)(\frac{3\mu U}{\sigma})^{-1/3} \quad \sqrt{N_s}\, tanh\left(\frac{N_L}{2}\right) \qquad \textbf{(Equation 2-4)}$$

Where N_L is the dimensionless bubble length, and N_s is the dimensionless number for surface tension gradient effect. The value of N_L describes the degree of mobility of the interface. The relationship between the two dimensionless number is:

$$N_L = \frac{\left(\frac{2}{(P)_C}\right)\frac{L_B}{r_C}\left(\frac{3\mu U}{\sigma}\right)^{-1/3}}{\sqrt{N_S}} \qquad \textbf{(Equation 2-5)}$$

Where $2/(P)_c$ is a empirical constant obtained experimentally (during their experiments they found a value of 1). And they factored N_S into an empirical parameter β in the form (they got a value of 5 cm during their experiments):

$$N_S = \frac{\beta}{r_C} \qquad \textbf{(Equation 2-6)}$$

The pore constriction contribution according to Falls *et al.* (1989) has the form:

$$\mu_{app}^{con} = a_F\, \mu\, \left(\frac{3\mu U}{\sigma}\right)^{-1} \qquad \textbf{(Equation 2-7)}$$

Here the parameter a_F depends on the geometry, equivalent capillary radius R, number of lamellae per unit length n_L and the number of constrictions per unit length n_{pc}

$$a_F = \begin{cases} \xi_1 n_L R \;\; if\; (n_L < n_{pc}) \\ \xi_2 \;\; if\; (n_L > n_{pc}) \end{cases}. \qquad \textbf{(Equation 2-8)}$$

During their experiments they found (ξ_1=0.56 and ξ_2=0.037)

From the work of Hirasaki and Lawson (1985), and Falls *et al.* (1989) some conclusions can be listed.

1. At low shear, the apparent viscosity varies with the -1 power of gas velocity for the effect of constriction.
2. At higher rates, the viscosity approaches varying with -1/3 power or -2/3 power. If velocity is too high N_L is small and $tanh(N_L/2) \rightarrow N_L/2$; then apparent viscosity will approach a slope of -2/3. The dependence of apparent viscosity on the velocity is proportional to the -1/3 power of velocity when the foam is bulk foam or the velocity is low for individual lamellae, and to the -2/3 power of velocity for individual at high velocity.
3. The dependence of the apparent viscosity on the capillary radius at a constant velocity is proportional to: 5/2 power of the radius for radii that are small compared to the bubble radius and, second power of the radius for radii that are large compared to the bubble radius, Wei Yan (2006).
4. The dependence of apparent viscosity on the foam texture is proportional to: -2.0 power of the equivalent bubble radius for bubble radii that are small compared to the capillary radius and, -3 power of the equivalent bubble radius for bubble radii that are large compared to the capillary radius.

Jeong and Carapcioglu (2003) conducted experiments in glass micro-models to study the different contributions of foam to viscosity, and for their system the most important contributions were contributions of the second and the forth terms of equation 2-1.

$$\mu_{app} = \mu_{app}^{liq} + \mu_{app}^{shape} + \mu_{app}^{grad} + \mu_{app}^{con} \qquad \textbf{(Equation 2.9)}$$

These dependencies of viscosity on the velocity are the cornerstones of most of the mathematical models of foams.

2.6 Foam Modeling

Two of the most used approaches to model foam transport in porous media are the empirical and the mechanistic. Mechanistic approaches can be complete in principle, but the process to obtain reliable parameters can be complex. Empirical approaches are limited by the detail used to describe foam rheology and mobility. Mechanistic approaches include the bubble population-balance model, network/percolation theory, catastrophe theory, and filtration theory.

There is no consensus about the best approach for modeling foam in porous media. There are general principles used to guide model development (Zhou and Rossen 1995). It is generally accepted that foam should not be treated as a separate phase in porous media. Agreement exists on the concept that water mobility is the same function of water saturation with foam as without foam (Bernard *et al.* 1965) and that gas mobility in foam is controlled by foam texture (Falls *et al.* 1989).

Foam models do not need to be mechanistic to be capable of accurately describing foam transport. Kovscek (1998) suggested that successful models of foam transport at the field scale should have the following attributes:

- Reduced gas mobility in the presence of foam.
- Non-Newtonian foam flow behavior.

- Foam property variability with surfactant concentration.
- Accurate representation of surfactant transport, partitioning, and adsorption.

Models need to predict foam transport while capturing the spatial and temporal variability of foam properties, according to Radke *et al.* (1990).

2.7 Empirical Methods

Foam mobility in porous media can be expressed in terms of relative permeability and effective viscosity in the same way as for flow in porous media for Newtonian and non-Newtonian fluids:

$$\lambda_f = \frac{Kk_{rf}}{\mu_f} \qquad \textbf{(Equation 2.10)}$$

In empirical methods of foam transport, either gas mobility or viscosity or both are altered in the presence of foam based on experimental results, field observations, hypothesis or conjecture. Empirical expressions for gas mobility are usually expressed as a function of flow rates and surfactant concentration but make no explicit reference to foam texture.

One of the most used empirical methods is the “Mobility Reduction Factor” approach, which is explained in chapter 7.

2.8 Mechanistic Methods

The major challenge to developing a mechanistic foam simulator is tracking changes in foam texture. These changes result from dynamic mechanisms of *in-situ* lamella creation and coalescence, which in turn, results in changes in the gas mobility and pressure gradient. The concept of tracking the bubble population has been used in many methods for foam simulation Kovscek *et al.* (1993 and 1997).

The most important things that the “Mobility Reduction Factor” approach and the “Bubble population model” have in common is that they modify the gas relative permeability and/or the viscosity of the gas phase. However, in the bubble population model the gas relative permeability is multiplied by the gas flowing fraction.

In the mechanistic models, the conservation equations are solved with the dynamics of generation and destruction of foam.

2.9 Phase behavior

2.9.1 Solubilization

The volumes of hydrocarbon and water dissolved within the micellar solution are quantities of considerable practical interest since the bleding of oil and water to form a single thermodynamically stable phase is often purpose of amphiphiles. That amount of water and oil in a micellar solution is termed “solubilized volumes

are V_w and V_o, denoting water and oil respectively. Since V_w and V_o depend on the amount of amphiphile present, it perhaps better to consider them per unit amount of surfactant. Thus “solubilization parameters” SP_o and SP_w have been defined for oil and water, respectively, as

$$SP_o = \frac{V_o}{V_s} \quad \text{and} \quad SP_w = \frac{V_w}{V_s}$$

Where V_s is the volume of surfactant contained in the micellar phase.

At low salinity the volume of oil dissolved in the aqueous micellar phase is very small. An increase in the electrolyte concentration results in an increase in the solubilization of oil (see table 2-2). For Winsor type I systems, very little water is in the organic phase and virtually all the water is contained in the micellar phase. SP_w is therefore essentially constant as long as Winsor type I behavior is maintained. When the Winsor type III regime is reached, water is expelled from the micellar phase and SP_w decreases. At the same time, the oil uptake in this phase continues to increase up to the point where all the oil present in the system is solubilized. A Winsor type II system is then obtained and further increase in the salinity results in a constant value of SP_o, while SP_w is seen to decrease regularly. It is interesting to point out that in general no abrupt discontinuity in the physical properties of the micellar solution is observed in SP_o curve when the Winsor type I / type III boundary is crossed, nor in the SP_w curve at the type III/type II boundary (Viscosity may be an exception).

The SP_o and SP_w curves intersect inside the three-phase domain. At that point the micellar phase contains equal amounts of water and oil and the

corresponding solubilization parameter is noted SP*, the salinity at this point is called optimal salinity.

There are different approaches to describe the behavior of surfactants under different conditions in two-phase systems; some of these techniques are listed in table 2-1. The use of these approaches will depend of the degree of analysis needed.

Table 2-1 Approaches to predict surfactant behavior

Name of the method	Description	Author
R Ratio	Interaction Energy Ratio (Lipo-Hydro)	Winsor,1954
HLB	Hydrophile-Lipophile Balance	Griffin 1949, Davies 1957
HLR	Hydrophile-Lipophile Ratio	Krugliakov 1993
CER	Cohesive Energy Ratio	Beerbower, 1971
PIT	Phase Inversion Temperature	Shinoda 1964
TPR	Three Parameter Representation	Puerto and Reed 1983
SAD	Surfactant Affinity Difference	Salager 1979
HLD	Hydrophilic-Lipophilic Deviation	Salager 1979
NAC	Net Averaged Curvature	Acosta 2003
SPC	Surfactant Partition Coefficient	Márquez 1995
HCNE	Hydrophobe Carbon number equation	Solairaj *et al*. 2012

Griffin introduced the concept of hydrophilic-lipophilic balance “HLB” to quantify for relative affinity of surfactant for water and oil. The need to classify emulsifiers according to their emulsion-stabilizing (O/W or W/O) qualities led Griffin (1949) to use a quantitative but empirical basis for the HLB. To determine the HLB it was either necessary to perform a tedious series of emulsification experiments or alternatively to employ one of several empirical equations which Griffin proposed for nonionic surfactants. Several efforts has been made to extend this concept for ionic surfactants, Davies did it according to Lin et al. (1973). This method doesn’t take into account the effect of other variables like salinity, hardness, temperature, alkalinity, co-solvent, or co-surfactant. Winsor (1954) introduced the *R*-ratio that relates relatives energies of interaction between the surfactant adsorbed at the interface and the aqueous and oil phases surrounding it. It takes into account the molecular effects at the interface, but is still limited by the fact that energies of interaction cannot be measured experimentally. The same problem exists with the Cohesive Energy Ratio approach by Beerbower (1971).

Fig 2-7 is a representation of how a surfactant molecule can interact with the aqueous phase, and with the organic phase.

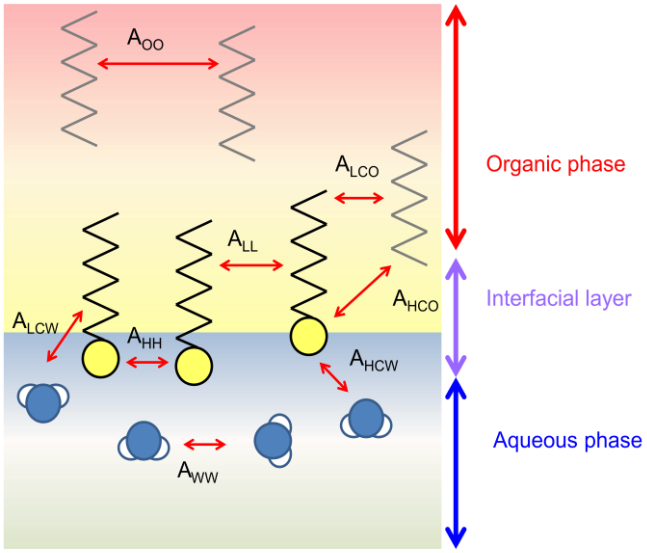

Figure 2-7 Interaction between surfactant molecules, and molecules in aqueous and organic phases. Adapted from Kumar and Mittal (1999)

$$R = \frac{A_{CO} - A_{OO} - A_{LL}}{A_{CW} - A_{WW} - A_{HH}}$$ (Modified Winsor R-ratio) (**Equation 2.11)**

$$A_{CW} = A_{HCW} + A_{LCW}$$ Interaction of surfactant with aqueous phase.

(**Equation 2.12)**

$$A_{CO} = A_{LCO} + A_{HCO}$$ Interaction of surfactant with the organic phase.

(**Equation 2.13)**

(*A*=Molecular Interaction energies, *R*=Modified Winsor ratio (A_{LL}=Molecular Interaction energies between tails of surfactants, A_{HH}=Molecular Interaction energies between heads of surfactants, A_{HCW}=Molecular Interaction energies between heads of surfactants and water, A_{oo}=Molecular Interaction energies

between hydrocarbon molecules, A_{LCO}=Molecular Interaction energies between surfactant tail and hydrocarbon molecules. A_{LCW}=Molecular Interaction energies between surfactant tails and water molecules).

There are different ways to move from lower phase micro-emulsion (Winsor I, i.e., surfactant preferentially soluble in water leading to o/w microemulsion in equilibrium with excess oil, when sufficient oil is available) to upper phase (Winsor II, i.e. i.e., surfactant preferentially soluble in oil leading to w/o microemulsion in equilibrium with excess brine, when sufficient brine is available) according to Winsor approach, the common way is to change salinity from low salinity to high salinity. But the transition can be made increasing the lipophilic to hydrophilic portion of the surfactant blend. See table 2-1. This concept was used for qualitative purposes in the selection of surfactants blends in chapter 7.

Table 2-2 Ways the interaction between portions of surfactant modifies the Winsor R ratio.

Variable	Interaction Energy	R
Amphiphile hydrocarbon chain length increase	A_{CO} increase	Increase
Aqueous phase salinity	A_{CW} decrease	Increase
Aqueous phase elecrolyte valence increase (Na^+ to Ca^{2+})	A_{CW} decrease	Increase
Oil phase length (Hydrocarbon) increase	$(A_{CO}-A_{OO})$ decrease	Decrease
Temperature Increase (ionic surf)	A_{CW} increase	Decrease

For an increase in R, the change in phase behavior is: Winsor I→ Winsor III→ Winsor II as indicated in table 2-3

To analyze the change when the length of the hydrocarbon increases, one needs to know the relationships of the interaction energies. This can be simplified as:

$$A_{CO} = \alpha_1 (SACN)(ACN)$$

(**Equation 2.14)**

$$A_{OO} = \alpha_2 (ACN)^2$$

(**Equation 2.15)**

Here: *ACN* = Alkane carbon number of the hydrocarbon.

SACN = Number of carbon atoms in the surfactant alkyl group

Table 2-3 Equivalence between *SAD* and Winsor *R*-ratio

R	**Winsor type**	***SAD***
< 1	I	< 0
1	III	0
> 1	II	> 0

Shinoda (1964) proposed a method based on the determination of phase inversion temperature “PIT”. It takes into account the effect of formulation variables (salinity, oil, additives), but in practice this technique can be applied only to ethoxylated nonionic surfactants, since ionic surfactants show opposite sensitivity to temperature.

A more general method of characterizing surfactant formulations for specific oil was first introduced by Salager *et al*. (1979) and further improved by Salager, (1999); Witthayapanyanon *et al*. (2008); Marquez *et al*. (1995); and Acosta *et al*. (2008). They developed an empirical correlation for classical surfactant structures, including the formulation variables salinity, temperature, alcohol type and concentration and surfactant type. They expressed the correlations as indicated in table 2-3

Table 2-4 Correlation to estimate the surfactant affinity difference

Surfactant	Equation
Anionic	$\frac{SAD}{RT} = \ln S - K\ ACN - \mathrm{f}(A) + \sigma - a_T(T - T_o)$
Cationic	$\frac{SAD}{RT} = \ln S - K\ ACN - \mathrm{f}(A) + \sigma - c_T(T - T_o)$
Non-ionic	$\frac{SAD}{RT} = bS - K\ ACN - \phi(A) + \sigma - EON + n_T(T - T_o)$

The Surfactant Affinity Difference correlation (see table 2-4) can be used to predict trends in phase behavior.

The typical interactions in the correlation can be generalized for each parameter as:

- Dipole-induced dipole interaction between the surfactant and the oil phase (i.e. *K parameter*). See table 2-5
- For ionic surfactants: Weakening of the hydrogen bonds between water molecules with increase of temperature. Table 2-6 (i.e. a_T and c_T parameters)

- For non-ionic surfactants: Weakening of the hydrogen bonds between the molecules of water and the oxygen in the ethylene oxide groups with temperature (i.e. n_T parameter). See table 2-7.
- For non-ionic surfactants: The salting effect (i.e. *b* parameter)
- The effect of alcohol f(A) for ionic surfactants and ϕ(A) for non-ionic.
- The characteristic curvature of the surfactant (i.e. σ parameter)

Table 2-5 Dipole-induced dipole interaction between the surfactant and the oil phase according to Acosta *et al.* (2003) and Kumar *et al.* (1999)

Surfactant	***K***
Anionic	0.1 - 0.16
Cationic	0.15 - 0.2
Non-ionic	0.17

Typical values for the parameters for correlations in table 2-2 are in tables 2-3, 2-4 and 2-5 from Acosta *et al*. (2003) and Kumar *et al.* (1999)

Table 2-6 Weakening of the hydrogen bonds between water molecules with temperature according to Acosta *et al*.(2003) and Kumar *et al.* (1999)

Parameter	*Value (Units)*
$\boldsymbol{a_T}$	0.01 K^{-1}
$\boldsymbol{c_T}$	0.02 K^{-1}

Table 2-7 Weakening of the hydrogen bonds between the molecules of water and the oxygen in the ethylene oxide groups with temperature and the salting parameter.

Parameter	*Value (Units)*
n_T	0.05 – 0.1 (ca. 0.06 K^{-1})
b	0.13 for NaCl and 0.1 for $CaCl_2$

The effect of alcohol in some cases can be simplified to linear correlations:

$$f(A) = \phi(A) = m_A C_A$$

(**Equation 2.16)**

Then for short alcohols (e.g., methanol or ethanol) m_A >0, for equi-patrition alcohols (e.g., sec-butanol and ter-pentanol) m_A=0, and for lipophilic alcohols (e.g., n-butanol and n-pentanol) m_A<0. In any case the longer and more linear the alcohol chain, the higher will be the absolute value of m_A.

For non-ionic surfactants "σ *-EON* " represents the characteristic curvature of the surfactant, and for ionic surfactants "σ". Typical values are shown in fig 2-8

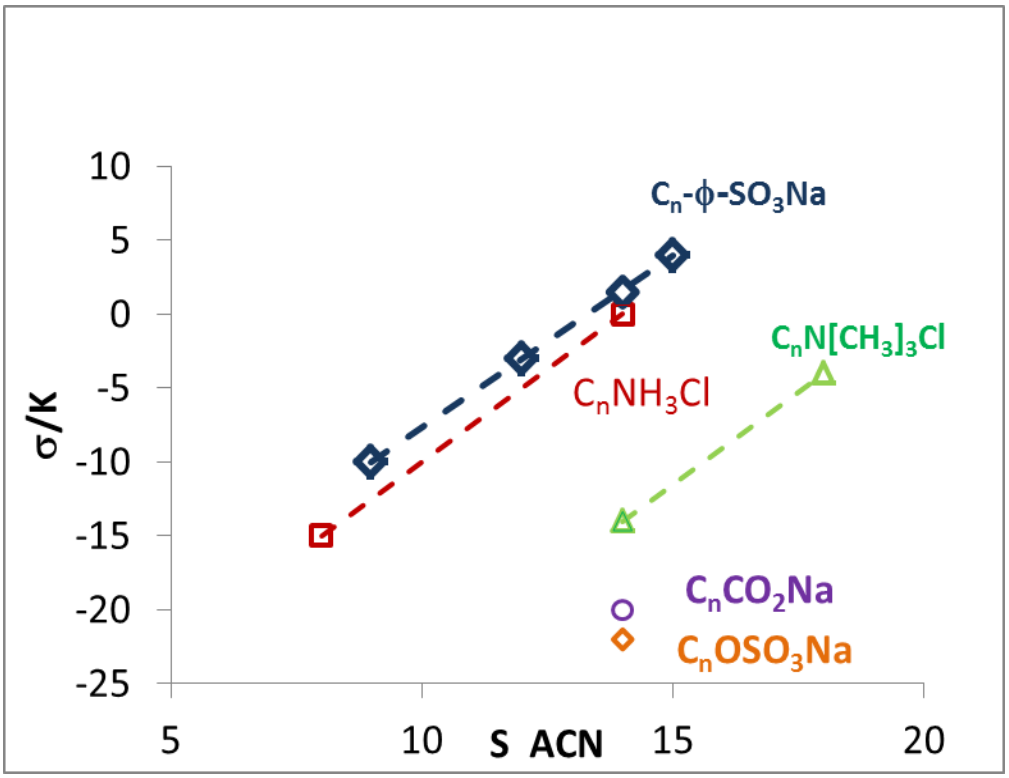

Figure 2-8 Characteristic curvature of surfactants. Adapted from Kumar *et al.* (1999)

Each surfactant has its own characteristic curvature, but the most relevant observation is the relationship between the surfactant alkane carbon number and the surfactant curvature to dipole-induce dipole interaction. This has the form:

$$\frac{d\left[\frac{\sigma}{K}\right]}{d[SACN]} \approx 2.25 \qquad \textbf{(Equation 2.17)}$$

According to *Stubenrauch* (2009), this equation can be extended to non-ionic surfactants in the form:

$$\frac{d\left[\frac{\sigma - EON}{K}\right]}{d[SACN]} \approx 2.25 \qquad \textbf{(Equation 2.18)}$$

These correlations can be used to understand the effect of the different variables and the concept is similar to the HLB, in the context of indicator of the micro-emulsion type according to the table 2-3

2.10 Surfactants in phase behavior

The HLB concept (Hydrophile-Lipophile Balance) is not a good tool to predict the performance of surfactants or surfactants blends when electrolytes are present and when temperature is far from room temperature, but at least it can give us basic information using Davies' approach according to Guo *et al* (2006).

The concept of HLD (Hydrophile-Lipophile Deviation) is a more robust technique than the HLB to understand surfactants' performance. The methodology takes into consideration salinity, temperature, hydrocarbon type, length of hydrophile and lipophile. Acosta (2003) used the concept of NAC (Net Averaged Curvature) to generate an equation of state to predict phase behavior and even to predict physicochemical properties of microemulsions. In the NAC approach the HLD concept is the basis of the model.

$$HLD = \frac{SAD - SAD_{ref}}{RT}$$

(**Equation 2.19)** (Hydrophilic-Lipophilic Deviation)

$$NAC = \frac{HLD}{L} = H_n = \left|\frac{1}{R_o}\right| - \left|\frac{1}{R_w}\right|$$

(**Equation 2.20)** (Net Averaged Curvature)

If there is information about the phase behavior for the surfactant system with specific kind of hydrocarbons, the concept of “Three Parameter Representation” by Puerto and Reed (1983) can be used to infer the behavior of the actual crude oil if the molar volume of the crude oil is know. This method consists of a graph of optimal salinity (S*) vs. oil molar volume with curves of constant solubilization parameter superposed (i.e. SP*). When the domain excludes oils of very high and very low molar volumes, this representation is found to be unique.

Chapter 3

PROPERTIES OF MATERIALS AND PHASES

In this chapter measurements of some interfacial and transport properties for crude oil and some surfactants are reported. The objectives of these measurements are:

- Verify that the crude oil is free of contaminants and can be used as representative of the crude oil in the formation.
- Identify that under basic conditions some activity of components in the crude oil present chemical activity.
- Determine the kind and proportion of solvent needed to dilute dead oil to the viscosity of live oil.
- Verify the observation that the crude oil wets some kind of surfaces after ageing at high temperature.
- Quantify the viscoelasticity at room temperature of some surfactant blends with potential to foam at 94°C.

These measurements were required to plan experiments in chapter 7, and for the analysis of the results.

3.1. Crude Oil IFT

It is important to have a representative crude-oil sample (representative of the oil in place at reservoir conditions) when designing an enhanced oil recovery (EOR) process. Because the process is based in interfacial phenomena, it is required that the crude oil be free of surface active materials such as emulsion breakers, scale inhibitors, or rust inhibitors. A simple test to verify contamination of the oil samples is to measure the interfacial tension (IFT) of crude oil with synthetic brine, as suggested by Hirasaki and Zhang (2004). These measurements were made with a pendant drop/emerging bubble apparatus with automatic video data acquisition and fit, using the regression variant method of the mathematical model resulting from the Young-Laplace equation, and geometrical relationships for curvature radii, described by Rusanov and Prokhorov (1996).

Pendant drop method: The basic principle for the interfacial tension measurement using the pendant drop technique is to let a drop dangle loose (or in this case a bubble cling) at the end of a capillary tube. The drop (or bubble) is distorted from a spherical shape because of the effect of gravity. The pressure forces in mechanical equilibrium at every point of the drop include a Young-Laplace term at the curved interface, and two hydrostatic terms for each fluid (this is equivalent to weight and buoyancy), de Gennes *et al*. (2004). The resulting differential equations are solved numerically, treating the interfacial tension as an adjustable parameter, whose value is adjusted until the computed numerical solution matches with the experimental shape of the drop. The accuracy that can be achieved is about 1% according to de Gennes *et al*. (2004).

Interfacial tension for the crude oil samples. In order to calculate the interfacial tension it was required to measure the specific gravity of brine and oil. This was done with a 25 ml Gay-Lussac bottle (pycnometer), these values are reported in the Table 3-1 as well as the IFT, initial and final, for samples that were placed in synthetic brine in tests up to 4 h.

Table 3-1 IFT values of dead crude oil measured at 25°C in 5% NaCl

Crude Oil	IFT_o (dyne/cm) Initial value	IFT_{eq} (dyne/cm) Equilibrium value	SG (25°C/25°C)
KU-F 62A	28.7	25.5	**0.923**
KU-F 1271	28.4	26.4	**0.926**
KU-G 43	28.6	23.4	**0.926**
AKAL-C3086	**32.8**	**28.5**	**0.922**

The values of interfacial tension reported in Table 3-1, are of the order of magnitude expected when there is no significant contamination with surface active agents according to Hirasaki and Zhang (2004). Values of IFT vs time are in fig 3-1 and are within the range of IFT for crude oils in brines according to Fanchi (2006).

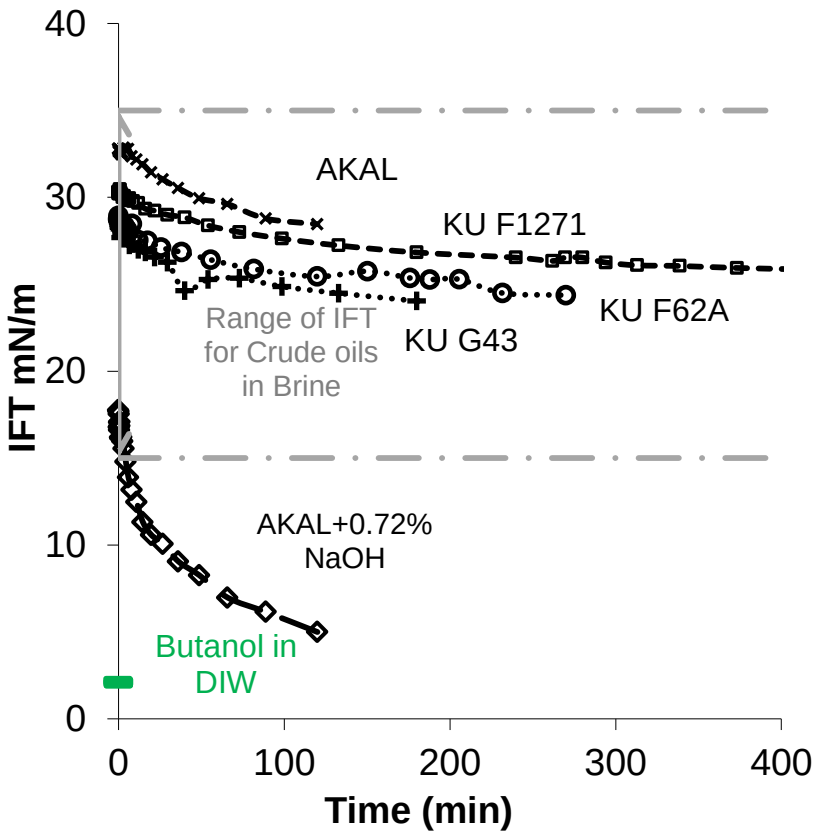

Figure 3-1 IFT Of crude Oil in 5% NaCl Brine at room temperature.

Figure 3-1 indicates that the IFT changes in time and took almost 3 h to have a constant reading of IFT. Butanol pre-equilibrated in DI water was used as a blank to confirm accuracy of the apparatus, its measured value was 1.9 dyne/cm, 5% higher than the value reported by Morrison and Ross (2002)

3.2. Crude Oil viscosity

Viscosity of five dead crude oil samples was measured as a function of temperature. Four of the samples were from different wells and measured as received. A fifth one, taken from the biggest sample received, was treated as

suggested by UT and filtered at UT at 50°C in a open system (i.e. atmospheric pressure).

Four of the samples presented similar viscosity in the temperature range from 25 to 80°C (fig 3-2). The sample treated at UT had higher viscosity, indicating that the filtering procedure will change the properties of the dead crude oil, apparently through losing part of the volatile components. (see appendix 3B, fig 3B-2)

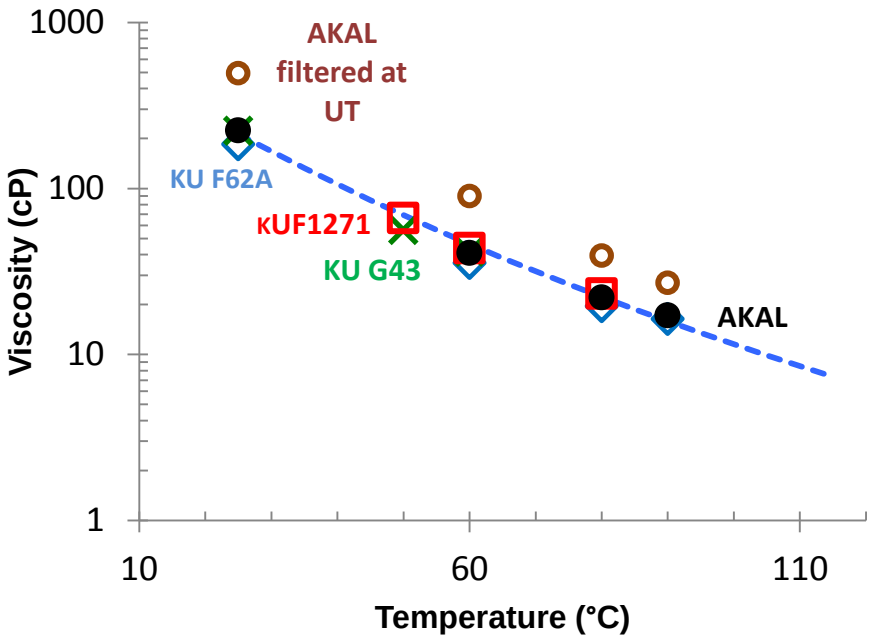

Figure 3-2 Viscosity as function of temperature for dead crude oils, and a dead oil filtered at 50°C. Samples received from KU-F62A, KU-F1271, KU-G43 and AKAL-C3086.

The continuous line in fig 3-2 is a fit for untreated samples of the mathematical form indicated in fig 3-3; the outlier is the AKAL-C3086 (filtered), which was interpreted to have lost volatiles when heated. The sample AKAL-C3086 was analyzed later in an improved apparatus of the falling sphere viscometer

developed by Lopez *et al.* (2009), constructed for measurement of viscosities as a function of temperature for sealed and opaque solutions. But if measured in an open viscometer (i.e. Brookfield DV III+) the viscosity increased as indicated in Appendix 3B, fig 3B-2.

The viscosity measurement has to be conducted quickly or using closed viscometer to prevent loss of light components.

The viscosity for PEMEX Sample AKAL-C3086 at four different temperatures was measured using the Brookfield DV-III Rheometer (Couette viscometer). Results are shown in fig 3-3. The extrapolated viscosity at 113°C (i.e. reservoir temperature), coincides with the viscosity measured using the falling sphere viscometer. (see apparatus picture in Appendix 3E, fig 3E-1)

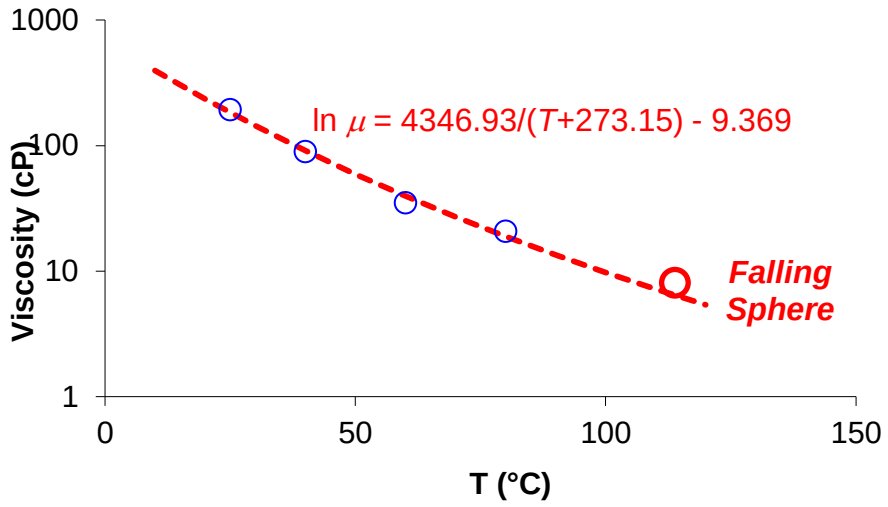

Figure 3-3 Viscosity of crude oil measured in the Couette flow viscometer, comparison of extrapolated value via regression with the value measured with the falling sphere viscometer. Viscosity in equation is in cP and temperature in Celsius.

Nelson (1983) studied the importance of conducting experiments with surfactants for EOR applications with the live crude oil. During experiments he compared results of crude oil pressurized with methane, crude oil diluted with iso-octane to obtain the same viscosity as live oil, and synthetic crude oil pressurized with methane. For the particular system studied he found no difference of oil-recovery efficiency using methane to pressurize or diluting with iso-octane. Nelson reviewed different aspects of phase behavior and recovery efficiency applied to live oil, dead oil, dead oil diluted with solvents (aliphatic and aromatics), and synthetic oil represented by blends of (iso-octane, decalin, 1-methyl naphthalene) with dead oil. For the crude oil of his study neither the concept of EACN nor the Hilderbrand solubility parameter was useful in reproducing phase behavior or oil recovery from core floods. Core floods showed no differences in oil recovery between recombined live oil and oil diluted with solvents to obtain the viscosity of live oil including surfactants.

Iso-octane was used for making a simulated live oil, i.e., with the same viscosity at reservoir temperature. However, adding isooctane to the AKAL dead crude oil produced precipitation of asphaltenes. Ratios of crude oil:isooctane ranging from 4:1 to 9:1 at room temperature showed immediate precipitation of asphaltenes.

Cyclohexane was mixed at room temperature with dead oil presenting minimal precipitation of asphaltenes at low proportions of cyclohexane.

For the studies in this research the dead oil was diluted with cyclohexane to the viscosity of the live oil. The viscosity of live oil is indicated in fig 3-4. To find the proportion of cyclohexane needed, different blends were prepared in sealed pipettes adding a SS440 gold-coated sphere. Using the falling sphere viscometer viscosity was measured and by interpolation the required cyclohexane content was calculated as shown in fig 3-5.

As a safety measure no recombined dead oil with methane was used during experiments. Instead the approach of diluting the dead oil with solvent was used, but this is not a warranty that this procedure is equivalent to use of recombined dead oil with methane.

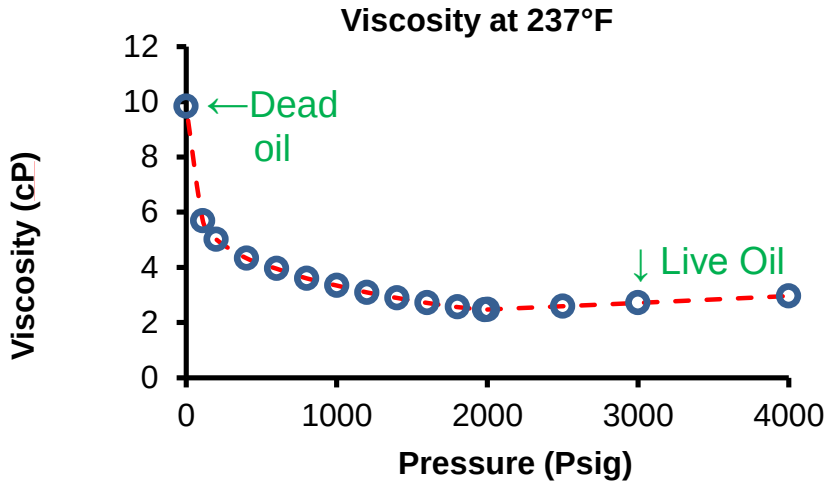

Figure 3-4 Oil viscosity at reservoir temperature as a function of pressure. Adapted from Core Laboratories, Inc Page 10 of 15, File: RFL 81350 (Dallas, TX) PETROLEOS MEXICANOS, Well 2075, Cantarell

Fig 3-4 gives the viscosity as a function of pressure for the crude oil.

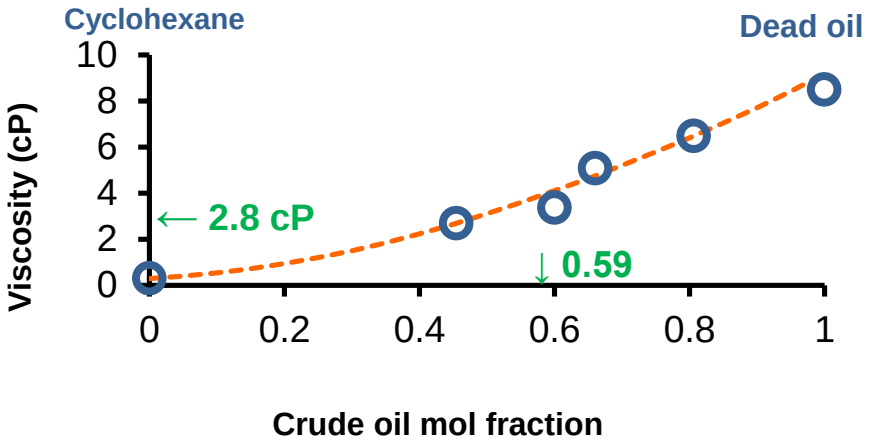

Figure 3-5 Viscosity of crude oil – cyclohexane blends, at 237ºF as a function of molar fraction. Every experimental point is the Average of 20 measurements Precision error less than 3%

Cyclohexane 16.3% mass = 18.7% volume = 41.25% mol

The mol fraction of AKAL dead crude oil to match the viscosity of live crude oil is 0.59. *The mol fraction was calculated using a molecular weight for the dead crude oil of 303 kg/kg-mol measured by Core-Labs.*

For interpolation a similar form of the Grunberg and Nissan equation, reported by Poling *et al.* (2001) was used.

$$ln\mu = x_1 ln\mu_1 + x_2 ln\mu_2 + x_1 x_2 (A + B(x_1 - x_2)) \qquad \textbf{(Equation 3-1)}$$

Where "x_1" is mol fraction of dead oil, "x_2" is mol fraction of solvent used, "μ" is simulated live oil viscosity and A,B dimensionless constants of the equation.

Fitting the data from figure 3-5 to the model of equation 3-1 gave the values of *A*= 1.5 and *B*= - 0. 89

Table 3-2 Viscosities of fluids at reservoir temperature (237ºF)

Component	Viscosity (cP)
Cyclohexane	0.284
Dead crude Oil	8.5

After fitting, the equation 3-1 was used to interpolate the composition of cyclohexane and dead oil to the live oil viscosity.

Table 3-2 gives a comparative table of average molar mass for the different oils, and viscosities.

Table 3-3 Viscosity of different simulated live crude oils vs Live crude oil and dead oil at reservoir temperature (237ºF) .

Oil	Molar mass (g/mol)	Viscosity (cP)	Pressure (Psia)
Rice Simulated live oil	212.7	2.8	14.7
UT Simulated live oil	170.2	2.0	14.7
Live oil	176.3	2.8	3514.7
Dead crude oil	303 (*)	8.3	14.7

3.3. Acid Number

The crude oil samples analyzed presented a low acid number. Total Acid Number by Non-aqueous Titration was 0.18 mg KOH/ g Oil, and Acid Number converted from Soap Number by Aqueous Titration was 0.018 mg KOH/ g Oil, Liu *et al.* (2010); but the presence of alkali at very high pH produced some activity reducing the IFT of crude oil. Evidence of this activity was observed during IFT measurements in presence of NaOH and was presented in fig 3-1. The carboxylic groups, often present in molecules of the heavy end fraction of crude oil, form strong bonds to the positively charged sites on the carbonate surface according to Zhang *et al*. (2006). Thus, the water wetness is decreased as the amount of carboxylic material in the crude oil increases. The amount of carboxylic material can be quantified as an acid number (AN, expressed in term of mg of KOH/g), and the AN of the crude oil appeared to be one of the important wetting parameters for carbonates.

3.4. Contact Angle.

The crude oil used during experiments presented the tendency to wet the surface of rocks after ageing. The process of making the system oil wet is faster if ageing is done at high temperature. The contact angle of some rocks was measured before ageing, and after ageing at 120°C for 1 week. The results are presented next.

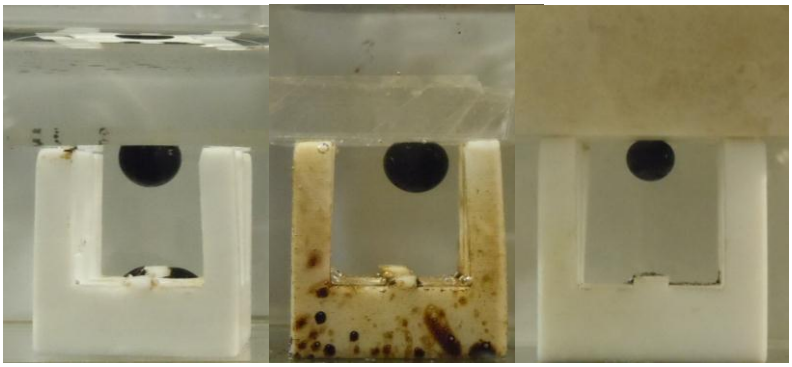

Material	Quartz	Calcite (Iceland spar)	Marble
Water receding angle (deg)	63	32	30

Figure 3-6 Water receding contact angles at room temperature

Figure 3-6 indicates the water receding contact angle at room temperature of crude oil in different pristine rocks after being cut and lapped (see Appendix 3F). The contact angle was measured as well for samples of crude oil-rock aged for more than a week at 120°C. Pristine rock samples were cut and lapped and cleaned with water, dried in the oven and, after cooling, cleaned with toluene. Then rocks were contacted with crude oil in a sealed container at 120°C for more than a week. The rock samples after cooling were immersed in synthetic seawater and contact angle measured. Values of contact angle are included in fig 3-7


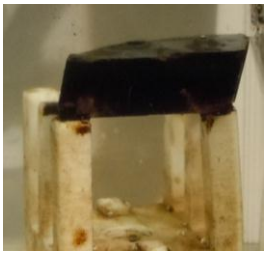


Material	Quartz	Calcite (Iceland spar)	Marble
Water advancing angle (deg)	176	180	174.3
Temperature (°C)	25	25	120

Figure 3-7 Water advancing angle after ageing. There was no big effect with temperature, only small decrement for marble, so for this rock was reported at 120°C

After ageing the rocks in crude oil, the resulting systems were oil wet for the three surfaces studied.

It has been reported by Chen and Mohanty (2012) that adding cationic surfactants like benzalkonium chloride alters wettability of oil-calcite systems to more water wet conditions. To confirm their observation for the present system marble rock with crude oil after ageing was contacted with seawater, and then benzalkonium chloride (i.e. BTC 8358) in seawater was added to measure contact angle. The result was an intermediate wet condition with contact angle close to 90° as indicated in fig 3-8

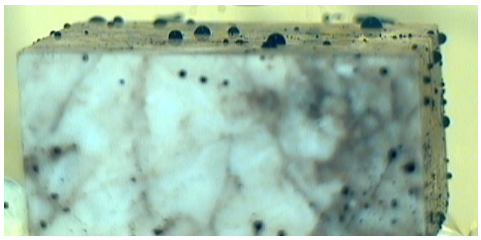

After contacted with 1% BTC 8358 in seawater at room temperature the contact angle was measured to be close to 90°

No change incontact angle for the Iceland spar.

Figure 3-8 Water advancing angle

The same was done for a blend of LB+C_{16-18}AOS on marble and Iceland spar. All the oil was released by low IFT; no information on change in wettability could be obtained because there was no oil left.

3.5. Surfactant viscoelasticity

Some blends of surfactants analyzed in chapter 7 presented viscoelasticity at room temperature. The rheograms are included in this section and discussion about those results.

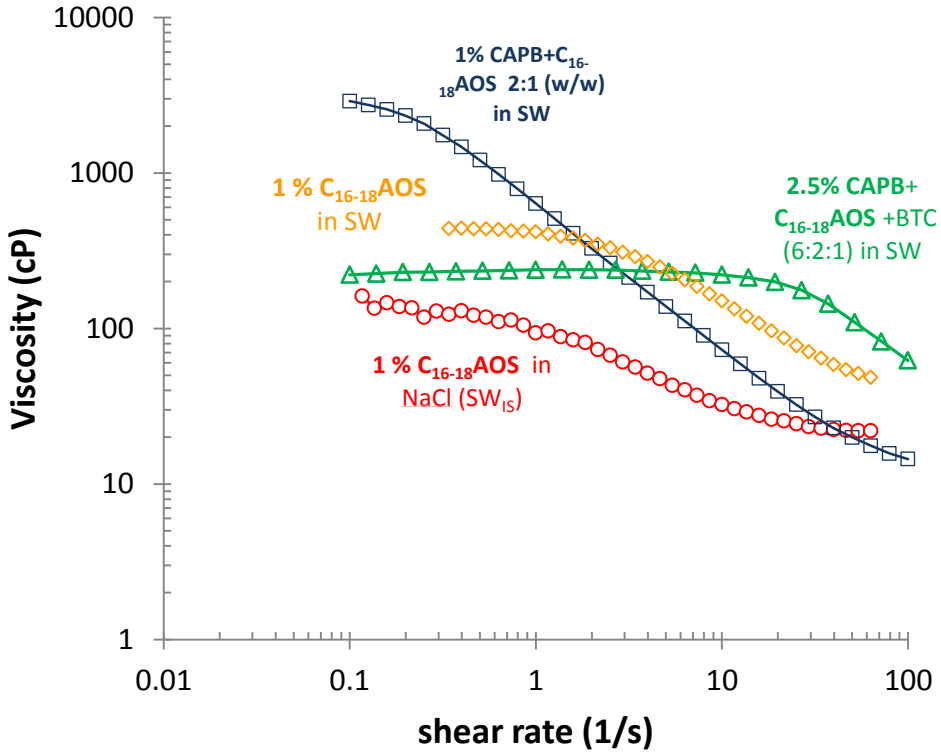

Figure 3-9 Viscosity curve for surfactant blends at 25ºC.

Most of the surfactants showing good performance as foamers at high temperature were shear thinning and presented viscoelasticity at room temperature, but the viscoelasticity decreased as the temperature was increased. The effect of viscoelasticity is more pronounced as the concentration of surfactant increases.

Figure 3-9 includes several examples of surfactants being shear thinning. The C_{16-18}AOS in seawater had some solubility problems. It phase separates in seawater if not mixed continuously, has higher viscosity than in NaCl brine, and was viscoelastic in both cases. For a blend of CAPB+ C_{16-18}AOS the shear thinning effect was observed as well, but the viscosity decreased if some cationic

surfactant is added like BTC 8358. (See chapter 7 for more details about these surfactants)

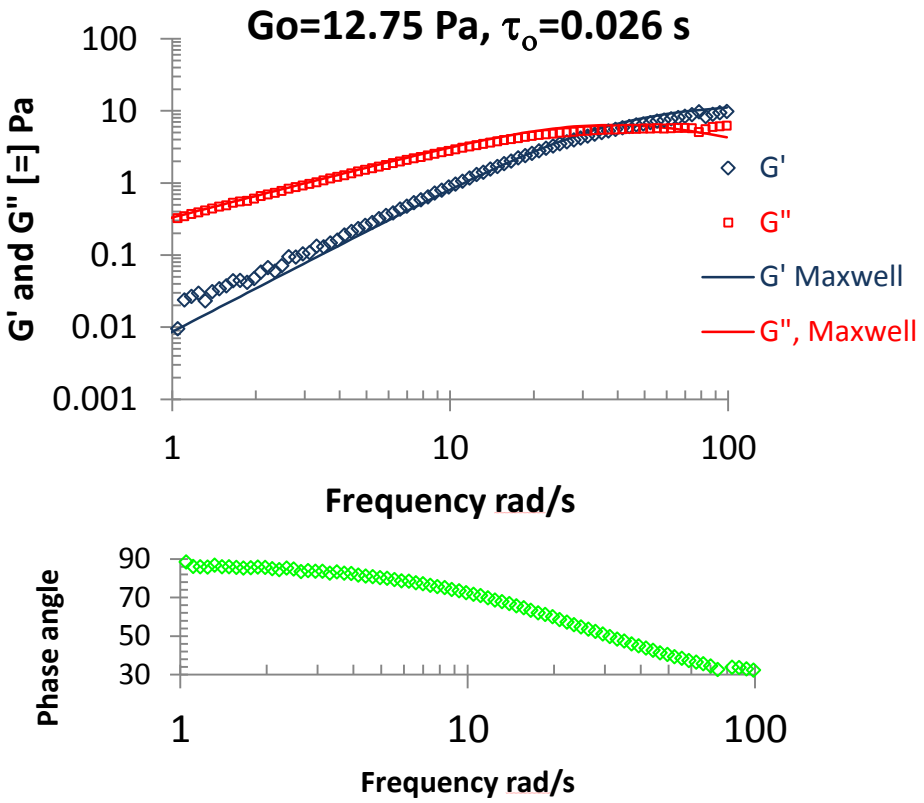

Figure 3-10 2.5% in Seawater CAPB+$C_{16\text{-}18}$AOS+BTC (6:2:1). Continuous line is the fit to the Maxwell model. Rheometer: Rheometric Scientific Inc, ARES.

The viscoelasticity of the blend CAPB+C1618AOS+BTC (6:2:1) was observed at first glance when prepared solutions recoiled while mixing; then after measurements, this observation was confirmed, and quantified in fig 3-10. Elasticity dominates at frequencies higher than 40 rad/s, and the solution requires frequency less than 1 rad/s to be purely viscous. This system has behavior like (or similar to) that of a Maxwell model with spring and dashpot in series. (See appendix 3C for details about Maxwell model)

As the temperature increases the viscosity approaches the viscosity of water, as indicated in fig 3-11, for two surfactant blends described in detail in chapter 7.

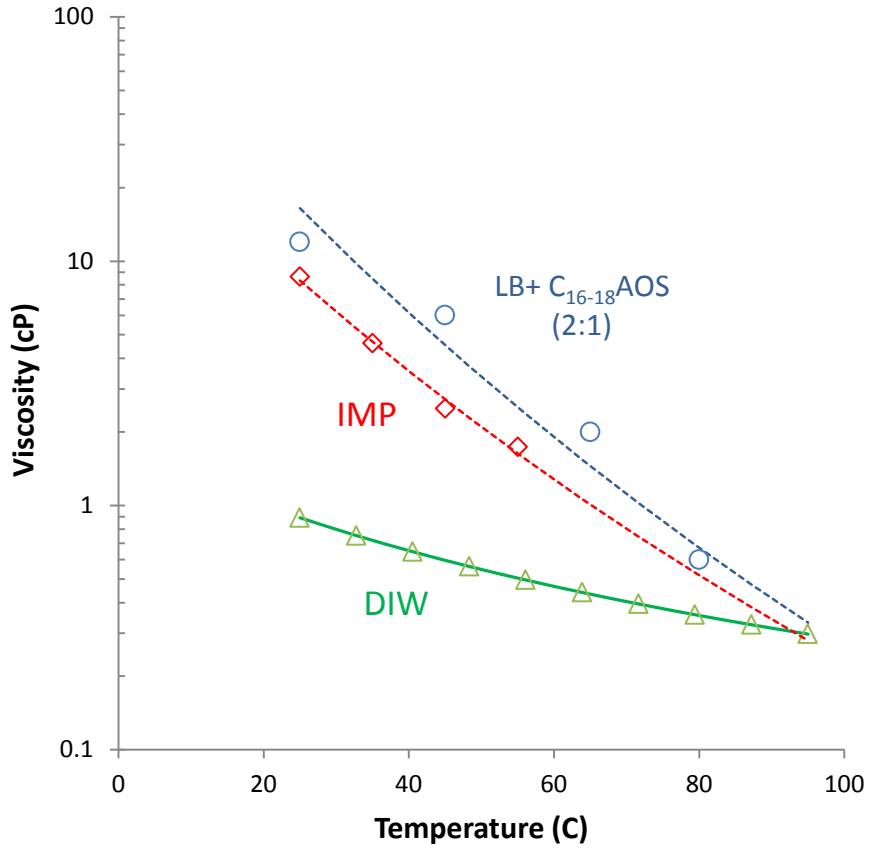

Figure 3-11 The viscosity measurements were done at 300 1/s of shear rate in order to compare. Fitted to Andrade-Eyring equation.

The viscosity measured at high shear rate (300 1/s) follows the form of Andrade-Eyring with temperature.

$$\eta = \eta_{\infty} exp\left(\frac{E_{\eta}}{RT}\right) \qquad \textbf{(Equation 3-2)}$$

Where η is viscosity, and the parameters of the equation 3-2 are: η_{∞} and E_{η}

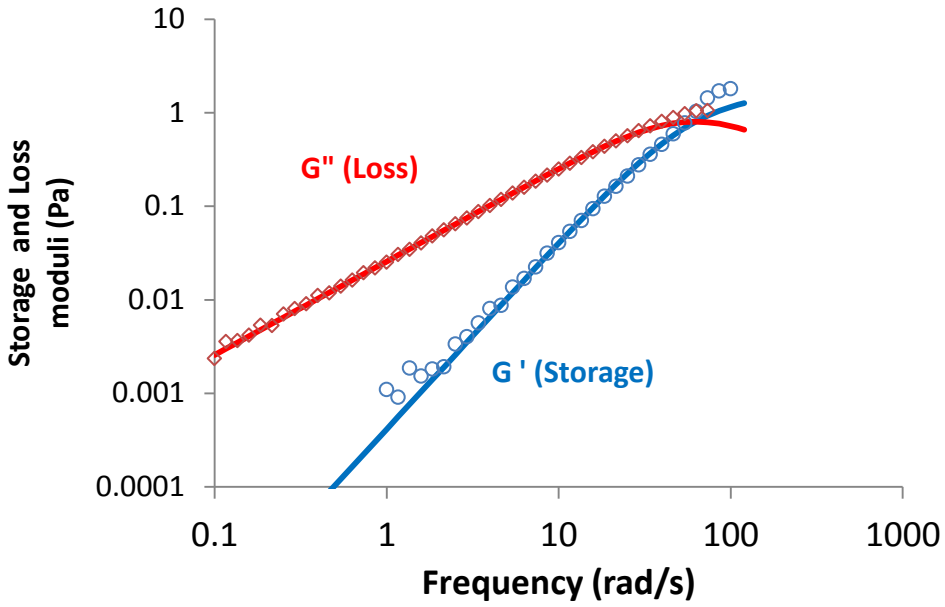

Figure 3-12 Room temperature rheogram for LB+$C_{16\text{-}18}$AOS 1% in Seawater. Continuous lines are the best fit to Maxwell model τ_o = 0.016 s, *Go*=1.607 Pa

The single-relaxation-time description using Maxwell model holds over 3 decades for the system, for the blend of LB and $_{C16\text{-}18}$AOS used in this work as indicated in fig 3-12.

According to Macosko (1993) the crossover of storage and loss moduli at low frequency is expected for concentrated polymer solutions, but for diluted systems of rod-like particles and random coils the moduli may approach each other at high frequency without cross over. Larson (1998) discussed the rheology of entangled wormy micellar solutions, and found that those systems, like ordinary polymer solutions show pronounced viscoelastic effects. Lopez-Diaz and Castillo (2010) found that wormlike micelles of zwitterionic + anionic surfactants behaved as Maxwellian fluids at frequencies less than 100 rad/s. Kuryashov *et al*. (2010)

Investigated the effect of temperature on the rheological behavior of cylindrical micelles of zwitterionic and anionic surfactants. They discuss that the drop in viscosity with temperature was directly related with the decrease in relaxation time with temperature and that the loss modulus dominated in a wide spectrum of frequencies at higher temperatures. The behavior was similar for anionic surfactants forming worm-like micelles, according with Kalur *et al.* (2005), while adding just salt or hydrotrope. Kumar *et al*. (2010) reported similar trend with the use of zwitterionics with added hydrotropes, emphasizing that in the case of the zwitterionics the net charge of the head group is smaller allowing the surfactant molecules to directly form cylindrical micelles even in DI water. Moreover the addition of salt may have little influence in the rheology. Varade *et al.* (2007) studied mixed surfactant systems of anionic with non-ionic. The effect of relaxation time decreasing with temperature was the same as in the previous cases, but the difference between loss and storage moduli after the crossover was not severe. However, they added co-solvents, which will change the packing of micelles.

A simplistic approach to justify the worm-like behavior can be done using the concept of critical packing parameter from Israelachvili (1991). A cartoon adapted from Lopez-Diaz and Castillo (2010) is used as a reference for discussion (see fig 3-13).

The critical packing parameter (CPP) is defined as:

$$CCP = \frac{v}{L_c a_o}$$ **(Equation 3-3)**

Here “v “ is the volume of the hydrocarbon chain or chains, “L_c “ is the critical chain length, or how far the chains can extend, and ” a_o “ is the optimal area, or head group equivalent area. The concept of CCP is equivalent to the concept of “surfactant number” by Stokes and Evans (1997).

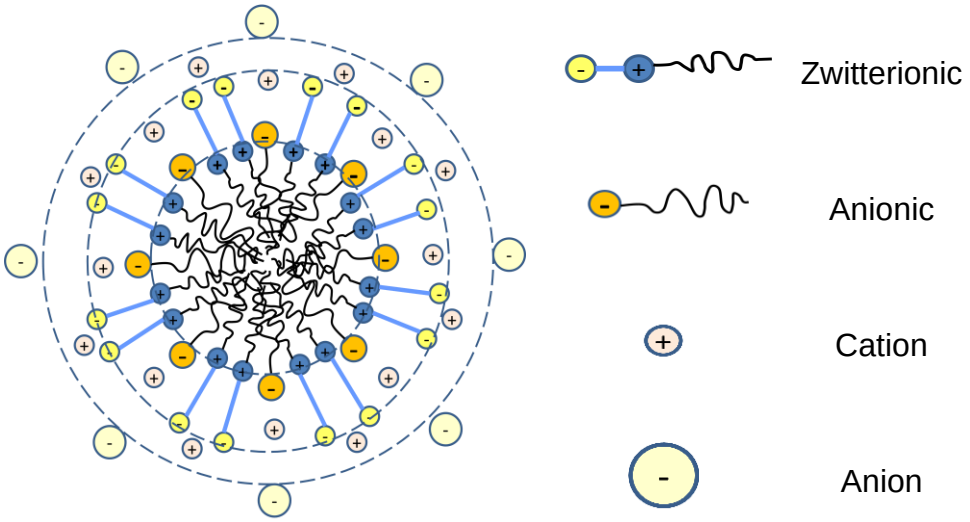

Figure 3-13 Cartoon of cross section of worm-like micelle, adapted from Lopez-Diaz and Castillo (2010)

When the surfactant blend is made of Zwitterionic + Anionic in a molar ratio close to 2:1, as indicated in figure 3-13, two contributions for changing critical packing parameter may be happening: the increase of the volume of the lipophilic group and the reduction in repulsion of the head groups. For this particular case (i.e., zwitterionic and anionic in a molar ratio 2:1) the gegenion of the anionic surfactant can fit in the arrangement as well.

Spherical micelles are formed when critical packing parameter is less than 1/3, and cylindrical micelles will form between 1/3 and 1/2 according to Israelachvili

(1991). In table 3-3 the two contributions listed can produce transformation of micelles from spherical to cylindrical shape. For the incorporation of anionic surfactant within a zwitterionic micelle the volume of the tails will increase, and the repulsion between charges will decrease because of the positioning of the anionic surfactant and its counter-ion.

Table 3-4 Contribution to critical packing parameter in the scenarios described (i.e. Idealized scenario)

Contribution	Description	$\frac{3v}{L_c a_o}$	*CPP*
	Spherical micelle	2/2	1/3
Volume of tails (chain packing)	Volume increase by the lipophilic group from 2 to 3	3/2	1/2
	Spherical micelle	3/3	1/3
Electrolytes and head groups	Decrease of the hydrophilic area or repulsion from 3 to 2	3/2	1/2

Note: See that in the third column is the ratio of areas, area of the head group and area of the base of a cone. See Appendix 3G for comparison of all the surfactants blends analyzed during the research.

(*Numbers in table 3-4 are of the symbolic values, just to explain how the packing parameter may change under changes in volume of the molecule to generate a change in the shape of the micelle.)*

Viscoelasticity was observed when $C_{16\text{-}18}$AOS was prepared in NaCl, and the effect was stronger when the system was studied in presence of divalent ions (it may phase separate if divalent cation concentration is too high). The main contribution to the change from spherical micelles to worm-like micelles may be

the decrease of the area of repulsion of the charged heads when electrolytes are added.

If one of the contributions is not enough, the other will help. In the case of AOS in seawater the electrolytes will screen electrostatic repulsion between surfactants, but for the blend of LB + AOS, both contributions are important.

Table 3-3 indicates that using the blend of surfactants in a proportion 2 to 1 will be enough to change from spherical to cylindrical micelle, but of course in this case the effect of the charge of the head group will contribute as well in favor or larger aggregates. In the case of AOS, worm-like micelles can be obtained just decreasing the area of repulsion by adding electrolytes.

According to Israelachvili (1991), the effect of temperature is complex. He stated that charged micelles shrink under the effect of temperature increase, non-ionic micelles grow, and zwitterionics behave between charged and non-ionic (see prediction of rheology at 94°C in Appendix 3D).

3.6. Surfactant Surface tension

Surface tension was measured for LB+$C_{16\text{-}18}$AOS 2:1 (w/w) in seawater, and the value as function concentration is in fig 3-14. The method used was the drop volume (weight-volume) method, or drop counting method. The stalagnometer used was LAUDA TVT1, and measurements were done at room temperature.

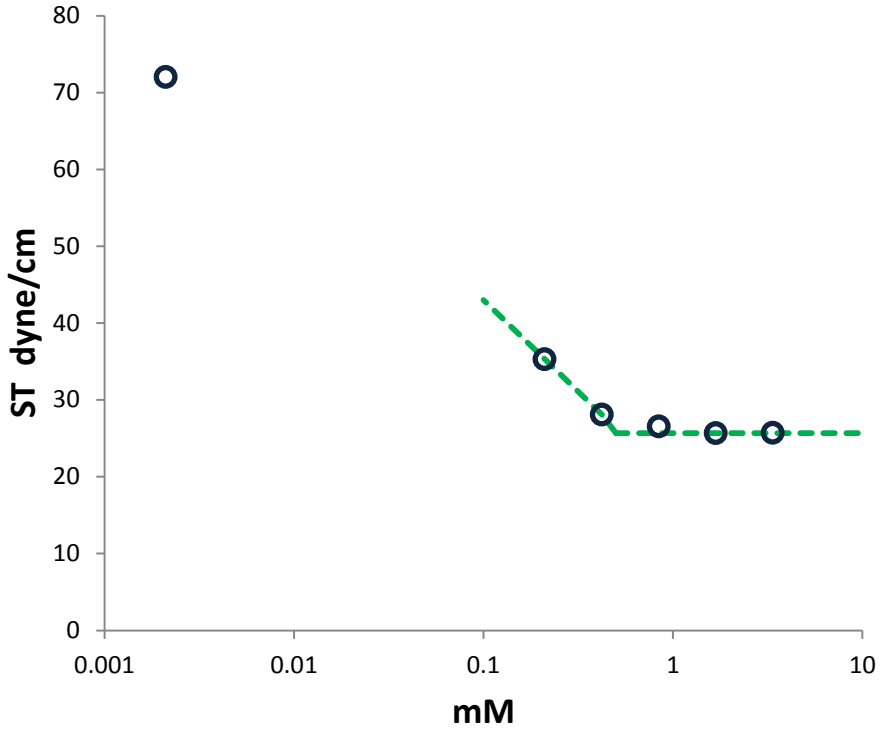

Figure 3-14 Surface tension for LB+C_{16-18}AOS 2:1 (w/w) in seawater at 25ºC

According with Yildirim *et al.* (2005) the method can be extended with correction factor when Weber number exceeds $1x10^{-5}$, to take into account inertial effects for high velocity during injection. For this system at the injection rate of close to 1mL/s, the actual surface tension will be 1% higher than that reported by the apparatus. The correction needed is comparable to other experimental errors.

When very viscous fluids are analyzed a correction is needed, but it is negligible if Ohnesorge number is less than 1 and Bond number less than 1. For the measurements with the stalagnometer and the needle gage 16 the dimensionless numbers calculated are in table 3-5.

Table 3-5 Typical dimensionless number during measurements.

Dimensionless number		Value
Weber	$N_{We} = \frac{2\rho v^2}{D\sigma}$	5x10^{-6}
Ohnesorge	$N_{Oh} = \sqrt{\frac{N_{Ca}}{N_{Re}}} = \frac{\mu}{\sqrt{\sigma\rho D}}$	0.8
Bond	$N_{Bo} = \frac{\Delta\rho g D^2}{\sigma}$	0.14

The viscosity was calculated approximating the shear rate with 8 *v* / *D* with a value of 5 s^{-1} a viscosity of 100 cP. *V* is the average velocity in the needle during injection and D the inner diameter of the needle, *g*=gravity, σ=surface tension, ρ= flowing fluid density, μ=viscosity of injected fluid, $\Delta\rho$= density difference between phases.

Chapter 4

ANHYDRITE DETERMINATION IN CARBONATE FORMATIONS

4.1 Introduction

The advantages of the use of alkali in anionic surfactant formulations for EOR applications are well known. Previous experiments have demonstrated gravity-driven enhanced recovery of oil when interfacial tensions are low following spontaneous imbibition of such formulations into oil-wet carbonate rock Hirasaki and Zhang (2004). Studies conducted by Seethepalli *et al*.(2004) have shown that the use of anionic surfactants in presence of sodium carbonate can not only reduce oil-brine interfacial tension but also change wettability from oil wet to intermediate/water-wet conditions for carbonate surfaces (i.e. limestone, marble, dolomite and calcite). In these previous studies, some common reasons to use sodium carbonate are listed: The high pH produces natural surfactants in-situ by the reaction with the naphthenic acids in the crude oil. The carbonate suppresses the concentration of calcium in the brine. Sodium carbonate reduces ion exchange, mineral dissolution, and adsorption of anionic surfactants. The carbonate precipitates do not exacerbate permeability compared with silicates and hydroxides. Moreover, sodium carbonate is inexpensive.

Presence of anhydrite is unfavorable in flooding with surfactants with low tolerance to divalent ions (e.g. calcium and magnesium), Alkali in surfactant flooding sequesters divalent ions and reduces surfactant adsorption. When the

alkali is sodium carbonate and anhydrite or gypsum is present, the anhydrite will dissolve and precipitate as calcium carbonate. Anhydrite or gypsum at a level of only 0.1% in dolomite rock with porosity of 23% is enough to retard the breakthrough of a 1% by mass sodium carbonate solution by 0.7 pore volume as indicated in fig 4-1 and fig 4-2. The analysis for fig 4-1 is consistent with results reported by Liu (2008). Different alkalis will react as well with anhydrite.

The analysis of figs 4-1 and 4-2 is based on the assumption that anhydrite will consume the sodium carbonate, producing a precipitate of calcium carbonate (Hirasaki, 2005 and 2006).

$$CaSO_{4\,(s)} + Na_2CO_{3\,(aq)} \rightleftarrows 2\,Na^{+}_{(aq)} + SO^{2-}_{4\,(aq)} + CaCO_{3\,(s)}$$

(Equation 4-1)

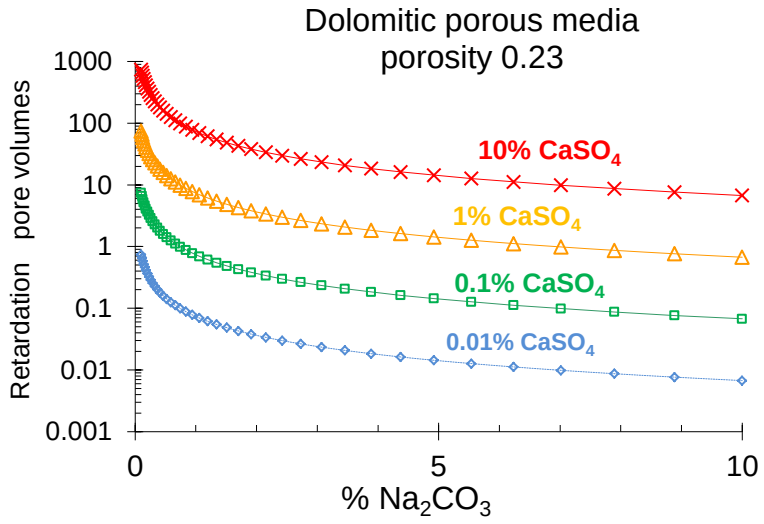

Figure 4-1 Relationship of the retardation time and mass percentage of $CaSO_4$ in dolomite rock

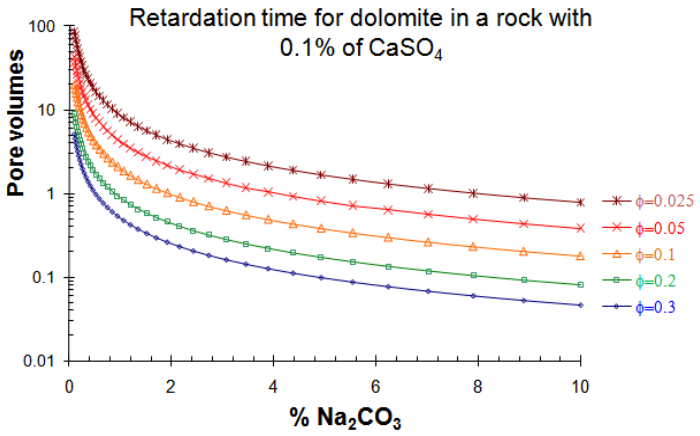

Figure 4-2 Relation of retardation time and porosity or the rock; the effect worsens for less porous media.

The retardation of sodium carbonate in a formulation may be as much as several pore volumes if the concentration of sodium carbonate is below 1%, and the effect is increased if the concentration of anhydrite is higher (fig 4-1) or if the porosity of the rock is lower (fig 4-2). Thus, even small proportions of anhydrite are important in designing an EOR formulation if use of sodium carbonate is to be considered.

The objective of this study is to develop a tool to predict the presence of anhydrite in a formation, and to employ the tool for a particular formation as an example of its applicability. The basic idea is to collect the information from the reservoir's water analysis and use it with available brine software to see if the water was in contact with the solid minerals of interest, in this particular case with anhydrite. A second method is direct analysis of core samples using inductively coupled plasma (ICP).

4.2 Anhydrite determination

Alkali in surfactant flooding can sequester divalent ions and reduce surfactant adsorption. When the alkali is sodium carbonate and anhydrite (or gypsum) is present, the anhydrite will dissolve and precipitate as calcium carbonate. An anhydrite level of only 0.1% in the rock is enough to retard the breakthrough of a 1% sodium carbonate solution by approximately 0.7 pore volume, which would greatly reduce effectiveness of a process having surfactants sensitive to divalent ions. Different alkalis will also react with anhydrite.

A methodology is presented to estimate the anhydrite present in the reservoir. The method is based on brine software analysis of produced water compositions and inductively coupled plasma (ICP) analysis of core samples. X-ray powder diffraction (XRD) can detect anhydrite when it is abundant, but will not be able to detect the low amounts that can still be harmful to chemical EOR. XRD was used to verify the mineralogy of the rock. X-ray photoelectron spectroscopy (XPS) was used to obtain surface composition for comparison with bulk composition of the rock.

Produced water and core samples were analyzed from a high-temperature, high-salinity carbonate reservoir, which is a candidate for surfactant EOR. Ten water analyses were obtained from ten wells in five formations. The formation brines ranged from 3-to-20% of TDS. The reservoir rock was mostly dolomite, and reservoir temperature was about 120°C. The saturation index calculated for all formation waters at high salinity (higher than seawater) was positive, indicating

over saturation with anhydrite. The saturation index was calculated with ScaleChem for high salinity and PHREEQC, which is limited to lower salinity. The elemental composition of rock samples dissolved in acid was determined by ICP. The mass percent of anhydrite was computed from the elemental analysis.

When these methods were applied to the dolomite reservoir of interest, they strongly indicated that anhydrite was present in sufficient amounts to preclude use of sodium carbonate in a surfactant recovery process.

4.3 Information about the seawater and formation brines

In this study the salinity of the local seawater was higher than typical seawater (DOE, 1994); the percentage excess of the main ions may be seen in fig 4-3. Figs 4-4a and 4-4b indicate the concentrations of the different cations and anions in the wells sampled in the study (wells may belong to the same or different reservoirs or the same or different geological formations).

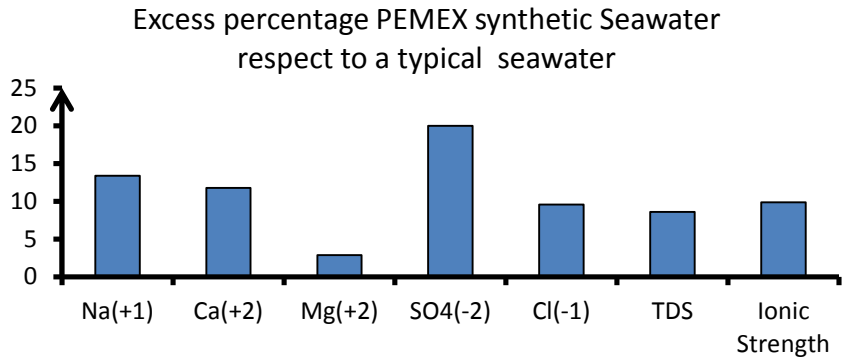

Figure 4-3 Excess of the main ions respect to typical seawater and ionic strength.

One of the main characteristics of the different water analyses is that the concentration of sulfates is less than the concentration of sulfates in seawater (fig

4-4b), but the concentration of calcium is higher in most of the formation brines from the wells (fig 4-4a) than in seawater. The alkalinity is also higher in the brines than in seawater. This higher alkalinity is important in the solubility of different minerals, but not controlling in the saturation with respect to calcium sulfate. The analysis of the seawater is important if it was used in the drilling process. If the water used in the drilling process is over saturated in any mineral, it may precipitate in pore space near the well and mislead the analysis of the rock if core material is extracted for analysis. False positive with respect to a mineral may change the strategy of tailoring surfactants for a specific EOR application, increasing the final cost of the process.

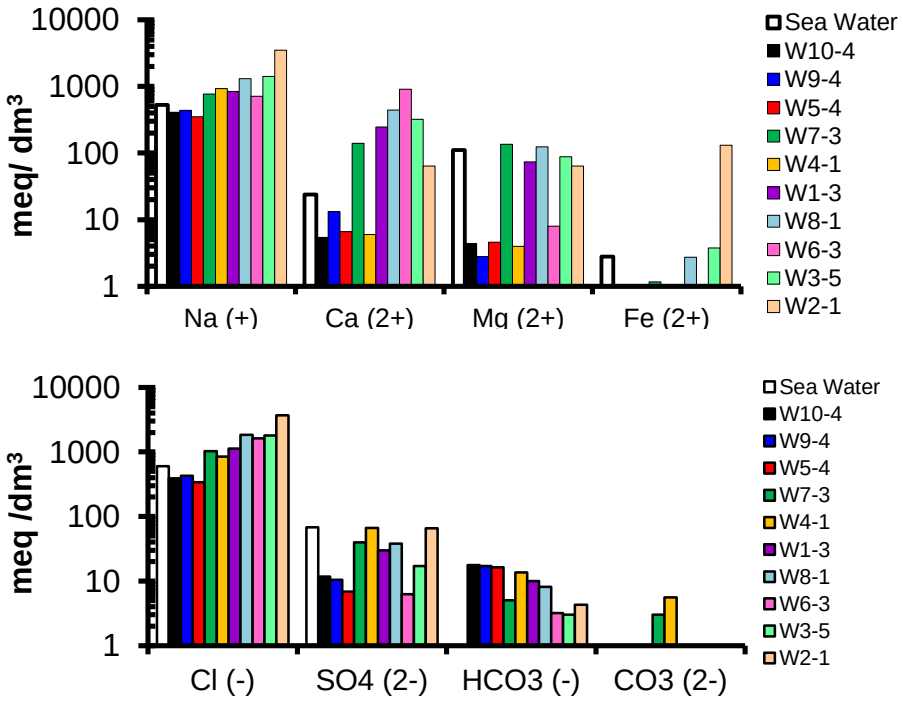

Figure 4-4a (above) and 4-4b (below) indicate the composition of the water for the different wells in this study. Fig 4-4a is for cations and fig4-4b is for anions expressed in mili-equivalents per liter.

The first approach to solve the task was to verify the saturation of different minerals in the water samples and to use applicable software to predict the thermodynamic properties of the brines and whether they are in equilibrium with solid phases.

4.4 Description and validation of software

Different software can be used to predict the thermodynamic properties of brines. Each type of software has pros and cons, but in this study the main interest is precise prediction of saturation level of components, in order to infer if calcium sulfate is or is not present in the formation.

To successfully use any software, a complete water analysis is needed. The concentration of the cations and anions is needed as well as the pH and the alkalinity of the sample. If the pH and alkalinity are not known, the analysis can still be performed if the concentration of dissolved gases is known (e.g. CO_2, H_2S, etc.), or if the partial pressure of the CO_2 in the gas phase in equilibrium with the brine is known. It is required to know the temperature and the pressure of the reservoir and to know the exact conditions when the water analysis was done. Any depressurization of the sample or release of CO_2 to the atmosphere will change the calculation, as well as exposing the water sample to an atmosphere containing carbon dioxide.

Initially two software packages were selected to be used during the study (PHREEQC and ScaleChem), but a third option was later included for comparative purposes (ScaleSoftPitzer), because some inconsistencies with respect to the database were found in the Pitzer model with PHREEQC. The third software package was used to verify the performance of PHREEQC once the database was modified. The ScaleSoftPitzer has the advantage that includes the effect of pressure, which is one of the limitations of PHREEQC.

ScaleChem is very flexible and complete software, but is a licensed software. PHREEQC is free software, but presented no consistency with respect to the database for the activity model parameters and for the solubility products. It is recommended that users of a software package be familiar with the activity models used and with the available database. PHREEQC has the advantage that the data base can be viewed and modified, and it has the advantage of being an open code. PHREEQC is recommended for experienced users to make preliminary studies because the code can easily be modified to take into account variables not obvious at first glance like the pressure. However, this tool must be evaluated for the system under consideration.

Most of the commercial software uses the activity model proposed by Pitzer, and this was the model selected to be used with the software PHREEQC. In this model the activity coefficient requires two contributions. One is the long-range contribution, which uses the extended Debye-Huckel term (the first term of the

right hand side of equation 4-2). The other is the short-range contribution, which has the extra viral coefficients with respect to molality, as indicated in the last two terms on the right hand side of equation 4-2.

$$ln\gamma_{\pm} = -A_P|z_+z_-| + B_P^{2-2}m\frac{2\nu_+\nu_-}{\nu} + C_P m^2\frac{2\,(\nu_+\nu_-)^{3/2}}{\nu}$$

(Equation 4-2)

$$A_P = A\left[\frac{\sqrt{I_m}}{1+b\sqrt{I_m}} + \frac{2}{b}ln\left(1+b\sqrt{I_m}\right)\right]$$

(Equation 4-3)

$$B_P^{2-2} = 2\beta_0 + \frac{2\beta_1}{\alpha_1^2 I_m}\left[1-\left[1+\alpha_1\sqrt{I_m}-0.5\alpha_1^2 I_m\right]exp\left(-\alpha_1\sqrt{I_m}\right)\right]$$
$$+\frac{2\beta_2}{\alpha_2^2 I_m}\left[1-\left[1+\alpha_2\sqrt{I_m}-0.5\alpha_2^2 I_m\right]exp\left(-\alpha_2\sqrt{I_m}\right)\right]$$

(Equation 4-4)

Parameters for these equations can be found in Lee (2008) and Ott and Boerio-Goates (2000). No consistency was found in the Pitzer database used by PHREEQC. Parameters for calcium sulfate coincided with Ott and Boerio-Goates, but for magnesium sulfate the data were extracted from Lee. Another inconsistency of the database was the solubility product, but the database called “Pitzer.dat” was modified using the tables reported in Stumm and Morgan (1996). If the software does not include the effect of pressure, this can be added by

modifying the database of the solubility product to include the pressure effect. For anhydrite the parameters can be found in Monnin (1990), and the correction is obtained with equation 4-5:

$$\ln K_{SP} = \ln K_{SP}^{0} - \frac{\Delta V_r^o}{RT}(P - P_o) - \frac{\Delta K_r^o}{2RT}(P - P_o)^2$$

(Equation 4-5)

Three different tests were used to select the software packages for this study. The first test is to see if they agree with experimental data in the trend of saturation temperature with respect to anhydrite in a process in which sulfate is removed from seawater. Seawater is used in this initial simulation because we need to know whether we can inject seawater in the proposed EOR process for the reservoir of interest without having precipitation of any salts. A second test is to verify if the software can predict the solubility of calcium sulfate in deionized (DI) water at different temperatures. A third test is to calculate the solubility of calcium sulfate in highly salty water (ca. 20% of NaCl). The results of these tests are presented in fig 4-7. All three of the above software packages predict more less the same results for water systems at low salinity (i.e. salinity close or less than seawater), but differences can be found at high salinity (between seawater and 20% of sodium chloride). For this reason a validation of the software was required.

As indicated above the three packages were used to compare predicted changes in the saturation temperature of anhydrite as different percentages of sulfate were eliminated from seawater. The three predicted similar trends, as indicated

in fig 4-5, but the difference in predictions increased as more sulfate was replaced by chloride.

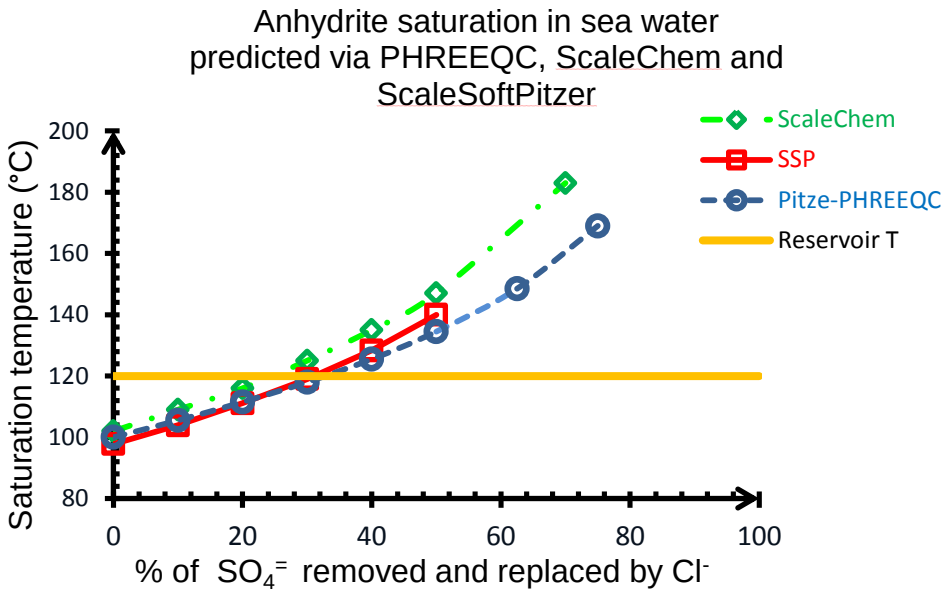

Figure 4-5 Saturation temperature respect to anhydrite for the seawater once the sulfate is removed in different proportions. Temperatures higher than the values delimited by the curve are for over saturated samples, below the curve the sample is under-saturated.

Fig 4-6 indicates that the error in region between 50° and 100°C is less when ScaleChem was used to predict anhydrite solubility for DI water. ScaleChem is also better for the 20% NaCl solutions of fig 4-7, especially for temperatures above 90°C. More details about the analysis of the robustness of the different software, pros and cons, and important observations are discussed in the appendix 4B, and the effect of pressure is shown as well. Fig 4-7 was constructed using experimental values from Partridge *et al*. (1929), and good agreement was found using ScaleChem; the error is higher using PHREEQC. To

minimize the error shown in fig 4-7 using PHREEQC the Pitzer database was used but a revision was needed for solubility product of anhydrite. For high salinity the comparison was done using the experimental data reported by Blount and Dickson (1973). The extremes of solubility in DI water and 20% of NaCl cover the spectrum of the content of sodium chloride of the formation brines analyzed in this study.

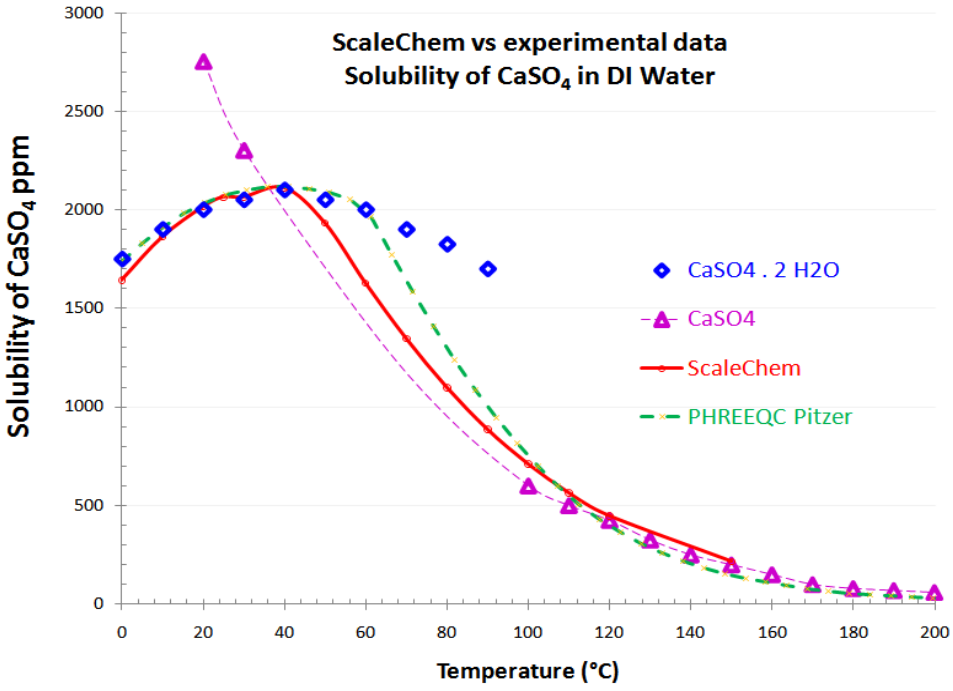

Figure 4-6 Prediction of the solubility of calcium sulfate at different temperatures using ScaleChem and PHREEQC at 1 atm or saturation pressure and for temperatures higher than the normal boiling point for water. For the software PHREEQC the database Pitzer was used, but the parameters for the solubility product equation for anhydrite were updated. The experimental values are reported by Blount and Dickson (1973) and Oli Systems Support.olisystems.com/Documents/Validation Data Sets/PredSO4.xls, 2011.

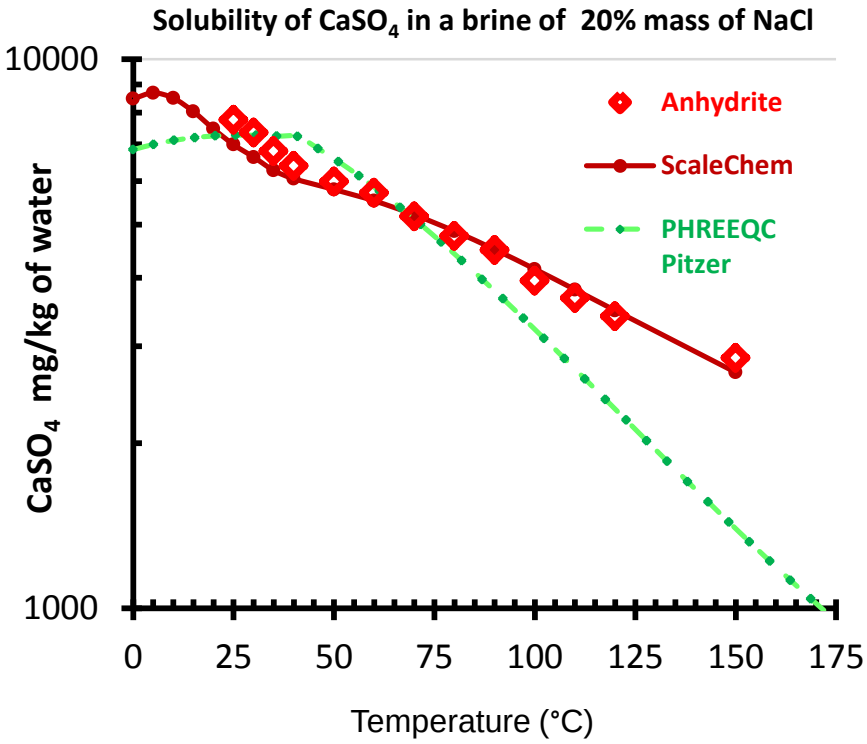

Figure 4-7 Solubility of calcium sulfate in a 20% mass NaCl brine at different temperatures. The experimental values are averages of different authors reported by Blount and Dickson (1973)

Oli Systems (2011) presented an exhaustive comparison of experimental data vs predicted results from ScaleChem, not only for the systems analyzed in this article, but for a large number of chemical species. Their extensive database can be used as a reference for additional validations.

4.5 Methodology

For each water analysis related to a specific well studied (each well belongs to different reservoir and formation) a thermodynamic analysis was done,

calculating the saturation index for all the different chemicals. The saturation index for a solid mineral is defined as departure from equilibrium:

$$CaSO_{4(s)} \overset{K_{sp}}{\rightleftharpoons} Ca^{2+}_{(aq)} + SO_4^{2-}{}_{(aq)}$$

(Equation 4-6)

The saturation ratio is the relationship between the actual activities product and the solubility product (which is the activity product that can be obtained at equilibrium), as shown here for anhydrite:

$$SR = \frac{a_{Ca^{2+}} a_{SO_4^{2-}}}{K_{sp}}$$

(Equation 4-7)

Then the saturation index is a logarithmic scale of the saturation ratio defined as:

$$\boldsymbol{SI} = \log_{10}(SR)$$

(Equation 4-8)

Using this definition of saturation index, a negative value will be obtained for under saturated brines, zero for saturated brines and, and positive values for oversaturated brines. Saturation and oversaturation of a mineral may be an indicator of the presence of that species in the formation.

After calculation of thermodynamic properties of the different water analysis, core materials from different wells were analyzed using XRD and ICP to verify the predictions of the software. Additional tests were done to verify if nondestructive

tests to rock material are possible. The rock was contacted with brine without sulfates at high temperature to measure solubilization of anhydrite via ICP.

4.6 Results

For ten different wells the saturation index with respect to anhydrite was calculated at different temperatures. Results are summarized in fig 4-8.

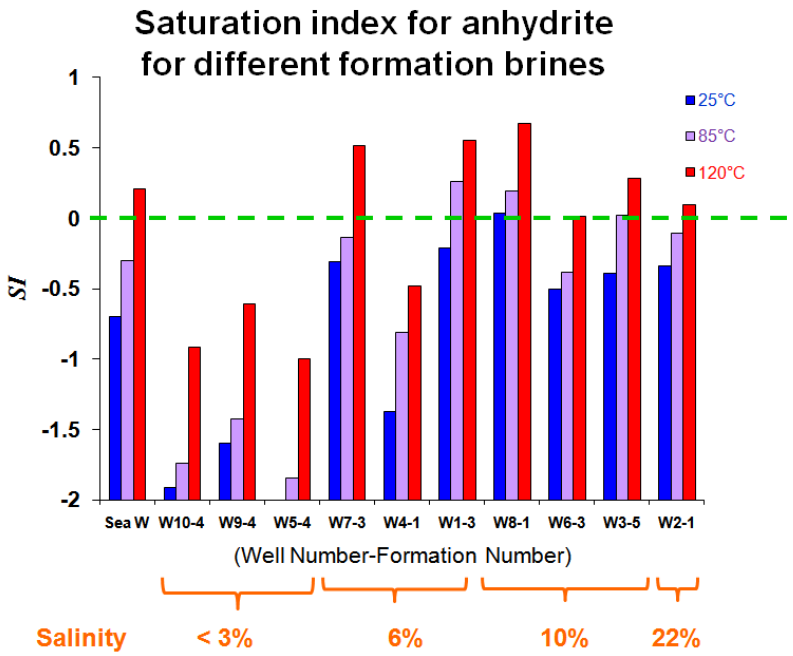

Figure 4-8 Saturation index for several wells, in different formations at room temperature, 85ºC and reservoir temperature (120º C). The green line indicates the saturation limit, higher values are oversaturation.

Most of the formation brines from the reservoirs of interest in our design for EOR are between 6% and 10% of total dissolved solids. The thermodynamic analysis in fig 4-8 indicates that at reservoir temperature of 120°C these brines are

saturated or oversaturated in anhydrite. Formation brines with salinity less than the salinity of seawater during the initial analysis presented under-saturation, but after detailed revision of the information for those wells, most of them were saturated or close to saturation. However, the analysis was strongly dependent on the depth of those samples (i.e. the formation), and a specific case is presented in the appendix 4C (fig 4C-7), where the salinity was low, but oversaturation existed.

The saturation index for most of the minerals is sensitive to the pH, anhydrite being an exception. The effect of the pressure should be considered for very high pressures, especially those samples close to saturation. In our system the pressure had a weak effect, no more that 4°C of difference in anhydrite saturation temperature for changes in pressure close to or higher than the reservoir pressure.

Different experimental techniques can be used to detect the presence of anhydrite in the rock, but this can be a problem when concentration of anhydrite is not high in the formation. To verify if anhydrite is one of the minerals present in the formation, X-ray powder diffraction is one alternative, but this technique may fail if the concentration of the anhydrite is less than 1%. Moreover, detection can be more difficult if the rock has more than three different minerals. Another technique consists of weighing a sample of 2 g and contacting with 0.5 of DI water for 12 h. After separating the aqueous phase, one precipitates the $SO4^{2-}$ of

the dissolved anhydrite using $BaCl_2$ and weighs the $BaSO_4$ formed. However, the detection limit is 0.6 wt% in the sample, according with Paulick *et al.* (2005). This value is not low enough for the method to detect all anhydrite contents that could significantly affect alkali/surfactant EOR processes, as indicated in the earlier discussion of figs 4-1 and 4-2.

A sample from one of the formations was cleaned with tetrahydrofuran (THF) and after that with chloroform-methanol azeotropic mixture. Then it was dried and ground in a shaker box before the X-ray powder diffraction. Fig 4-9 shows the sample, after being cleaned (left) and after being ground (right).

Figure 4-9 Sample from a carbonate reservoir before and after treated in the shaker box.

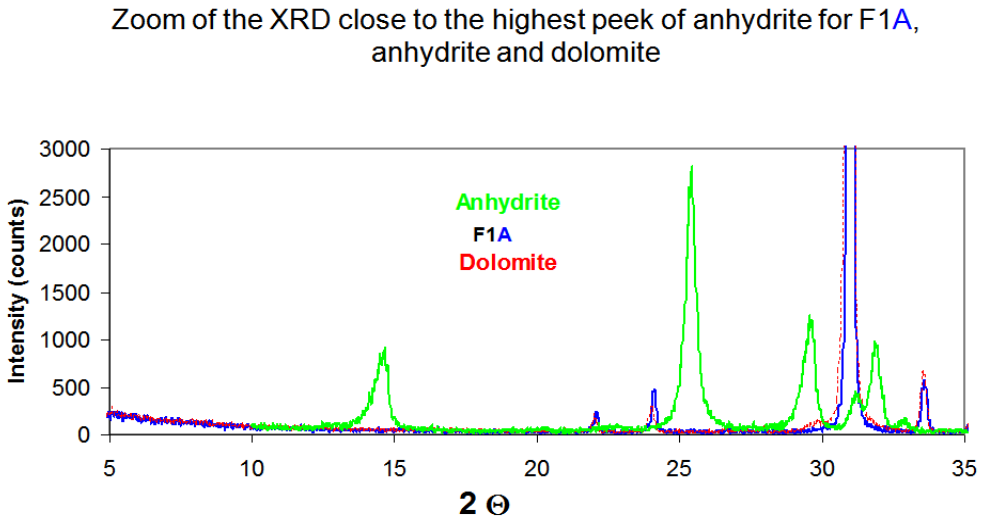

Figure 4-10 Zoom of a section of the response of the intensity for three different samples; anhydrite (reference 1), for the sample labeled (F1A) and dolomite (reference 2)

Fig 4-10 compares the response of the rock sample vs. two references; dolomite and anhydrite. This methodology was not conclusive about the presence of anhydrite in the sample. It is useful only for concentrations of anhydrite higher than 2% when more than two minerals are present; this detection limit was suggested by Alai *et al.* (2005). The complete comparison can be found in the appendix 4A. The apparatus used was the Rigaku D/MAX 2100 Ultima II Powder diffractometer.

Inductively coupled plasma (ICP) was used to confirm the composition of the rock (Perkin–Elmer Optima 4000 DV, Atlanta, GA, USA). A sample between 4 and 5 g of the rock was dissolved in HCl (1N) using between 120 and 150 ml.

The process of dissolution took more than 24 h. After 2 days the sample was diluted in a proportion 1 to 1000 using nitric acid 2%, then filtered using 0.2 μm syringe filter before the measurement. All the samples tested were soluble in the 1N HCl.

Fig 4-11 Sample before trimming (upper image), before cleaning after being cut (bottom left), and after the cleaning process (bottom right). Sample was dissolved in between 10% to 50% excess (assuming dolomite) of hydrochloric acid (1 N), and analyzed via ICP after dilution 1/1000 in aqueous solution at 2% in HNO_3

The results from ICP for this sample are given in table 4-1. They confirm the presence of anhydrite and provide the composition of the rock as well.

Using this elemental analysis as representative of the rock, the rock has the chemical form (on a molar basis):

$$1.0000\ \mathbf{CaCO_3} + 1.0784\ \mathbf{MgCO_3} + 0.0069\ \mathbf{CaSO_4} + 0.0009\ \mathbf{K_2CO_3}$$

This represents ca. 0.49% (mass base) of anhydrite, which is large enough to be important to consider for sodium carbonate consumption (Hirasaki *et al*. 2005 and 2006)

Table 4-1 Elemental analysis of the rock after ICP

Element	mg/dm^3
Ca	7.490
Na	0
S	0.04
Fe	0
Mg	4.866
K	0.013

Additional samples were analyzed for anhydrite content using the same methodology. The results are summarized in fig 4-12.

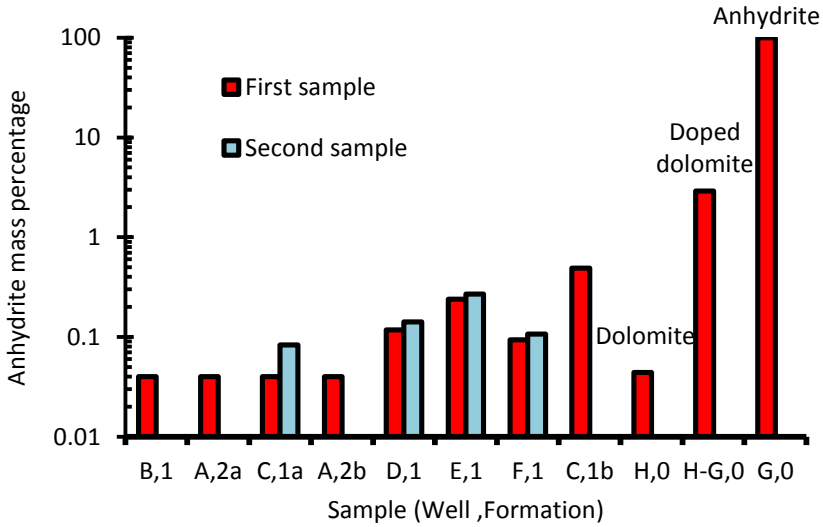

Figure 4-12 Samples of rock formation, dolomite used in adsorption experiments, and doped dolomite. All of them presented anhydrite.

Samples (B,1), (C,1), (D,1), (E,1) and (F,1) are from rocks of different wells but the same kind of formation.

Samples (C,1a) and (C,1b) are from the same well, the same formation, but from different parts of the core.

Sample (H,0) was commercial dolomite powder used as material to run a control experiment. The control sample which was labeled as sample (H-G,0), is a mixture of commercial dolomite (H,0) doped with anhydrite (G,0) and the concentration measured via ICP coincides with the proportions used to make it.

All the samples were in the range of calibration for the ICP apparatus, and every three samples a quality control sample was measured as well.

Sample rocks that seemed heterogeneous by naked eye presented no more than one order of magnitude difference in anhydrite percentage, for example samples (C,1a) and (C,1b) in fig 4-12.

Additional samples were contacted with formation brine, replacing the sulfate with an equivalent amount of Cl^-. After a week of equilibration at 90°C, these water samples were analyzed by ICP using dilutions of 1 to 2 and 1 to 3 with HNO_3 2%. Small, adjacent samples from a piece of core material showed total agreement with respect to sulfate content (42.42 g of rock contacted with 200 ml of brine without SO_4^{2-}). Thus, nondestructive tests can be used to quantify anhydrite, but the content of anhydrite must be considered in the design of the test when the content of anhydrite is high. The software used in this study was

used in the design of the experiment to make sure that complete dissolution of anhydrite occurred.

XRD was used to verify the mineralogy of the rock. X-ray photoelectron spectroscopy XPS can be used to obtain surface composition for comparison with bulk composition of the rock, but the accuracy of XPS is poor approximately ±10%, and the detection limit varies from ~0.1 to 1.0 at %, deVries (1998). Core samples were cleaned with the technique described for the other two methodologies, and samples were analyzed and the results are consistent with the pervious findings. Figure 4-13 is one of the analyses where all the peaks are visible in the graph without zooming. The labels for Cl, Si, Al at their respective binding energy appear in the figure, but not peaks were detected, neither for Sulfur (i.e. 230.9 eV for S2s, 163.6 S2p1/2 and 162.5 eV for S2p3/2). In the case of sulfur was expected because is present close to the detection limit according with the ICP. This technique measures surface chemistry, not bulk chemistry and results from three samples taken from 1cm^3 of rock are in the table 4-2

Table 4-2 Atomic percentage for analyzed samples

	C	O	Mg	Al	Si	Cl	Ca
	26.75	55.26	7.03	0	0.26	0.26	10.44
	25.04	55.8	7.98	0	0.08	0.3	10.81
	23.9	55.16	9.12	0	0.02	0.36	11.43
average	25.23	55.406	8.0433	0	0.12	0.3066	10.893
stdev	1.4344	0.3442	1.046	0	0.1248	0.0503	0.5002

According to the table, some solvent may be present in the surface of the rock, but the main difference respect to the ICP analysis of the bulk rock and the XRD, is that the rock seems not to have only dolomite on the surface, but calcite. This is consistent with thermodynamics. The rock in formation brine at reservoir temperature and a partial pressure of CO_2 of 0.1 atm is oversaturated in calcite and under-saturated in dolomite. Even at room temperature if the partial pressure of CO_2 is 0.01 atm the situation is the similar according with simulations using PHREEQC Pitzer.

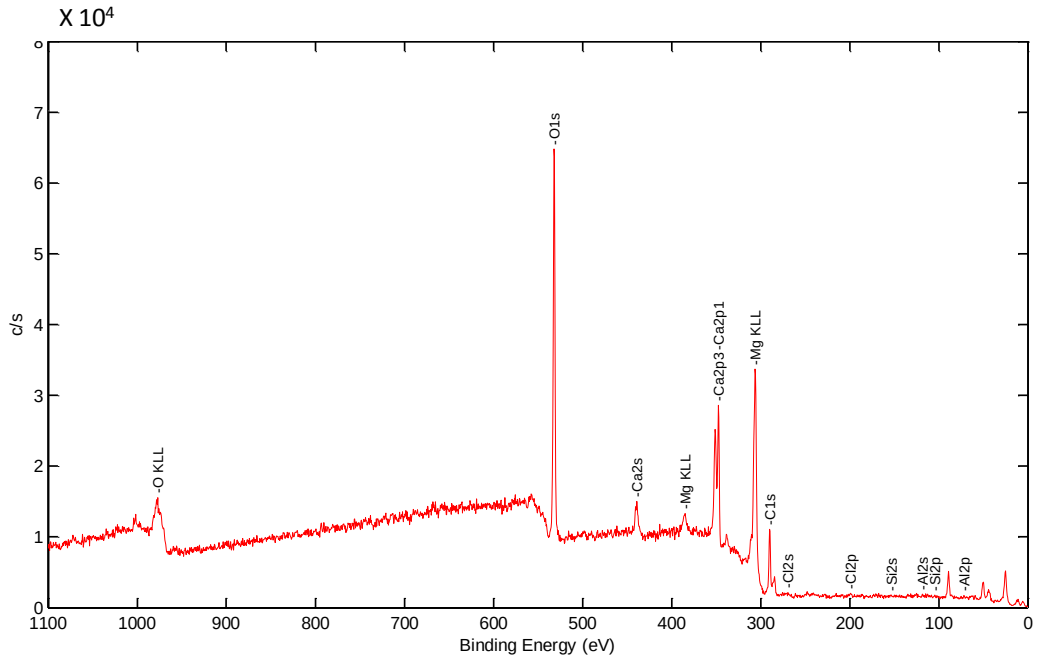

Figure 4-13 XPS for core sample. The only detectable peaks in the image are those for OKLL, O1s, Ca2s, Ca2p1/2, Ca2p3/2, MgKLL, Mg2s, Mg2p1/2, Mg2p3/2

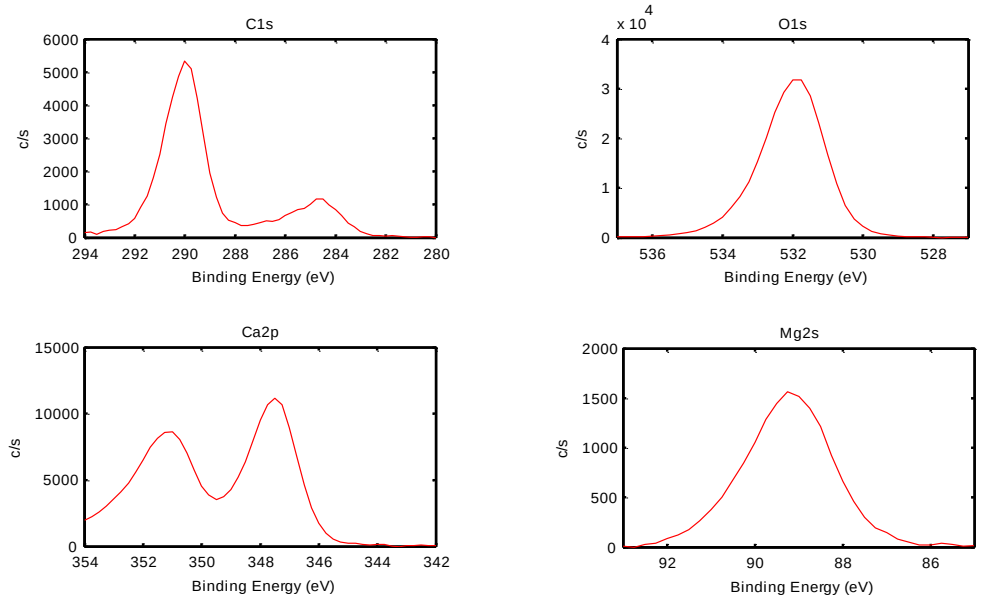

Figure 4-14 Peaks for quantification of O, C, Ca and Mg

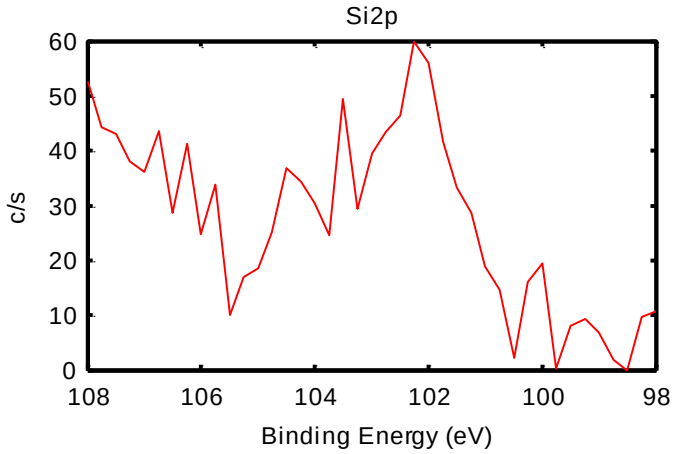

Figure 4-15 The Si was quantified with the peaks at 99.8 eV and 99.2eV, but the result in two of 3 analysis was out of the detection limit, and no signal appear as well in 149.7 eV

4.7 Conclusions about the chapter

Thermodynamic analysis of formation brines with existing brine software can be used to calculate saturation index of minerals in a reservoir and, in particular, determine whether anhydrite is present in the formation. However, the analysis cannot determine the amount that is present.

XRD lacks the sensitivity to detect whether anhydrite is present in formation rocks at low concentrations which would produce detrimental effects on alkali/surfactant processes.

In contrast, ICP using a solution of dissolved rock in 1N hydrochloric acid was a reliable method. It was able to measure not only the content of anhydrite, but also the overall composition of the rock and the proportions of different minerals

ICP was also used to measure the presence of anhydrite in a rock sample nondestructively by equilibrating it with a formulated brine at a specific temperature for several days. The brine formulation and equilibrium conditions were set in order to achieve reliable results, i.e. to assure that the brine could dissolve all the anhydrite present without becoming oversaturated.

Acknowledgments in this Chapter

Dr. Haiping Lu and Dr. Mason Tomson from Brine Chemistry Consortium at Rice University.

Chapter 5

STATIC ADSORPTION AND ANALYTICAL METHODS TO MEASURE SURFACTANTS

5.1 Overview of Chapter 5

This chapter contains the description of techniques to measure: concentration of the surfactants, thermal stability of surfactants, and adsorption of surfactants on dolomitic rocks. It briefly describes as well studies to test if scale inhibitors, chelating agents or sacrificial agents have potential to reduce adsorption of surfactants on rocks.

During static adsorption experiments blends of IOS (Internal olefin sulfonate) and AAC (alkyl alkoxy carboxylates) were equilibrated for at least two days with dolomite and isotherms were obtained. Two different titration techniques were needed in order to quantify both the IOS and the AAC. The IOS was measured via low pH Epton's titration, and the carboxylate quantified after two-phase high pH titration measured the total surfactant concentration.

Adding scale inhibitors to surfactant solutions had a mild reduction on the adsorption (ca. 20% reduction), but not all the inhibitors produced clear injectable solutions. Polyacrylate improved the aqueous stability of the surfactants, and produced clear solutions.

When the dolomite was contacted with polyacrylate in seawater, and after that rinsed and then equilibrated for 2 days with surfactant, considerable reduction of the adsorption was observed (ca. 80%), so this was identified as a potential solution to minimize adsorption during EOR processes for blends of IOS and AAC in dolomites.

Aqueous stability of the blend AAC and IOS (i.e. $C_{28}(PO)_{25}(EO)_{25}COONa$ + $C_{15\text{-}18}$ IOS) seems to be strongly dependent of the salinity. The IOS in seawater was thermally stable at 90°C, but AAC seems to form aggregates. This blend of IOS+AAC in seawater for 2 days was thermally stable respect to surfactant activity, but the pH was reduced to a value close to 4, indicating a certain degree of instability of the surfactant blend. However, when contacted with dolomite the surfactant solution was buffered and the pH did not change.

The initial blend IOS+AAC (i.e. $C_{24}(PO)_{25}(EO)_{56}COONa$ + $C_{19\text{-}23}$ IOS) was unstable at high temperature and its activity was reduced considerably in 2 days.

The addition of foam boosters (e.g. Laury betaine, Cocamidopropyl betaine and sulfobetaine) to the IOS-AAC blend was studied but not considered as an alternative because the proportion required to have clear aqueous solutions was high (higher than 2 to 1 mass ratio). The proportion 2 to1 between zwitterionic and anionic is a common requirement for other formulations studied for foaming blends, and will be discussed in the Chapter 7.

The stability of the Cocamido propyl betaine was measured at 100° C, at neutral pH and at low pH buffer with the use of HPLC. The CAPB was stable at 100° C

at neutral pH in sea water. After 3 months of aging, the activity loss was less than 4% (half life time of 4.6 years), but at low pH of 3.88 the loss in activity at 100°C was nearly 23% (half life of 0.66 years). At higher temperature of 125° C and low pH the degradation is faster (half life of 6.5 days).

HPLC is a reliable method to measure concentration of zwitterionic surfactants. Two-phase titration can be used as well. The stability of formulations containing zwitterionic surfactants and their aqueous solution properties will be discussed in Chapter 7.

Initial estimation of adsorption of a blend of Cocamidopropyl betaine, AOS and an alkyl trimethyl ammonium chloride indicates the same order of magnitude as the adsorption measured with the anionic surfactants, but more research is needed to confirm this initial determination.

The Surfactants Studied in this section include:

AAC = $C_{24}PO_{25}EO_{56}COONa$ or $C_{28}PO_{25}EO_{25}COONa$

IOS = $C_{19\text{-}23}SO_3Na$ or $C_{15\text{-}18}SO_3Na$

ZI (CAPB , LB, LHSB)

5.2 Methods to quantify surfactants

Anionic surfactants can be determined in aqueous solutions by Epton's method or two-phase titration. Then the method can be used to measure adsorption of surfactant by powder dolomite in static adsorption experiments.

The static adsorption of blended anionic surfactants of dissimilar hydrophobic moieties (R_1 and R_2) but ending with similar hydrophilic moieties; i.e., R_1-$\mathbf{SO_3^-Na^+}$ and R_2-$\mathbf{SO_3^-Na^+}$.

The UT formulations for this field application are made also of anionic surfactant blends but with dissimilar hydrophobic and hydrophilic moieties; i.e., R_1-$\mathbf{SO_3^-Na^+}$ and R_2-$\mathbf{CO_2^-Na^+}$ or a carboxylate moiety. The Epton's method does not apply to carboxylates and only determines total surfactant active at low pH, not individual, surfactant concentration. Thus, the Epton's two-phase titration method can determine only one of the surfactants, R_1-$\mathbf{SO_3^-Na^+}$, in UT blend.

Research of different procedures for determining static adsorption of blends containing carboxylates has been done. A procedure, named here Bromocresol or high pH two-phase titration has been adapted for determining both total surfactant adsorption and individual surfactant adsorption of the recent UT formulations.

Table 5-1 UT formulations for this research

Name	Formula	Molar mass	% mass
Old UT Blend			
Enordet 0342H	**C_{19-23} IOS**	398	**50**
Old UT Carboxylate	**$C_{24}PO_{25}EO_{56}CO_2Na$**	4259	**50**
New UT Blend			
Petrostep S2	**C_{15-18} IOS**	351.5	**50**
UT Carboxylate	**$C_{28}PO_{25}EO_{25}CO_2Na$**	2956.6	**50**

5.3 Analytical techniques to measure concentrations during static adsorption experiments.

The following four procedures, three of them briefly described below, were tested but only Bromocresol (BC) method was successfully applied. The method is simple and did not require expensive equipment. The technique is a colorimetric titration and requires only burettes, pipettes volumetric cylinders, centrifuging tubes and a centrifuge.

1. **HPLC** Detects Mass of Components Based on Their Retention Times.

Procedure needs more research because retention time was similar for both components of the UT blend (i.e. Carboxylate and IOS). Overall concentration can be measured with precision, but concentration of each component requires more research. Only partial separation of the surfactants was possible; a fraction of the carboxylate elutes first, then the rest of the carboxylate elutes with the IOS. The HPLC worked well for zwitterionics; details are reported in section 5.9 to measure thermal stability of CAPB.

2. **Epton's Two-Phase Titration** Detects moles based on Ion-Pairing for only anionics such as sulfates and sulfonates; e.g., sulfonated Internal olefins and sulfonated alpha olefins.

Before BC method was developed, it was used for determining only IOS in UT blend. This technique can only be used for rough quantification of adsorption if it

is assumed that there is no preferential adsorption for one of the components, it is so because mole fraction of IOS in the blends used is large

(See description in the appendix 5A)

3. **Potentiometric Titration** Detects moles based on Ion-Pairing for either anionics such as IOSs at pH <7 or Soaps (Carboxylates) at pH ≥ 10

Tested successfully once by diluting sample to be titrated with 3.5% NaCl buffered to pH = 11.

This technique was not used, because electrode was not designed to operate at pH higher than 10, and only at pH of 11 was it able to completely quantify the carboxylate.

4. **Bromocresol Two-Phase colorimetric titration d**etects moles based on Ion-Pairing for anionics. High pH buffer is needed to measure carboxylate in a sample or total amount of surfactant if carboxylate and another anionic surfactant are present. (See description in the Appendix 5A, 5B and 5C)

   Analytical technique for Bromocresol 2-Phase colorimetric high pH titration:

   Table 5-2 describes the sample preparation, buffer formulation and dye concentration needed for the titration.

Fig 5-1 is a collection of snapshots of the titration process. The endpoint is when the upper phase is colorless; at this point all the surfactant and the bromocresol green had formed ion-pairs with the titrant.

Table 5-2 Sample preparation

Sample preparation		
	Description	Volume (ml)
Sample	Surfactant solution (concentration ~ 2 mM)	2
Buffer	High pH phosphate buffer	6
Organic phase	$CHCl_3$ (Chloroform)	5
Dye	Bromocresol Green	1 *
Titrant	TEGOtrant A100 or Hyamine (2 mM) **	To be measured
High pH phosphate buffer		
	Description	Volume (ml)
Diphosphate	$Na_4P_2O_7$ 10 H_2O (17.28 g/l. i.e. 65 mM)	300
Tripolyphosphate	$Na_5P_3O_{10}$ (23.91 g/l, i.e. 65 mM)	100
Propanol	n-propanol	80
Indicator Bromocresol Green		
	Description	
BCG	Bromocresol green (60 mg/l)	

**If concentration or volume change a calibration curve is required, otherwise running a blank is enough.*

*** If the volume of titrant needed during titration exceeds 8 ml, it is recommended to prepare the titrant in aqueous solution containing 1/6 of n-propanol for better results.*

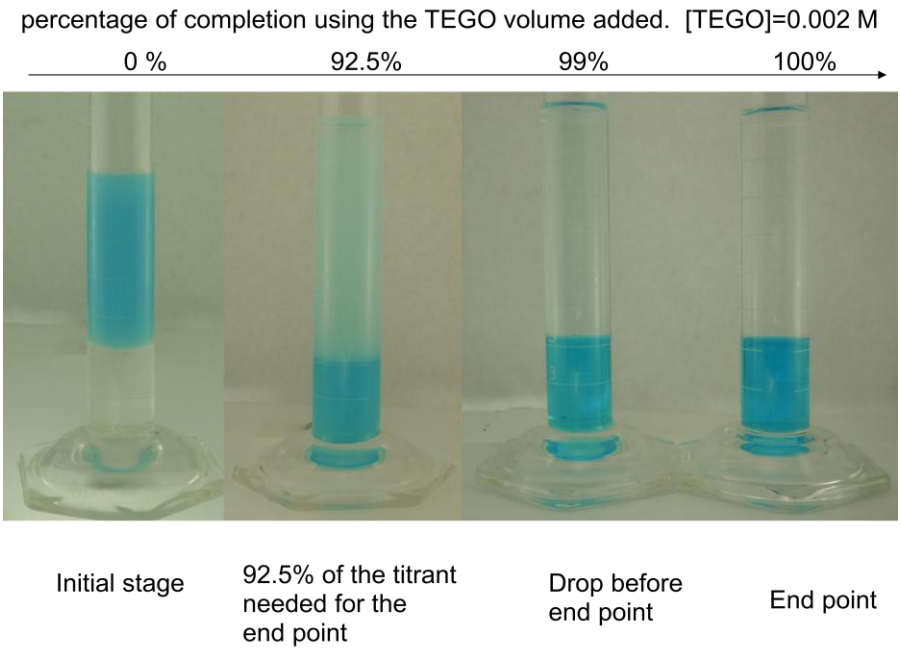

Figure 5-1 High pH titration. It is recommended centrifuging during the titration to accelerate the process of titration. The endpoint is when the upper phase becomes colorless. If more than 100% of the volume of liquid phase is increased during titration, it is recommended prepare the titrant at the same concentration of alcohol that the buffer (1/6), and at the same ionic strength.

The adapted BC method (Bares, 1969) was systematically tested against other well known methods. Figure 5-2 is a graph of test results from titrating Sodium Dodecyl Sulfate (SDS) potentiometrically and colorimetrically by either Epton's or BC, using cationic TEGO as titrant. The linearity, from test results of the controls, is a strong indication that BC method can be also used to determine anionic surfactants at elevated pH, which is a requirement to determine "soap"-like anionic surfactants such as carboxylates. Figure 5-3 is to indicate that if the amount of BC is different from sample to sample, a calibration curve is required because bromocresol green is an anionic

molecule that, like the surfactant, forms ion pairs with the cationic titrant, a factor which needs to be taken into consideration.

Thus, from Figures 5-2 and 5-3, two colorimetric techniques for quantifying blend of ionic surfactants were successfully tested because

1. Methylene blue as indicator at low pH (<3), determines **only IOS in blend**
2. Bromocresol Green as indicator at high pH (>10) determines total anionic surfactant.

Total = Carboxylate+IOS in blend; thus, **Carboxylate = Total - IOS**

Next section's experiments will include the other surfactant, carboxylate, in the UT blend.

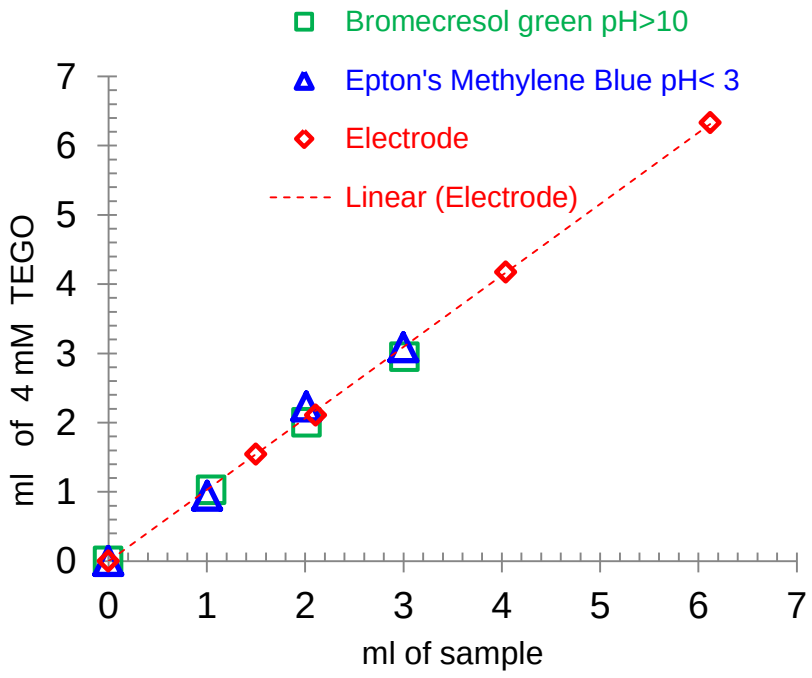

Figure 5-2 Comparison of different techniques for titrating SDS

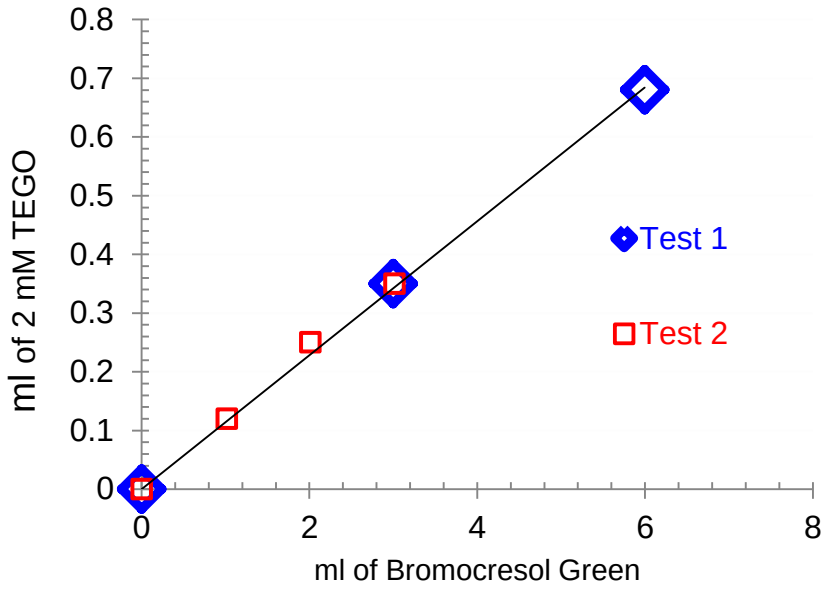

Figure 5-3 Effect of bromocresol greenfor titration at high pH. Amount of BC needs to be taken into account during the titration, not the same for methylene blue as indicator. The bromocresol green is an anionic indicator and forms ion-pairs with titrant.

5.4 Quantification of both, IOS and Carboxylate surfactants in UT Blends

Surfactant concentration of three blends, combining the two colorimetric methods (low pH and high pH two phase titrations), were determined before static adsorption test. The purpose of the three tests is:

1) Validate potential to measure IOS and alkyl alkoxy carboxylate in a blend of surfactants.
2) Measure thermal stability of a surfactant blend of IOS and AAC.
3) Compare adsorption using surfactant solutions with different scale inhibitors or sacrificial agents in powder dolomite.

Table 5-3 Composition of UT blend during calibration

Blend	Description	Mass ratio	Molar ratio
Test case 1	**C_{19-23} IOS: $C_{24}PO_{25}EO_{56}CO_2Na$**	0.3: 1	3:1
Old UT	**C_{19-23} IOS: $C_{24}PO_{25}EO_{56}CO_2Na$**	1:1	10:1
New UT	**C_{15-18} IOS: $C_{28}PO_{25}EO_{25}CO_2Na$**	1:1	8.4:1

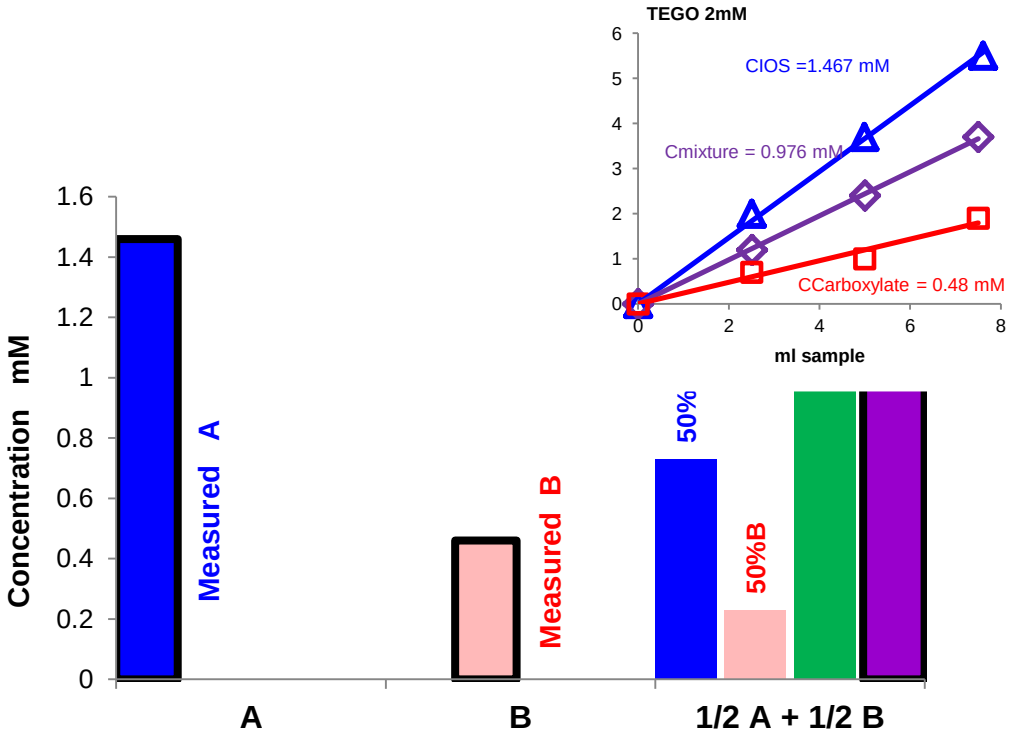

Figure 5-4 Verification of titration techniques (1) of (2)
Titrations at high pH, BC
Test Case IOS $_{19-23}$: $C_{24}PO_{25}EO_{56}CO_2Na$ 3:1 Molar

- **Blue: 1.467mM Enordet 0342**
- **Purple: 0.976 mM Mixture**
- **Red: 0.48 mM Carboxylate solution**

Bares (1969) indicated during his research that the molar mass of the carboxylate may influence the stoichiometry of the titration when long lipophiles are used. This first test case is to verify the technique with blends of AAC and IOS, and the stoichiometry.

Figure 5-4 is Test Case summarized as a bar chart. The insert with the titration test results is shown to give an appreciation of experimental work done to create each bar. The green bar is the expected total surfactant concentration resulting by adding equal volumes of surfactant solution A (IOS), and surfactant solution B (AAC). Each having a concentration needed to end up with a molar ratio 3 to 1. Purple bar is the measured value. Then the resulting solution represented as purple bar (i.e. AOS:AAC, 3:1) was analyzed again using both techniques (i.e. low pH and high pH two phase titration) to quantify the concentration of each surfactant. Results are shown in fig 5-5.

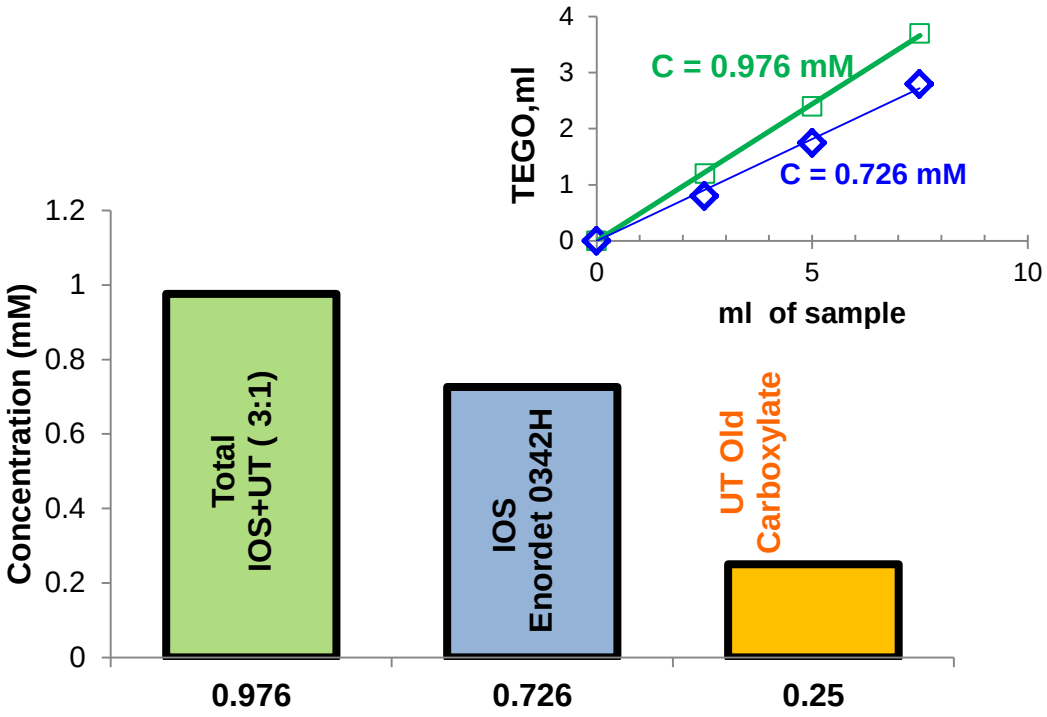

Figure 5-5 Verification of titration techniques (2) of (2)
Titrations at high pH, BC
Test Case IOS $_{19\text{-}23}$: $C_{24}PO_{25}EO_{56}CO_2Na$ 3:1 Molar
Titrations at high pH (bromocresol green)

- **mixture from previous (Figure 5-4)**
- **Titration at low pH (methylene blue)**
- **mixture**

Test Case molar ratio was 3:1 and measured by colorimetric titration 2.9:1: an error 3.3%, which is considered acceptable. The methodology proposed can thus be used to measure IOS and AAC.

5.5 Colorimetric two-phase titrations, to measure thermal stability of $C_{24}PO_{25}EO_{56}CO_2Na$ in UT_{Old} Blend and addition of polyacrylate to improve aqueous stability.

5.5.1 Aqueous Stability

The aqueous solution of the old UT blend changes its color, turbidity and homogeneity at 90ºC with time. To understand if the stability of blends of IOS and alkyl alkoxy carboxylates depends on temperature, the concentration of Old UT blend as function of time was briefly investigated to learn some of the surfactants' characteristics in brines of interest.

Surfactant solutions with the Old UT Blend (i.e. $C_{24}PO_{25}EO_{56}CO_2Na$ and $C_{19\text{-}23}$ IOS) produced aggregates at 90°C after a day. To improve stability, adding scale inhibitors was investigated as an alternative.

Figure 5-6 is a picture of blend and individual surfactants in seawater after being heated at 90°C for one week. Appearance of all samples was altered from that at ambient temperature where blend and carboxylate formed clear solutions and IOS solution was cloudy but without the oily layer.

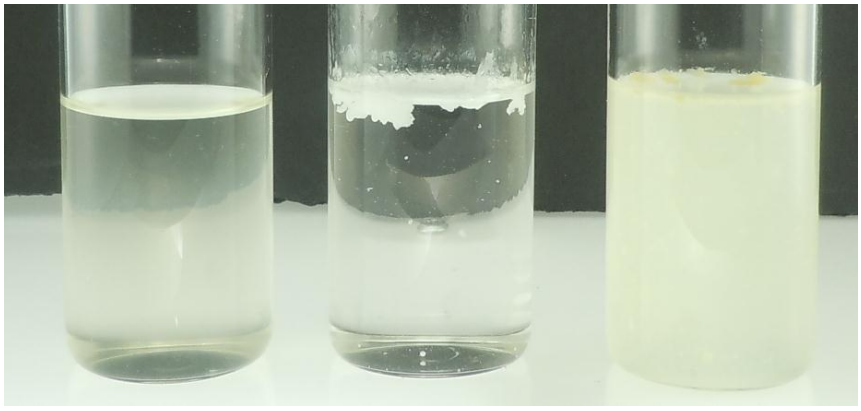

0.5% Initial UT Blend **0.25% Initial UT Carboxylate** **nea0.25% IOS**

Figure 5-6 Appearance of samples after at 90°C for a week in seawater. Carboxylate and Blend samples at room temperature then heated for 1 week.

Concentrations of surfactants in heated samples were determined and test results are represented in Figure 5-7. Overall and carboxylate molar concentrations dropped to 47% and 30% of initial values.

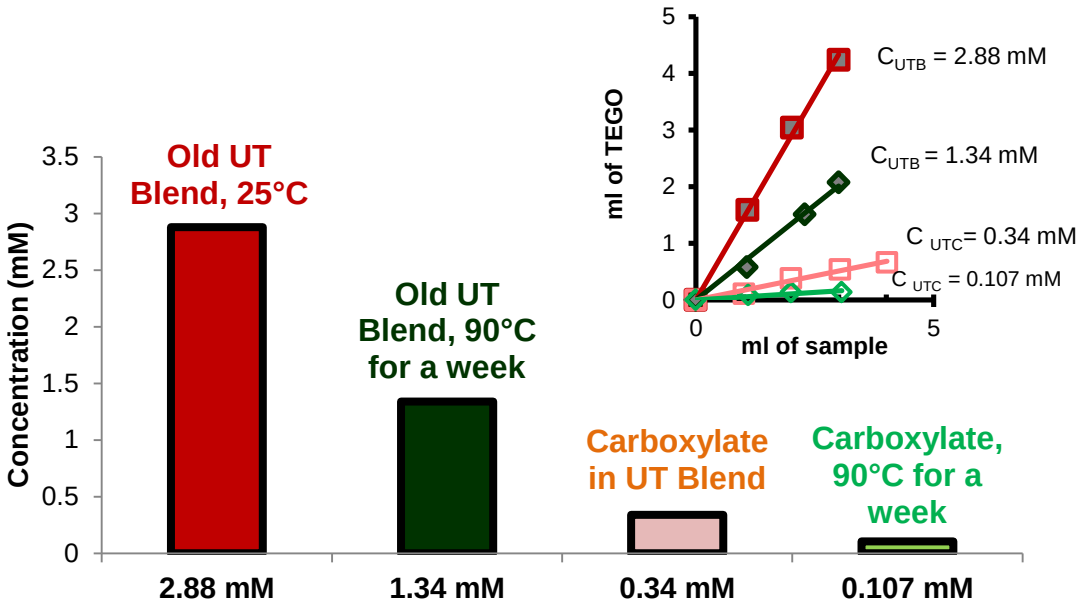

Figure 5-7 Test Results of thermal stability UT $_{old}$, 1-week testing in seawater at 90°C

Addition of polyacrylate, DTPMP and SPA

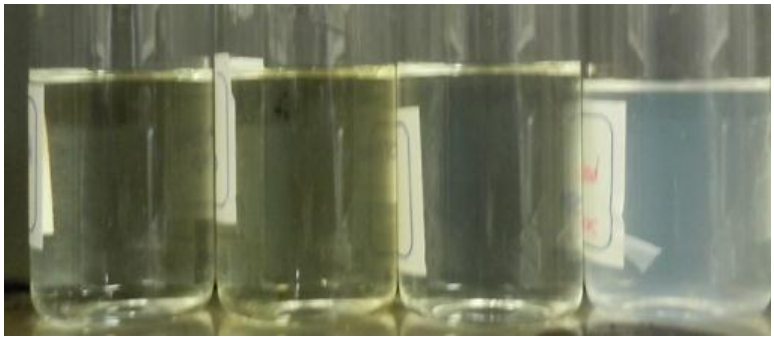

Additive	PA (2.1 kDa)	DTPMP	SPA	-
ppm	500	50	50	-

After 2 weeks at 90°C

Figure 5-8 Effect of adding polyacrylate to Old UT Blend. Formulation remained clear for longer time than without, a similar effect is observed with DTPMP and SPA with mild cloudiness.

A similar sample adding polyacrylate (PA) in Figure 5-8 (compare first vial with the last one, control) was equilibrated with dolomite (not shown) and titrated to determine adsorption in the presence of scale inhibitor. Test results, are in Figure 5-9 and summarized in Table 5-4, appear to indicate that adsorption is dissimilar for the two surfactants; the mass ratio changed from 50/50 to 30/70. Sulfonated polyacrylic acid (SPA) did not reduce the adsorption, and diethylenetriamine penta(methylene phosphonic acid) (DTPMP) was not considered because it produced acidic surfactant solution with potential to consume $CaCO_3$. DTPMP decreases the pH of aqueous solution to less than 2 at 10000 ppm.

Others additives were briefly studied and a summary of the test results is shown in Figure 5-10.

Table 5-4 Polyacrylate contacted with dolomite

UT_{old}	**IOS : Carboxylate**	
	Mass	**Molar**
Initial 25°C	**0.5 :0.5**	**0.91 :0.09**
Blank 90°C	**0.5 :0.5**	**0.91 : 0.09**
Dolomite 90°C	**0.3 : 0.7**	**0.80 : 0.20**

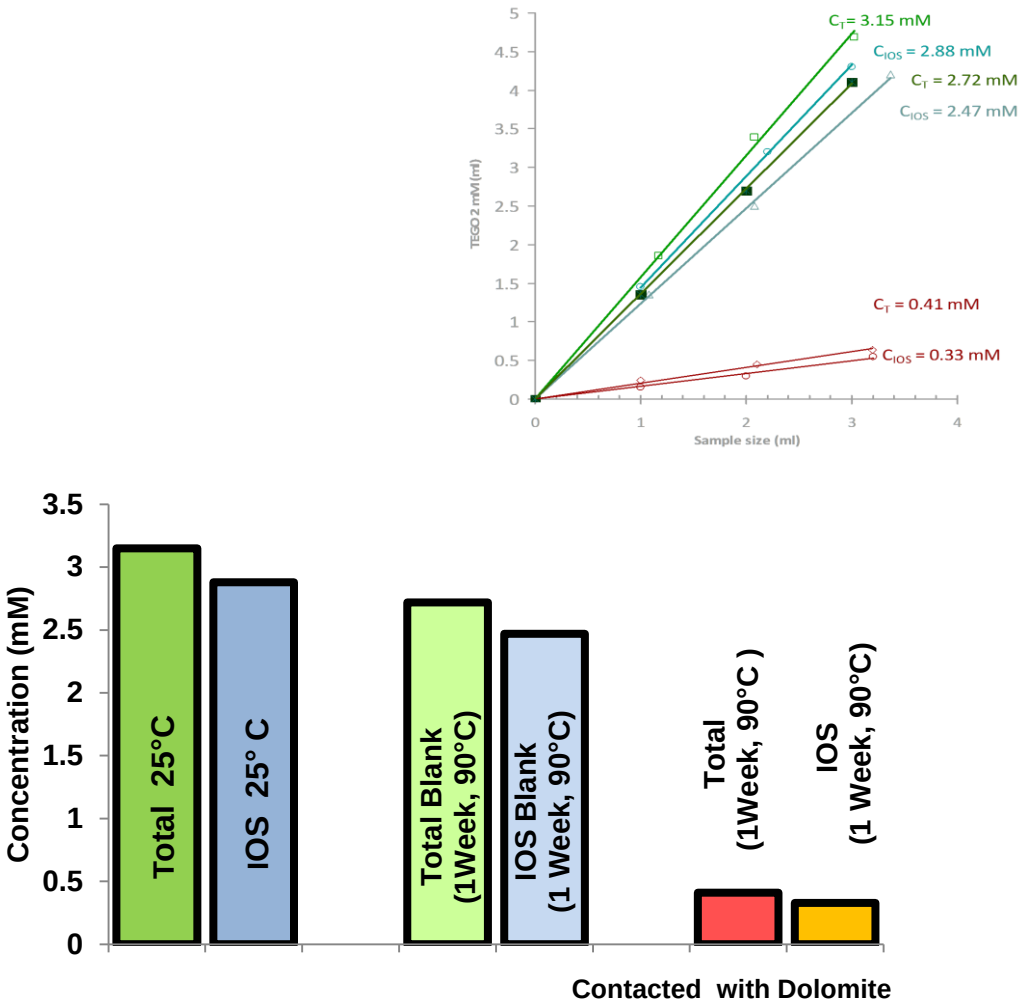

Figure 5-9 UT_{old} + Polyacrylate 500 ppm 1- week 90 ° C

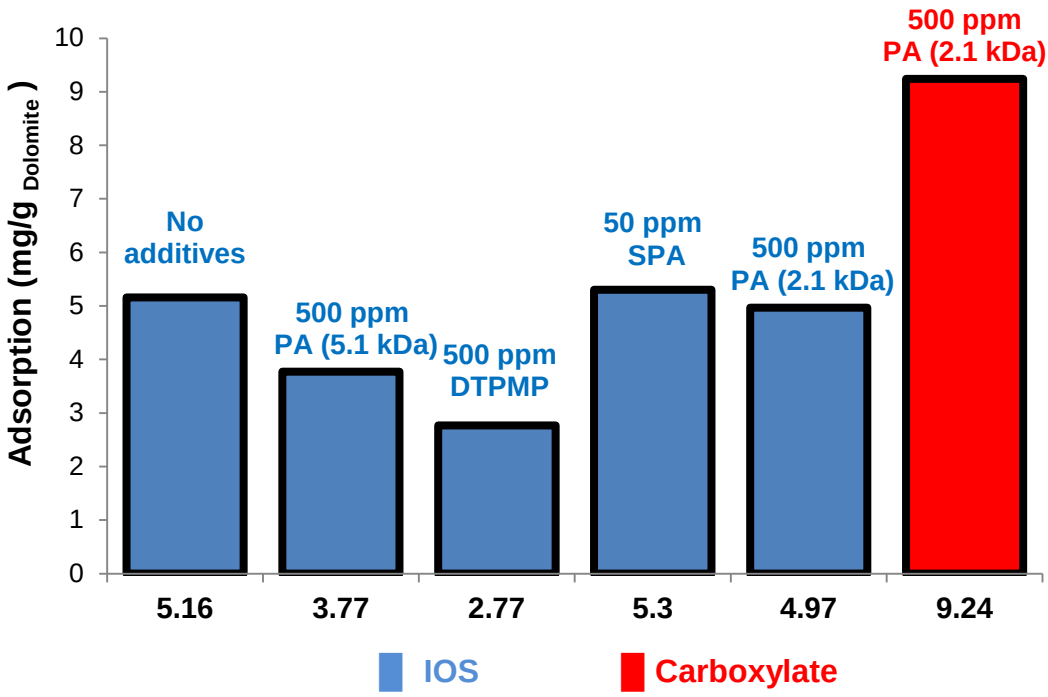

Figure 5-10 Effect of additives on static adsorption on dolomite powder of the Old UT Blend. The bars are plateau values.

Adsorption of IOS on powder dolomite with different scale inhibitors or sacrificial agents it is plotted in Fig 5-10. The carboxylate adsorption was not measured, except for the sample with polyacrylate added.

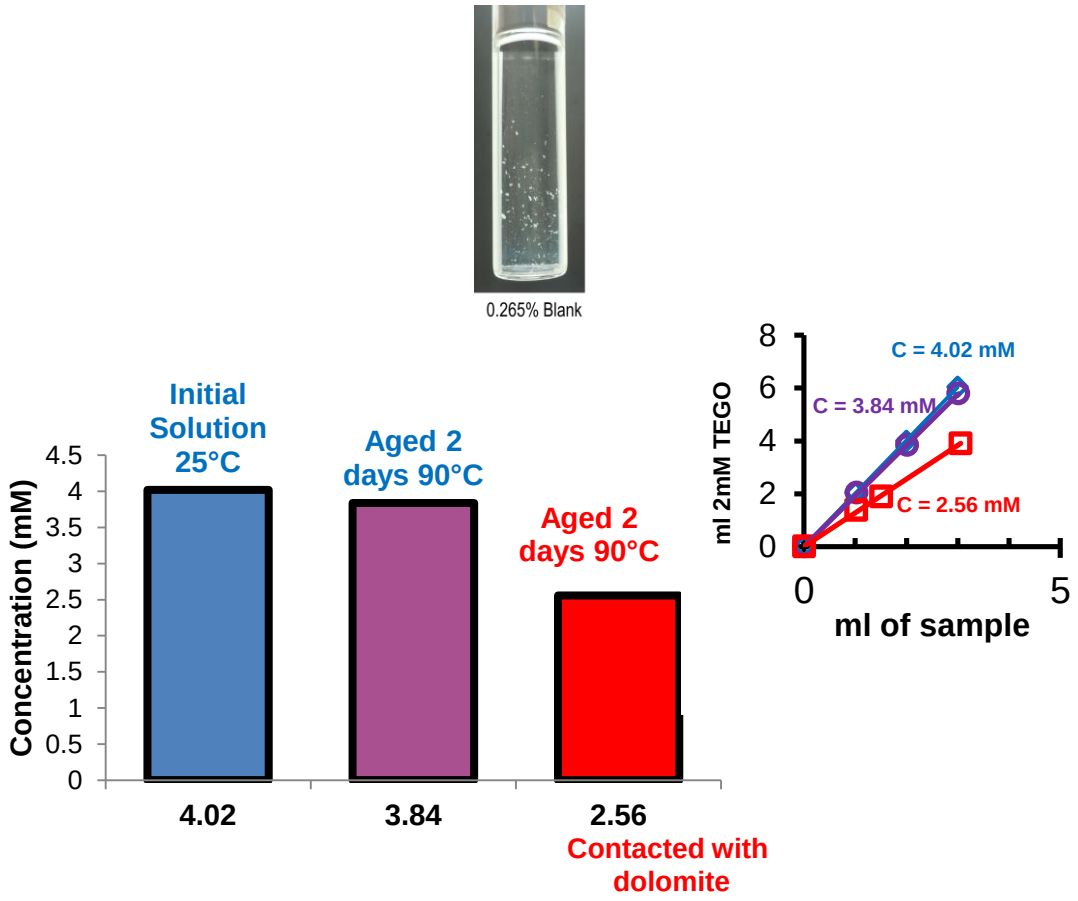

Figure 5-11 Total Surfactant Concentration, aged 2 days at 90° C

Blue: Initial
Purple: Blank
Red: Solution contacted with dolomite
Picture: sample titrated contained aggregates

The measurements may be overestimations of adsorption, because most of them produced some precipitate. (see picture in upper section of figure 5-11). This is not the case for the sample with polyacrilate added, because the reulting aqueous surfactant solution was clear.

5.6 Colorimetric two-phase titrations measuring adsorption of $C_{28}PO_{25}EO_{25}COONa$ and C_{15-18} IOS in UT_{New} Blend.

The titration technique discussed above was used to measure adsorption of each component of the surfactant in the new UT Blend. The samples of different initial concentrations were prepared adding powder dolomite and sealed in glass ampoules, then mixed continuously and aged for 2 days. Results are indicated in fig 5-12.

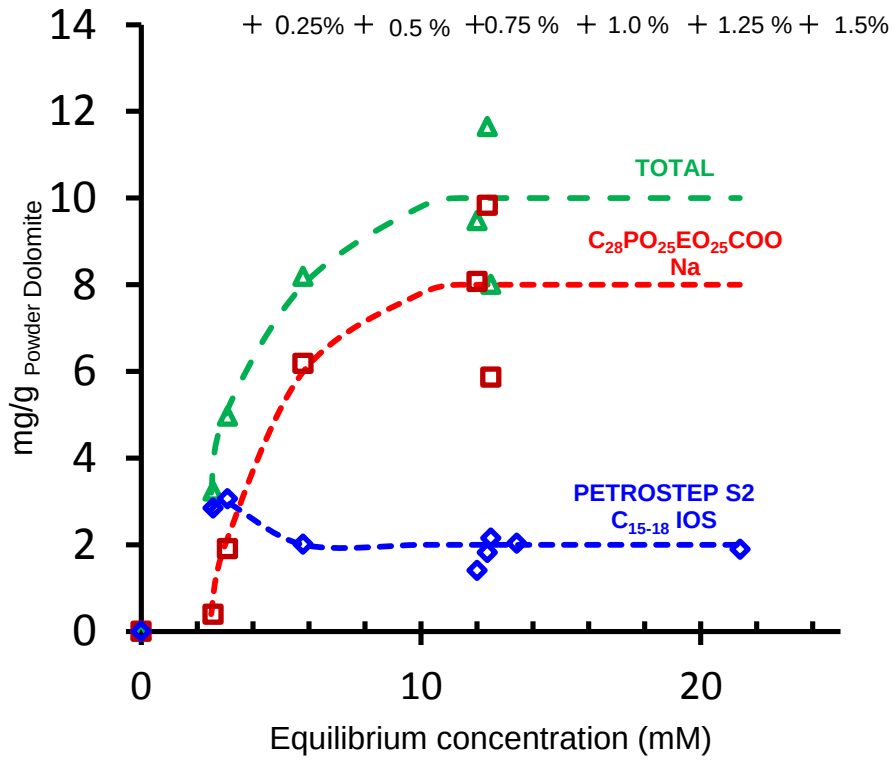

Figure 5-12 Static adsorption; UT_{New} Blend in Seawater at 90°C. The powder dolomite used for this study has a surface area of 1.2 m^2/g, and surface area of PEMEX rock ranges from 0.12 m^2/g to 0.98 m^2/g

Adsorption of the two surfactants on powder dolomite indicates that carboxylate will adsorb preferentially, Fig 5-12.

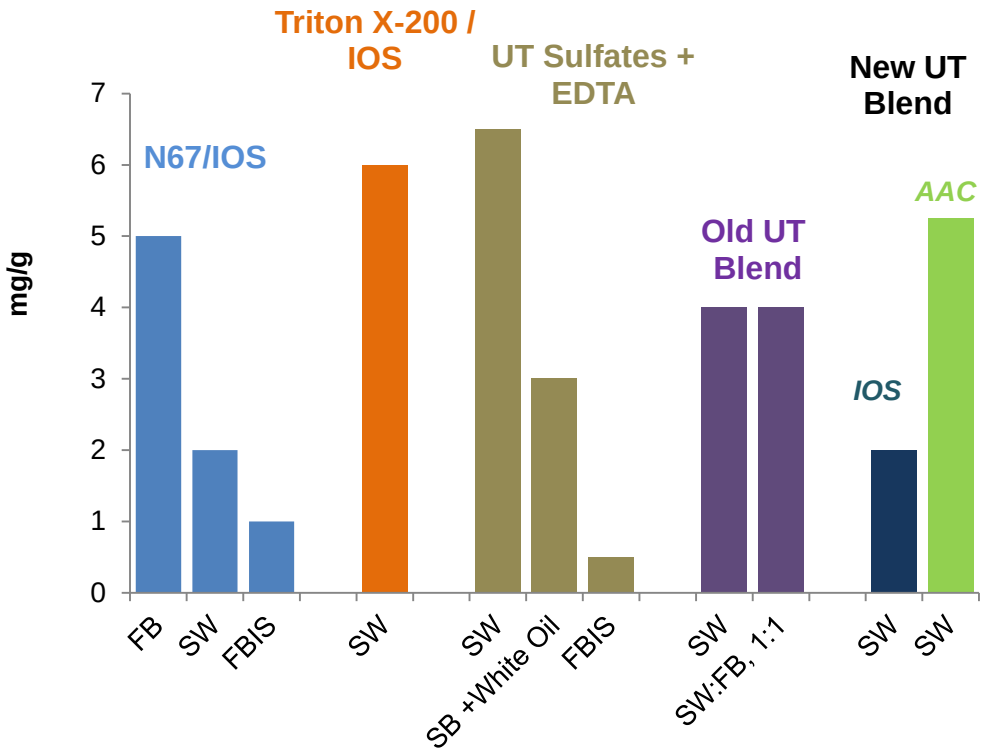

Figure 5-13 Summary of static adsorption test results. Static Adsorption at 90°C : Comparison at ~0.5 wt%.
SW = Seawater, FB = Formation Brine, FBIS = NaCl Brine with Formation Brine ionic strength, SB= 6% NaCl + 0.1% $CaCl_2$.

Comparison of static adsorption for different surfactants (shown in fig 5-13) indicates that salinity and the ratio of divalent to monovalent cations have strong effects. In the case of the old UT blend of AAC-IOS the effect on adsorption of the IOS (i.e. bars in purple) with changes in salinity is not important. For this old UT Blend only the adsorption of IOS was measured. The New UT blend has less

adsorption of the shorter-chain IOS, but the adsorption of the AAC is high (i.e. light green bar)

5.7 Thermal behavior

5.7.1 Thermal behavior of 1% Individual surfactants in DI Water at 90°C ($C_{28}PO_{25}EO_{25}COONa$ and C_{15-18} IOS)

UT formulation appears not to be stable in seawater at 90°C. Some tests about thermal stability were conducted to see if the stability can be improved.

Figure 5-14 Aqueous surfactant solutions in DI water after ½ week

Table 5-5 Thermal behavior of 1% Surfactant in DI Water at 90°C

Surfactant	Appearance	pH	mMolar
Petrostep S2 (fresh)	Clear	6.5	28.45
Petrostep S2 (1 week)	Clear	2	26.1
$C_{28}PO_{25}EO_{25}CO_2Na$(fresh)	Clear	6.5	1.93
$C_{28}PO_{25}EO_{25}CO_2Na$ (1 week)	Very cloudy	3.75	0.603

Surfactant solutions of IOS and AAC were prepared in DI water, and aged for a week at 90°C. Both IOS and AAC exhibited decreases in the pH and surfactant activity, and for the AAC the aqueous stability of the surfactant solution was poor after a week. Results for this test are in Table 5-5 and in fig 5-14, a photograph of samples of both surfactants after 4 days at 90°C.

5.7.2 Thermal behavior of 1% surfactant blend in seawater, 90 °C ($C_{28}PO_{25}EO_{25}COONa$ and $C_{15\text{-}18}$ IOS, 1:1)

Surfactant solution is clear after two weeks at 90°C, pH is decreasing, but surfactant concentration is not changing by the second week within experimental uncertainty. In Table 5-6 the values of pH and the activity of surfactant indicate that even the activity almost remains constant within; production of acidic components occurs at higher temperature.

5.7.3 Thermal behavior of 1% surfactant blend in seawater, contacted with dolomite 90 °C ($C_{28}PO_{25}EO_{25}COONa$ and C_{15-18} IOS)

pH remains unchanged when dolomite is present, indicating the buffer capacity of the rock. If generated acid is responsible of the instability of the aqueous solution, then the dolomite rock may eliminate the problem.

Table 5-6 1% Surfactant in seawater, contacted with dolomite 90°C

Surfactant	pH	Concentration (%)
New UT Blend	6.5	1%
New UT Blend (2nd Day)	4.5	0.98%
New UT Blend (2nd Week)	4.0	0.98%

5.7.4 Sacrificial agents to reduce adsorption.

Potential to use polyacrylate as a sacrificial agent. In previous studies to verify thermal stability of blends of AOS and AAC several chelating agents, sacrificial agents and scale inhibitors indicated that polyacrylate improved aqueous stability of the surfactant solution, so its effectiveness reducing adsorption was analyzed.

Both Old UT Blend, and New UT Blend were investigated. In the first case the analysis was done adding polyacrylate (MM ~ 2100g/mol from Sigma-Aldrich) to the surfactant solution and comparing the adsorption. In the second case the same procedure was used, except that an additional step was done where the

dolomite was first contacted with polyacrylate in seawater, then rinsed in seawater, and finally contacted with the surfactant solution. In this last test the adsorption was reduced close to 80%; results are summarized in fig 5-15. Apparently once polyacrylate is adsorbed, it is very hard to get it to be desorbed.

In fig 5-15 an additional test result is included, corresponding to the estimation of the adsorption of the IMP surfactant formulation (i.e. a blend of cocamidopropylbetaine, AOS and CTAB) in powder dolomite. For this last test the value reported in the figure is an estimate, assuming all the components are adsorbed in the same proportion, the only surfactant measured was the AOS in excess with respect to the cationic using high pH two phase titration.

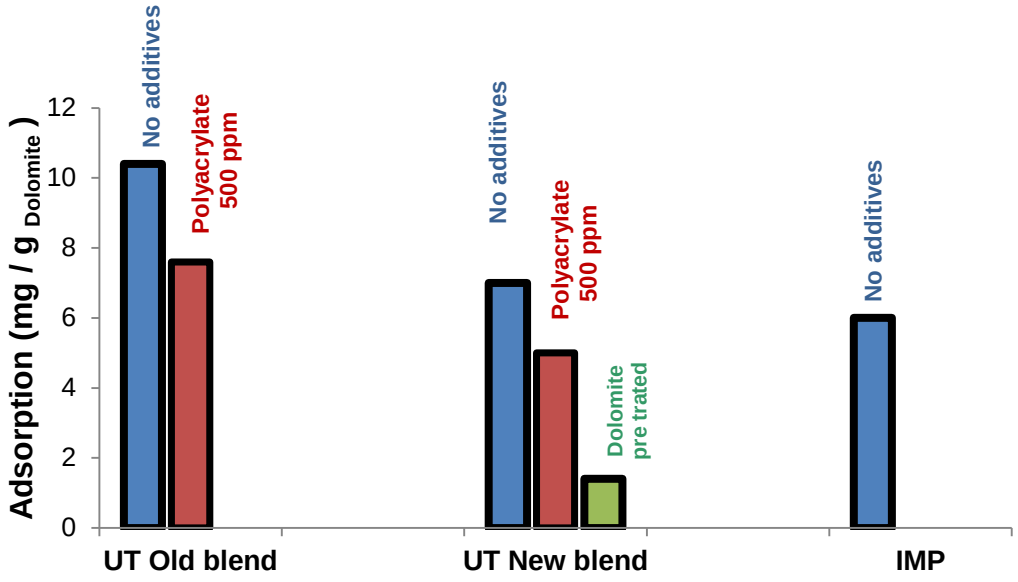

Figure 5-15 Adsorption estimation. The estimation was done measuring IOS or AOS, as an indicator of total adsorption and assuming all the components are adsorbed in the same proportion.

5.8 Remarks

Figure 5-15 is gives estimate of adsorption on powder dolomite. This estimation was done titrating only the IOS or AOS present in the blend using low pH two phase titration for the UT blends and high pH titration for the IMP blend. The IMP blend is a mixture of Zwitterionic, Anionic and Cationic surfactants.

Actual adsorption has to be determined analyzing each surfactant component, and this was done with the New UT blend and the total adsorption was higher than the initial estimation. Thus, fig 5-15 was done for comparison purposes. Fig 5-12 shows the actual values of adsorption for the New UT Blend.

For the New UT Blend analysis of individual components indicates 42% higher adsorption than the predicted measuring only IOS, so each component should be measured individually.

An additional test was done for the New UT blend. First the powder dolomite was contacted with polyacrylate in sea water at 500 ppm and aged for 2 days at 90°C, then the dolomite sample was rinsed with seawater, then sample was contacted with surfactant solution for 2 days at 90°C, and the adsorption of IOS was measured. The adsorption was reduced 80%. Additional work has to be conducted in this path to verify the potential of using polyacrylate as sacrificial agent with this type of surfactant blends.

The concept of high-pH, two-phase titration, was used to quantify surfactant and to estimate adsorption, assuming that the blend of surfactants will behave without any preferential adsorption of any of the components. If this is the case a rough

estimate of adsorption is possible if it is assumed as well that the carbonate rock will buffer any change in the pH during the equilibration process with the rock.

5.9 Thermal stability of Cocamidopropyl betaine

Previous experiments in our group (Leyu Cui, 2011) indicated that CAPB will hydrolyze at 125°C if pH is low or high. Additional tests were done at temperature close to reservoir temperature. These tests were done at neutral pH and at low pH using acid buffer solution. Results verified previous findings, but the decomposition of the CAPB was found to depend on temperature, and its dependence is reported here.

Degradation of CAPB was analyzed via HPLC, and decomposition was measured respect to the component present in higher proportion $CH_3(CH_2)_{10}(C_8H_{15}N_2O_3)$. The sample was aged at high temperature and low pH. After ageing for 3 months at 100ºC and pH 3.89 (i.e., Acetic acid / Sodium acetate buffer in DI water) a decomposition of 15.9% was measured after using HPLC, and the aqueous solutions with higher degree of decomposition turned yellowish and more turbid as shown in Fig 5-16

The same analytical technique to quantify CAPB was used by Haefliger (2003) and Im *et al.* (2008), and concluded to be suitable and reliable for CAPB.

Sample	1	2	5	4	5	6
pH	7	7	7	3.89	3.89	3.89
T (°C)	25	100	125	25	100	125
Age (month)	3	2	3	3	2	0.1
Activity	100	98	98	100	84.1	77
Brine	SW	SW	SW	DIW	DIW	DIW

Figure 5-16 Surfactant solutions of CAPB. Samples with higher degree of degradation are yellowish, and the one at 125°C turned cloudy as well.

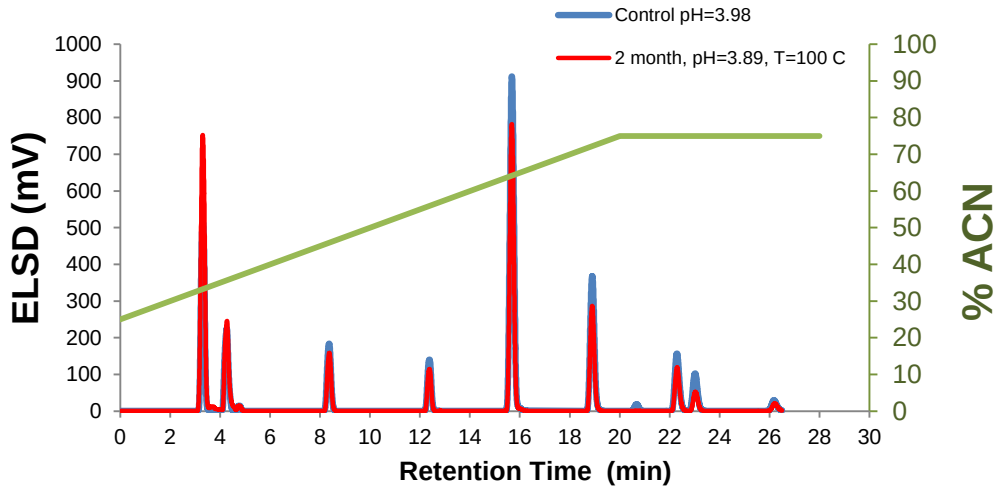

Figure 5-17 Chromatogram of CAPB at low pH buffer

The Lauramidopropyl betaine peak was used for the kinetics. Different betaines had different degree of degradation or hydrolysis. The comparison of the signals for the control sample of CAPB in 3.9 pH buffer and the sample aged for 2 months at 100°C is given in fig 5-17. The comparison for the two major peaks is in fig 5-18; apparently the longer lipophile has higher degree of hydrolysis, as summarized in table 5-7. It also shows that more hydrolysis occurs for longer lipophiles though there are a couple of exceptions.

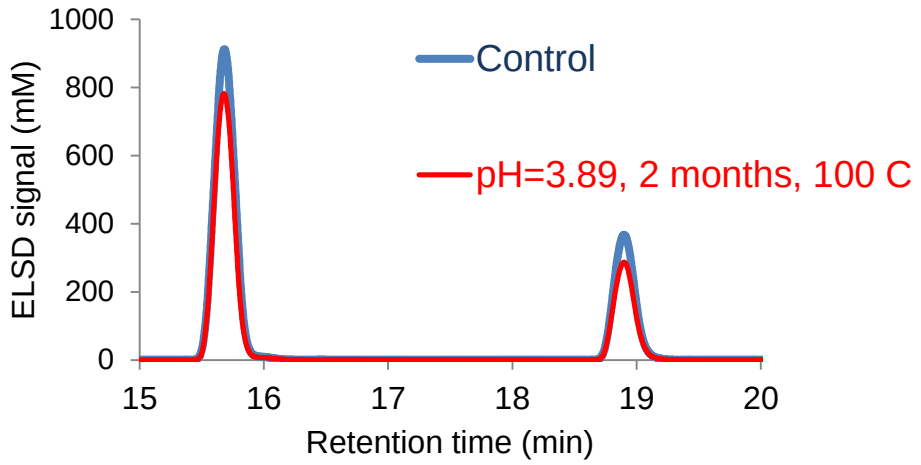

Figure 5-18 Peaks for the Lauramidopropyl betaine and Myristamidopropyl betaine in the CAPB sample

LAPB = $CH_3(CH_2)_{10}(C_8H_{15}N_2O_3)$

$CH_3(CH_2)_n(C_8H_{15}N_2O_3)$ for LAPB, n=10

Table 5-7 Reduction of activity in a 3.89 pH buffer after 2 months of ageing at 100°C.

n	% of total area in the blank	% Reduction in activity
6	8.88	13.17
8	6.63	17.78
10	**46.92**	**15.92**
12	19.26	21.47
14	16.12	36.48
16	2.20	25.18
Total	**100.00**	**20.38**

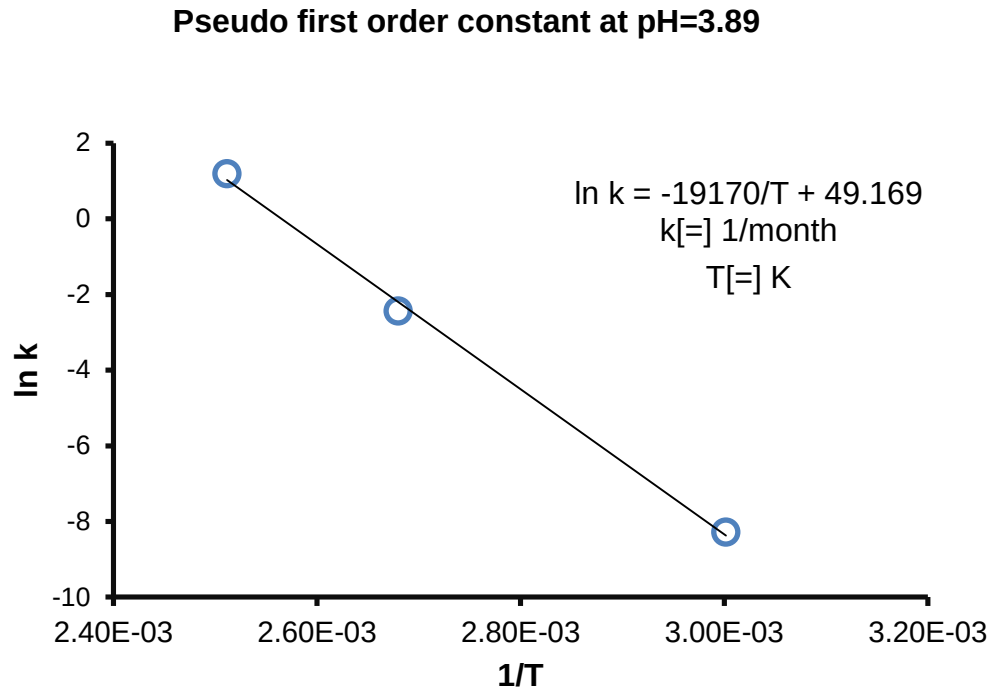

Figure 5-19 Dependence of pseudo first order constant with temperature at pH = 3.9

Using the Lauramidopropyl betaine decomposition as an indicator, the pseudo first order Arrhenius constant and activation energy can be estimated (Ea/R=19170 K, A=2.258x10^{21} $month^{-1}$).

A generalized elemental reaction kinetics for hydrolysis of amides can be written in the form similar to the proposed by Talley (1988)

$$-r_A = \left[k_H[H^+] + k_N + k_{oH}[OH^-]\right][CAPB] = k[CAPB]$$

The half-life values for the different conditions are in table 5-8:

Table 5-8 CAPB Half-life as a function of pH and temperature.

Brine	T(°C)	pH	t ½ days
SW	100	7	1780
Acetic buffer	100	3.9	241
Acetic buffer	125	3.9	6.5
1% Na_2CO_3	125	11.3	1.4

If we assume the same order of magnitude for the activation energy in the hydrolysis at high pH, the pseudo first order reaction constant dependence of temperature and pH can be visualized in fig 5-20.

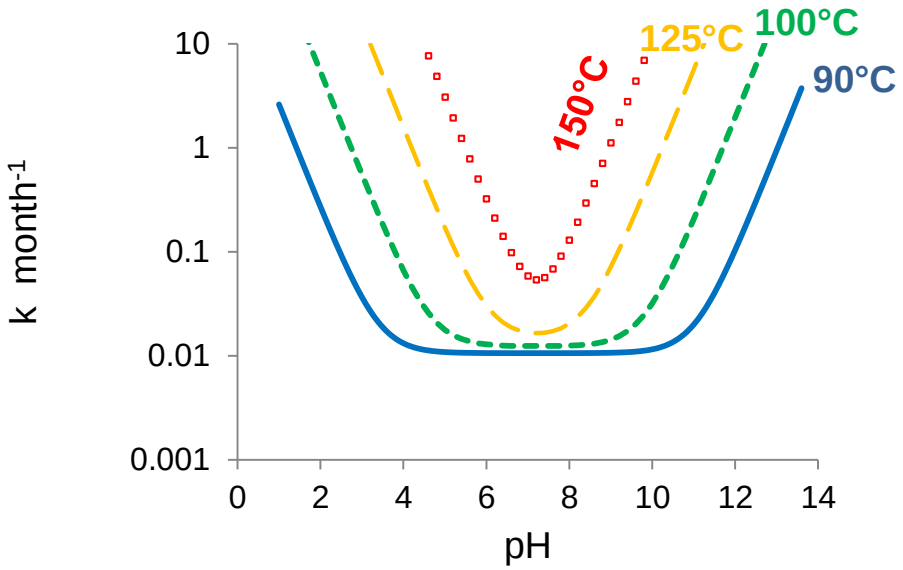

Figure 5-20 Pseudo first order constant rate for hydrolysis of CAPB

According to fig 5-20, the half-life for CAPB at 90°C between pH 4 and 10 is 5.8 years, but at 125°C it is two orders of magnitude less at these two limits and strongly dependent on pH.

In a nutshell CAPB is not recommended for temperatures higher than 90°C.

Chapter 6

DYNAMIC ADSORPTION EXPERIMENTS, MODELING AND SIMULATION

6.1 Introduction

The analysis of the transport of solute in a porous medium can be done using different approaches, all of them having in common that the pore space or porosity is divided into different forms or portions of the total porosity. Bai and Roegiers (1997) indicated that different transport processes take place within the macropores, the mesopores and the micropores. Each region deserves special attention for mathematical modeling.

Salter and Mohanty (1982) classified the porous network as three different regions called flowing, dendritic and isolated. The flowing fraction represents the fluid in the network of pores through which a phase flows in at least one throat and out at least one. The dendritic fraction of a phase is connected to the flowing fraction but does not exhibit flow itself (i.e. cul-de-sac pores). The isolated fraction of a phase is completely surrounded by a phase through which no diffusion can occur.

Using these previous ideas or concepts, and generalizing Salter and Mohanty's definitions, mathematical models can be proposed to study the transport of phases in porous media

6.2 Mathematical Model for dynamic adsorption

A mathematical model can be used to understand and to predict the adsorption of surfactants in consolidated porous media, and the model can be tuned or tested by analyzing experimental results.

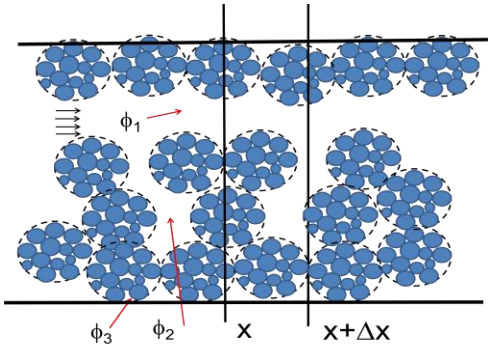

Figure 6-1 Figure Cartoon to simplify the porous structure of a rock (1 is the flowing fraction, 2 is the dendritic, and 3 is the micro porous)

A simple cartoon is sketched to justify the physics supporting the mathematical model in fig 6-1. By zoom of the pore structure three different pore regions can be idealized. In this model it is assumed that the flowing chemicals can be distributed in all the regions. In the appendix 6B of this chapter a detailed cartoon of the pore structure is sketched.

These three regions of pore space are identified as:

The porous flowing fraction (ϕ_1)

The porous network surrounding clusters of grains or dendritic portion (ϕ_2)

The porous zone within the clusters of particles or micro porous region (ϕ_3).

The equations for mass balance of a chemical species for each fraction of porous space can be written for the sake of simplicity one-dimensional.

(Note: *See nomenclature section after chapter 8*)

Mass balance equation for porous flowing fraction:

$$C_1\, v_1\, A\ \varphi_1|_{\,x} - C_1\, v_1\, A\, \varphi_1|_{\,x+\Delta x} + A\ \varphi_1 \left(-D_1 \frac{\partial C_1}{\partial x}\right)\Big|_x - A\ \varphi_1 \left(-D_1 \frac{\partial C_1}{\partial x}\right)\Big|_{x+\Delta x}$$

$$+ k_{c12} p_{12} \Delta x (C_2 - C_1) = \frac{\partial (C_1\ A\ \varphi_1\, \Delta x)}{\partial t}$$

(Equation 6-1)

Porous “non flowing” or “dendritic” fraction section is conceptualized eliminating the dispersion, but the advection term will be kept for discussion purposes, but in the final model used in the simulation is not taken into account.

$$C_2\, v_2\, A\ \varphi_2|_{\,x} - C_2\, v_2\, A\, \varphi_2|_{\,x+\Delta x} - k_{c12} p_{12} \Delta x (C_2 - C_1) + k_{c23} p_{23} \Delta x (C_3^C - C_2)$$

$$= \frac{\partial (C_2\ A\ \varphi_2\, \Delta x)}{\partial t}$$

(Equation 6-2)

And for the Clusters of particles the transport of tracer can be done with diffusion inside the cluster, this part is different respect to Mohanty’s model, because he assumes no transfer of components in this region:

$$\frac{1}{r^2}\left[\frac{\partial}{\partial r}\left(r^2 D_3 \frac{\partial C_3}{\partial r}\right)\right] = \frac{\partial C_3}{\partial t}$$

(Equation 6-3)

The connection between zones (2) and (3), can be modeled with the boundary condition, i.e. the diffusion of solute in the cluster equals mass transfer between both sections:

$$k_{c23}p_{23}\Delta x(C_3^C - C_2) = \left(-D_3\frac{\partial C_3}{\partial r}\Big|_{r=R}\right)\left(\frac{a_{sph}}{V}\right)(A\Delta x)\left(\frac{\varphi_3}{1-\varphi_1-\varphi_2}\right)$$

$$\left(\frac{a_{sph}}{V}\right) = \frac{3}{R_{sph}}(1-\varphi_1-\varphi_2)$$

(Equation 6-4)

Then the differential equations are:

$$-v_1\frac{\partial C_1}{\partial x} + \frac{\partial\left(D\frac{\partial C_1}{\partial x}\right)}{\partial x} + \frac{k_{c12}a_{v12}}{\varphi_1}(C_2 - C_1) = \frac{\partial C_1}{\partial t}$$

$$-v_2\frac{\partial C_2}{\partial x} - \frac{k_{c12}a_{v12}}{\varphi_2}(C_2 - C_1) + \frac{k_{c23}a_{v23}}{\varphi_2}(C_3^C - C_2) = \frac{\partial C_2}{\partial t}$$

$$\frac{1}{r^2}\left[\frac{\partial}{\partial r}\left(r^2 D_3\frac{\partial C_3}{\partial r}\right)\right] = \frac{\partial C_3}{\partial t}$$

(Equation 6-5 a,b and c)

$$k_{c23}a_{v23}(C_3^C - C_2) = \frac{3\varphi_3}{R_{sph}}\left(-D_3\frac{\partial C_3}{\partial r}\Big|_{r=R}\right)$$

(Equation 6-6)

All those equations can be written in dimensionless form as:

$$f_1 \frac{\partial C_1}{\partial \tau} = -b_1 \frac{\partial C_1}{\partial \chi} + \frac{f_1}{N_{Pe1}} \frac{\partial^2 C_1}{\partial \chi^2} + N_{St12}(C_2 - C_1)$$

$$f_2 \frac{\partial C_2}{\partial \tau} = -b_2 \frac{\partial C_2}{\partial \chi} - N_{St12}(C_2 - C_1) + N_{St23}(C_3^C - C_2)$$

$$\frac{\partial C_3}{\partial \tau} = \frac{\left(\frac{L}{R_{sph}}\right)^2}{N_{Pe23}} \frac{1}{\zeta^2} \left[\frac{\partial}{\partial \zeta}\left(\zeta^2 \frac{\partial C_3}{\partial \zeta}\right)\right]$$

(Equation 6-7 a,b and c)

The boundary condition between phase 2 and 3 is

$$N_{St23}(C_3^C - C_2) = \frac{3 f_3}{R_{sph}} \left(\frac{L}{R_{sph}}\right)^2 \left(-\frac{\partial C_3}{\partial \zeta}\Big|_{\zeta=1}\right)$$

(Equation 6-8)

These equations are in agreement with those proposed by Bai and Roegiers (1997) but they coupled the boundary condition with the mass balance in the dendritic porous fraction and assumed equal concentration on the surface of the cluster with that of the dendritic region. If the mass transfer between void fractions 2 and 3 is neglected, and the advection in the dendritic fraction 2 is small, the system of equations simplifies to those found by Piquemal (1993), which are valid for mass transfer including the dead-end pores. This is the model we will call double porosity model or capacitance pore model.

$$f\frac{\partial C_1}{\partial \tau} = -\frac{\partial C_1}{\partial \chi} + \frac{f}{N_{Pe1}}\frac{\partial^2 C_1}{\partial \chi^2} + N_{St12}(C_2 - C_1)$$

$$(1-f)\frac{\partial C_2}{\partial \tau} = -N_{St12}(C_2 - C_1)$$

(Equation 6-9 a and b)

This model is similar to the semi-heuristic model used by Coats and Smith (1964) for axial flow, and the model from Warren and Root (1963) for radial flow, but they lumped the dispersion coefficient with the flowing fraction. However in their reports the flowing fractions of most of the experiments were in a limited range between 0.9 and 1.0. The same approach was found in other publications, but caution is needed when this is implemented in systems where flowing fraction changes considerably, i.e., it is better to use the present form where *f* is retained explicitly in the term f/N_{Pe1}. The above authors instead wrote the mass balance for the flowing fraction as:

$$f\frac{\partial C_1}{\partial \tau} = -\frac{\partial C_1}{\partial \chi} + \frac{1}{N_\chi}\frac{\partial^2 C_1}{\partial \chi^2} + N_{St12}(C_2 - C_1)$$

(Equation 6-10)

The model written here can be generalized for the three porous regions in all directions as (e.g. 1 for macro pores or flowing fraction, 2 for dendritic fraction, and 3 for micro pores):

$$-\underline{v}_1 \cdot \underline{\nabla}\,(C_1) + \underline{\nabla} \cdot \left(\underline{\underline{D}}_1 \cdot \underline{\nabla}\, C_1\right) = \frac{\partial C_1}{\partial t} + \sum_J \frac{k_{c1J} a_{v1J}}{\varphi_1}\left(C_1 - C_J\right) + \frac{k_{c1S} a_{v1S}}{\varphi_1}(C_1 - C_1^S)$$

$$-\underline{v}_2 \cdot \underline{\nabla}\,(C_2) + \underline{\nabla} \cdot \left(\underline{\underline{D}}_2 \cdot \underline{\nabla}\, C_2\right) = \frac{\partial C_2}{\partial t} + \sum_J \frac{k_{c2J} a_{v2J}}{\varphi_2}\left(C_2 - C_J\right) + \frac{k_{c2S} a_{v2S}}{\varphi_2}(C_2 - C_2^S)$$

$$\underline{\nabla} \cdot \left(\underline{\underline{D}}_3 \cdot \underline{\nabla}\, C_3\right) = \frac{\partial C_3}{\partial t} + \frac{k_{c3S} a_{v3S}}{\varphi_3}(C_3 - C_3^S)$$

(Equation 6-11 a, b and c)

Each equation has an additional term, the mass transfer in the porous fraction between the fluid and its respective solid interface. This is needed if the chemical has potential to be adsorbed (e.g. adsorption of surfactants). In the case of an inert tracer, the last term of the right hand side of the equation is discarded.

Considering that the chemical analyzed is a surfactant and adsorption is possible, additional conservation equations are needed. The three additional equations to track the surfactant on the surface of the rock on each portion of space are:

$$\frac{\partial C_1^S}{\partial t} = \frac{k_{c1S} a_{v1S}}{g_{1(C_1^S)}}(C_1 - C_1^S)$$

$$\frac{\partial C_2^S}{\partial t} = \frac{k_{c2S} a_{v2S}}{g_{2(C_2^S)}}(C_2 - C_2^S)$$

$$\frac{\partial C_3^S}{\partial t} = \frac{k_{c3S} a_{v3S}}{g_{3(C_3^S)}}(C_3 - C_3^S)$$

(Equation 6-12 a, b and c)

Assuming that the exchanging solute equilibrates instantaneously during adsorption with the solid phase, and considering that exchange sites are distributed randomly through the media, the equations for the porous space can be simplified to:

$$-\underline{v}_1 \cdot \underline{\nabla}\,(C_1) + \underline{\nabla} \cdot \left(\underline{\underline{D}}_1 \cdot \underline{\nabla}\, C_1\right) = \frac{\partial C_1}{\partial t}\left(1 + F_1' \frac{(1-\varphi)}{\varphi}\right) + \sum_J \frac{k_{c1J} a_{v1J}}{\varphi_1}\left(C_1 - C_J\right)$$

$$-\underline{v}_2 \cdot \underline{\nabla}\,(C_2) + \underline{\nabla} \cdot \left(\underline{\underline{D}}_2 \cdot \underline{\nabla}\, C_2\right) = \frac{\partial C_2}{\partial t}\left(1 + F_2' \frac{(1-\varphi)}{\varphi}\right) + \sum_J \frac{k_{c2J} a_{v2J}}{\varphi_2}\left(C_2 - C_J\right)$$

$$\underline{\nabla} \cdot \left(\underline{\underline{D}}_3 \cdot \underline{\nabla}\, C_3\right) = \frac{\partial C_3}{\partial t}\left(1 + F_3' \frac{(1-\varphi)}{\varphi}\right)$$

(Equation 6-13 a, b and c)

This simplification reduces the number of differential equations to three per component; then the model is easier to handle, and the number of parameters to estimate is reduced. The concept of instantaneous equilibrium and sites distributed randomly throughout the porous media was studied before by Schwartz *et al.* (2000), but they assumed a linear relationship between the adsorbed species concentration and the bulk concentration and they neglected the last term or adsorption and diffusion in the micropores. Van Genuchten and Wierenga (1976), used the same principle of instantaneous adsorption using the Freundlich isotherm in a porous medium, but using boundary conditions applicable for semi-infinite media. Lapidus and Amudson (1952), analyzed the effect of instantaneous adsorption vs and approach where they incorporated rate

of adsorption for one porosity model, finding no difference at low flow rates. They discussed the problem of the semi-infinite boundary conditions as well, but single porosity model was assumed. Sardin *et al*. (1991) presented a broader spectrum of different mathematical models and simulated the effect of having different geometries in the clusters of particles representing the micro pores. They also compared the effect of instantaneous equilibrium or adsorption/desorption kinetics for the adsorbed species, but no experiments were included in their report.

Simplification of previous equations can lead us to different models used by researchers in the past, and the limitation on each model can be understood directly from the steps needed to obtain those simplified models from the general model here presented.

The previous approach with different degree of simplification has been used in different fields (e.g., environmental engineering, petroleum engineering and chemical engineering) to model flow and the transport of components in porous media. Warren and Root (1963) studied flow in naturally fractured reservoirs, Coats and Smith (1964) studied transport of inert species in porous media, Brusseau *et al*. (1989) analyzed the transport of solutes that suffer sorption. Bringham *et al.* (1961) and Bai *et al.* (1995) studied transport of fluids in miscible displacement. Mohanty *et al.* (1983) measured and modeled the transport of different species during inmiscible displacement studies.

Bai *et al*. (1995) used a simplified version of the model presented here, and only included the macro and the meso portions of pore volume, resulting in the following set of equations

$$f\frac{\partial C_1}{\partial \tau} = -\frac{\partial C_1}{\partial \chi} + \frac{1}{h\,N_{Pe}}\frac{\partial^2 C_1}{\partial \chi^2} + a(C_2 - C_1)$$

$$(1-f)\frac{\partial C_2}{\partial \tau} = -\frac{1}{b}\frac{\partial C_2}{\partial \chi} + \frac{1}{N_{Pe}}\frac{\partial^2 C_1}{\partial \chi^2} - a(C_2 - C_1)$$

(Equation 6-14 a and b)

with the following boundary conditions (i.e. Newman boundary condition at the outlet, which they refer to as a finite core boundary condition)

$$\left.\frac{\partial C_1}{\partial \chi}\right|_{\chi=1} = 0$$

$$\left.\frac{\partial C_2}{\partial \chi}\right|_{\chi=1} = 0$$

(Equation 6-15 a and b)

Bouhroum and Bai (1996) studied experimentally and numerically the previous model for unconsolidated porous media, but they had two regions of the porous space, one of high permeability and another of lower permeability. It was necessary to include the advection term in the second equation because the contrast of permeability between regions was only of 1 order of magnitude.

Nevertheless they did not include the dispersion term in the low permeability region.

This set of equations is similar to model used by Coats and Smith (1964). Coats *et al*. (1994) used different boundary conditions (Dirichlet boundary condition at infinity, or what Bai called infinite core boundary condition), and they neglected advection and dispersion in the meso portion of porous volume. It is called the capacitance pore model:

$$f\frac{\partial C_1}{\partial \tau} = -\frac{\partial C_1}{\partial \chi} + \frac{1}{N_{Pe}}\frac{\partial^2 C_1}{\partial \chi^2} + a(C_2 - C_1)$$

$$(1-f)\frac{\partial C_2}{\partial \tau} = -a(C_2 - C_1)$$

$$\log_{\chi\to\infty} C_1 = 0$$

(Equation 6-16 a, b and c)

They lumped the flowing fraction and the Peclet number in the dispersion term, but this may be justified because they worked in a narrow range of lowing fraction form 0.9 to 1, worked at high flow rates from 25 ft/day to 715, and high tracer concentrations Ca^{2+} (Tracer was 5% $CaCl_2$ –Original solution 5% NaCl) and permeabilities from 0.5 to 210 darcy. Jastl *et al.* (1988), used the same model, but they argued that the boundary condition of infinite core is only valid for high Peclet numbers (Fig 6.2). They discussed about how the geometry of the

dead ends affects the flowing fraction and reported a mild dependence between flowing fraction and velocity.

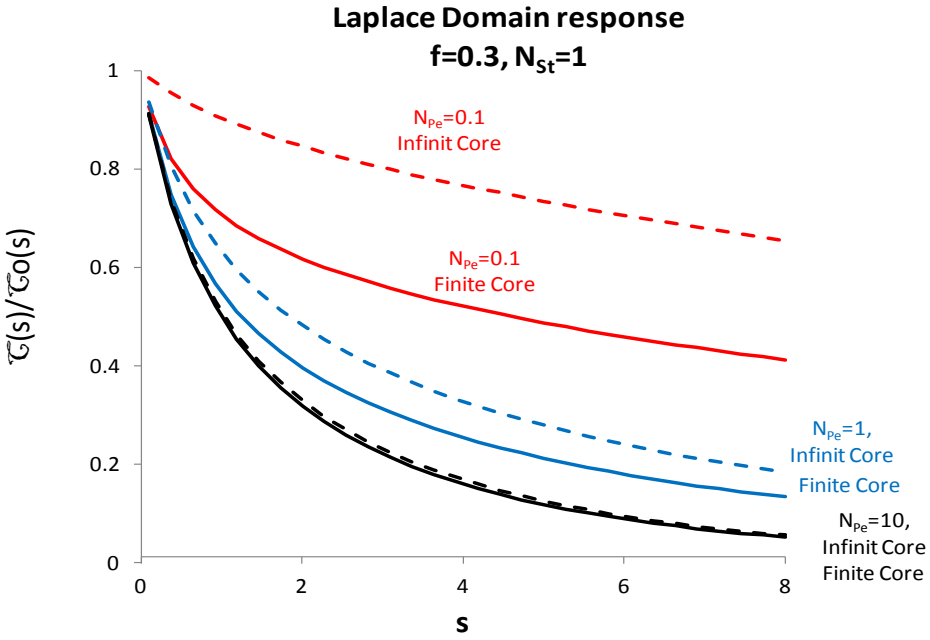

Figure 6-2 Laplace domain response if double porosity model is used. Two different boundary conditions were used; infinite core boundary condition, and finite core boundary condition in order to compare. For high Peclet number, the selection of the boundary condition is trivial, but for Peclet number less than 10 will give difference between both models.

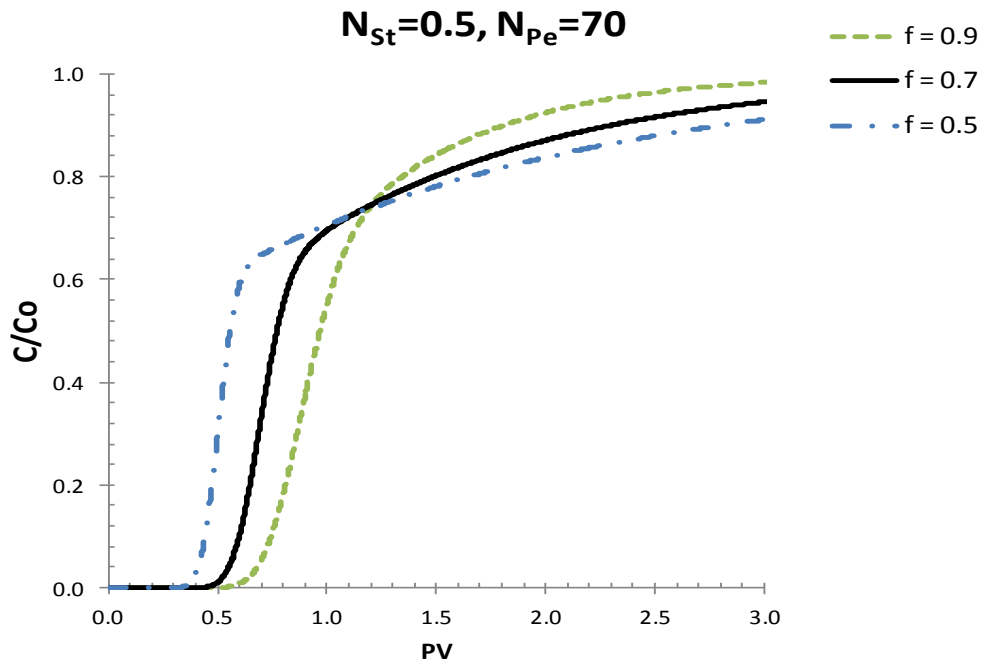

Figure 6-3 Double porosity model, using finite core boundary condition. For high Peclet numbers the flowing fraction will give different breakthrough. High values of Peclet number, hasn't considerable effect on the response respect to infinite core boundary condition, compare with Mohanty *et al*. (1983) where they used Coats and Smith model.

Beaker (1977) used Coats and Smith model to study miscible flooding in cores of different composition. Berea sandstone (L=22.86 cm, K=175 md, ϕ=0.215, L/D=4.52) and vugular limestone (L=9.4 cm, K=5.4 md, ϕ=0.119, L/D=1.24) with velocities from 0.04 to 20 ft/day were studied. Most of the work ranged in flowing fractions from 40% to 70%, but most of the data are close to a flowing fraction of 64%. In this velocity range they found that mass transfer coefficients and dispersion coefficients depend on approximately the first power of velocity.

Dispersion coefficient:

$$D = k_1 v^{n1}$$

(Equation 6-17)

n_1= 1.0 for limestone and 1.25 for sandstone

For the mass transfer coefficient:

$$k_c a_v = k_2 v^{n2}$$

(**Equation 6-18**)

n_2= 0.84

Results from Beaker (1977) using Coats and Smith model suggest that the Peclet number and the Stanton number are almost insensitive to velocity in the range of flow rates where they worked. His observations are important and relevant if parameter estimation is needed using experimental information, and must be considered in the experiment design. Those problems can be avoided by conducting experiments with homogeneous rock samples of different lengths, but caution is needed selecting the outlet boundary condition. Fig 6-2 illustrates the influence of using the different boundary condition in the outlet for the “finite core” approach or “infinite core” approach presenting different results when Peclet number is when long cores are used, the effect of selecting the approach of finite core or infinite core will be important if Peclet number is less than 1.

The trends observed about dispersion are consistent with other experiments done by Brigham (1974) when he obtained values for n_1 of 1.24 for 0.47mm spheres using unconsolidated sandpacks, 1.20 for 0.1 mm spheres, and 1.19 for Berea sandstone using the same mathematical model. Salter *et al.* (1983) reported for n_1 values close to 1.16 and k_1=0.269 (D[=]cm^2/s, u interstitial velocity [=]cm/s), and Mohanty *et al.* (1983) determinate for n_1 a value close to 1.

The Coats and Smith model must be written in a more fundamental approach like the one proposed and the boundary conditions modified as required for finite cores, if flowing fractions are expected in wide range of values.

Brigham *et al.* (1974) studied the effect of boundary conditions, and Bai recommended use of the boundary for finite cores. Mohanty *et al.* (1983) describes neatly in detail the problems of the Coats and Smith model. Especially at high flowing fractions the model predicts multiple solutions in studies of tracer analysis, and Mohanty also detected problems with the model at low flowing fractions. He suggested to write an additional mass balance for the different regions of the dendritic fraction.

Piquemal (1992, 1993) presented two simplified models, and presented all theoretical background using two equations, one for the macropores, and another for the mesopores. The first model is similar to the Coats and Smith, but the dispersion term is consistent with the physics of the problem, not lumping flowing fraction and dispersion, and the boundary conditions are for finite cores. The second model has two equations as well, but the mesopore space is treated

as the micropore region presented in this thesis. The aggregates of particles can be modeled as spheres, cylinders, parallelepipeds or layers, and diffusion may take place within the aggregates. The boundary condition at the interface between the macropore and the mesopore were simplified, to get rid of one parameter (i.e. the mass transfer coefficient), but they included a new parameter, which is the diffusion in the mesopore region. In the latest model he used finite core boundary condition for the effluent (i.e. second type boundary condition).

Mennella *et al.* (1999) strongly emphasized the enormous error predicted for the mass balance using the Coats and Smith boundary conditions (i.e. infinite core boundary condition) even after good fit of experimental data. Manella *et al*. also considered the use of the proper boundary condition for a finite core to find the unique solution, with consistent mass balance. They indicated the best experimental conditions to avoid the problem of insensitivity of the model to the parameters, or avoid the problem on non-uniqueness of the parameters. That paper is a good reference in order to plan experiments and avoid the problem on non-uniqueness, and suggests using slowly diffusing tracers or running experiments at high flow rates.

Rowe and Booker (1990) used a similar approach to model the transport and sorption of contaminants in a 3-D fractured network, using a linear relationship between the concentration of the adsorbing species in the fluid phase and the solid.

Taking into consideration all the ideas and conclusions of previous works of the scientists listed before, and understanding the importance of each region in porous space, a mathematical model is presented and used to compare experimental results. The model will take the form of equation 6-13, but more details are included in the section 6.5. The equations should be written for surfactant and tracer.

Some of the simplifications will be verified as well, to analyze the impact of those assumptions.

The dynamic adsorption of surfactants in dolomitic cores was measured, studied and analyzed. The analysis of the adsorption was done using a mathematical model and simulating the experiments with the adjusted parameters.

During the experiments of this research, the transport of different chemical species were tracked (e.g. inert tracer, and two surfactant species), so the equation for tracer and surfactant were written and solved numerically, using the parameters after fitting process, and with the aid of the adsorption isotherms previously studied. (The surfactant blend was modeled as one single species in the simulations).

6.3 Experimental dynamic adsorption (Rock, Brine, Tracer and Surfactant)

Before starting dynamic adsorption studies with the proposed UT surfactant blend, the injectability behavior of the surfactant solution was tested and, in order to save well characterized field-core material for dependable tests, a plug of

Silurian outcrop was used as a first control material or reference material. Test results in a plug of Silurian indicated that test solution can be injected without loss of permeability. Then work proceeded with testing of actual Akal formation plugs.

Part I (Injectability test and control experiment using outcrop core)

Injectability test at 94 °C:

Silurian rock, 3.81 cm in diameter and 7.62 cm in length, was prepared for testing the proposed UT surfactant blend with potential to recover PEMEX-simulated-live crude oil. The Silurian plug was saturated with formation brine and 1% of blended **C_{15-18} IOS Petrostep S2 / $C_{28}PO_{25}EO_{25}COONa$ (50/50 by weight)** was injected in seawater.

Procedure to prepare Silurian plug and to perform dynamic adsorption analysis:

A 0.5 micron filter is placed, near inlet in flow lines for filtering all fluids while being injected.

Place plug in coreholder with an overburden of not less than 500 psi.

Evacuate and saturate with formation brine.

Measure permeability.

Place core inside the oven and heat to 94°C while injecting formation brine.

Several tracer analyses at different flow rates are recommended to be performed before the injection of surfactant. Most of the tracer tests were conducted injecting chemicals in seawater.

After reaching test conditions, of 94°C and ~40psi back pressure, start injecting surfactant solution.

Test surfactant solution injectability with pressure drop.

Collect effluent samples at 0.5 ml intervals and analyze effluent for surfactant.

Test surfactant solution injectability with pressure drop at different flow rates if required after the adsorption measurements were completed.

If no loss of permeability is observed, proceed with testing.

Continue with the injection of a couple of pore volumes once the surfactant concentration in the effluent has reached the concentration in the injection.

Inject ca. 10 PV of sea water to pre-clean the system for the dynamic adsorption test, and then continue with the cleaning/desorption process using ca. 20 PV of IPA-DIW blend.

Collect effluent samples and analyze effluent for surfactant.

Repeat the procedure using Formation core material.

Part II

Procedure to perform dynamic adsorption test for Akal plugs:

Select 3 Cantarell plugs, cleaned and characterized previously.

Align the plugs in the coreholder with an overburden of not less than 500 psi

Evacuate and saturate with formation brine to measure Pore Volume (PV).

6.3.1 Measure permeability.

Confirm PV measured by Injecting formation brine with tracer bromide.

Perform different tracer tests at different flow rates to verify flowing fraction.

Locate prepared plugs inside oven and, while injecting formation brine, heat to 94°C.

After reaching test conditions, of 99°C and ~40psi back pressure, start injecting surfactant solution.

Collect effluent samples at 0.5 ml intervals and analyze effluent for surfactant.

Continue with the injection a couple of pore volumes once the surfactant concentration in the effluent has reached the concentration in the injection.

Inject ca. 10 PV of sea water to pre clean the system, and then continue with the cleaning/desorption process using ca. 20 PV of IPA-DIW blend.

Collect effluent samples and analyze effluent for surfactant.

Figure 6-4 Different views of a low permeability sample from the formation.

Figure 6-5 Different views of a high permeability sample from the formation.

Samples with low permeability were used for this experiment (Fig 6-6 of the rock permeability ranges from 1.7 – 6 mD). Samples with high permeability were excluded for this study, because edges need to be filled for complete sealing. The filling material could be controversial when interpreting the dynamic adsorption test results. (Fig 6-5, permeability ranges from 45 – 510 mD), samples for experiments should be cylindrical without big vugs (fig. 6-4).

For the dynamic adsorption experiments, two cores were prepared: one of them using a high permeability Silurian Dolomite (250 mdarcy), and another stacking three cores from PEMEX rock with low permeability ranging from 1 to 4 mdarcy with an overall permeability of 1.3 mdarcy.

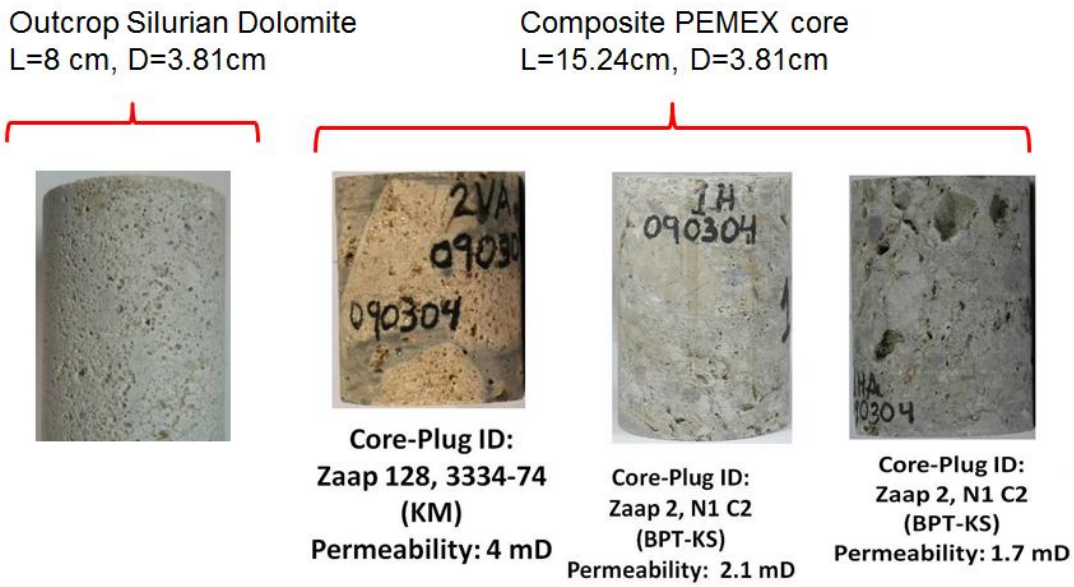

Figure 6-6 Actual cores used during dynamic adsorption experiments.

Preparation of the cores is important to prevent misinterpretation of results. The test is conducted at high temperature, so the sleeves surrounding the core within the core holder should tolerate harsh conditions of temperature, and overburden pressure. Figure 6-7 indicates the order of application of the different heat shrinking sleeves used.

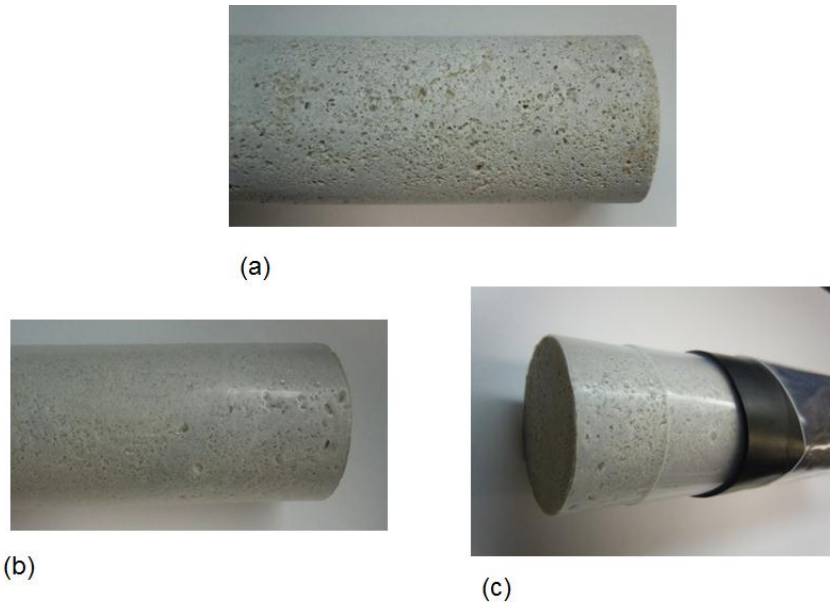

Figure 6-7 Core sample preparation. a) Silurian dolomite, b) Silurian with teflon shrinking sleeve, c) Silurian core with two internal teflon shrinking sleeves, one solvent resistant shrinking sleeve, and one external teflon shrinking sleeve.

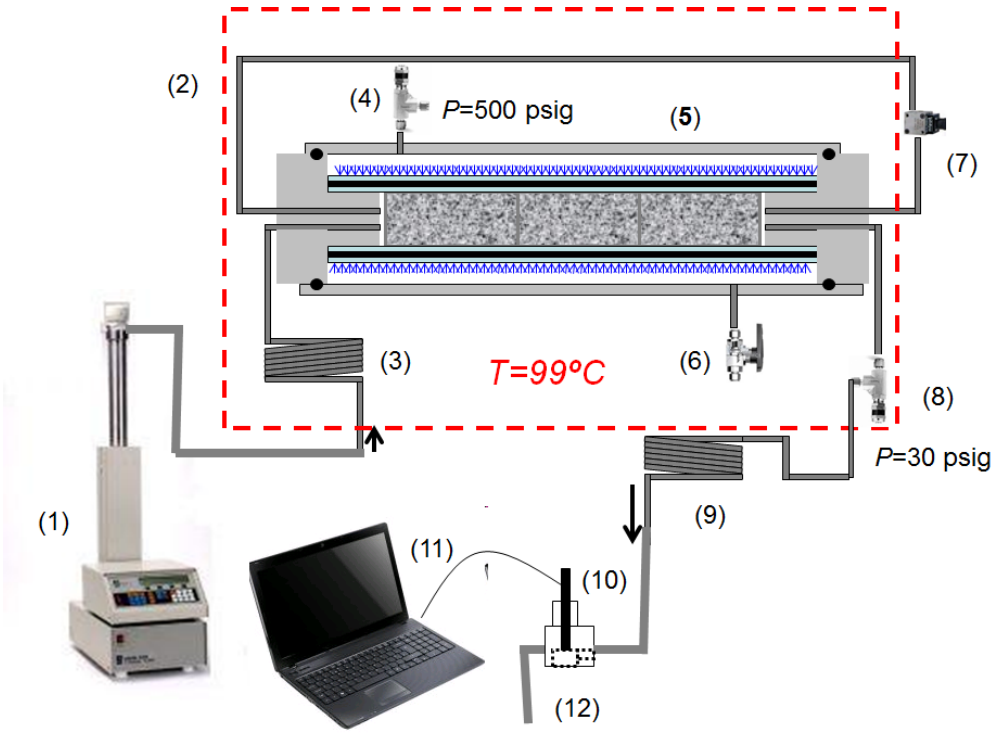

Figure 6-8 Experimental setup. (1) Syringe ISCO Pump 260D for injection of surfactant and tracer, (2) Blue M Constant temperature chamber, (3) Heat exchanger, (4) Relief valve to maintain overburden pressure up to 500 psi, (5) Exxon Core Holder, (6) Filling valve, (7) Validyne pressure transducer, (8) Relief valve to maintain back pressure, (9) Heat exchanger, (10) Bromide electrode, (11) National Instruments data acquisition and computer, (12) Collection line to measure surfactant.

The figure 6-8 lists all the components of the experimental apparatus and details about the fittings.

The methods of Chapter 4 (for brine analysis) were used to find change in ionic content of injected brine when equilibrated with dolomite rock. Under seawater conditions the change of ionic strength by contacting the brine with the rock is negligible, so that the bromide electrode can be used without interference. Information about brine during the tracer experiments are given in table 6-1

Table 6-1 Brines used for surfactant solutions and for tracer analysis.

	Brine 1	Brine 1	Brine 2	Brine 2
	g/L	mol/l	g/l	mol/l
$CaCl_2$	1.300	0.011713	1.300	0.011713
$MgCl_2 6H_2O$	11.20	0.055099	11.20	0.055099
Na_2SO_4	4.80	0.033798	4.80	0.033798
KCl	0.00	0.000000	0.00	0.000000
NaBr	0.155	0.001492	0.35	0.003401
NaCl	27.00	0.461999	27.00	0.461998
NaHCO3	0.00	0.000000	0.00	0.000000
TOTAL	44.45	0.564101	44.65	0.566011
I (mol/L)		0.765		0.767

A tracer was needed to determine the flowing fraction within the rock (i.e. consolidated porous media). The tracer used was bromide (i.e. sodium bromide). Levy and Chambers (1987) conducted experiments and found that bromide can be used as a conservative tracer in soil-water studies. A bromide electrode was used to quantify the tracer during the experiment. The electrode was calibrated for different brine compositions, and the concentration of the tracer was selected in a range where ionic strength buffer condition prevails. A calibration curve is presented (fig. 6-9), but if only a small range of concentration is involved, a linear relationship can be used.). Some ions can produce interference (e.g. OH^-, Cl^-, I^-, S^{2-}, CN^-, NH_3, $S_2O_3^{2-}$) or complexation (e.g. Bi^{3+}, Cd^{2+}, Pb^{2+}, Sn^{2+}, Tl^{3+}) as

reported by Umezawa *et al.* (1995). The aqueous solutions of interest have different anions except for chloride, which may interfere if a threshold limit is exceeded. Hence, the bromide concentration selected was high enough to be detected by the electrode, but low enough to prevent change in density or ionic strength (Ganjali *et al.* 2003).

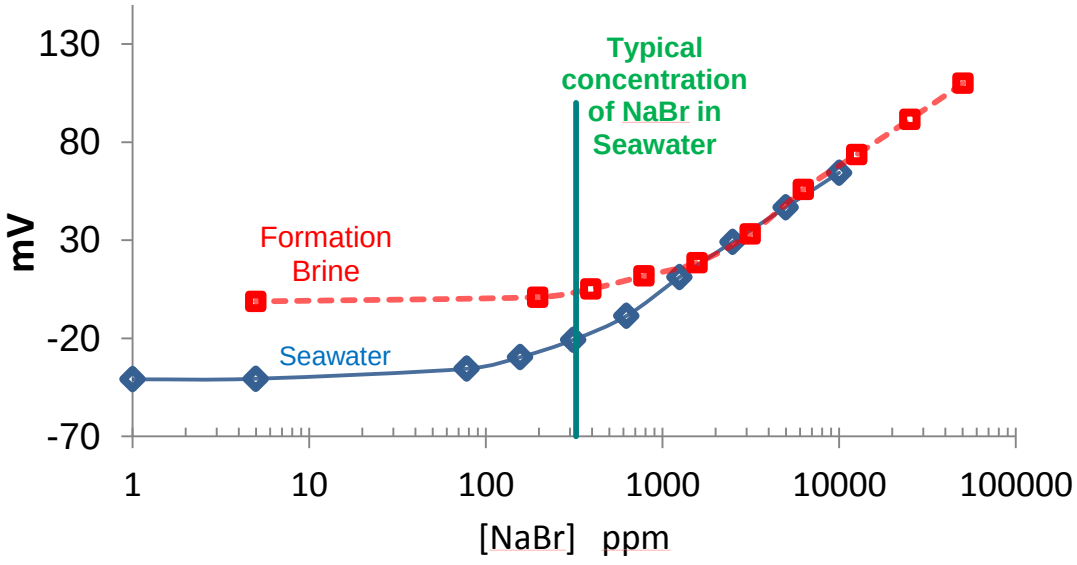

Figure 6-9 Seawater and formation brine fit well the Nikolsky-Eisenman equation. The activity coefficients were calculated using Pitzer's ion-interaction model. Red dashed line and blue are the fitted curves using NE model.

$$E = Eo + \frac{RT}{n_i F} \ln\left[\gamma_i C_i + \sum K_{i,j} \left(\gamma_j C_j\right)^{\frac{Z_i}{Z_j}}\right]$$

(Equation 6-19)

If activity coefficients can be evaluated, according to Hall (1996) the Nikolsky-Eisenman equation for ion-selective electrodes (eq. 6-19) can be used to relate the voltage from electrode to bromide concentration when chloride to bromide ratio is high, but the interference parameter (i.e., $K_{i,j}$ for Cl^-/Br^- pair) is constant only for diluted brines. For high salinity the parameter depends on the salinity and may not be linear close to the threshold limit. So calibration curve is recommended; non Nikolsky behavior was observed in some cases according to Umezawa *et al.* (1995).

To quantify both surfactants two different titration techniques were selected, one colorimetric two phase titration at low pH to quantify the Internal olefin sulfonate, and another colorimetric two phase titration at high pH to quantify both surfactants, the IOS and the POEO Carboxylate ($C_{n1}(PO)_{x1}(EO)_{y1}COONa$). This titration technique was explained in detail previously in Chapter 5.

6.4 Results of adsorption

6. 4.1 Results of adsorption for the Silurian outcrop dolomite.

There was no problem of injectability during the study of dynamic adsorption for the Silurian dolomite. The permeability measured at the beginning of the experiment was 253.6 mdarcy, and after the injection of surfactant during the adsorption test, after 20 PV of injecting surfactant solution the permeability was 251.7 mdarcy.

The test was done at 94ºC and the surfactant injected in seawater at 1% m/v (The surfactant blend was a mixture 1:1 mass of IOS to Carboxylate). The surfactant injection flow rate was 1.75 cm^3/min for this test.

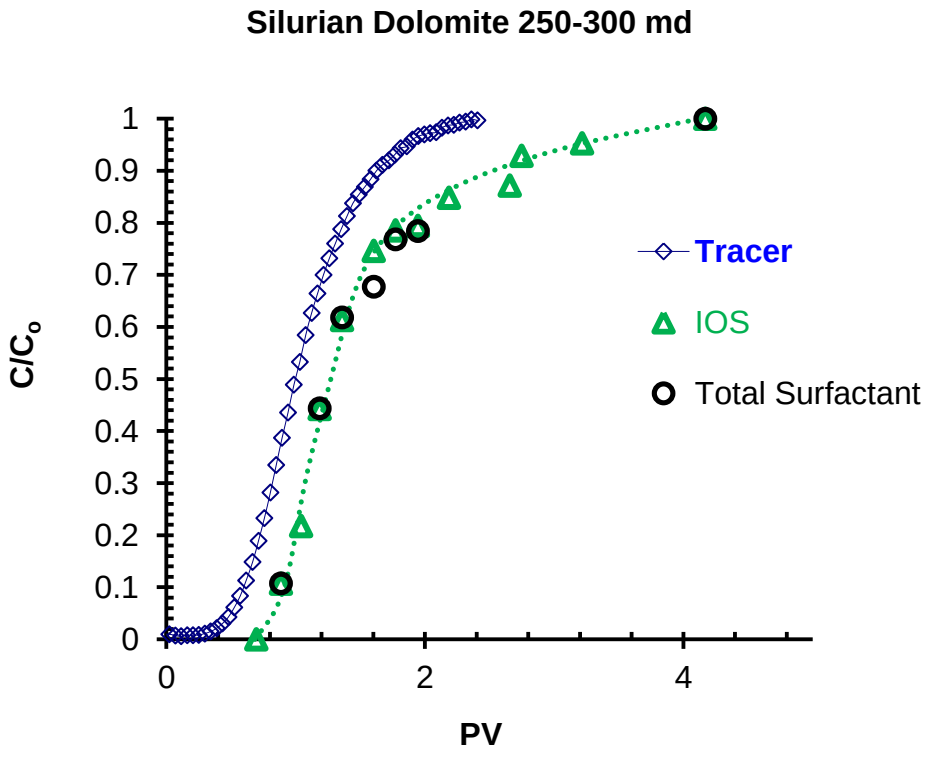

Figure 6-10 Surfactants and tracer response in the effluent from Silurian dolomite after injection of a step signal of both tracer and surfactant, 94°C.

The ratio between IOS and Carboxylate in the effluent was in the range between 50/50 to 48/52; no considerable preference for either surfactant was observed during the first three pore volumes of the experiment. The injection ratio was close to 50/50 (mass).

Table 6-2 Silurian Dolomite adsorption/retention, UT blend

Method	Adsorption mg/g_{Rock}
Mass balance	0.44
Retardation mid point tracer vs surfactant in effluent	0.287
IPA-DI water flush	0.41

The Adsorption was calculated using three different approaches:

Mass balance during the adsorption process. A continuous slug of surfactant is injected into the core. The history of the surfactant in the effluent is recorded to quantify the adsorption (fig 6-10). In this approach the pore volume of the rock and the dead volumes of the flowing lines, fittings and heat exchangers are required.

Mid point retardation of surfactant respect to tracer. This technique is valid only when the adsorption isotherm is linear, and when the flowing fraction is 1, so is not recommended as a reliable method, but can be used as a quick estimate (fig 6-10).

Mass balance during the desorption process. Cleaning of the rock with 10 pore volumes of sea water, followed by injection of 20 PV of IPA-DIW (50/50). The desorption can be estimated via quantification of surfactant in the effluents.

The adsorption calculated by mass balance during desorption or cleaning process is 0.41 mg/g of rock, 7% smaller than the value measured during the adsorption process reported in table 6-2; this can be caused by permanent retention of surfactant. A similar phenomenon was observed in another experiment with a rock with less permeability and possibly higher surface area.

6.4.2 Results of adsorption for the Composite Zaap rock.

The test was done at 99ºC and the surfactant injected in seawater at 1% m/v (The surfactant blend was a mixture 1:1 mass of IOS and Carboxylate). The surfactant injection flow rate was 1.7 cm^3/h (less than 0.8 ft/day of interstitial velocity).

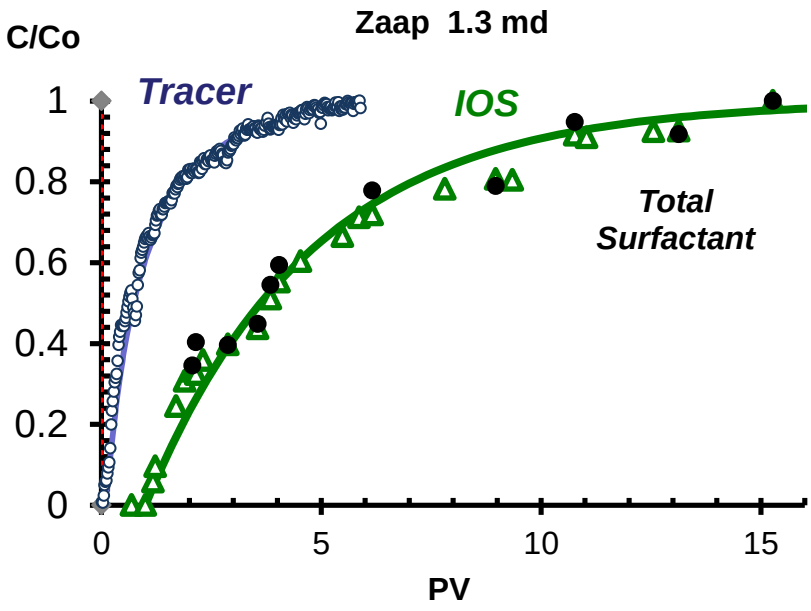

Figure 6-11 UT Surfactants and tracer response in the effluent after contacting composite PEMEX rock at 99°C

Results are shown in figure 6-11 and adsorption calculated in table 6-3. Initially IOS/Carboxylate in the effluent was 41/59; thus IOS was adsorbed preferentially. The ratio continued to grow monotonically to the injected ratio of 50/50 after 10 PV. Figure 6-12. (See appendix 6A)

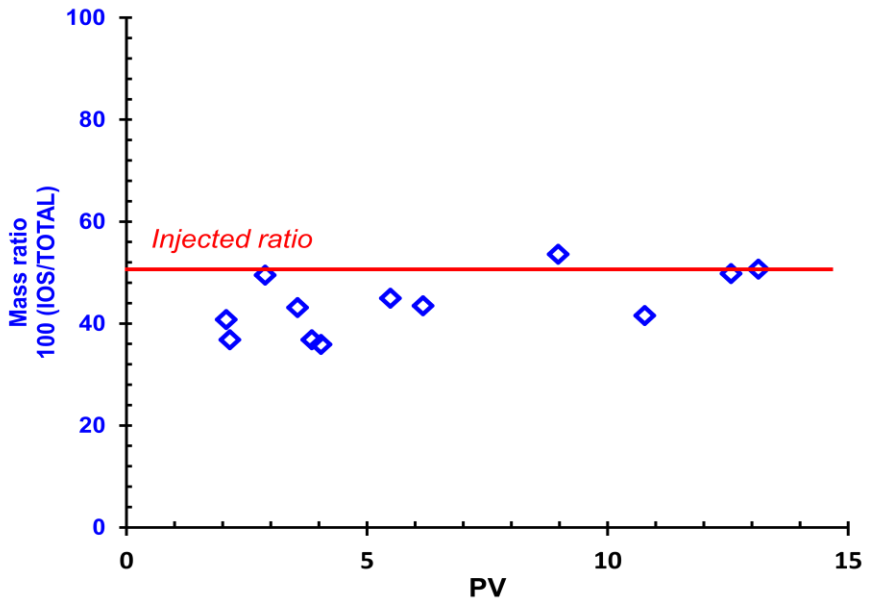

Figure 6-12 Mass ratio of IOS respect to the total surfactant blend in the effluent.

The surfactant adsorption does not show considerable preference for any surfactant, but is important to clarify that the molar ratio of IOS to carboxylate is close to ten.

Table 6-3 PEMEX Composite Dolomite adsorption/retention

Method	Adsorption mg/g_{Rock}
Mass balance	2.09
Retardation mid point tracer vs surfactant in effluent	1.78
IPA-DI Water flush	1.73

The adsorption calculated by mass balance during desorption process is 17% smaller than the value measured during the adsorption process, this can be caused by permanent retention of surfactant. The difference between the two results is higher in this case; one factor can be the higher surface area (area per unit mass), and the lower permeability, trapping more surfactant.

Remarks about results:

PEMEX rock has

(1) an order of magnitude higher adsorption than Silurian,

PEMEX 2 mg/g_{Rock} vs. Silurian 0.4 mg/g_{Rock}.

(2) two orders of magnitude lower permeability than Silurian dolomite,

PEMEX 1.3 md vs. Silurian 250 md.

This could be caused by the difference in pore size and/or surface area. Blake-Kozeny equation predicts this relationship between specific area and permeability.

$$a_v = \frac{6\phi^{3/2}}{\sqrt{150\,K_{perm}}} \qquad \textbf{(Equation 6-20)}$$

Neither Silurian nor PEMEX rock presented plugging during the experiment; pressure drop remained constant during the experiment. Permeability remained constant before and after surfactant injection.

Before reaching equilibrium concentration, PEMEX rock had mild preference for **C15-18 IOS Petrostep S2** over **$C_{28}PO_{25}EO_{25}COONa$** .

Tracer analysis was used to estimate flowing fractions and parameters described in the mathematical model written for prediction of adsorption in rock. The model predicted all experimental cases, and the predictions are presented in the next section.

6.5 Mathematical Model proposed

Writing all the equations in dimensionless form for the proposed model:

$$-b_1\frac{\partial C_1}{\partial \chi}+\frac{f_1}{N_{Pe1}}\frac{\partial^2 C_1}{\partial \chi^2}-N_{St12}(C_1-C_2)=f_1\frac{\partial C_1}{\partial \tau}\left(1+F_1'\frac{(1-\varphi)}{\varphi}\right)$$

$$-b_2\frac{\partial C_2}{\partial \chi}+N_{St12}(C_1-C_2)+N_{St23}\left(C_3^{surf}-C_2\right)=f_2\frac{\partial C_2}{\partial \tau}\left(1+F_2'\frac{(1-\varphi)}{\varphi}\right)$$

$$\frac{a}{N_{Pe23}}\left(\frac{1}{\zeta^2}\frac{\partial}{\partial \zeta}\left(\zeta^2\frac{\partial C_3}{\partial \zeta}\right)\right)=\frac{\partial C_3}{\partial \tau}\left(1+F_3'\frac{(1-\varphi)}{\varphi}\right)$$

(Equation 6-20 a,b and c)

And the boundary condition:

$$N_{St23}\left(C_3^{surf}-C_2\right)=3f_3\frac{a}{N_{Pe23}}\left(-\frac{\partial C_3}{\partial \zeta}\right)\Big|_{\zeta=1}$$

(Equation 6-21)

Simulation of the dynamic adsorption experiment:

The system of equations was be solved numerically, by discretization in axial direction for macro and dendritic fraction, and in radial direction for the micro pore region.

$$-b_1 \sum A_{ij}^{(a)}\, C_{1\,j} + \frac{f_1}{N_{Pe1}} \sum B_{ij}^{(a)}\, C_{1\,j} - N_{St12}(C_{1\,i} - C_{2\,i}) = f_1 \frac{\partial C_{1\,i}}{\partial \tau}\left(1 + F'_{1\,i}\frac{(1-\varphi)}{\varphi}\right)$$

$$-b_2 \sum A_{ij}^{(a)}\, C_{2\,j} + N_{St12}(C_{1\,i} - C_{2\,i}) + N_{St23}\left(C_{3\,i}^{surf} - C_{2\,i}\right)$$

$$= f_2 \frac{\partial C_{2\,i}}{\partial \tau}\left(1 + F'_{2\,i}\frac{(1-\varphi)}{\varphi}\right)$$

$$\frac{a}{N_{Pe23}} \sum B_{jk}^{(r)}\, C_{3\,ik} = \frac{\partial C_{3\,ij}}{\partial \tau}\left(1 + F'_{3\,ij}\frac{(1-\varphi)}{\varphi}\right)$$

(Equation 6-22 a,b and c)

For the boundary condition between dendritic and micro porosity:

$$N_{St23}\left(C_{3\,i}^{surf} - C_{2\,i}\right) = -3f_3 \frac{a}{N_{Pe23}} \sum A_{N+1\,k}^{(r)}\, C_{3\,ik}$$

(Equation 6-23)

The system of equations was solved with implicit differential equations solver, using finite-differences for axial discretization, and orthogonal collocation for radial discretization within the cluster of the micro porous zone.

6.6 Simulation of dynamic adsorption (Model parameters fitting)

Three different cases are analyzed using simulation. The first two were done with the results of the experiments, and a third case was selected from literature Mannhardt *et al.* (1992) to see the potential of having the simulation tool developed , and to see the performance of our model with experimental results from a different source .

Case I: Study of dynamic adsorption at 99°C using a composite of dolomite formation rocks with low flowing fraction and low permeability, injecting continuous slug of a blend of anionic surfactants.

Case II: Study of dynamic adsorption at 94°C using Silurian outcrop dolomite with high flowing fraction and permeability, injecting continuous slug of a blend of anionic surfactants.

Case III: Adsorption of anionic or amphoteric surfactant in dolomite rock, using a finite slug, to see the importance of satisfying adsorption. In this case experimental data from literature were used.

All the simulations were in agreement with the experimental data, and the parameters were obtained by history match, but initial guess was needed. The initial guess was obtained by simplifying the model to double porosity model, and using semi analytical solution in Laplace domain and with regression analysis. This initial guess was done only for tracer. The double porosity model gave a good guess for flowing fraction, Peclet, and Stanton numbers needed to history match experimental data with the triple porosity model for tracer. For surfactant

the same order of magnitude of dispersion and mass transfer coefficients were used, and the parameters for the surfactant isotherm were those found from static adsorption experiments.

The determination of initial guess for the parameters used to represent the transport of the tracer. As initial guess the simplified double porosity model was used.

In this case the simplified dimensionless differential equations are:

$$f\frac{\partial C_1}{\partial \tau} = -\frac{\partial C_1}{\partial \chi} + \frac{f}{N_{Pe}}\frac{\partial^2 C_1}{\partial \chi^2} - N_{St_{12}}(C_1 - C_2)$$

$$(1-f)\frac{\partial C_2}{\partial \tau} = N_{St_{12}}(C_1 - C_2)$$

(Equation 6-25 a and b)

And the dimensionless boundary conditions:

$C_1\big|_{\chi=0} = 1$ Continuous slug injection

$\left.\frac{\partial C_1}{\partial \chi}\right|_{\chi=1} = 0$ No gradient or adsorption in the downstream distributor

(Equation 6-24 a and b)

The set of equations and boundary conditions in real and Laplace domain are in the Table 6-4

Table 6-4 Simplified equations for initial guess

Equation	Laplace domain	Description
$f\frac{\partial C_1}{\partial \tau}=-\frac{\partial C_1}{\partial \chi}+\frac{f}{N_{Pe}}\frac{\partial^2 C_1}{\partial \chi^2}-N_{St_{12}}(C_1-C_2)$	$s\,f\,\Psi=-\frac{d\Psi}{d\chi}+\frac{f}{N_{Pe}}\frac{d^2\Psi}{d\chi^2}-N_{St_{12}}(\Psi-\Xi)$	Flowing fraction
$(1-f)\frac{\partial C_2}{\partial \tau}=N_{St_{12}}(C_1-C_2)$	$(1-f)\,s\,\Xi=N_{St_{12}}(\Psi-\Xi)$	Non-flowing fraction
$C_1\big\vert_{\chi=0}=1$	$\Psi\big\vert_{\chi=0}=\frac{1}{s}$	Continuous slug injection
$\left.\frac{\partial C_1}{\partial \chi}\right\vert_{\chi=1}=0$	$\left.\frac{d\Psi}{d\chi}\right\vert_{\chi=1}=0$	No gradient in the downstream distributor

Coupling the set of differential equations the resulting model in Laplace domain is:

$$\frac{f}{N_{Pe}}\frac{d^2\Psi}{d\chi^2}-\frac{d\Psi}{d\chi}+-\left(s\,f+N_{St_{12}}\left(1-\frac{N_{St_{12}}}{N_{St_{12}}+s(1-f)}\right)\right)\Psi=0$$

(Equation 6-25)

The solution of this equation in Laplace domain is:

$$\Psi = \frac{1}{s}\left[\frac{\exp(\lambda_1 \chi) - \left(\frac{\lambda_1}{\lambda_2}\right)\exp(\lambda_1 - \lambda_2)\exp(\lambda_2 \chi)}{1 - \left(\frac{\lambda_1}{\lambda_2}\right)\exp(\lambda_1 - \lambda_2)}\right]$$

(Equation 6-26)

The eigenvalues are calculated from the characteristic equation as:

$$\lambda_{1,2} = \frac{N_{Pe}}{2f}\left\{1 \pm \sqrt{1 + 2s\left(2\frac{f}{N_{Pe}}\right)\left(f + \frac{N_{St_{12}}(1-f)}{N_{St_{12}} + s(1-f)}\right)}\right\}$$

(Equation 6-27)

This analytical solution in Laplace domain contains the three parameters to predict the transport of the tracer, the flowing fraction f, the advection to dispersion ratio (i.e. Peclet number) and the mass transfer to advection ratio (i.e. Stanton number)

The response of concentration of the tracer, can be transformed into Laplace domain, and using non linear regression, the flow parameters can be fitted. The figure below shows the results of the regression for the Case I and the resulting parameters are indicated as well in fig 6-13.

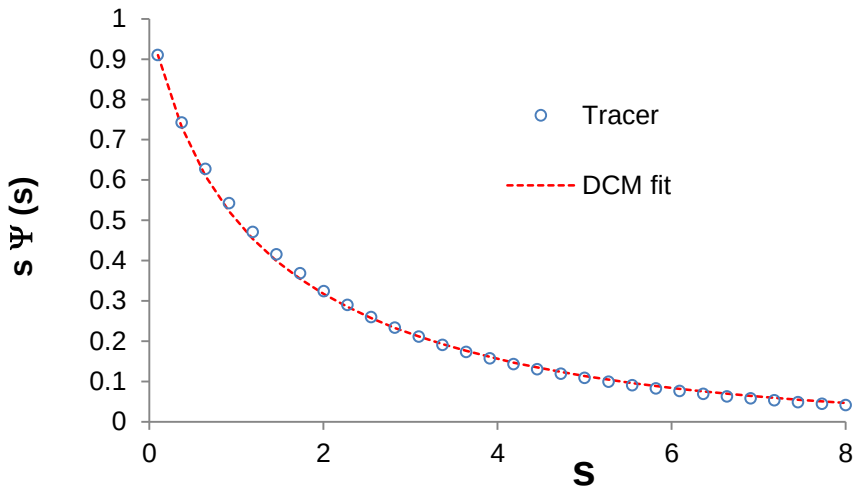

Figure 6-13 Parameters used during the fitting in Laplace domain, *f*=0.3, N_{St12}=1, N_{Pe12}=20

CASE I Simulation of the dynamic adsorption 99°C using a composite of dolomite formation rock with low flowing fraction and low permeability. The parameters of the triple porosity model were obtained by history match of the response of the tracer and the surfactant. The initial parameters used in the fitting process, were those of the double capacitance model. For the adsorption isotherm the values of the static adsorption were used. The surface area in this case is one order of magnitude higher than the surface area of the high permeability rock (i.e. Silurian dolomite).

The model for the adsorption isotherm was the Langmuir simplified as:

$$C_i^s = \frac{K\ a_v\ C_i}{ks + C_i}$$

(Equation 6-28)

$$C_i^s = \Gamma_i \, a_v$$

(Equation 6-29)

And the concentration is defined as the surface concentration, but per unit volume, as indicated in equation 6-31.

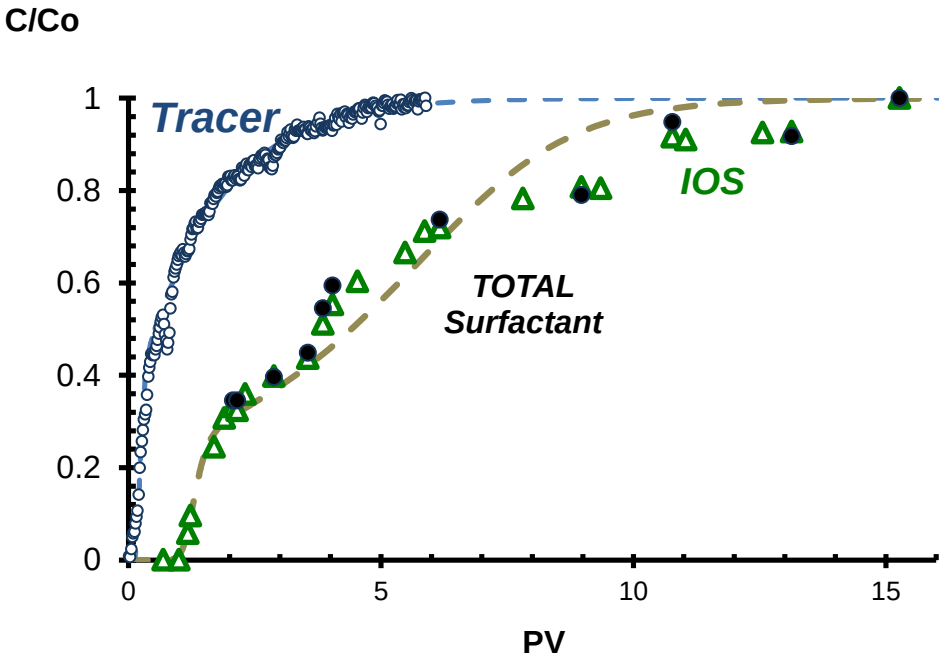

Figure 6-14 Comparison of the response of tracer and surfactant using the triple porosity model for the low permeability composite core. Parameters are listed in table 6-5.

Table 6-5 Parameters for simulation after fitting

Parameter	Value	
Case	I	II
f_1	0.275	0.9
f_3	0.3	0.05
N_{St12}	1.0	0.56
N_{St12S}	1.75	0.672
N_{Pe1} / f_1	29.09	19.33
N_{Pe1S} / f_1	14.54	7.77
ϕ	0.15	0.14
$3a/N_{Pe23}$	5	5
$K\ a_v/C_{so}$	0.702	0.087
Ks/C_{so}	0.2	0.2

CASE II Simulation of dynamic adsorption at 94°C using Silurian outcrop dolomite with high flowing fraction and permeability, using a blend of anionic surfactants.

Order of magnitude of most of the parameters are the same for the Case I and Case II, the only difference was the surface area, and the simulation matched the experimental data, indicating that the most probable reason for the difference in the adsorption was the surface area.

For case I the flow rate was slow, and the flowing fraction is small compared with case II. Table 6-5 lists the parameters after fitting and the Péclet and Stanton numbers between both cases scale linearly with length.

The model can be used to plan experiments of dynamic adsorption and to predict results of these tests. The information needed is the results of tracer analysis, and static adsorption experiments to know the equilibrium isotherms for the surfactant-rock system.

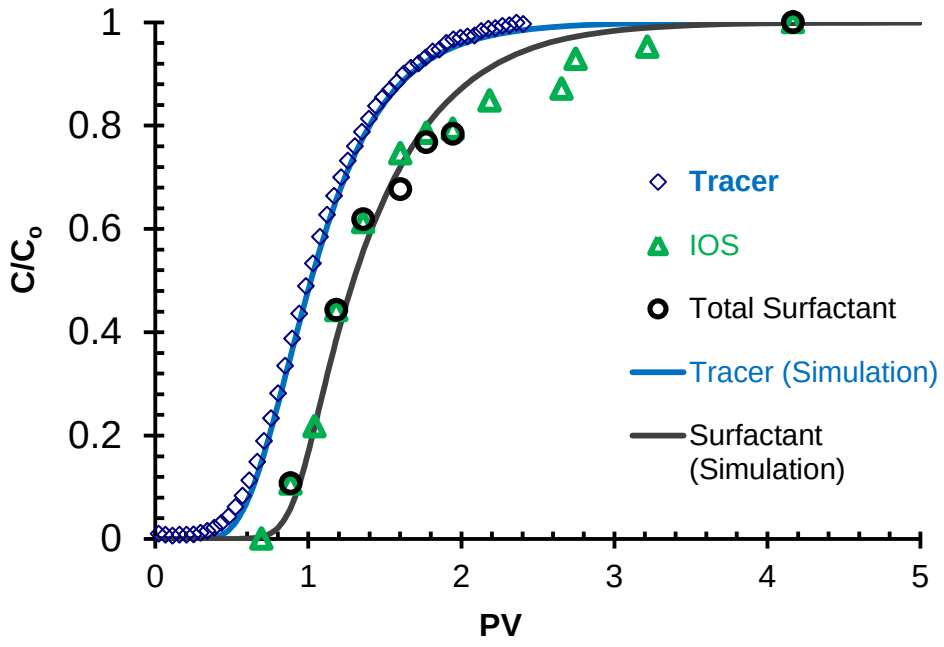

Figure 6-15 Tracer and surfactant comparison of the response using the triple porosity model for the high permeability Silurian outcrop core. Parameters are listed in table 6-5.

Case III: Dynamic adsorption of anionic and amphoteric foam-forming surfactants. Different approaches can be used to measure adsorption in consolidated porous media, one is to inject a finite slug, and another approach is to use a continuous slug. Mannhardt *et al.* (1992 and 1993) used the finite slugs to study adsorption of different kinds of surfactants in different types of rocks.

The mathematical model of triple porosity model was used to simulate the experimental data presented by Mannhardt *et al.* (1992 and 1993), and the effect of hysteresis is discussed.

Reversible adsorption will be like a chromatographic process, and the irreversible adsorption is the other extreme. For EOR applications there is interest in both phenomena.

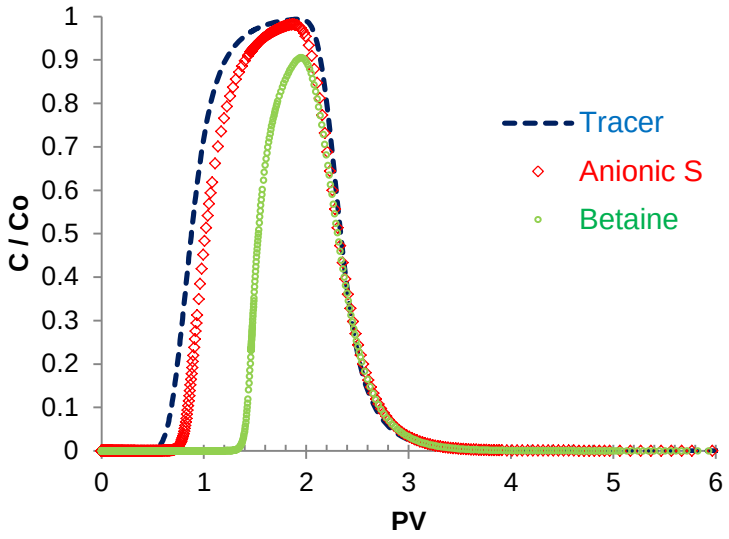

Figure 6-16 Simulated response of a finite slug of Anionic or Amphoteric surfactant respect to a tracer in dolomite rock, assuming adsorption 100% irreversible.

For the response on simulation assuming irreversible adsorption (Fig. 6-16), one important observation respect to this case is the delay in the rear end of the concentration curves between tracer and surfactant is negligible if irreversible adsorption is assumed (i.e. Maximum degree of hysteresis). It is important to clarify that the results from this simulation are for injection of anionic or amphoteric, but not both. To include both, additional experiments for isotherms are required for the binary blend under different proportions, and that kind of experiment was not discussed in that article. The parameters used in the simulation are in table 6-6

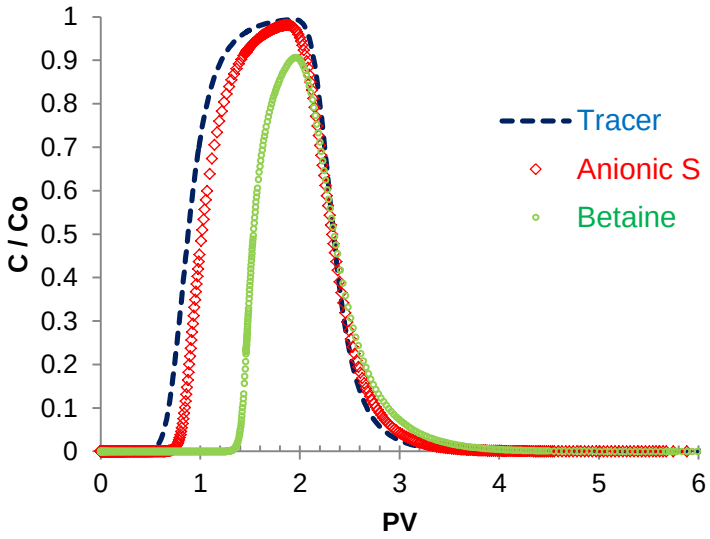

Figure 6-17 Simulated response of a finite slug of Anionic or Amphoteric surfactant respect to a tracer in dolomite rock, assuming that some desorption may occur.

If the simulation is done, letting a fraction of the surfactant be adsorbed reversibly, or indicating a level of hysteresis, there is a small delay in the rear end of the concentration curve approaching 3PV of production (Fig 6-17), this

phenomenon is observed in the experimental results reported by Mannhardt *et al.* (1992).

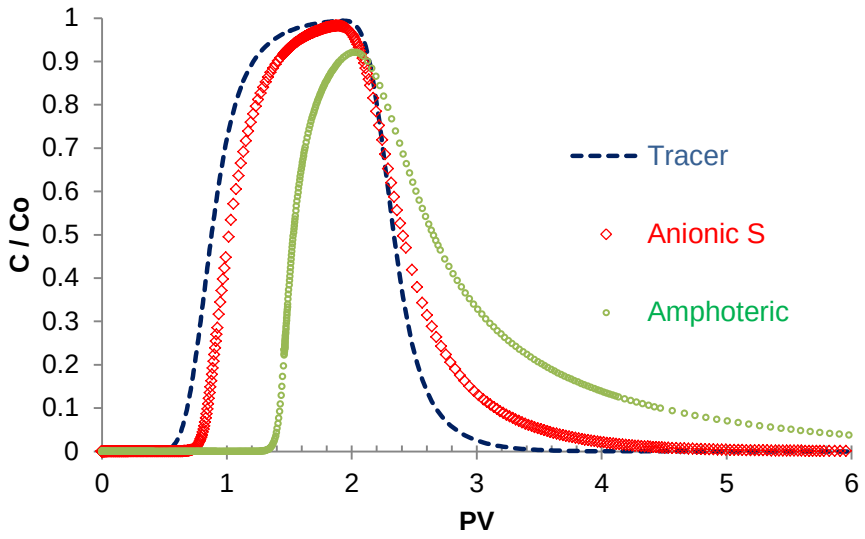

Figure 6-18 Simulated response of a finite slug of Anionic or Amphoteric surfactant respect to a tracer in dolomite rock, assuming adsorption is reversible.

If no hysteresis is specified in the adsorption isotherm, there will be a delay in the curves, but area under the curves will be the same for all components, so no adsorption will take place, but chromatographic separation respect to tracer as indicated in fig 6-18

Table 6-6 Parameters for simulation in case III, for the three different scenarios.

Parameter	Value
f_1	0.85
f_3	0.1
N_{St12}	0.5
N_{St12S}	0.5
N_{Pe1} / f_1	65.88
N_{Pe1S} / f_1	35.29
ϕ	0.18
$3a/N_{Pe23}$	1
$K\ a_v / C_{so}$	0.05
Ks/C_{so}	0.2

The difference between figures is the degree of hysteresis, the first simulation is for irreversible adsorption, the second one for desorption only 10% of the equilibrium value, and the last one for reversible adsorption or chromatographic process. The degree of hysteresis is defined as the ratio of the desorption isotherm, respect to the adsorption isotherm.

Reviewing the results of the simulation, it seems that the experimental results from Mannhardt *et al*. (1992) may present a certain degree of reversibility, this can be observed on the experimental curves of the surfactant respect to tracer in the rear end of the finite slug, there is a certain degree of retardation of the

signal, that is not observed in the irreversible adsorption simulation, to validate this hypothesis further experimental measurements are required.

This behavior in the simulation suggests the use of continuous slugs to quantify adsorption rather than short finite slugs. Another reason for using continuous slugs is to warranty satisfying adsorption.

In all the simulations a Langmuir type isotherm was used.

Observed surface areas using BET technique (Table 6-7) indicate that variation up 1 order of magnitude on dolomitic rocks is possible, but the BET apparatus used for this measurements is in the detection limit, so another method should be used to verify this possibility.

Observations by Neeraj Rohilla in our lab, verifies the possibility of these differences using NMR technique (Fig 6-19).

Table 6-7 Surface area measured in different dolomites

Cores	BET Surface Area (m^2/g)
Powder Dolomite I	1.18±0.13
Carbonate Formation Core A Zaap 10,25 N1, BTP-KS	0.12
Carbonate Formation Core B CANT 1024D, N1, C2, BTP-KS	0.20±0.02
PEMEX rock ground 2092 D, Caja 10 C-10/12 f18 BTP-KS	0.98 ±0.1

The measurements were done using Micrometritics ASAP 2010, accelerated surface area and porosimetry system by Yu Bian.

Previous studies discussed in previous chapters (Anhydrite detection for EOR applications) indicated that all the rocks were composed of dolomite, and analysis of the surface using XPS confirms that this is also true for the surface.

From atomic analysis of the surface, the most probable composition of the rock surface is given in table 6-8

Table 6-8 Analysis of the surface of the rock.

Component	Mass %
$CaMg(CO_3)_2$	83.5
$CaCO_3$	16.1
SiO_2	0.4
Total	100

Table 6-9 XPS analysis. Atomic percentage of the surface of PEMEX rock

Run	C	O	Mg	Al	Si	Cl	Ca
1	26.75	55.26	7.03	0.00	0.26	0.26	10.44
2	25.04	55.8	7.98	0.00	0.08	0.3	10.81
3	23.9	55.16	9.12	0.00	0.02	0.36	11.43
Average	25.23	55.406	8.043	0.00	0.12	0.306	10.893
StDev	1.434	0.344	1.046	0.00	0.125	0.0503	0.5003

The XPS analysis (table 6-9) was done used a sampled cleaned with solvents (Toluene, THF, Methanol and Chloroform) and saved in glass bottle for more than a year. XPS is a technique that can be used to calculate the empirical formula of homogeneous surfaces, and the atomic basis detection limit is 1% or 0. 1%.

Comparison of T2 and S/V spectrum between Zaap 2 rock and Silurian outcrop

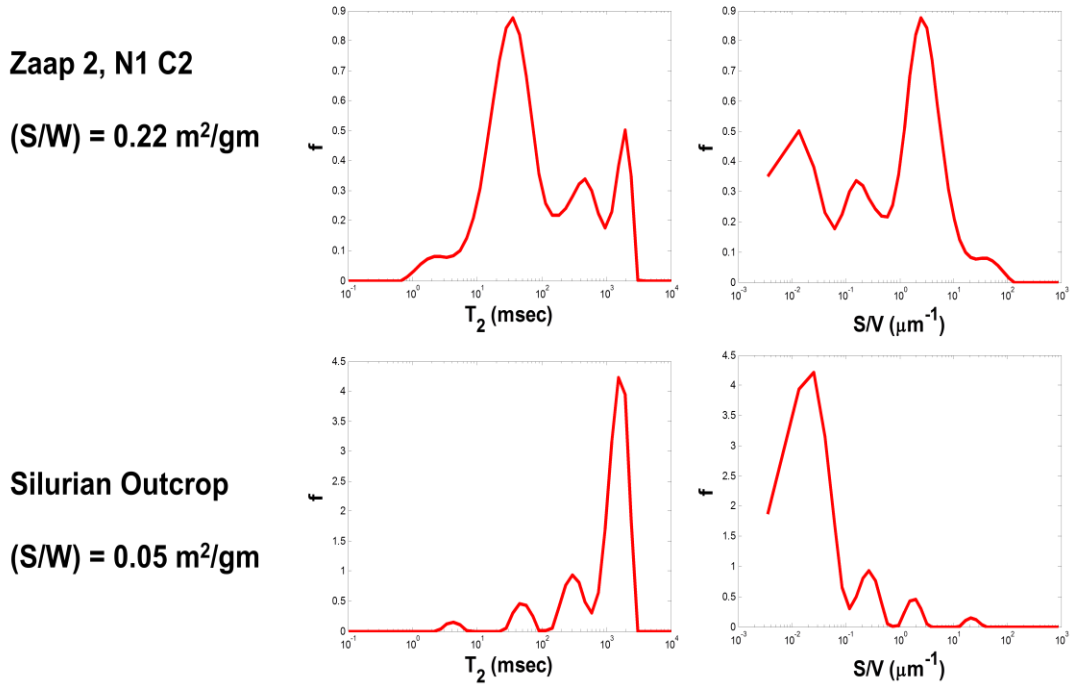

Figure 6-19 Preliminary results of surface area using NMR (Tests done by Neeraj Rohila)

6.7 Conclusion of Chapter 6

Adsorption can be measured using dynamic adsorption experiments, knowing the actual flowing properties of the rock samples, i.e. knowing the flowing fraction and the actual surface area of the rock. Those results can be used to scale up the process if the composition of the rock is known, and the flowing properties.

Simulation can be used to plan experiments or to characterize the rock if the adsorption isotherms are known.

Surface area of the rock plays an important role in the adsorption, and a suitable process to measure the surface area is required.

Chapter 7

FOAM AND OIL EXPERIMENTS

Summary

The overall objective of the chapter is to study formulations selected to develop an EOR process. This was done by tailoring foams for simultaneously reducing remaining oil saturation and controlling fluid mobility in fractured carbonate reservoirs at ~ 94°C. The approach is to find a surfactant formulation that will foam with nitrogen as to deliver the foamed surfactant solution over a large volume of the fractured reservoir. The surfactant solution in the foam must lower IFT and/or alter wettability so liquid spontaneously imbibes into the matrix and increases the water saturation in the matrix. The increased liquid saturation will increase the liquid relative permeability and thus enhance the rate of liquid gravity drainage. If the wettability is altered and/or IFT lowered sufficiently, the draining liquid will be enriched in oil.

Relevant results about this chapter are:

- Formulation capable to transport surfactant as foam at 94°C, formulated in sea water.
- Experimental technique to produce data of foaming systems at high temperature.

- Methodology to conduct core floods in sand packs using foaming surfactants aided by the background of phase behavior in “surfactant blend ratio- salinity ratio maps” to choose the most favorable conditions of blend composition and injection salinity to achieve good oil recovery.
- Mathematical model able to reproduce the foam strength behavior observed in sand packs with the formulations studied.
- Visualization of oil recovery mechanism from matrix using micro-channels surrounded by glass beads to mimic matrix and fractures respectively.

This chapter is divided in five sections:

7.1. Foam studies with oil recovery using “Surfactants ratio – salinity ratio” maps to select injection conditions for oil recovery.
7.2. Screening of surfactant blends to produce strong foams.
7.3. Mathematical model and parameter fitting capable to simulate the foam experiments.
7.4. Gravity drainage – imbibition experiments in high temperature Amott cells and foam imbibition apparatus.
7.5. Visualization of oil recovery mechanisms in a simulated fracture-matrix system using micro channels filled with oil.

7.1. Foam studies with oil recovery using “Surfactants ratio – salinity ratio” maps to select injection conditions for oil recovery.

7.1.1 Surfactants used in oil recovery study with foam.

A list of surfactants used during the first stage of the study and some properties are included in table 7-1. For details about surfactants see Appendix 7A.

Table 7-1 Surfactants blends used in core floods

Surfactant	Formula	Notes MM(g/mol) HLB*
Avanel S70	$C_{12\text{-}15}H_{25\text{-}31}(\text{-O-}C_2H_4)_7\text{ -}SO_3^-\ Na^+$	**MM=601** **HLB=13.9**
$C_{20\text{-}24}$IOS	$CH_3(CH_2)_n(CH_2)_2CH[SO_3Na]CH[OH](CH_2)_2(CH_2)_mCH_3$ $CH_3(CH_2)_n(CH_2)_2CH[SO_3Na]=CHCH_2(CH_2)_mCH_3$	**MM=428** **n+m=14** **HLB=7.55**
Triton X200	C_9H_{19}  $(\text{-O-}C_2H_4)_{8.6}\text{-}SO_3^-\ Na^+$	**MM=684.4** **HLB=14.87**
$C_{20\text{-}24}$IOS	$CH_3(CH_2)_n(CH_2)_2CH[SO_3Na]CH[OH](CH_2)_2(CH_2)_m$ CH_3 $CH_3(CH_2)_n(CH_2)_2CH[SO_3Na]=CHCH_2(CH_2)_mCH_3$	**MM=428** **n+m=14** **HLB=7.55**
Old UT Carboxylate	$C_{24}H_{49}(PO)_{25}(EO)_{56}CO_2Na$	**MM=4259** **HLB=29.43**
$C_{19\text{-}23}$ IOS Enordet 0342H	$CH_3(CH_2)_n(CH_2)_2CH[SO_3Na]CH[OH](CH_2)_2(CH_2)_mCH_3$ $CH_3(CH_2)_n(CH_2)_2CH[SO_3Na]=CHCH_2(CH_2)_mCH_3$	MM=398 **HLB=8.03**
UT Carboxylate	$C_{28}H_{57}\ (PO)_{25}(EO)_{25}CO_2Na$	**MM=2956.6** **HLB=17.3**
$C_{15\text{-}18}$ IOS Petrostep S2	$CH_3(CH_2)_n(CH_2)_2CH[SO_3Na]CH[OH](CH_2)_2(CH_2)_mCH_3$ $CH_3(CH_2)_n(CH_2)_2CH[SO_3Na]=CHCH_2(CH_2)_mCH_3$	**MM=351.5** **HLB=10.16**

(*) Calculated with Davies, and Lin and ECL method, suggested by Guo (2006)

In chapter 2 some guidelines about the use of different surfactants were described. Alkoxylated sulfonates or carboxylates can be used in the formulation of surfactants to perform with high optimal salinity and tolerance to hardness, and blending them with IOS can help in achieving aqueous solutions suitable for injection and in tuning optimal salinity of alkoxylate as needed.

An appropriate index to classify surfactants was discussed in chapter 2. Those indices are important when the surfactants are used in formulations containing electrolytes, and applied at high temperature, but the HLB approach is used as the first handy tool to organize them.

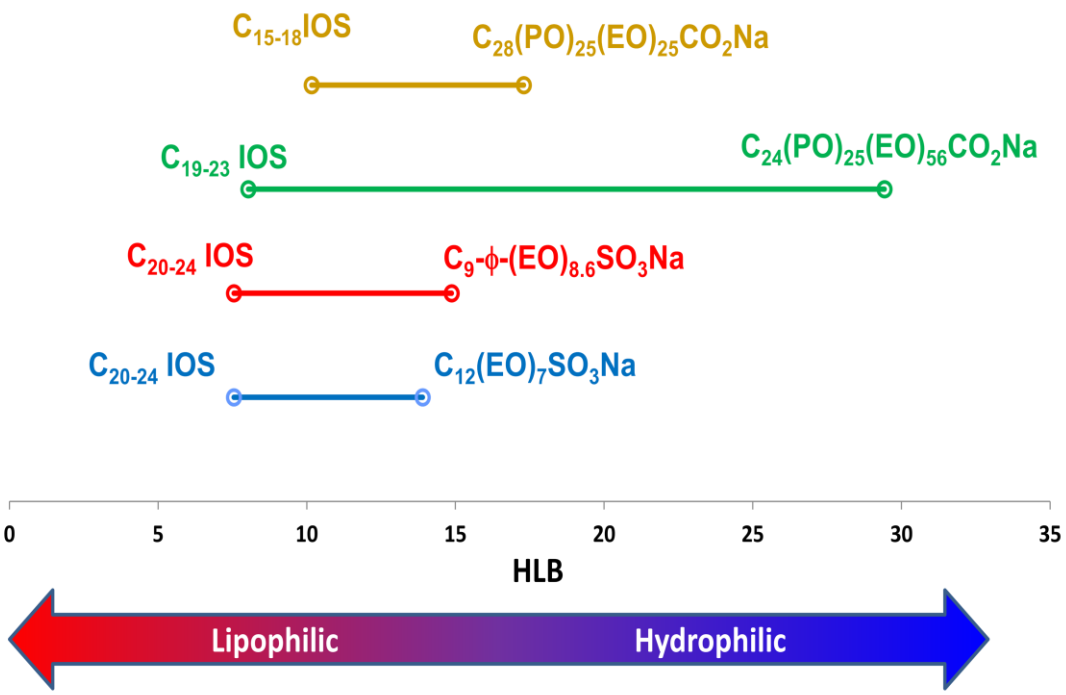

Figure 7-1 Binary anionic surfactant blends used in the research. Using Davies' approach for HLB, and calculated with tables given by Guo *et al* (2006)

As described in chapter 2, there are different ways to move the fluid phases-system from Winsor Type I to Winsor Type II. Most of the researchers use salinity scans to select the optimum conditions to obtain middle phase microemulsions (Winsor Type III). In the present study the approach of blending surfactants is used at fixed salinities in the range between seawater and formation brine. (See Table 7G-1 in Appendix 7G)

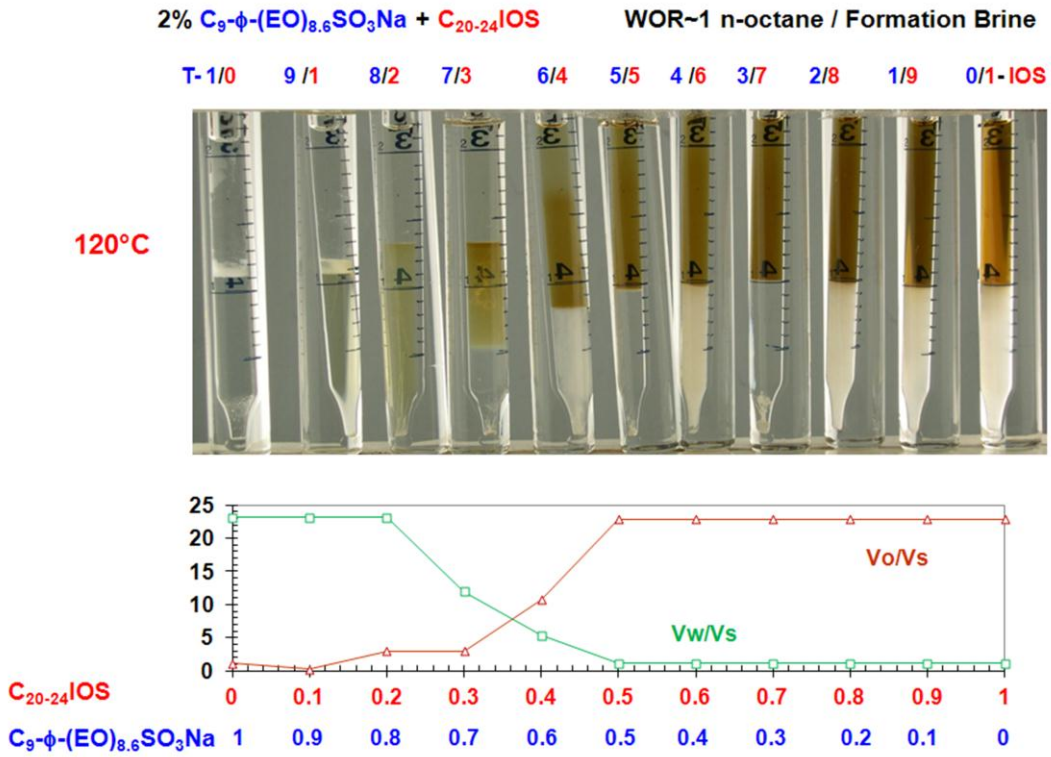

Figure 7-2 Surfactant blend scan used characterize the surfactants. Optimal blend concept developed by Puerto et el. (2012). (Photo cortesy by Maura Puerto)

In Fig 7-2 is a representation of the phase behavior of the 2% surfactant blends in formation brine at 120°C. Under these conditions a concentration of 0.36 % of IOS and 0.64% of alkyl aryl ethoxylated sulfonate gave optimum surfactant

proportions (optimum is where $V_o/V_s = V_w/V_s$). For this particular combination of surfactants in formation brine and n-octane, the optimum ratio of surfactants is almost insensitive to temperature according to measurements done at 70°, 90° and 120°, but solubilization was reduced 50% from 70° to 120°C .

This formulation was tested in core flood experiments with synthetic crude oil using silica sand, and in a specially designed foam-imbibition apparatus. The equipment used in core floods and foam experiments is described in the next section.

7.1.2 Materials and Methods for the Core flood experiments, and foam experiments in sand packs.

The core floods and foam experiments were done in set up shown in Figure 7-3. Description of the apparatus operation is as follows:

For core floods with crude oil:

Stage I:

- The porous media holder is removed, cleaned and dried.
- New silica sand (Ottawa White Silica Sand 20/40 from U.S. SILICA), after being cleaned is poured into the porous media holder, and compacted with a pneumatic shaker or pneumatic vibrator with a cylindrical weight at the top of the sand pack. This is done until the height of the sand pack is maintained constant.

- The porous media is assembled, maintaining compression using 51/2 rubber stoppers at the both ends protected by a 200 Mesh screen to prevent direct contact of the sand with the rubber stopper, and to prevent the sand from entering the lines.
- The assembled sand pack is evacuated using a vacuum pump and when the gauge pressure is -29 inHg, the vacuum line is closed, and the pump stopped. The vacuum should be maintained for at least 1 h, to verify complete sealing.
- The pore volume of the sand pack is measured using formation brine, or the brine required during the experiment.
- The brine permeability is measured using brine.
- The porous media holder is assembled in the oven, and connected to the rest of the components.

Stage II:

- Crude oil is then injected after in-line 0.5 μm filter, from top to bottom, and pressure drop measured, the irreducible water is calculated with a mass balance, and end point relative permeability is measured at room temperature.
- Formation brine is then injected from bottom to top, to leave the system at residual oil condition, and end point water relative permeability is measured at room temperature.

Stage III:

Note: Bold numbers refer to fig 7-3 (numbers in bold are used to identify elements of the equipment)

- The system is started injecting formation brine. This is done for several pore volumes to make sure no more oil is produced at test conditions of temperature and backpressure.
- A slug of surfactant is injected, for a fraction of pore volumes (ca. 1/4), after this surfactant injection is maintained at desired flow rate to be co- injected with nitrogen.
- Pre-purified gas nitrogen (**1**, Matheson Tri Gas Nitrogen Compressed) is injected to the oven controlling the flow rate through a gas flow controller (**2**, Matheson flow controller Model 8270, 0-20 sccm, using a Matheson mass flow transducer 8272-0421).
- Check valves (**3, 5** Swagelok poppet check valve, 5 psig) are located before and after a heat exchanger (**4**) which is inside the oven where the temperature is maintained at 94°C.
- The nitrogen gas is mixed with the surfactant solution before being injected to the sand pack in the cross (**6**).
- The surfactant solution is continuously mixed and filtered (**8**, Pump inlet filter 0.5 μm) in the suction of a HPLC pump (**9**, ISCO Model 2350, 0-10 cm^3/min), then passes through a check valve (**10**, Swagelok poppet check valve, 5 psig) before a heat exchanger (**11**) located

inside the oven, after this point the surfactant solution is mixed in a cross (**6**) where nitrogen is co injected,

- The thermocouple (**7**, Omega Type K) measures the co-injection temperature, between the thermocouple and the bottom of the column there is a tap (**12**) that measures gage inlet pressure using the pressure sensor (**24**, Validyne pressure sensor DP7).
- The mixture of nitrogen and surfactant solutions are fed into the packed 20-40 mesh silica sand column (ID=2.29 cm, H=15 in).Sand Pack of L=38 cm, D=2.29 cm, K=100 darcy.
- Three internal taps (**13, 14** and **15**) are located at different heights to measure pressure drops across the packed bed every 6 inch (distances from bottom to the taps are 1½ in, 7 ½ in and 13 ½ in respectively).
- The effluent of the column is passed through a check valve (**16**, Swagelok poppet check valve, 5 psig) and mixed with a small continuous water flow rate (ca. 0.1 cm^3/min), using a ISCO pump (20, ISCO Model 260D Syringe Pump with ISCO Series Pump Controller, 0.001 -107 ml/min, max pressure 7500 psi.
- This pump (**20**) measures the injection pressure (pressure was recorded during the experiment), and is used to maintain open a relief valve (18, Swagelok proportional relief valve RL3 10-225 psi) to minimize oscillation at the outlet pressure, acting as a back pressure regulator.

- The relief valve (**18)** was setup in the range of pressure from 30-40 psig. The set-point pressure to open will depend on the desired conditions of experiment, and to prevent flashing of any component within the liquid blends.
- The outlet of the relief valve is conducted to a heat exchanger (**19**) to cool the effluent.
- The cooled effluent is collected in vials (**23**).
- Back-pressure is kept constant, even during more than one-phase flow, by an special arrangement , where small amount of water is constantly injected to keep flow-control open all the time (set up is suppressed from Figure 1)
- Liquid- Gas ratio is measured when desired by flipping 3-way valve (**21**) into an inverted burette (**22**).
- The history of the pressure at different times during the experiments were recorded with a PC using a validyne UPC2100 PCI Sensor Interface Card to process the signal of the validyne stainless steel low pressure sensors (**24,25,26,27** Validyne DP7).

7.1.2.a Diagram of equipment for foam experiments and core floods.

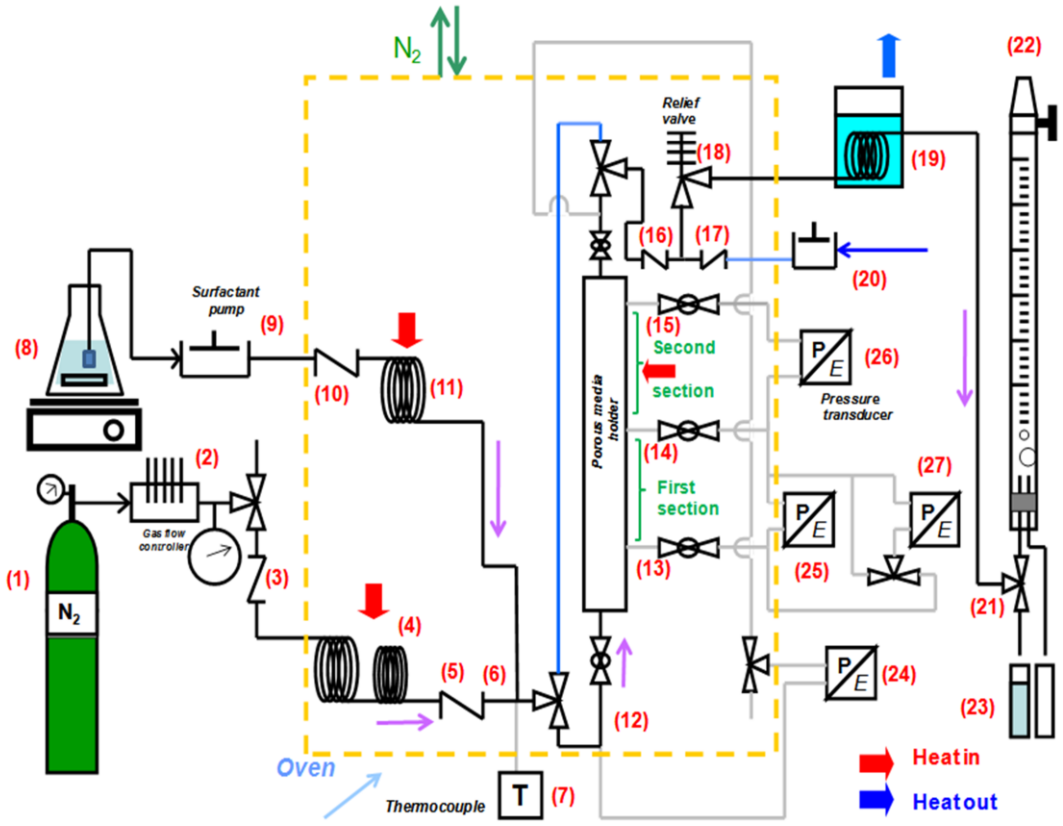

Figure 7-3 Experimental setup

Description of equipment was included in previous section 7.1.2, photographs are included in Appendix 7B. Not showing in the diagram:

- After the valve (12) there is a Tee with a valve in a line that connects the line with another Tee placed before the check valve 16 (not shown in the diagram *).
- Between the blue line in the diagram and the outlet of the column there is another connection with a valve (not shown in diagram *).

Notes:

The two heat exchangers have a *NTU* (**) higher than 3 at flow conditions so injection of gas and liquid will be at oven temperature.

- For safety reasons an atmosphere of nitrogen was maintained in the oven during experiments with crude oil.
- The heat exchanger to cool down the effluent operates at 0°C.
- The experimental set up was designed to study foam, but core floods were conducted as well, and foam experiments with and without crude oil.

Steady state was considered when the pressure reading did not change in time, and when the steady flow condition was reached (i.e. injection flow rates equal production flow rates)

(*) The purpose of these additional connections is to be able to operate the column with foam flowing upward or downward. Most of the experiments were conducted upward, but some additional tests were done to verify stability of foam flowing downward.

(**) *NTU* = Number of transfer units (dimensionless) = $U A / (\rho q Cp)$

U= Heat transfer coefficient, *A*=Heat exchanger area, ρ = Fluid Density, *q* = volumetric flow rate, *Cp*= Specific heat capacity of the fluid.

7.1.2.b Surfactant

See tables 7-1, 7-5 and Appendix 7A for more details about surfactants.

7.1.2.c Brine Composition used during experiments

During the foam experiments at 94°C, surfactant solutions were prepared in synthetic seawater. The composition of the synthetic seawater is in table 7-2; for additional details about seawater see chapter 4.

Table 7-2 Brines composition using stock salts.

Salt	Seawater (g/l)	Formation brine (g/l)	Brine Seawater ionic strength (g/l)
NaCl	27	106.03	44.639
$CaCl_2\ 2H_2O$	1.72	14.112	0
$MgCl_2\ 6H_2O$	11.2	1.23	0
Na_2SO_4	4.8	0.74	0

All aqueous solutions were prepared with DI water (18.2 MΩ-cm). All the brines were prepared with 30 ppm of Na_2SO_3 as oxygen scavenger.

7.1.3 Foam study with oil recovery using "Surfactants-ratio salinity-ratio" maps, to select injection conditions for high recovery (i.e. Phase behavior and core floods in foaming systems).

7.1.3 a Oil recovery with co-injection of surfactant and nitrogen.

Seven core floods were run to evaluate the surfactant blend from the foaming point of view. The conditions of the injection were selected at different conditions of salinity, and different surfactant ratios, and the injection compositions are in figures 7-4 and 7-14. The total surfactant concentration during the seven tests was 0.5%, and the salinity ranged from sea water to formation brine.

The potential of the surfactant blend to recover oil was indirectly analyzed using phase behavior with surfactant blend scans, but the effectiveness was analyzed with some gravity drainage-imbibition cell experiments described later.

To conduct experiments with foam in presence of crude oil, the phase behavior was needed to select the conditions required to potentially recover oil and to study the transport of phases.

Four different surfactant blend scans at different proportions of seawater-formation brine ratio were prepared with 1:1 (v/v) water oil ratio by the ***Research Scientist Maura Puerto*** to identify the transition zone from lower phase micro-emulsion to upper phase micro-emulsion. One of them at formation brine is presented in fig 7-4 together with the surfactant blends salinity map at 94°C. The injection conditions (salinity and surfactants ratio) of the surfactant aqueous solutions are included in the same figure. Most of the injection conditions were under optimum (i.e. lower phase micro-emulsion), expecting to be close to optimal conditions once the surfactant mixes with the formation brine present in the porous media. Test “6” was closer to optimum conditions, and this core flood

was the one with the earliest oil recovery. Test “3” was injected at over optimum conditions, to see the effect of this condition in a foaming system.

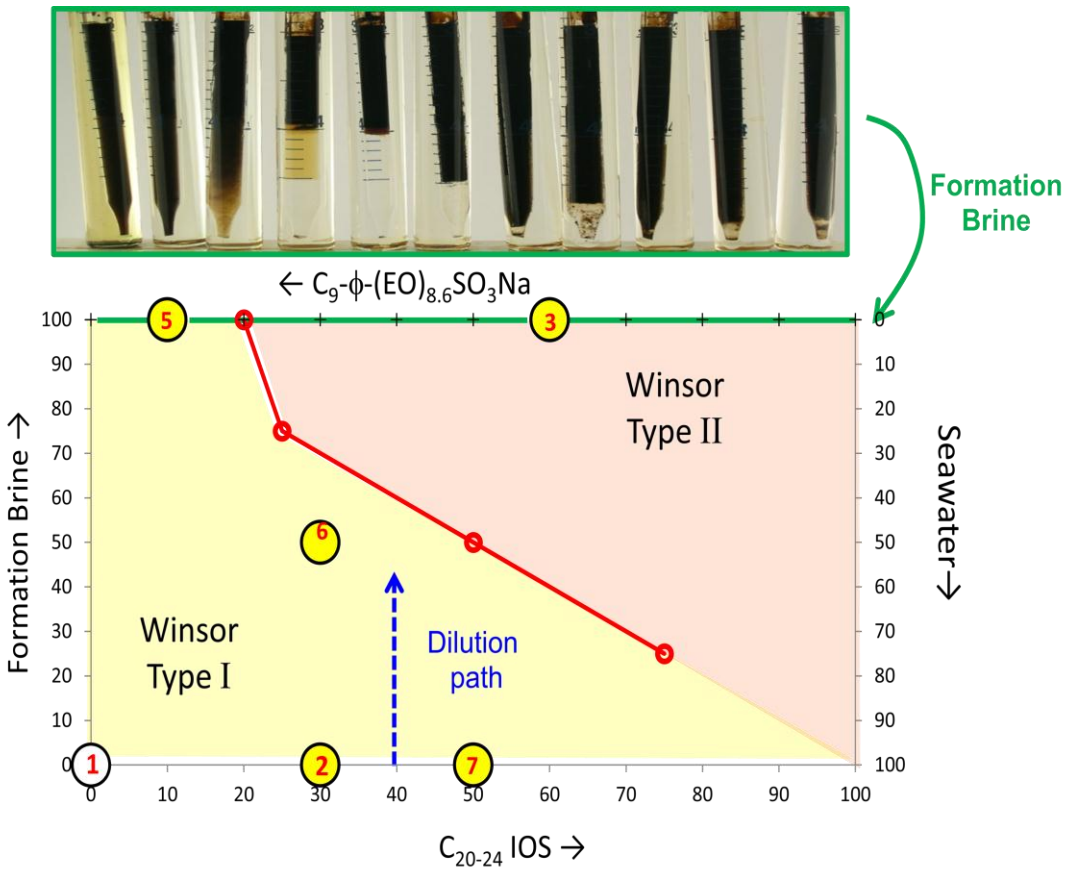

Figure 7-4 Phase behavior map, and graphic representation of the dilution path for foam experiments. The initial proportions of injected surfactant solutions are coordinates labeled with numbers, representing the test number. Proportions of brines and surfactants are in mass ratio.

In the abscissa of fig 7-4 the percentage of IOS in the surfactant blend is indicated; the complement is the Alkyl aryl ethoxylated sulfonate. On the left ordinate is the proportion of formation brine in the formulation; the complement is seawater, which can be read in the right ordinate in reverse order. The core flood experiments were conducted for initial conditions of formation brine, so the

direction of the dilution path is indicated in the figure going from bottom to top in all the cases.

This surfactant blend was used to obtain phase behavior but using simulated live crude oil (i.e. a blend of dead crude oil and cyclohexane as described in chapter 3); this simulated live oil is the oil used in the core floods. The resulting phase behavior can be summarized in fig 7-4.

The plot 7-4 is best estimate of optimal salinity based on the available samples. Optimal blend for formation brine is between 20 and 30% of C_{20-24}IOS as indicated in figure 7-4.

During experiments, the sand pack was initially under residual oil and formation brine, and the surfactant was injected at different salinities and different proportions of the surfactants in the blend. Fig 7-4 is a representation of conditions of injection phase behavior. The direction of the dilution paths can be visualized in the same figure, going from injection salinity to formation brine.

Tests “2”, “5”, “6” and “7” were injected at under optimum conditions, but for Test “3” the injection was over optimum. In the cases when the formulation was injected in Type I going towards dilution to Type II the oil recovery was high. For the case of Test “6”, which was close to transition Type I to Type II, the oil recovery started in an early fashion. The oil recovery during the different tests are summarized in fig 7-5.

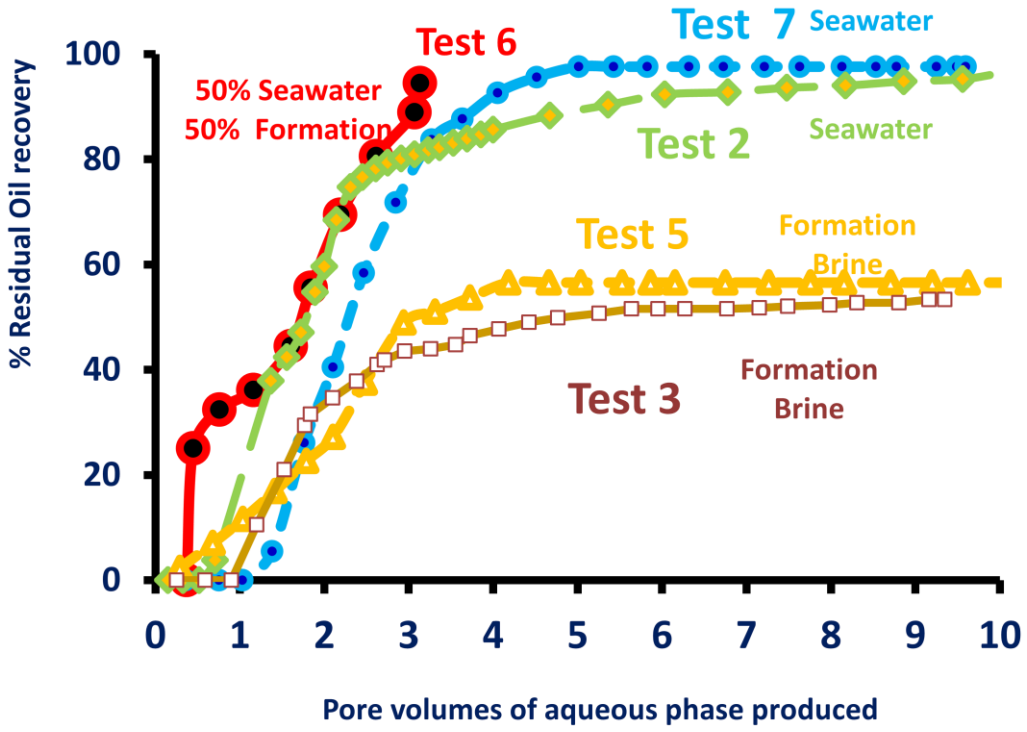

Figure 7-5 Oil recovery for different tests. Different foam tests were designed to conduct core floods, and measure oil recovery, and to qualify and quantify the foam at those different conditions.

To analyze the results a simplifying Capillary Desaturation Curve (CDC) can be used. The curves can be constructed using the UTCHEM mathematical model for CDC, or the model presented in the Appendix 7C, and the parameters for the model can be the fit of the curves presented by Stegemeier (1974) for non-wetting oil, and for wetting oil data from Anderson (2006). Fig 7-6 shows the point "A" which represents the conditions at the beginning of the experiment at actual flowing conditions; points B, B' and B" are the desirable values to achieve 95% of recovery of the residual oil for different scenarios presented in table 7-3.

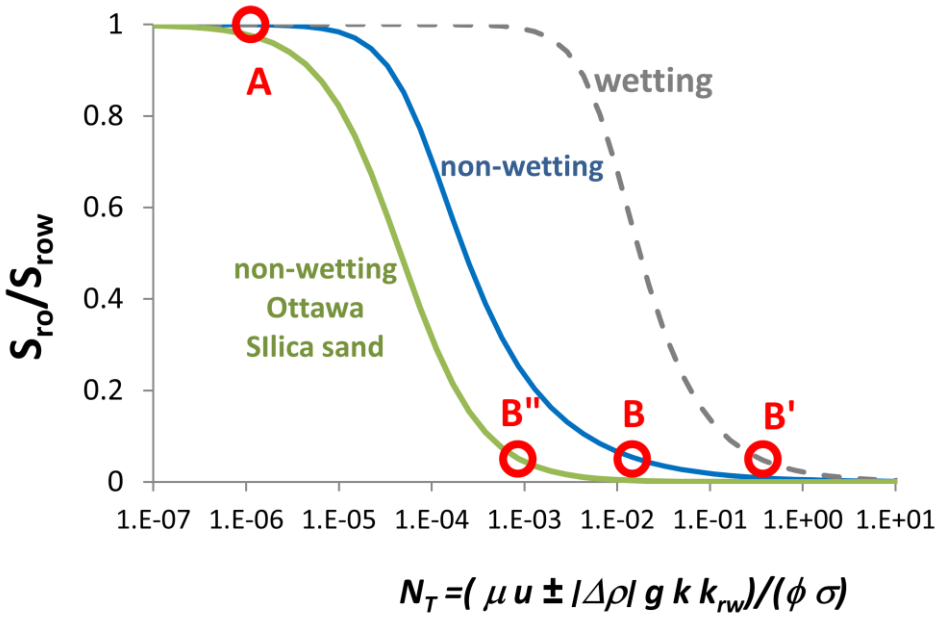

Figure 7-6 Capillary desaturation curves for the three scenarios presented in table 7-2. S_{or} is the residual oil, S_{row} the residual oil after water flood, and N_T is the trapping number. Positive sign is used for upward flow with aqueous phase, and negative for upward foam less dense than oil. Wetting means oil wet, and non-wetting is water wet. B stands for Berea sandstone, B' are different synthetic materials and B" is Ottawa Silica sand.

There are different ways to recover the residual oil according to the relationship between trapping number and the recovery of residual phase, this relationship can be observed in a CDC, like fig 7-6. One approach is the increase the flow rate, which is impractical because of the high pressure gradient and flow rate required. Another approach is to increase viscosity of the displacing fluid which may not be practical to apply if the expected permeability is low, because the required pressure gradient is high. A third approach is to decrease IFT.

The values of the pressure gradient, brine flow rate, viscosity or IFT required to recover oil according with the scenarios previously defined and with the aid of the relationship presented in fig 7-6 are in table 7-3

The trapping number is the vectorial sum of **capillary number** and the **capillary Bond number,** taking the direction of the average velocity for capillary number and the direction of gravity for capillary Bond number (see Appendix 7C). The dimensionless numbers are defined as:

$$N_{Ca} = \frac{\mu u}{\phi \sigma Cos\theta}$$ **Capillary number** **(Equation 7-1)**

$$N_{Bo} = \frac{\Delta\rho g k k_{rw}}{\phi \sigma Cos\theta}$$ **Capillary Bond number** **(Equation 7-2)**

Note: *Don't confuse* ***Capillary Bond number*** *with* ***Bond number*** *described in Chap.3 and* ***Imbibition-Drainage Bond number*** *represented by* $\mathbf{N_B}$*, defined in section 7.4.*

In equation 7-1 and 7-2, θ is the contact angle measured through the wetting phase. It is conventional to measure contact angles through the denser phase according to Reed and Healy (1984). The "$Cos\theta$" term is not included in some reports, and Sheng (2011) in his chapter 7 includes a table of the different forms to express the capillary number.

For the conditions of the experiment (see fig 7-10) capillary and capillary Bond number have the same order of magnitude (N_{Ca} ~ N_{Bo} ~ $1x10^{-6}$), in both cases $Cos\theta$ ~ 1 was an assumption.

Table 7-3 Conditions needed to recover residual oil for three different scenarios (i.e. a, b and c) and three different Oil-Rock systems (i.e. B, B' and B")

Case →	**Increase of flow rate (a)**		**IFT reduction (b)**	**Viscosity increase (c)**
Oil –Rock system↓	dp/dL (psi/ft)	Superficial velocity (m/s)	IFT Dyne/cm	η cP
Non-wetting (B)	70.4	0.52	$2.3x10^{-3}$	3886.2
Wetting (B')	1800	13.4	$1.0x10^{-4}$	99000
Non-wetting (B")	**4 - 14**	**0.03 – 0.1**	**0.01 - 0.04**	**230 – 770**

Values calculated for 100 darcy, 36% porosity and running core flood at 94°C. For the scenarios (b) and (c) brine flow rate was fixed to 1 cm^3/min. For case (a) and (c) the IFT was fixed to 25 mN/m. For case (a) and (c) the viscosity was 0.3 cP. B" is for Ottawa silica sand.

Table 7-3 illustrates that to recover 95% of the initial residual crude oil a considerable reduction of the IFT is needed. The values reported in table are from three different scenarios, and additional parameters for this kind of calculations can be found in Sheng (2011) and Anderson (2006). The capillary desaturation curves were constructed fitting experimental data reported by Pennell *et al.* (1996) for the Ottawa silica sand, by Gupta and Trushenski (1979) for Berea sandstone cores of non wetting oil, and by Dombrowski and Brownell

(1954) for wetting fluids. Parameters and equations to construct the curves are in the Appendix 7C.

Taking the values for Ottawa silica sand by Sheng (2011) or by Pennell (1996) for calculations of the CDC, a viscosity of 230 cP in the aqueous phase is needed to recover 95% of oil at the same flow rate. If the viscosity and the flow rate were maintained then an IFT reduction to 0.04 dyne/cm is needed to recover the same amount of oil. Another option to recover the residual oil without decreasing IFT or increasing viscosity is to use high flow rate or high pressure gradient, then a flow rate of 0.73 dm^3/min or pressure gradient of 4 psi/ft will satisfy the conditions for the same recovery.

From the previous analysis aided by the CDC curves, and from the ranges of flow rates and pressure drops measured in the tests, high oil recover resulted from having low IFT. Interfacial tensions in the range from 0.01 – 0.04 mN/m, corresponds to a solubilization parameter between 3-6 using the Huh correlation. The parameters “C” from the Huh correlation ranges between 0.34 and 0.48 for surfactants like ethoxylated alkyl phenols, AOS and Alkyl benzene sulfonates as reported by Sheng (2011). These values of solubilization are consistent with values observed in the phase behavior conducted by *Maura Puerto (2011)*.

The parameters appropriated to construct the CDC curve may be those for Ottawa Silica Sand, which is the sand used in our experiments, but the crude oil used in the experiments at first glance produced a mixed wet system (additional

wetting properties of the simulated live crude were reported in chapter 2). For this reason the other two scenarios were presented as well.

7.1.3 b Particular observations related to some core floods.

The experiments with low residual oil recovery of about 50% as shown in fig 7-5 can be understood as cases where formulations were far from optimum throughout the whole experiment.

The possibility of viscous emulsions and precipitation of asphaltenes during the core flood test “3” was confirmed from the appearance of the sand after the experiments. See fig 7-7 and 7-8.

a b

Figure 7-7 Sample a) is silica sand after test ”2” and sample b) shows the silica after test “3”.

The dark material present in the sand after the experiment was not soluble ether in IPA or heptane, but soluble in toluene, supporting the possibility of asphaltene precipitation or deposition.

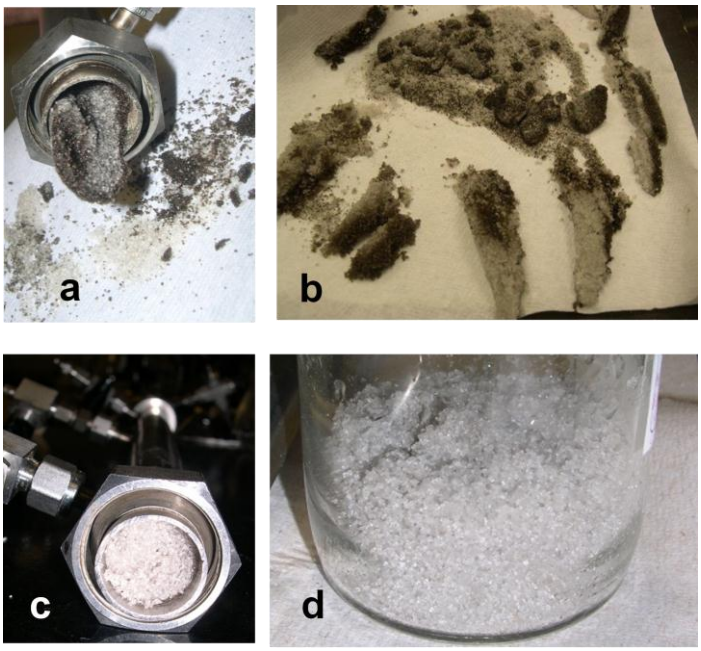

Figure 7-8 a) and b) Indicates how surfactant solution was cleaning the center of the sand pack but not portion of sand close to the walls of the column, material which was "wax-like" at the end of the core flood. Fig c) and d) are pictures of the sand pack at the end of the test "6"

Then the salinity and surfactant blend map is a robust tool to study systematically the transport of phases in EOR applications.

Two of the experiments are described in more detail, test "6" and test "7". During those experiments all the crude oil was produced at tested conditions, but several pore volumes were required to complete the recovery.

For the test "6" the injection composition was close to optimal conditions, as indicated in fig 7-4. Oil production started almost immediately after injection of surfactant solution. The sequence of fluids injected during the experiment, after having the system initially at residual oil saturation at 94ºC is listed below, see

upper picture of fig 7-10. For details about initial conditions of sand pack see table 7-4.

- From 0 PV to 0.35 PV, the injection was only brine at 0.5 cm^3/min of flow rate.
- After 0.35 PV of the injection of the brine surfactant at 0.5% was injected at the same salinity and flow rate of the first stage.
- After 0.6 PV of produced liquid, nitrogen was co-injected at 1.5 sccm.
- After 20 PV of produced liquid, the surfactant solution was replaced by brine at the same salinity.

Observations about this test include (see fig 7-9):

- Oil production started early after the injection of the surfactant.
- Surfactant breakthrough occurred close to 1 PV of liquid produced after surfactant injection.
- 2.5 PV of produced liquid after the start of surfactant injection was required in order to recover most of the crude oil.

The main objective was to verify the performance of the foam with this formulation, to know the conditions needed to have strong foam.

The presence of the oil was detrimental for foam strength. It required close to 10 PV of produced liquid for the foam to gain strength, as indicated in fig 7-10. The resulting lack of mobility control was responsible for the abundant mass of surfactant needed to recover most of the oil.

The configuration of flow is unfavorable from the fingering point of view (i.e. injecting foam from bottom to top) if foam is not strong in presence of oil. The criterion for stable displacement has the form indicated in equation 7-3 according to Lake (1989):

$$\left(M^{o}-1\right)U_{x}<\frac{k\,k_{r1}^{0}\left(\rho_{1}-\rho_{2}\right)g\,Sin(\alpha)}{\mu_{1}}$$

Equation (7-3) Criterion for stable displacement

Here the mobility ratio is defined as $M^{o}=\left(\frac{\mu_{2}}{\mu_{1}}\right)\left(\frac{k_{r1}^{0}}{k_{r2}^{0}}\right)$ **Equation (7-4)**

Note: Sub index “1” is for displacing fluid, and “2” for displaced fluid, and “α“ is the dip angle with respect to the horizontal.

If foam is weak, then M^{0} >1, and if foam is injected upward, $g\,\Delta\rho\,Sin\,\alpha$ < 0, then the flow is unconditionally unstable and fingering occurs and excessive surfactant solution will be required to complete the oil recovery. The same behavior was found during test “7”; the foam became strong after 5 PV of liquid produced, once the crude oil was produced, and the strength of the foam rose gradually and homogeneously through the sand pack. This behavior is different from stronger foams discussed later, which have more robustness from the foaming point of view.

Initial conditions of the sand pack during tests “6” and “7” were similar; specific data for the test “7”, are given in table 7-4.

Table 7-4 Initial condition of the porous media for test “6” and “7”

Initial oil saturation	**20%**
20/40 Ottawa Silica sand permeability in brine	133 darcy
Water end point relative permeability	0.24
Oil end point relative permeability	0.65

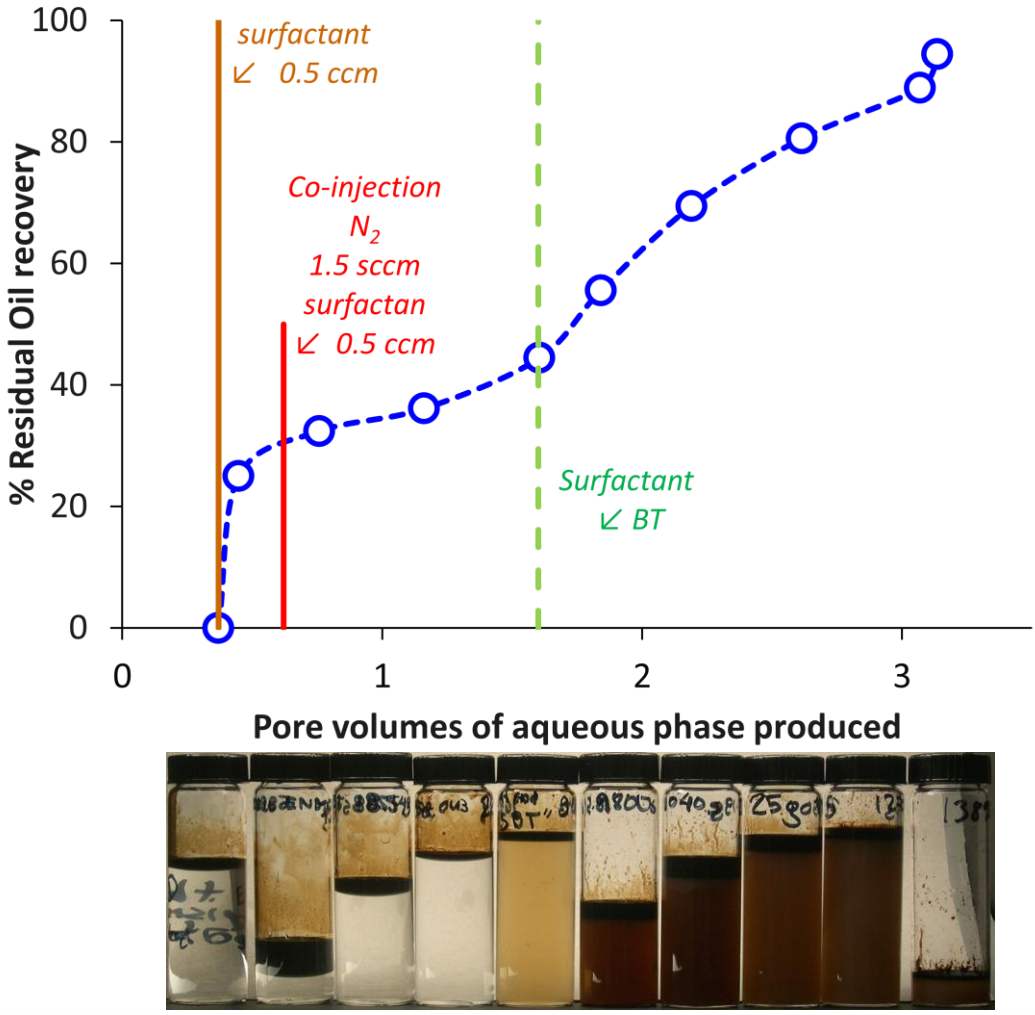

Figure 7-9 Oil recovery during test "6", the corresponding pressure gradient and apparent viscosity are in fig 7-10

The most significant difference between tests "6" and "7" was that the injection composition is close to optimal conditions of salinity in test "6", and an early breakthrough of crude oil was observed. In case of core flood during test "7" the oil breakthrough almost coincides with surfactant breakthrough (indicated by the dark color of solubilized oil in the aqueous phase), as observed in fig 7-11.

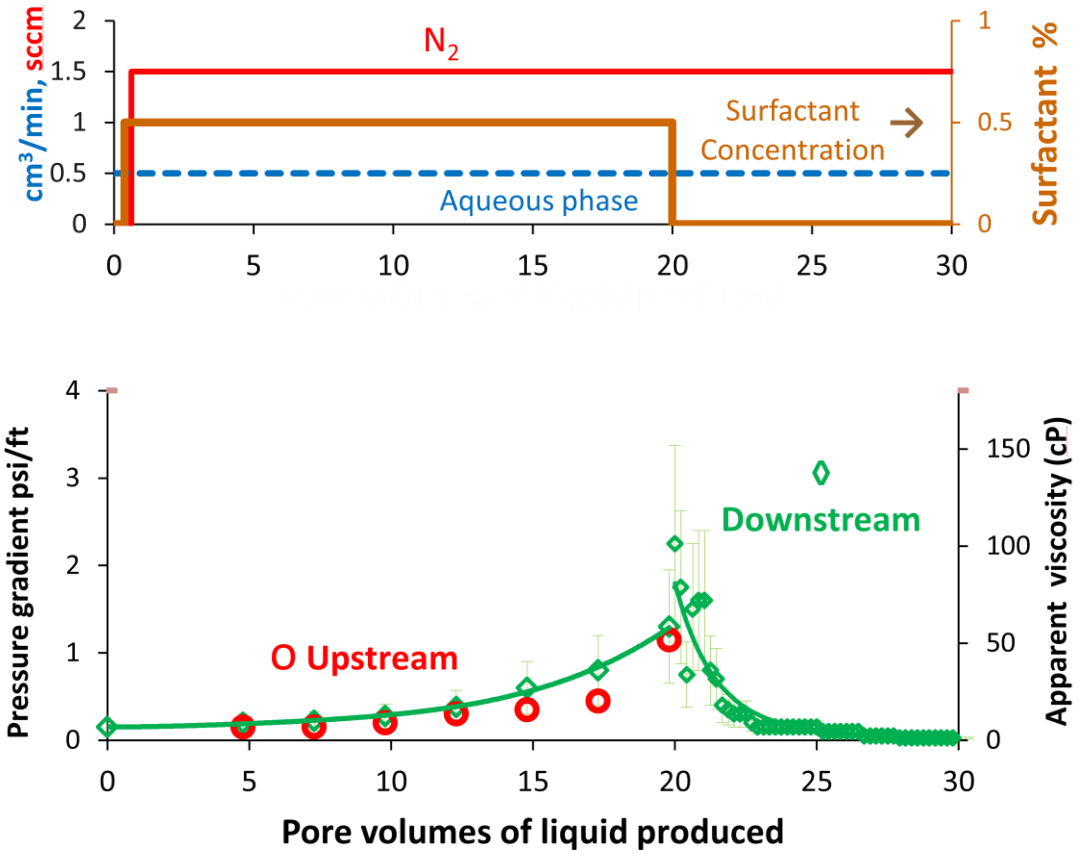

Figure 7-10. Flow sequence in test 6, and pressure gradient in the first half of the column (upstream section), and the second half of the column (downstream). The error bar in the downstream section of the column represents the range of pressure readings during the experiment. The flow direction is upward. During the first 20 liquid pore volumes the superficial velocity was 23 ft/day.

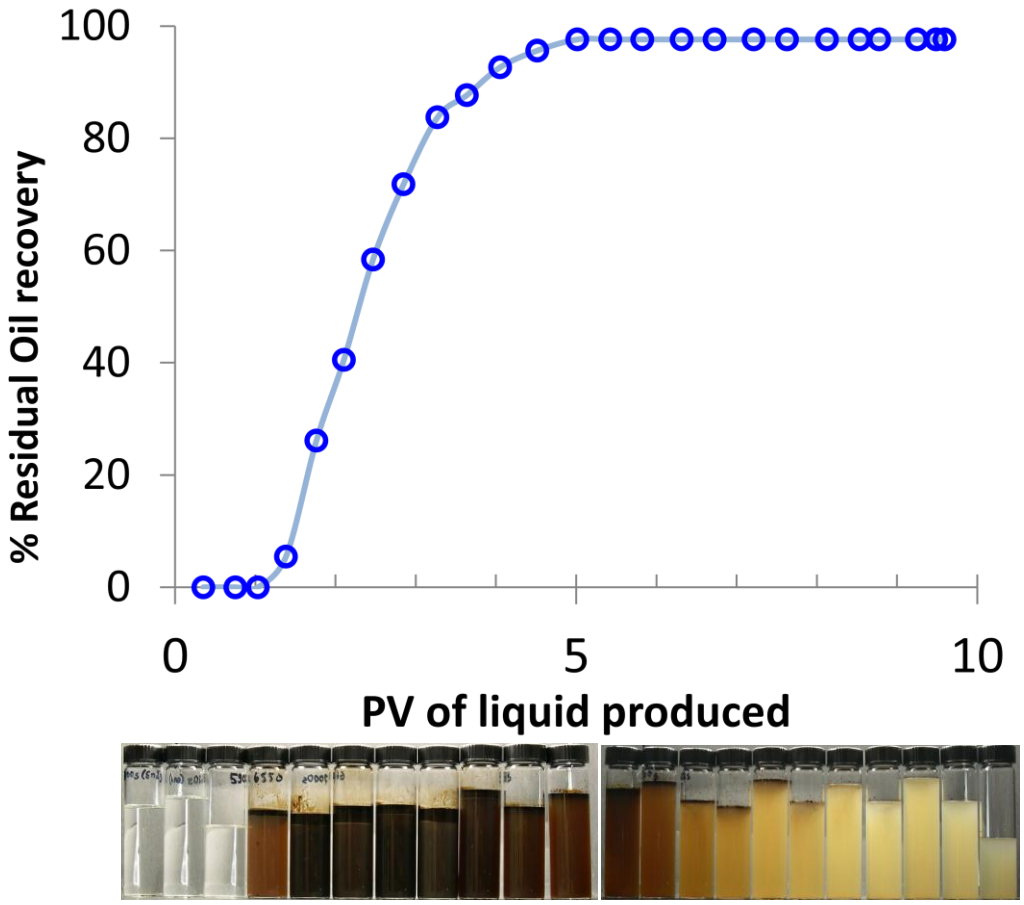

Figure 7-11. During test "7", 3/4 of pore volume of surfactant solution was injected, and then co-injection of surfactant solution and nitrogen were fed as indicated in fig 7-12.

The oil recovery during test "7" began after close to one pore volume of produced liquid, but it took more than 3 pore volumes to recover 95% of the crude oil. One possible reason for the slow recovery is the lack of mobility control during the co-injection of surfactant solution and nitrogen. The co-injected phases began to produce strong foam only once most of the crude was produced, as indicated in fig 7-12. The viscosity of the oil at 94ºC is ca. 3 cP, and the apparent viscosity of the surfactant solution / gas mixture started to increase after 6 pore volumes,

reaching and ultimately substantially exceeding this value. The increase of viscosity was recorded when the superficial velocity was 47 ft/day..

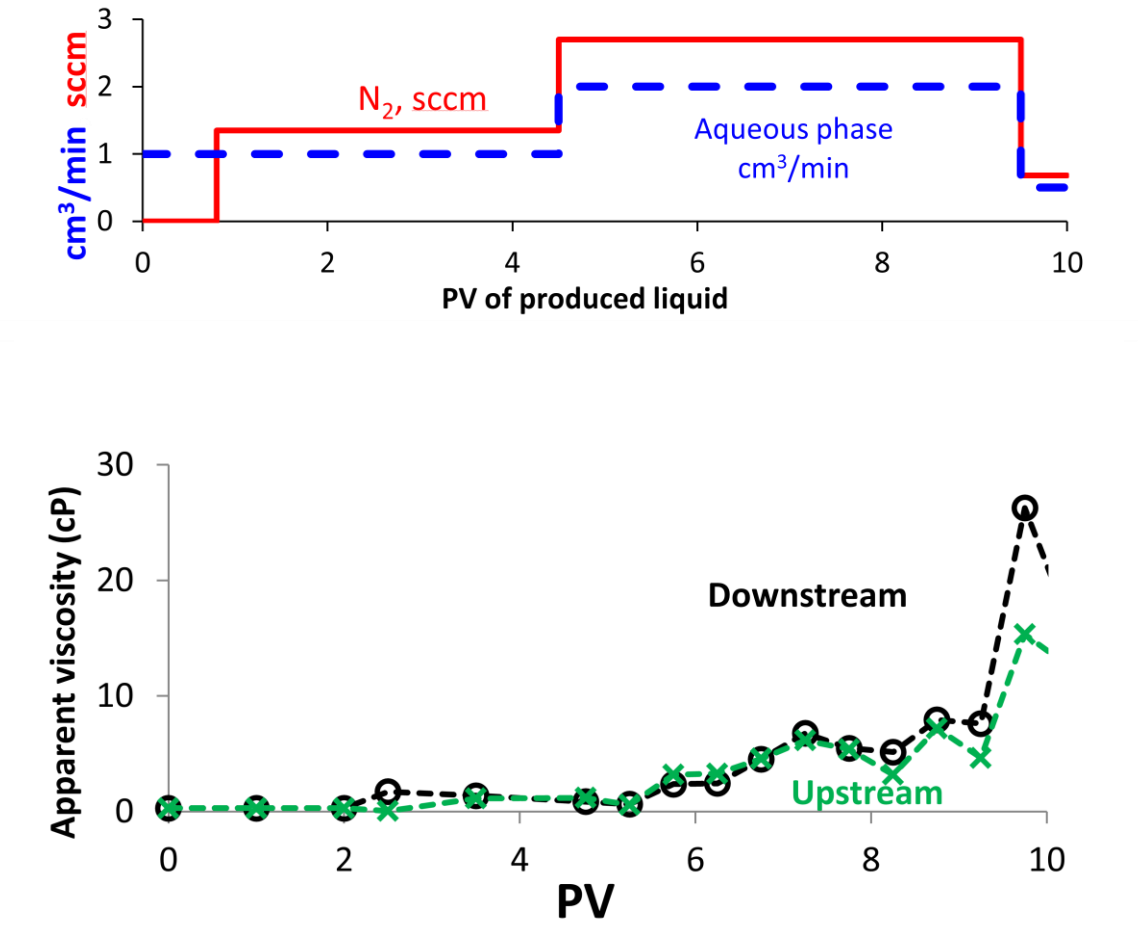

Figure 7-12 Upper plot indicates the sequence of injection of phases during test 7; aqueous phase is surfactant solution at 0.5%. The lower plot is the history of apparent viscosity in the first and second half of the sand pack.

7.1.3c. Foam during oil recovery experiments.

The objective of the experiment was to see the performance of the surfactant solution and the potential to foam. After recovering most of the residual oil, surfactant continued being co-injected with nitrogen to evaluate the strength of the foam at different flow rates at fixed quality. The resulting apparent viscosity at

different flow rates for the test “6” is presented and compared with another surfactant in fig 7-13.

The surfactant blend is compared with a reference case. The reference is a surfactant solution of $C_{16\text{-}18}$AOS prepared in NaCl with the same ionic strength as sea water. $C_{16\text{-}18}$AOS is a good foamer at high temperature, but can’t tolerate divalent ions and will be used as a reference case without adding divalent ions. More details about this AOS are disclosed in the screening of surfactant blends for foaming applications section, presented latter in section 7.2.

During the different tests of core flood, the foam was weak during the initial stages of the experiment when oil was present, once more than 95% of the crude oil was removed, the foam began to develop strength.

The apparent viscosity was calculated using Darcy law, using the absolute brine permeability of the sand pack and the total flow rate. Total flow rate was calculated as the sum of the liquid flow rate and the gas flow rate at injection conditions of pressure and temperature to the sand pack.

$$\mu_{app} = -\frac{k\,A\nabla p}{q}$$

Equation (7-5)

The pressure gradient is assumed to be the pressure drop per unit length between internal taps.

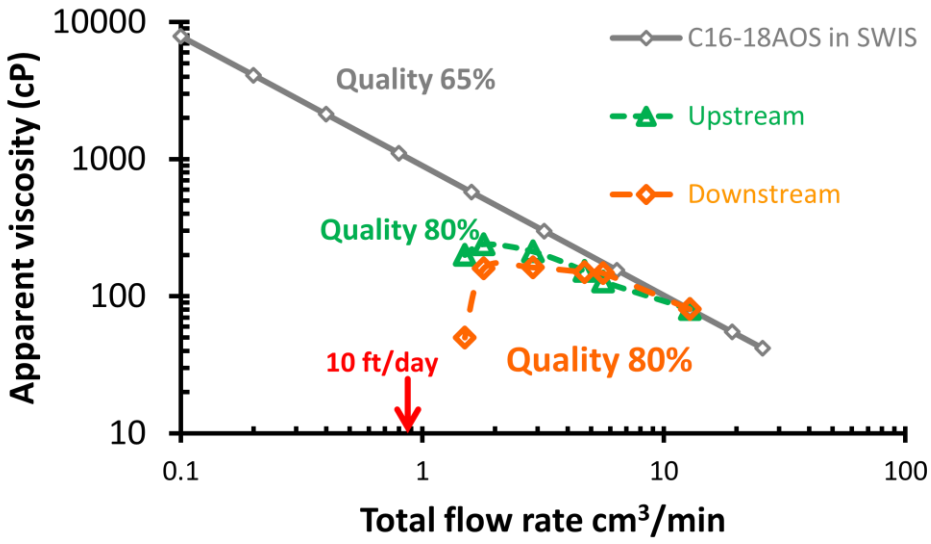

Figure 7-13 The plot corresponds to the mixture of Triton X200 (C_9-ϕ-$(EO)_{8.6}$ SO_3Na) and internal olefin sulfonate C_{20-24}IOS in proportion 70:30 (w/w). The green points are for the upstream section of the sand pack, the orange dots are for the downstream section of the column. Gray line is the benchmark and corresponds to values of apparent viscosity for C_{16-18}AOS, which is an AOS solution in sodium chloride in seawater ionic strength. 1 cm^3/min corresponds to 11.5 ft/day of superficial velocity.

The formulation of Triton X200 and IOS is foaming, but, as shown in fig 7-13, at low flow rates the foam loses strength, shear thinning effect disappears, and foam ultimately is weak at flow rates lower than 1 cm^3/s. The downstream section is weaker than the upstream. This behavior was observed with other similar surfactant blends and may be caused by the increase in quality as the expansion of gas proceeded downstream (see fig 7-15).

Another surfactant system with potential to recover oil was investigated; this surfactant blend was done with an alkyl polyethoxylate sulfonate ($C_{12}(EO)_7SO_3Na$) and IOS (C_{20-24} IOS). Two surfactant blend scans or phase behaviors are included in fig 7-14, which is the "surfactant blend– salinity blend phase map".

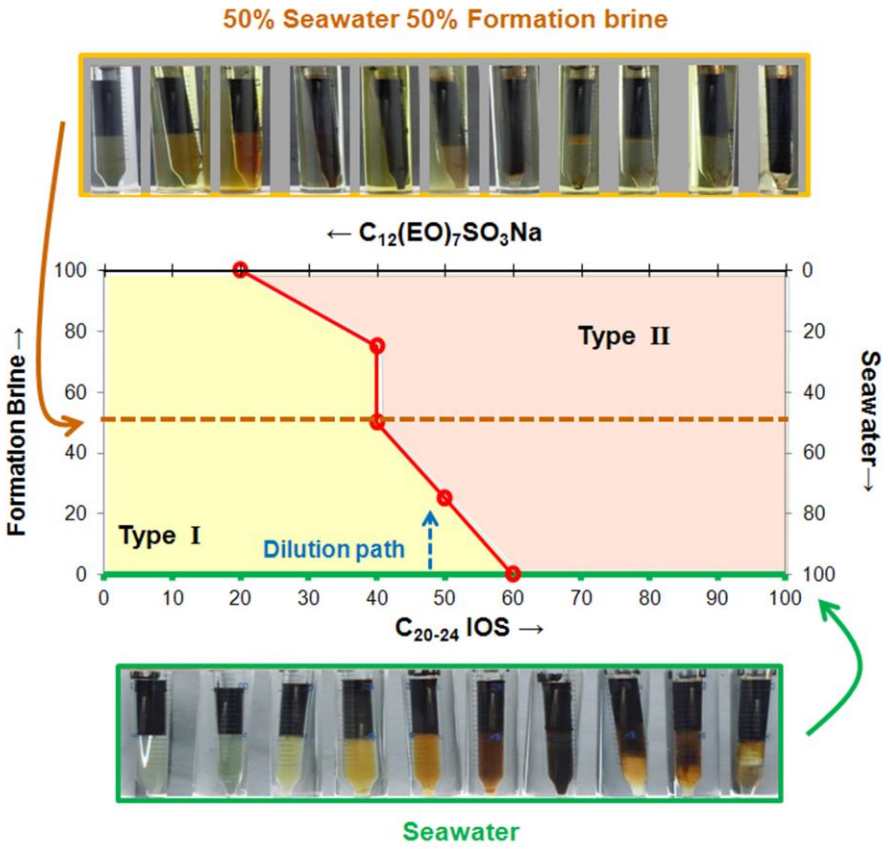

Figure 7-14 Phase behavior map, and snapshots of blend scan for sea water, and for 50% seawater- 50% formation brine.

Using the same method as before, core floods were conducted, though without oil, to evaluate foam for this formulation. Comparative results are shown in fig 7-15.

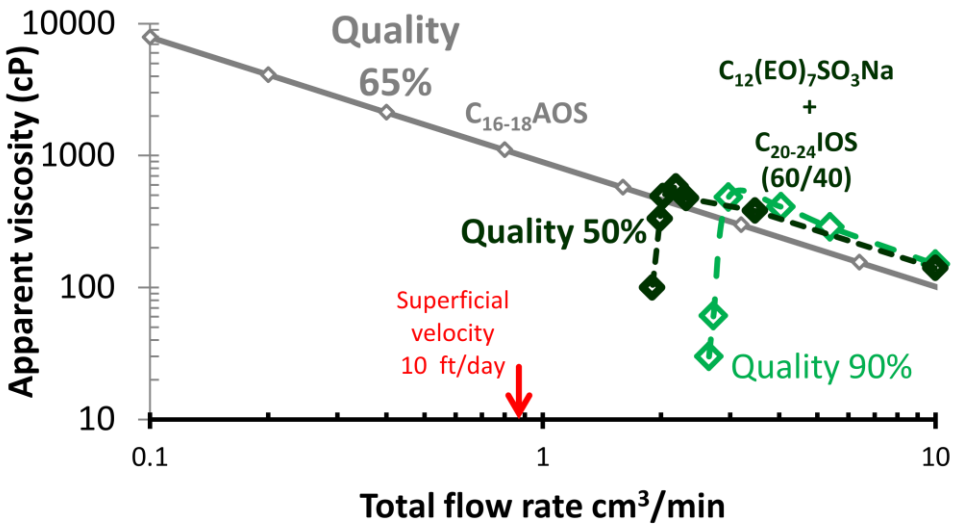

Figure 7-15 Foam apparent viscosity for the $C_{12}(EO)_7SO_3Na$ + C_{20-24} IOS blend (60/40) in sea water. Dark green diamonds are for 50% Quality and light green squares are for 90% quality. The gray line is for C_{16-18} AOS

The use of the $C_{12}(EO)_7SO_3Na$ + C_{20-24} IOS, 60:40 ratio (w/w) in sea water produced strong foam at high flow rates, but the strength started to fall at low flow rates, below 2 cm^3/min. The minimum flow rate for foam generation was higher for the lower quality (50%) foam compared to the higher quality foam (90%). Both sections of the sand pack maintain the same foam viscosity, and the foam with 50% of gas fractional flow will maintain its shear thinning behavior at

lower rate limit than 90% fractional flow foam. More details about foam strength dependence on quality are discussed in the next section.

The system $C_{12}(EO)_7SO_3Na$ + C_{20-24} IOS presented some strength of the foam, but during the start of liquid/gas co-injection the system presented some instability (see Fig. 7-16), and the propagation of the foam was not a sharp piston-like displacement, as seen in the propagation of more robust foaming blends discussed later in section 7. 2..

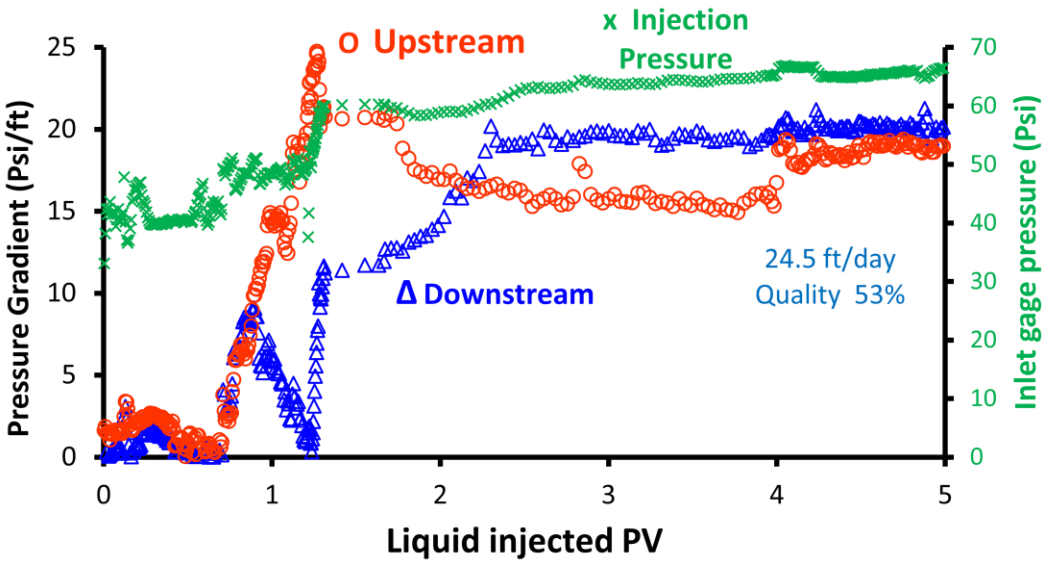

Figure 7-16 Transient of starting a foam experiment, with sand pack initially filled with surfactant solution. Gas flow rate was 5 sccm, liquid flow rate 2.5 cm^3/min for the first 0.75 PV, after that 1 cm^3/min. The system was operated flowing upward, the pressure gradient in the first and second half of the sand pack are indicated in the figure, total injection pressure is included as well in the right ordinate. System: $C_{12}(EO)_7SO_3Na$ + C_{20-24} IOS Blend 60:40 (w/w) in seawater. Superficial velocity at steady state was 24.5 ft/day and the foam quality 53%

Figure 7-16 shows the evolution of the pressure gradient and injection pressure in the sand pack once foam started being injected. The figure helps to visualize that the foam was propagating from upstream to downstream. After different operating conditions to obtain the relationship between apparent viscosity and flow rate seen in fig 7-15, a perturbation test was done. To verify the stability of the foam the surfactant solution was cut down for 8 min, then restored, and results are summarized in fig 7-17. It required close to 1 PV of produced liquid to reach steady state, and foam propagated from upstream to downstream reaching the same initial steady state, at these flow conditions.

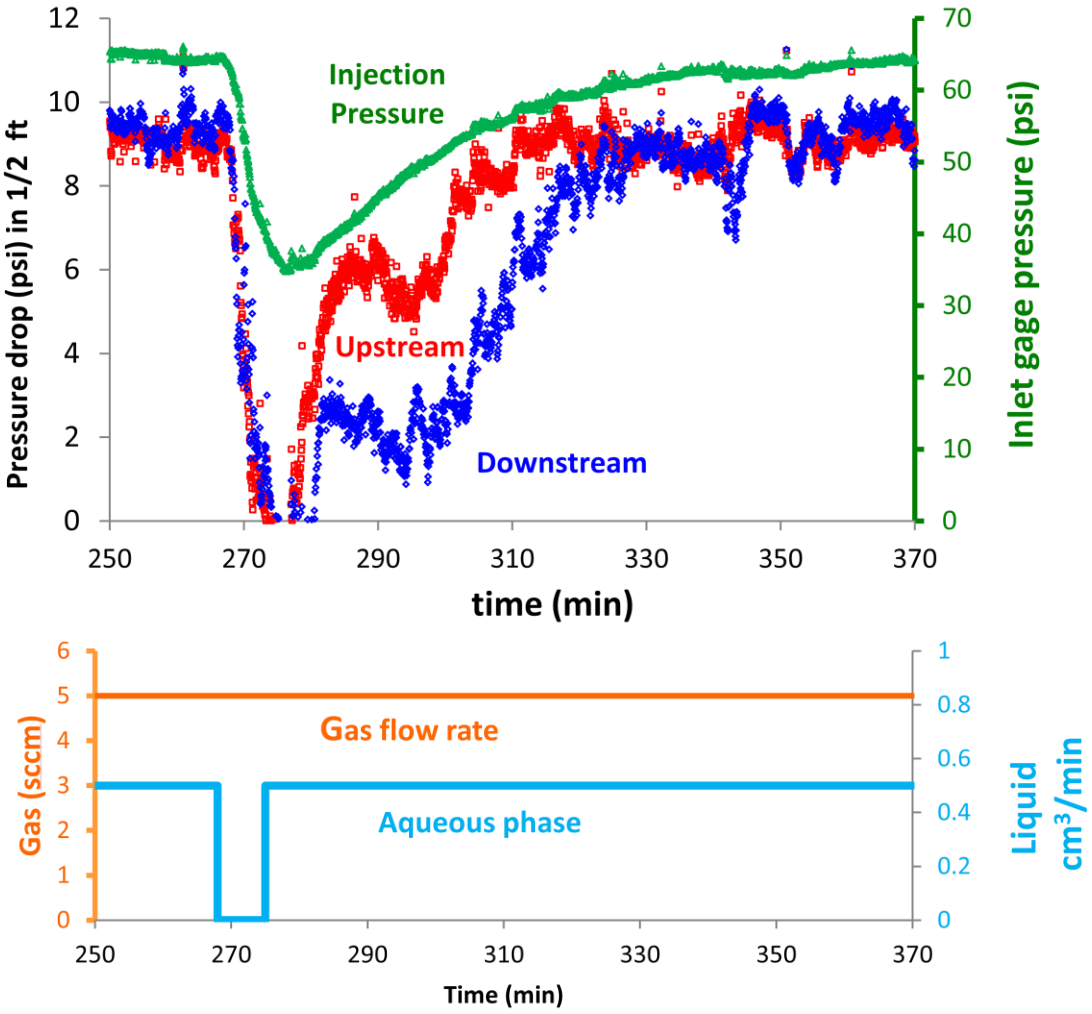

Figure 7-17 Pressure drop response during flow rate perturbation for the aqueous phase. 1 Liquid PV = 116 min @ 0.5 cm^3/min. After reaching steady state the aqueous phase was shut down for 8 min, and then resumed. System: $C_{12}(EO)_7SO_3Na$ + C_{20-24} IOS Blend 60:40 (w/w) in seawater. Steady state was reached with a superficial velocity of 21 ft/day and 73% quality.

These first two surfactant blends studied (i.e., C_9-ϕ-$(EO)_{8.6}$ SO_3Na + C_{20-24}IOS and $C_{12}(EO)_7SO_3Na$ + C_{20-24} IOS) showed high potential for recovering oil from the phase behavior, and some foaming properties which would improve mobility control, but their study was not considered in future tests because they were not

foaming at low flow rates (i.e. superficial velocity of 1 cm/min ~ 47.2 ft/day), they were sensitive to presence of oil, and they had limited commercial availability.

Other surfactant blends composed of alkyl polyethoxylated carboxylates listed in fig 7-1 with potential to recover oil were also tested, but had poor foaming behavior, see fig 7-18.

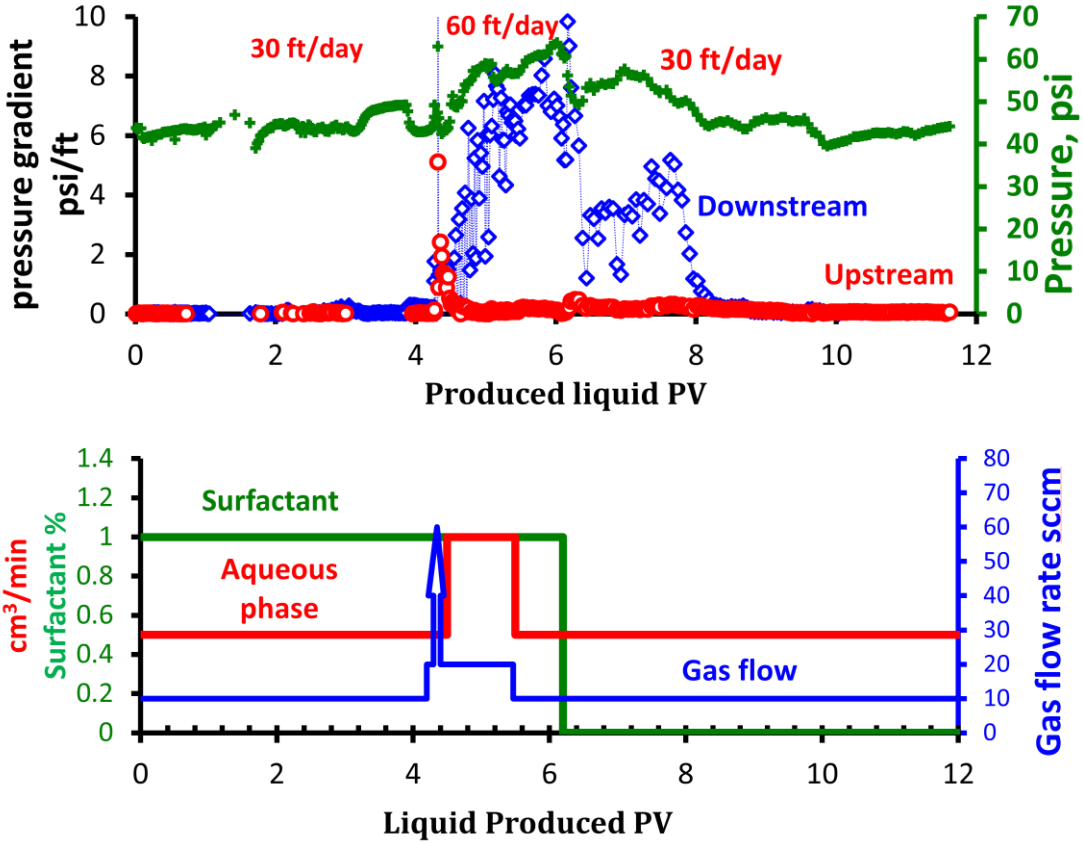

Figure 7-18 Transient of starting a foam experiment, with sand pack initially filled with surfactant solution. The system was operated flowing upward, the pressure gradient in the first and second half of the sand pack are indicated in the figure, total injection pressure is included as well in the right ordinate. System: $C_{28}H_{57}$ $(PO)_{25}(EO)_{25}CO_2Na$ + $C_{15\text{-}18}$ IOS in seawater

The system $C_{28}H_{57}$ $(PO)_{25}(EO)_{25}CO_2Na$ + $C_{15\text{-}18}$ IOS was not a good foamer, and required a big increase gas flow rate for short period of time to generate a pressure gradient in order to make it foam as can be seen in fig 7-18. After spiking (i.e. injecting a pulse of gas) the foam was propagated even at low flow rates, but the foam was only present in the downstream section of the column. Negligible pressure drop was detected in the first half of the sand pack.

Test results for the foam-flow behavior for this blend called UTB are presented in fig 7-18 and table 7-5. It was found that UTB failed to produce foam with the strength sought for the application in the gas-invaded zone of the formation of interest. Phase behavior indicates that the surfactant blend has potential to recover oil, but it should be improved to incorporate foaming behavior, using additives or secondary surfactants. The secondary surfactants added to UTB were Lauryl Betaine (LB), and Lauryl hydroxyl sultaine (LHS), well known foam boosters with hydrolytic stability and tolerant to divalent ions, as reported by Holmberg (2002).

Aqueous stability scan tests were performed for these secondary surfactants mixed with UTB, and reported in Appendix 7D. UTB with zwitterionics (LB and LHS) was prepared to evaluate foaming but the range of application is limited because of aqueous stability. Results in table 7-5 of foam strength in porous media for UTB and for UTB with added LB or LHS indicated that foam strength is limited.

The only combination of surfactants with potential to produce foam in the upstream section of the sand pack was that of test “9d”, which was done with a blend of surfactants in 70540 ppm of TDS at 1% total surfactant concentration using a mass ratio of UTB to LHS of 85 to 15.

Table 7-5 Comparison of foam strength for surfactant blends of $C_{28}H_{57}$ $(PO)_{25}(EO)_{25}CO_2Na$ + C_{15-18} IOS adding foam boosters LB and LHS, test 8 is included as a reference.

Test	Surfactant	Brine	Apparent viscosity , cP	
			Downstream	Upstream
8	C_{20-24}IOS/Avanel S-70	Seawater	500	500
9 a	UTB	Seawater	250	< 5
9 b	UT/LHS (85/15)	Seawater	350	< 5
9 c	UTB/LB (50/50)	Seawater	500	< 5
9 d	UTB/LHS(85/15)	UT Brine	600	150
9 e	UTB/LHS (90/10)	UT Brine	600	<5
9 f	UTB	UT Brine	< 5	< 5

Apparent viscosities reported at 1 cm^3/min of liquid flow rate, and a volumetric gas quality between 40 and 50%. The $PO)_{25}(EO)_{25}CO_2Na$ + C_{15-18} IOS blend is called UTB. UT Brine contains 70450 ppm TDS.

UT Brine was proposed by UT Austin using 50% brine having twice concentration of seawater, 27.5% formation brine and 22.5% DI water. This 70450 ppm TDS is near optimal salinity for the surfactant UTB in simulated live oil with 30% of cyclohexane in dead Akal oil. This combination of brines is impractical from the process point of view, see Appendix 7F for comparison of the brines.

Avanel S-70 = $C_{12}(EO)_7SO_3Na$

This UTB surfactant was not considered for additional foam tests because of its low foaming potential in seawater. Additional tests for oil recovery using UTB in a specially designed foaming imbibition cell will be presented later.

7.2 Screening of surfactant blends to produce strong foams.

A systematic study to find strong foaming formulations was required with several objectives in mind:

- Collect experimental data of foaming systems at reservoir temperature and seawater brine composition to fit parameters for foam models to be used in computational simulators to predict the transport of foam in porous media (e.g. fractured vuggy reservoir).
- Find a robust formulation, stable at reservoir temperature (i.e. at least up to 100°C), able to produce strong foam; reduce IFT and/or change wettability, and tolerant to divalent ions.
- Obtain a formulation to study some capillary phenomena in micro channels for understanding the mechanisms of transport of phases between fractures and matrix.

Taking into consideration listed requirements, and under literature review about surfactant properties, three families of surfactants were selected for the study, and one additional blend called IMP surfactant blend was evaluated as well.

The IMP surfactant blend contains a combination of surfactants of the homologous series from the families of surfactants studied in this work.

Many of the surfactant blends studied included a zwitterionic surfactant (e.g., betaine or sultaine) because they are known to have capabilities of strengthening conventional foams.

The same apparatus designed for this research fig 7-3 was used during the various experiments. Minor alterations of the experimental setup were required to evaluate the performance of foam in presence of oil, and to verify stability of foam flowing upward or downward.

The surfactants studied are listed in table 7-6, information about manufacturers and activities can be found in the Appendix 7A.

7.2.1 Surfactants used in the foam screening process.

Table 7-6 Surfactants used for screen surfactants blends for foaming in sea water and 94°C (Additional information about surfactants is found in the appendix 7A)

Surfactant	Formula	Notes
LHS	$[CH_3(CH_2)_{11}][CH_3]_2N^{(+)}CH_2CH[OH]CH_2SO_3^{(-)}$	MM=351.54
LB	$[CH_3(CH_2)_{11}][CH_3]_2N^{(+)}CH_2COO^{(-)}$	72.7% C_{12} , 27.5 % C_{14} MM= 279.12
CAPB	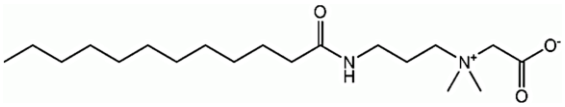	5.8% C_8, 5.6% C_{10} 53.6% C_{12}, 16.8% C_{14} 8.2% C_{16}, 10.1% C_{18} MM= 342.52
C_{14}AOS	$CH_3(CH_2)_{14}CH{=}CH_2(SO_3^-Na^+)$ $CH_3(CH_2)_{14}CH(OH)-CH_2(SO_3^-Na^+)$	MM=298
$C_{16\text{-}18}$AOS		70% Alkene 30% hydroxyl MM=340
$C_{20\text{-}24}$AOS		MM=410
BTC 8358	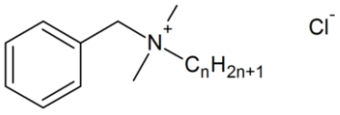	50% C_{14}, 40% C_{12} 10% C_{16} MM=342
DDAB	$[CH_3(CH_2)_{11}]_2[CH_3]_2N^+Br^-$	MM=463
CTAB	$[CH_3(CH_2)_{15}][CH_3]_3N^+Br^-$	MM=364
DTAB	$[CH_3(CH_2)_{11}][CH_3]_3N^+Br^-$	MM=264

The idea of using a combination of the surfactants listed above is:

- Produce clear aqueous surfactant solutions tolerant to divalent ions (Ca^{2+} and Mg^{2+}).
- Transport the surfactant solution as a foam in the fractured reservoir.
- Decrease IFT between crude oil and aqueous phase, or crude oil and microemulsion.
- Alter wettability of the rock.
- Have hydrolytic stability at 100°C.

The use of different kind of surfactants and blends among them was investigated.

1% of overall surfactant solutions in seawater or formation brine in the temperature range from 25°C to 94°C was studied for future application in an EOR process within a fractured, carbonate reservoir.

The first system studied was CAPB with $C_{16\text{-}18}$AOS as pseudo-binary surfactant blend, and then BTC was added to analyze the solubility of the pseudo-ternary surfactant blend. Here the terms pseudo-binary and pseudo-ternary apply to blends of types of surfactant (i.e. anionic, zwitterionic or cationic). In almost all cases each type of surfactant is a blend of species from a homologous series as indicated in table 7-6.

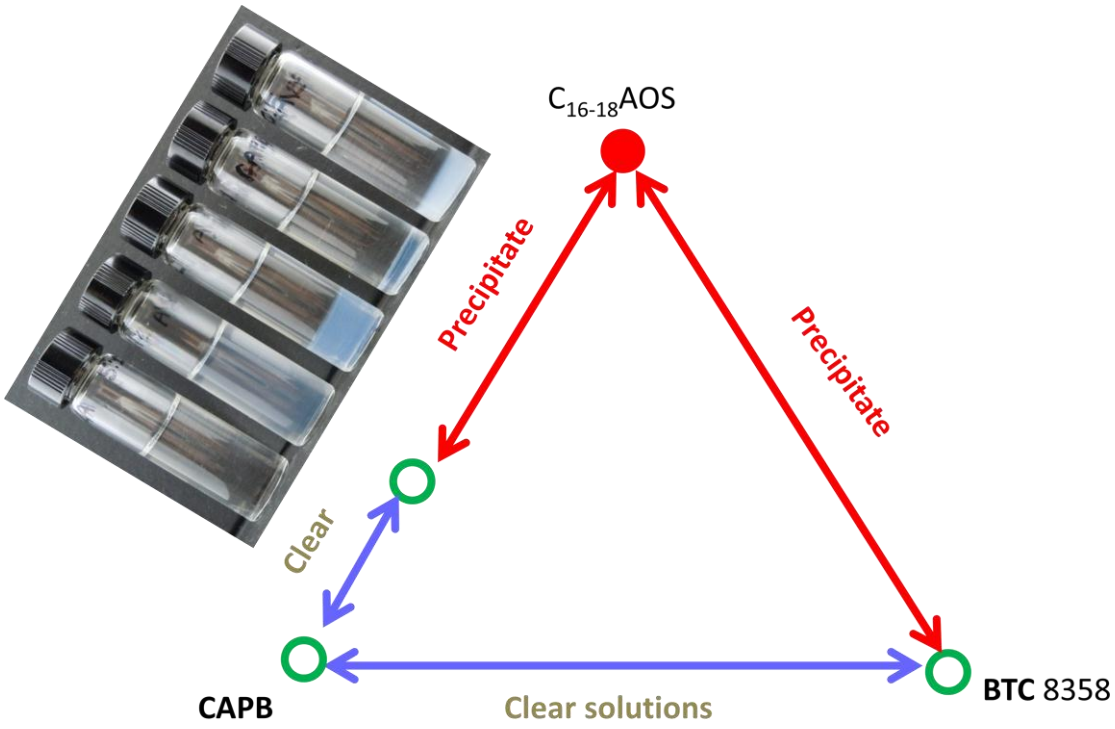

Figure 7-19 Solubility scan at 1% total surfactant concentration in synthetic seawater at 30°C, the trend remains at 94°C

For the pseudo-binary system CAPB - C_{16-18}AOS the solubility scan picture is represented in fig 7-19. The surfactant solution is clear when the mass ratio of CAPB to C_{1618}AOS greater than 2 and cloudy when the ratio is less than 2. The maximum of cloudiness is when the mass ratio is close to 1, this observation was a common phenomena with other anionic surfactants and will be discussed in Appendix 7-D. The solubility map for the pseudo-ternary system is indicated in fig 7-20.

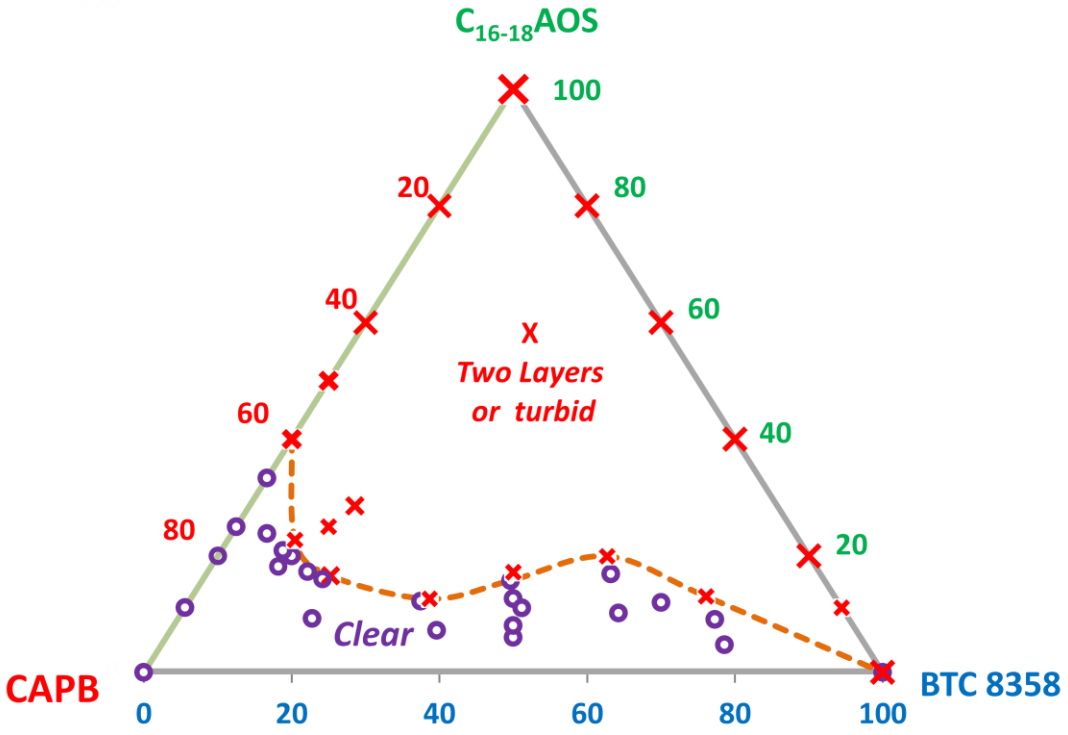

Figure 7-20 Solubility map for 1% total surfactant concentration in synthetic seawater at room temperature.

BTC is a blend of benzalkonium chloride as indicated in table 7-5 and contains 12% ethanol. This pseudo ternary system presented viscoelasticity at room temperature in the clear phase region close to the boundary between clear phase and turbid phase, with decreasing viscosity and viscoelasticity as BTC 8358 was added. A rheogram for the pseudoternary system of surfactants at fixed concentration can be found in chapter 3.

Another pseudo-ternary system studied was LB-AOS-BTC. Lauryl betaine is considerd to have better thermal hydrolytic stability compared to CAPB. Studies of instability of CAPB were reported in chapter 5. The use of lauryl betaine gave a similar solubility map as the CAPB as indicated in fig 7-21.

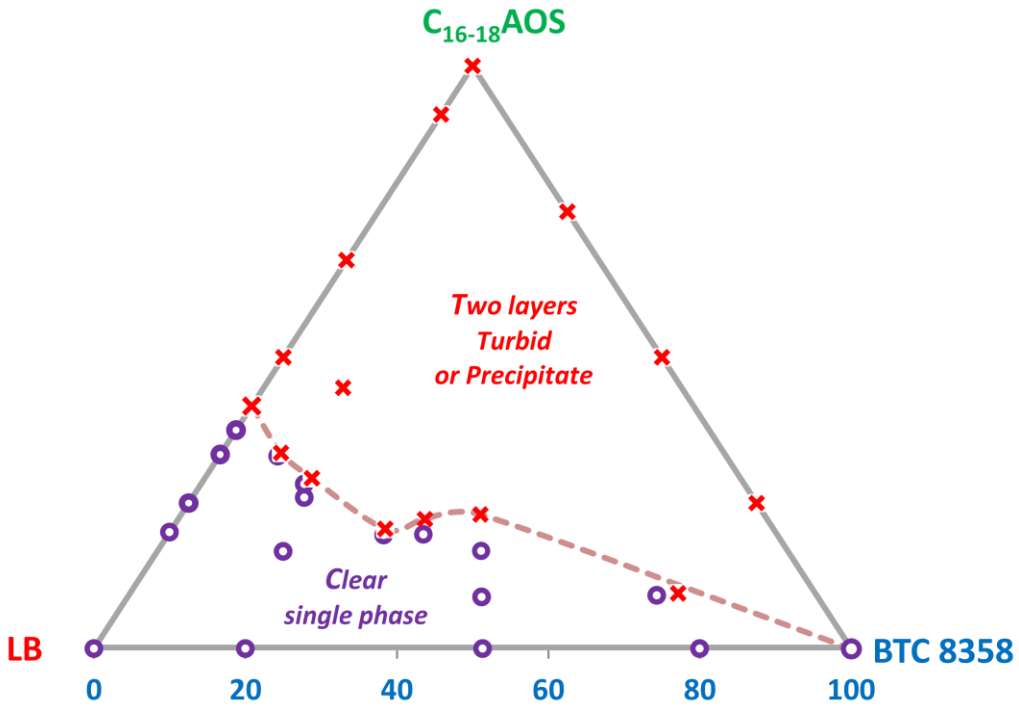

Figure 7-21 Solubility map at room temperature for the pseudo ternary surfactant system. 1% Overall surfactant concentration in synthetic seawater for LB-C_{1618}AOS-BTC.

Solubility scan for lauryl betaine and $C_{16\text{-}18}$AOS in synthetic sea water is included in fig 7-22

% LB	100	80	75	67	63	58	50	33	8	0
%C_{1618}AOS	0	20	25	33	37	42	50	67	93	100

Figure 7-22 Solubility scan at 1% total surfactant concentration in synthetic seawater at 30°C,the trend remains at 94°C

The C_{16-18}AOS by itself was viscoelastic in sea water, but phase separated after 6 h. If dissolved in NaCl Brine at same ionic strength it forms a clear aqueous phase at high temperature, and produces strong foam.

7.2.1.a Anionic-Zwitterionic blends:

Zwitterionic surfactants blended with anionic AOS surfcatnts produced viscoelastic, clear solutions, and produced strong foam. LB and CAPB when mixed with C_{16-18}AOS required ca 2 mass ratio to produce clear solutions, while LHS required 2.75.

Zwitterionic surfactants by themselves produced clear aqueous solutions in seawater, but were not viscoelastic at room temperature and were not able to foam in seawater in the sand pack by themselves at tested conditions.

C_{14}AOS produced similar behavior when mixed with zwitterionics in seawater to C_{16-18}AOS, and is soluble in seawater, but C_{20-24}AOS had solubility problems when salt was present by itself.

Some rheology measurements for these systems were reported in chapter 3

7.2.1.b Zwitterionic-Cationic surfactants:

The only cationic producing clear solutions, foam, and viscoelasticity when mixed with a zwitterionic was DDAB (didodecyldimethyl ammonium bromide). DDAB by itself in seawater is not clear, but solution became clear, viscoelastic and produced strong foam when mass ratio of CAPB to DDAB was greater than 3. Fig 7-23 shows the region of viscoelasticity and foaming capacity.

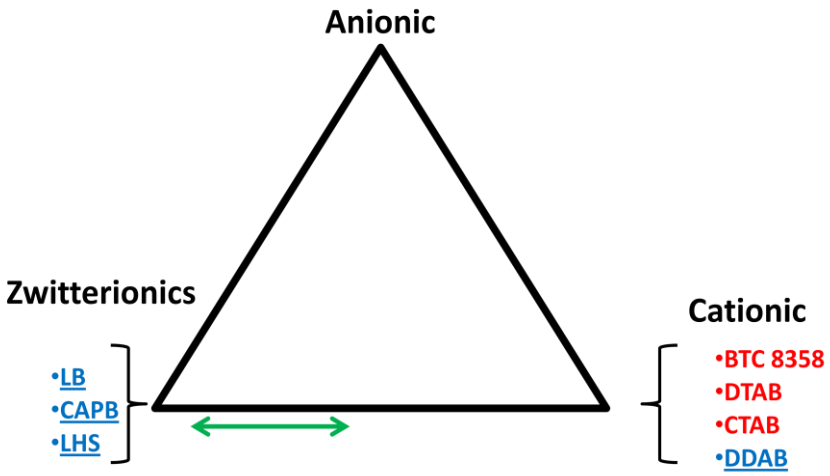

Figure 7-23 Viscoelasticity of cationic-zwitterionic blends. Didodecyldimethylammonium bromide was the only cationic surfactant able to produce viscoelastic solutions when mixed with zwitterionics in the region shown in the map.

CTAB by itself was unable to produce foam or viscoelastic fluid in seawater, but addition of a hydrotrope promoted clear solutions and viscoelasticity. The hydrotropes mixed with CTAB to produce clear and viscoelastic solutions are included in table 7-7.

Table 7-7 Hydrotropes

Name	Formula
Salicylic acid	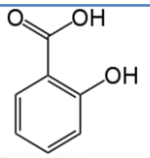
Acetyl salicylic acid	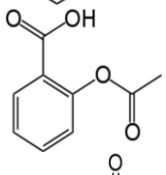
1-Naphtalene acetic acid	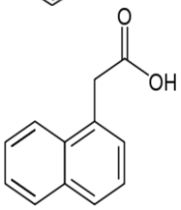
Sodium p-toluenesulfonate	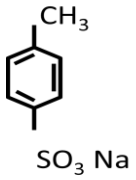
Sodium benzenesulfonate	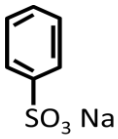

The viscoelastic solution produced by mixing CTAB with NapTS (Sodium para toluene sulfonate) was able to produce foam at 94°C. Non of these hydrotropes produced viscoelasticity when mixed with BTC8358 The use those hydrotropes with BTC 8358 produced precipitation.

All the surfactants blends during foaming tests with surfactants from table 7-5 presented viscosities close to the viscosity of water at 94°C, but were viscoelastic at room temperature. Some rheological properties of these surfactant blends are included and discussed in chapter 3.

7.2.2 Foaming study for C_{16-18}AOS

The first system to be analyzed was C_{16-18}AOS in NaCl brine at seawater ionic strength, and is used as a reference to compare the different formulations from foaming point of view. The evolution of foamstrength for this system is included in fig 7-24.

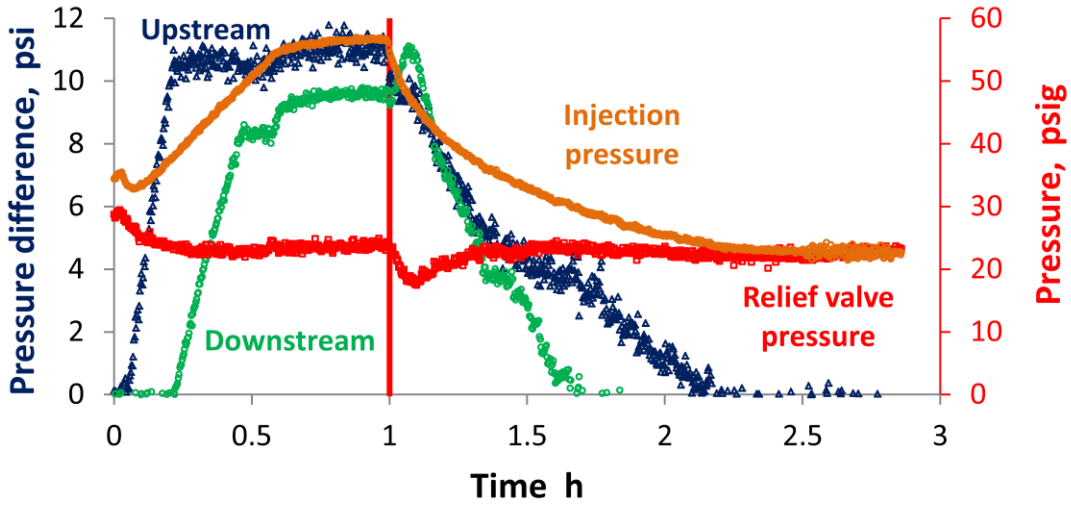

Figure 7-24 Transient of AOS foam. Before starting the co-injection, 0.5 PV of surfactant solution was fed. Co-injection starts at time zero. Injection was 2 cm^3/min of surfactant and 20 sccm of N_2. The foam quality at inlet conditions was 70%. Injection stopped after 1 h, and the system kept producing foam for additional 45 min. 1 PV of liquid injected is equivalent to 0.47 h, total superficial velocity 76 ft/day.
Surfactant: 1% C_{16-18}AOS in NaCl brine at seawater ionic strength.

The foam produced by 1% C_{16-18}AOS in NaCl brine at seawater ionic strength seems more stable than that of fig 7-16 with $C_{12}(EO)_7SO_3Na$ + C_{20-24} IOS Blend 60:40 (w/w) in seawater, and the system kept producing foam, even after injection was

stopped. This was not the case with the previous surfactant blends of alkoxylated sulfonates or carboxylates blended with IOS listed in table 7-1.

The foam apparently propagated with piston like displacement and required close to 1 PV of liquid injected to travel from bottom to top of the sand pack. This behavior seems consistent with studies done by Friedmann *et al.* (1991) reporting more than 85% of the gas within porous media remained trapped.

The foaming system $C_{12}(EO)_7SO_3Na$ + $C_{20\text{-}24}$ IOS Blend 60:40 (w/w) in seawater was not able to maintain strength once the injection of the liquid phase was stopped; the foam lost its strength as indicated in Fig 7-17.

After the first transient study with $C_{16\text{-}18}$AOS, different tests were done to see the effect of flow rate, and the effect of foam quality. A final test to see the effect of the crude oil is included as well.

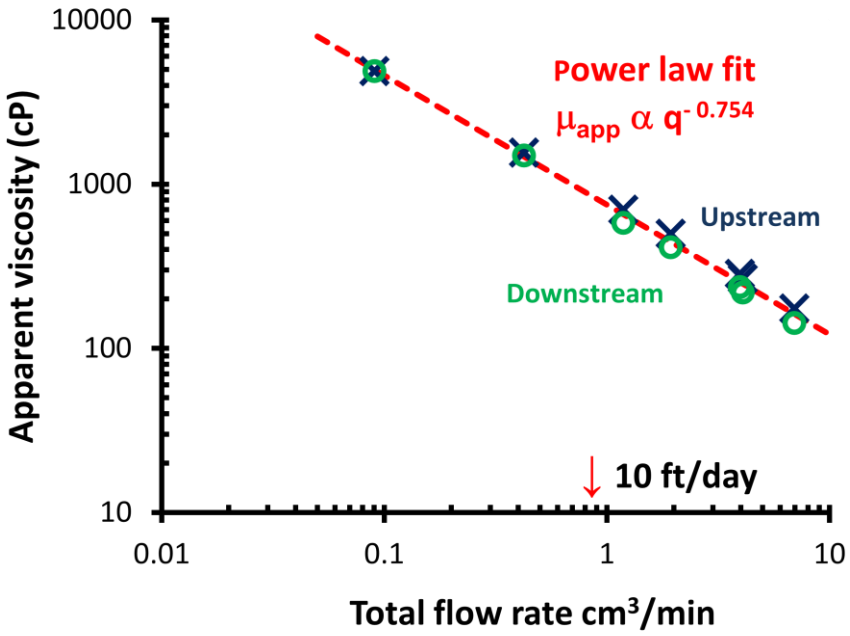

Figure 7-25 Apparent viscosity vs. total flow rate for quality between 0.7 and 0.78 at 94°C, 1% C_{16-18}AOS in NaCl brine at seawater ionic strength.

The behavior of the foam is shear thinning, and the difference between the downstream and upstream section is minimal (fig 7-25). The effect of quality is summarized in fig 7-26 for one total flow rate.

.

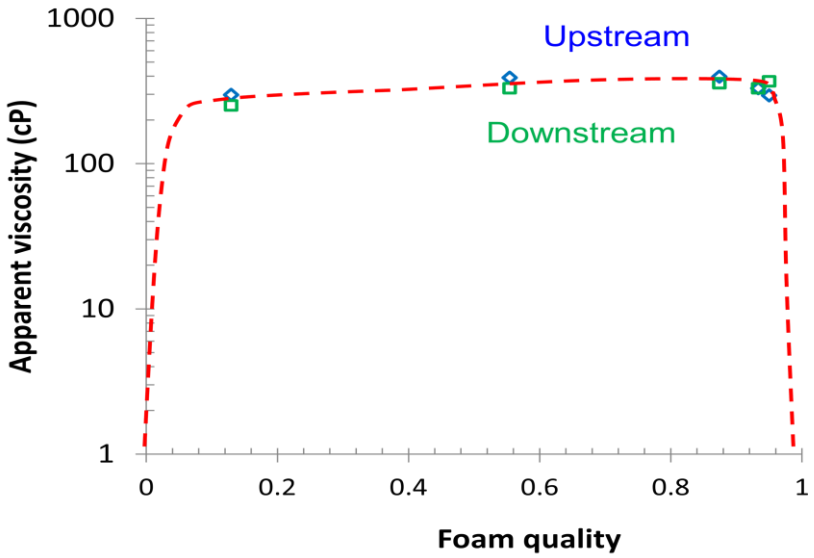

Figure 7-26 Foam quality effect on apparent viscosity at a total flow rate of 3 cm^3/min (superficial velocity 34.5 ft/day) , at 94°C, 1% C_{16-18}AOS in NaCl brine at seawater ionic strength.

The foam of C_{16-18} AOS in NaCl brine is robust in a wide range of quality. Quality may change while contacting the matrix, the aqueous solution will imbibe the rock, and the foam with increased quality will keep strength.

The effect of crude oil was briefly analyzed co-injecting crude oil, once the system was operating under steady state conditions. Crude oil was co-injected with surfactant solution and nitrogen for 25 min with the volumetric ratio of oil to surfactant solution was 1:10. The apparent viscosity of the system decreased but only by about 30% after 0.5 PV was injected. The initial apparent viscosity was restored once the crude oil injection was stopped. It took close to 1 PV of injected surfactant solution to recover its initial value as indicated in fig 7-27

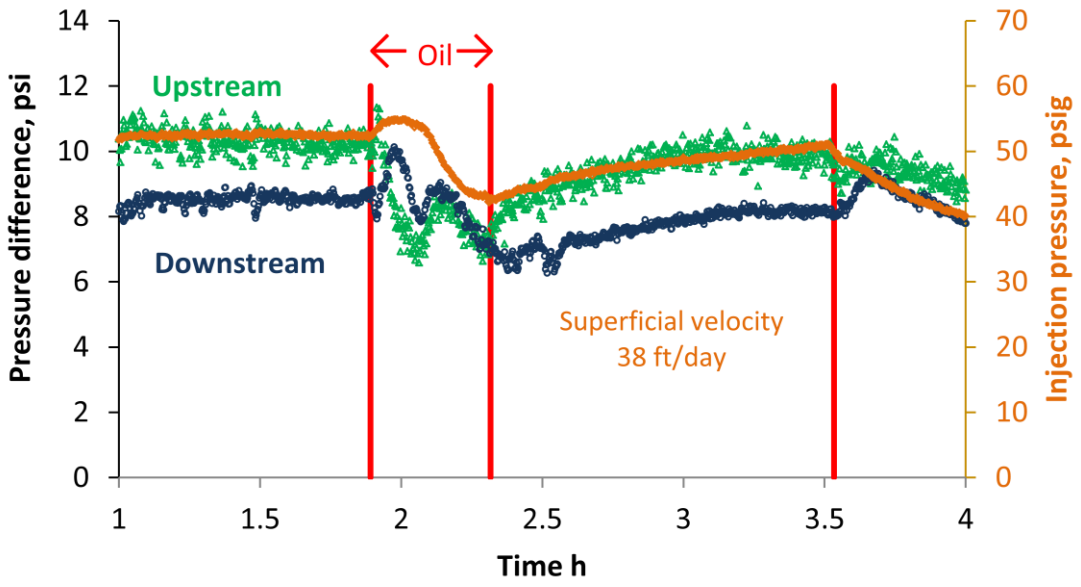

Figure 7-27 The surfactant flow rate was 1 cm^3/min, Nitrogen injection at 10 sccm. Oil injection was at 0.1 cm^3/min for 25 min, as indicated in the figure. After 3.5 h the flow rate was changed to ¼ of the previous.

The same kind of experiments were performed with most of the possible combinations of the surfactants given in table 7-5 which produced clear injectable solutions. Detailed reults will be presented in the next section for some systems, and a table with a summary of foam strength is presented at the end of this section.

7.2.3 Foaming study for LB+C_{16-18}AOS

A start up experiment similar to that described in the previous section was done with a blend LB and C_{16-18}AOS having a mass ratio 2:1 in synthetic seawater. In this case the addition of LB allowed to use the seawater with divalent ions witout any precipitation.

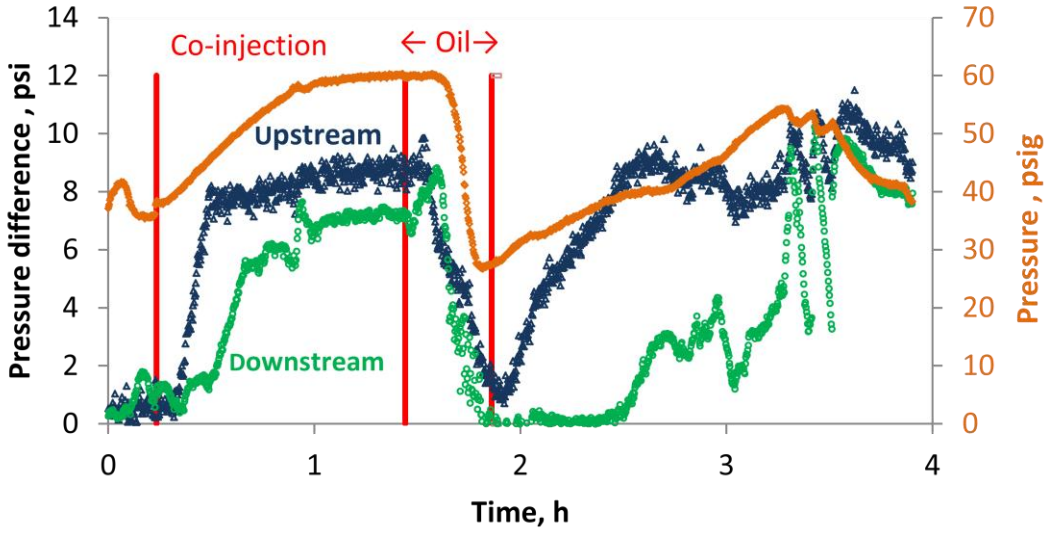

Figure 7-28 The surfactant flow rate was 1 cm^3/min, Nitrogen injection at 10 sccm. Oil injection was at 0.1 cm^3/min for 25 min, as indicated in the figure. Total superficial velocity 38 ft/day. 55 min of injection of liquid is equivalent to 1 PV . System: 1% LB+C_{16-18}AOS, 2:1 (w/w) in synthetic seawater

After different tests to see the effect of flow rate and foam quality the system was shut down, injected with 5 PV of surfactant solution, and then co-injection of nitrogen was resumed. The response is in fig 7-28. Several minutes after reaching steady state oil was injected for 25 min with an oil-to-brine ratio 1:10. During the co-injection of simulated live oil the pressure drop decreased, and the strength of foam was lost, but the strength of the foam began to be recovered once crude oil injection was stopped. For this system LB+AOS took more than 2 PV of liquid injected to reach steady state and recover the earlier apparent viscosity.

The difference between the system AOS and the LB+AOS in presence of oil was that in the case of the AOS, the effluent was a viscous emulsion of the oil, while

in the case of the AOS+LB the produced oil was able to travel through the plateau borders of the foam (fig 7-29). That is, the larger apparent viscosity for AOS during crude oil injection was likely largely due to emulsion formation.

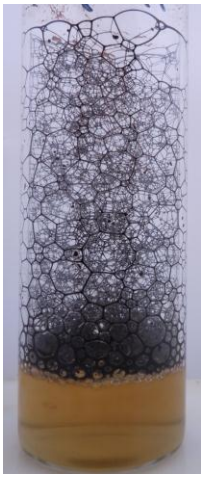

Figure 7-29 Production of oil, collected during co-injection of simulated live oil and foam. Surfactant: 1% LB+C_{16-18}AOS 2:1 (w/w) in seawater

Additional photographs of the oil in the plateau borders are in Appendix 7E.

7.2.4 Comparison of surfactants as foamers

The next table indicates the combinations of surfactants used during the experiments:

Table 7-8 Combinations of surfactants used in the foaming tests.

	Anionic			Zwitterionic			Cationic			
Test	C_{14}AOS	C_{16-18}AOS	C_{20-24}AOS	LB	CAPB	LHS	BTC	DTAB	CTAB	DDAB
16,17		x								
24	x			x						
15,26		x		x						
25			x	x						
14		x			x					
20		x				x				
27					x					x
21				x			x			
28		x		x			x			
29	x			x			x			
13							x			
23								x		
22									x	

The results of experiments are be presented in two sections, with a brief discussion and details. The first table 7-8 includes some results from the IMP formulation (i.e., a blend of CAPB, AOS and quaternary ammonium chloride) .

Table 7-9 Viscosities of foam at quality 70% and 1cm^3/min of liquid flow rate at 94°C Part I. Total surfactant concentration was 1% except for test 12.

Test	Surfactant	Brine	Oil	Flow	Apparent Viscosity (cP)	
					Downstream	Upstream
9	**IMP**	**SW**	**No**	**U**	**500**	**500**
10	**IMP**	**SW**	**No**	**D**	**650**	**500**
11	**IMP**	**SW**	**Yes**	**U**	**500**	**500**
12	**IMP (0.1%)**	**FB**	**No**	**U**	**370**	**370**
13	**BTC 8358**	**SW**	**No**	**U**	**< 5**	**< 5**
14	**C_{16-18}AOS + CAPB (1:2)**	**SW**	**No**	**U**	**660**	**602**
15	**C_{16-18}AOS +LB (1:2)**	**SW**	**No**	**U**	**700**	**700**

Flow: U=Upward, D = Downward

The formula from IMP produces strong foam over a wide range of qualities, table 7-9 only include results at 70% of quality. Additional experimental data for this blend is included in fig 7-30, where the shear thinning effect can be observed. The strength of the foam at different qualities is in figure 7-31.

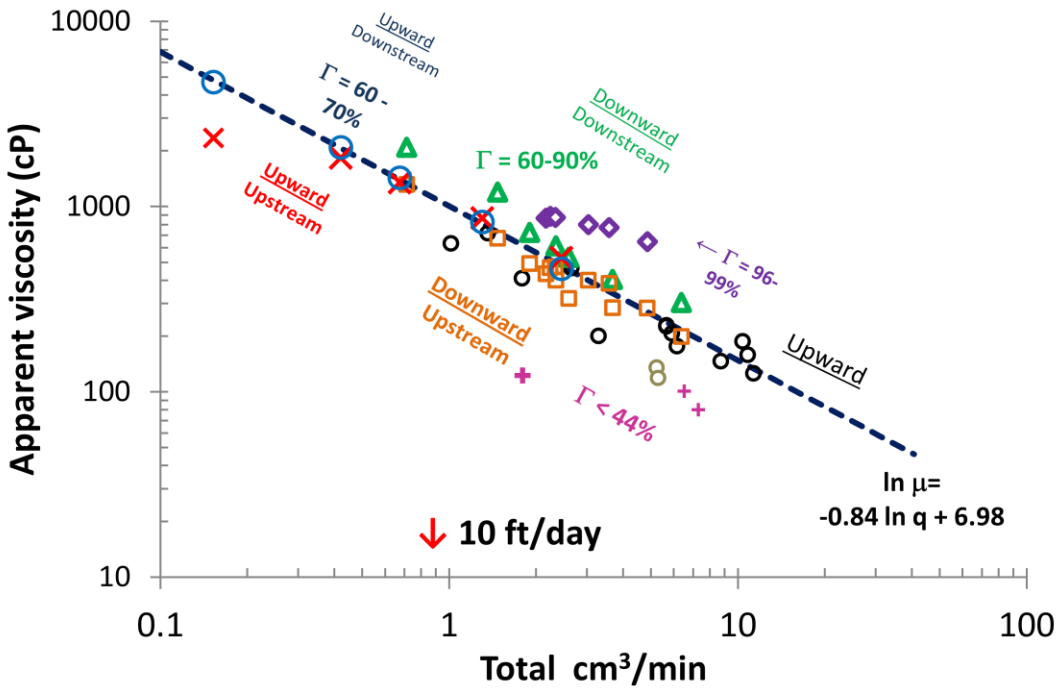

Figure 7-30 Apparent viscosities of three different experiments. Circles for upward flow. Triangles and Squares for downward flow. Outliers for downward flow are for high quality, greater than 96%, and less than 44%. Dashed line is for power law fit. System: 1% IMP in synthetic sea water.

This IMP formulation has a shear thinning behavior as indicated in figure 7-30, and seems to form homogeneous foam in both the downstream and the upstream regions of the sand pack. The outliers correspond to low values of quality less than 44%, and some other ones at high flowrate but just in the downstream section; see fig 7-31 to verify this tendency at constant flow rate.

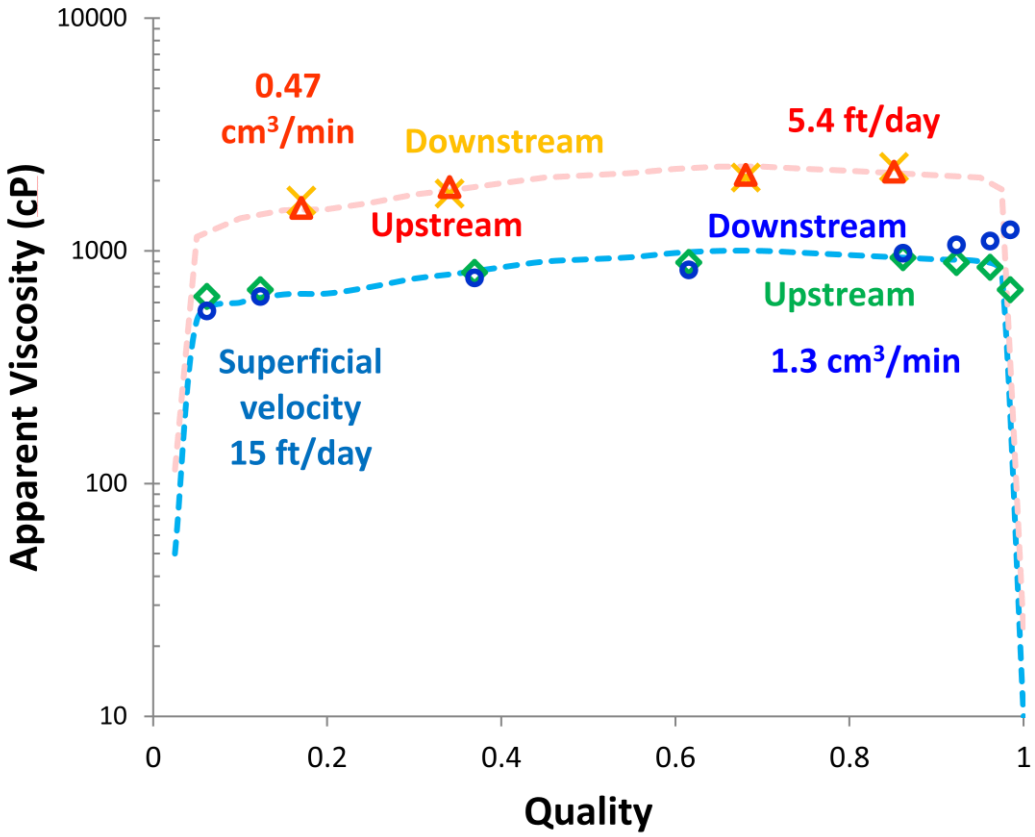

Figure 7-31 Effect of quality for IMP formulation at two different flow rates. 1% Surfactant concentration in synthetic seawater flowing upward. System: 1% IMP in synthetic sea water.

Additional transient experiments for this surfactant blend are in the appendix 7K

Table 7-10 Viscosities of foam at quality 70% and 1cm^3/min of liquid flow rate at 94°C , Part II. (Superficial velocity 38 ft/day)

Test	Surfactant	Brine	Oil	Apparent Viscosity (cP)	
				Downstream	Upstream
16	C_{16-18}AOS	SWIS	No	600	600
17	C_{16-18}AOS	SWIS	Yes	500-600	500-600
19	DDAB+CAPB (1:3)	SW	No	400	500
20	LHS + C_{16-18}AOS (2.75:1)	SW	No	740	740
21	BTC 8358+LB (1:1)	SW	No	< 5	<5
22	CTAB	SW	No	< 5	< 5
23	DTAB	SW	No	< 5	< 5
24	LB + C_{14}AOS (2:1)	SW	No	500	500
25	LB + C_{20-22}AOS (2:1)	DIW	No	400	400
26	LB + C_{16-18}AOS (2:1)	SW	Yes	60-600	1-600
27	CTAB + NapTS (1:1), 0.167%	SW	No	480	400
28	LB + C_{16-18}AOS + BTC (13:2:1)	SW	No	533	693
29	LB + C_{14}AOS +BTC (13:2:1)	SW	No	500	600

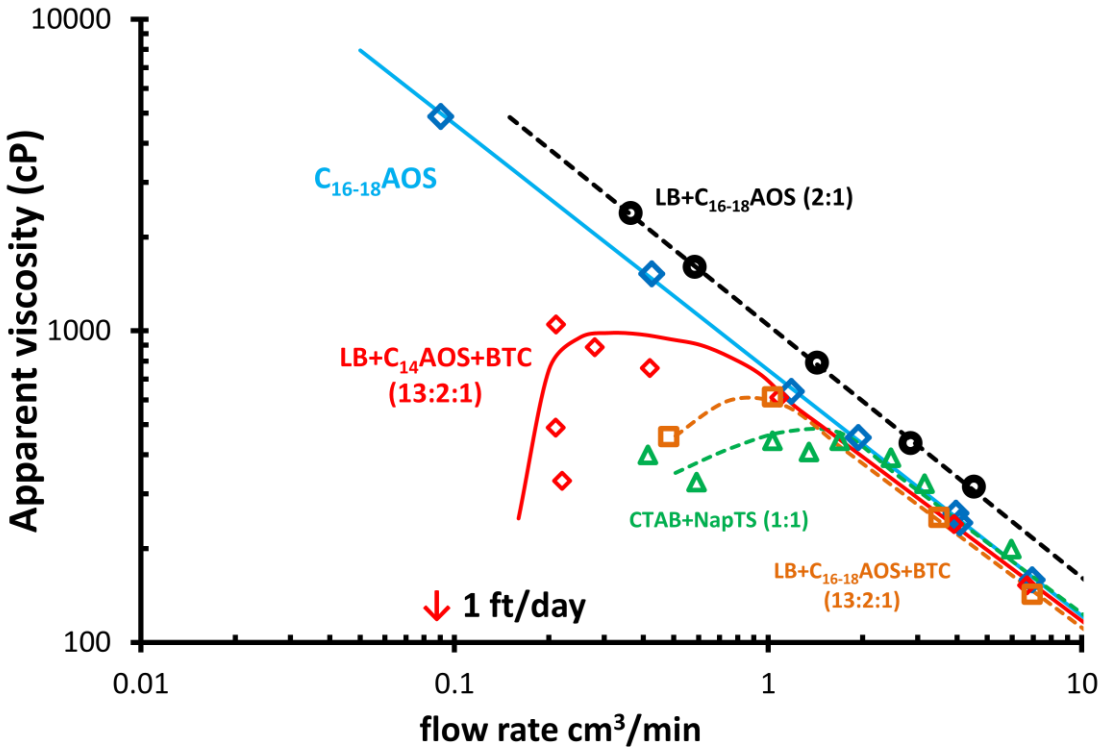

Figure 7-32 Comparison of foam strength for different surfactants at 94°C and 1% total surfactant concentration in a sand pack, using qualities between 60 -70%. Straight lines are for power law fit (n ca -0.8)

The majority of the surfactants follow the same trend as shear thinning, with a power law model, as indicated in fig 7-32. This behavior was briefly explained in chapter 2, but the most important finding from this research is that the trend respect to quality is similar. Blends of AOS with both LB and CAPB are like IMP blend in forming strong foam over a wide range of quality, and they were a little stronger at higher quality.

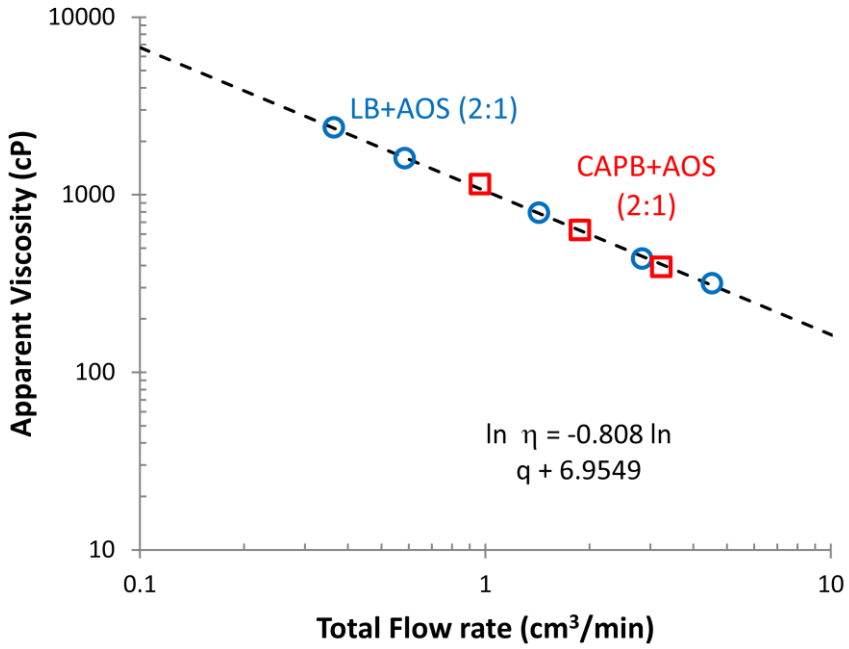

Figure 7-33 Viscosity of 1% surfactant solution in syntheric seaater. Red squares are for CAPB+C_{16-18}AOS at 50% quality, Blue cyrcles are for LB+ C_{16-18}AOS at 70% quality.

The shear thinninig effect and the viscosity of the nitrogen foam with LB+AOS and with CAPB+AOS are similar in seawater at 94°C, as indicated in fig 7-33. The effect of quality can be seen in the figure 7-34.

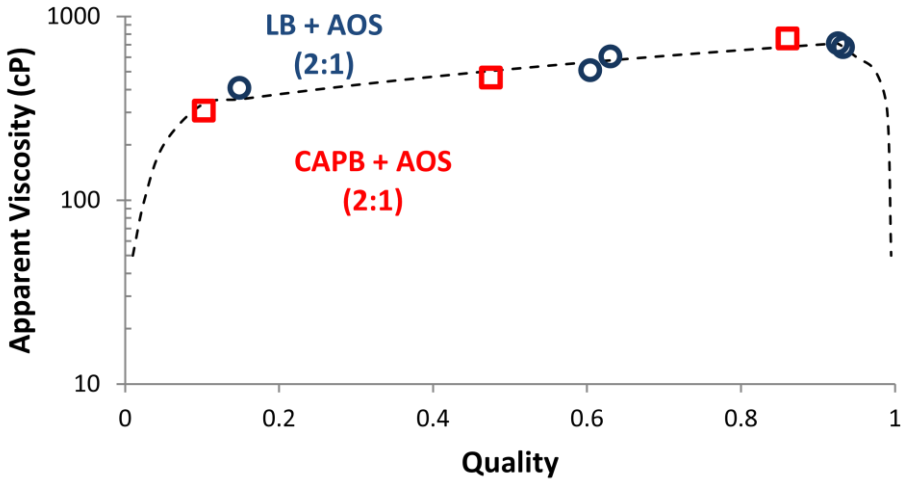

Figure 7-34 Effect of foam quality on apparent viscosity for CAPB+C_{16-18}AOS and LB + C_{16-18}AOS at 1% total surfactant concentration in synthetic seawater, 94°C and constant total flow rate of 2 cm^3/min, superficial velocity 23 ft/day

Most of the surfactant blends showing strong foam in table 7-9 and 7-10 had similar behavior with respect to foam strength relation to quality, but an exception was the cationic surfactant. The cationic surfactant blended with the hydrotrope in low concentration presented the opposite effect respect to quality, stronger foam with wetter foam as indicated in fig 7-35.

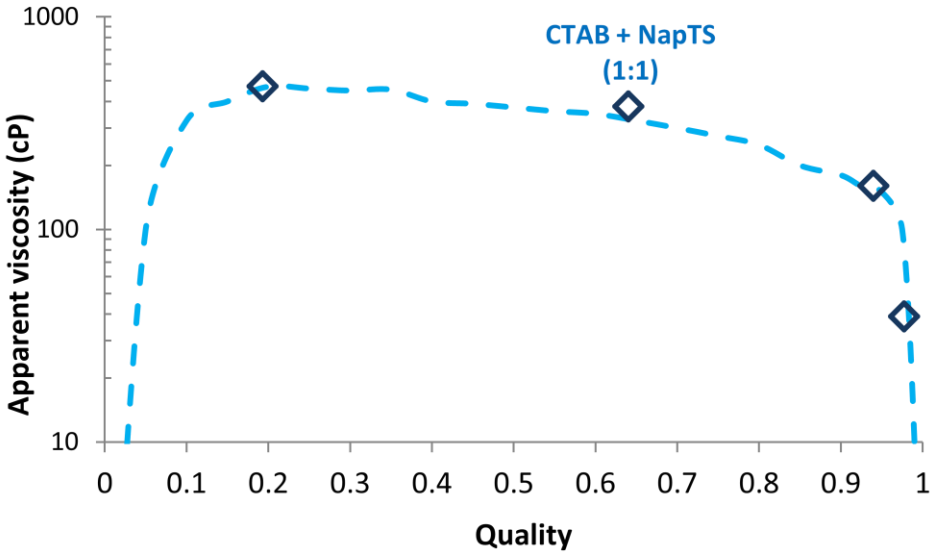

Figure 7-35 Effect of gas quality on foam viscosity for 0.33% Overall blend concentration in synthetic sea water at 94°C for a constant total flow rate of 3cm^3/min (34.5 ft/day of superficial velocity)

The results from the previous section formed a collection of experimental data and observations that were used to select a mathematical model, and to estimate the parameters of the model in order to reproduce the results of the foam behavior at steady state conditions.

The next section 7.3 describes briefly the methodology and the results of this process. The resulting mathematical model was able to reproduce results and observations of the exhaustive experimental process.

7.2.5 Observations about foam studies with oil recovery using "Surfactants ratio–salinity ratio" maps to select injection conditions for oil recovery, and the screening process of foaming surfactant blends.

Foams were created in situ by simultaneously flowing 0.1% to 1% surfactant solution and nitrogen through homogeneous-silica sand packs at 94°C. The surfactant blends, with potential to produce robust foams, were selected from Solubility Maps.

The study was done under the following constraints:

- 100-130 darcy Ottawa silica sand pack: L= 36.2-cm ID = 2.29-cm
- Foam qualities from 0.01 to 0.99
- Flow rates from 0.05 to 10cm^3 /min for each fluid.
- Injection from 30 to 120 psig.
- Minimum backpressure between 20 and 30 ± 0.1 psig.

Most of the experiments were conducted in synthetic seawater but, to evaluate the effect of divalent cations, additional experiments were also done with either formation brine or NaCl-only brine equivalent to seawater in ionic strength. Also evaluated were the presence of crude oil and the direction of flow with respect to gravity.

Test results from these foam experiments are as follows:

1) Stronger foam was generated when Triton X-200 to IOS ratio was higher
2) Stronger foam was generated at lower salinity for the system Triton X-200+IOS
3) Higher oil recoveries were obtained when injection composition was in the Type I region and injection salinity well below that of formation brine, closer to optimum.
4) Foam is weaker when crude oil is present; with AOS the strength was almost unaltered, but the produced oil, contrary to other cases, was a viscous emulsion.
5) Phase behavior map (surfactant blend – brine blend) can be used to plan core flood experiments.
6) Values of apparent viscosities ranged from 150 to 4000-cP for shear-thinning foams of 15% to 95% qualities.
7) Selected zwitterionic and anionic blends have potential for applications in hard-brines-and-high-temperature reservoirs.
8) Addition of cationic surfactant decreased foam strength at low flow rates.

7.3 Mathematical Model, parameters fit and simulation.

The mathematical model selected was the empirical method that uses the mobility reduction factor approach. This approach at different degrees of complexity has been incorporated in simulators like UTCHEM, ECLIPSE 200,

UTCOMP and STARS according to Zhang (2006), Hirasaki (1997), Kovschek (1998) and Rossen (1994). Other models were briefly introduced and compared in chapter 2.

This model is based on the fact that foam has no effect on the relative-permeability function for water, but has a strong effect reducing the relative-permeability function of the gas according to Renkema and Rossen (2007).

Then the expressions for relative-permeability for the aqueous phase or wetting phase assigned as (w) and gas phase (g) have the form:

$$k_{rw} = k_{rw}^{0}\left(\frac{S_w - S_{wc}}{1 - S_{gr} - S_{wc}}\right)^{nw}$$

(Equation 7-6) Relative-permeability for aqueous phase.

$$k_{rgT}^{f} = \frac{k_{rg}^{0}\left(1 - \frac{S_w - S_{wc}}{1 - S_{gr} - S_{wc}}\right)^{ng}}{\left(1 + fmmob\prod_{1=1}^{6} F_i\right)}$$

(Equation 7-7) Relative-permeability of gas as foam.

The terms in the denominator of the relative-permeability function for gas are the different contributions in reducing or maintaining the relative permeability of the gas as foam. Each of the different contributions is listed, and briefly described in table 7-11.

Table 7-11 Contributions to the mobility reduction factor.

Contribution	Description
F_1	Strengthen of foam for surfactant concentration
F_2	Gas mobility change as result of water saturation (*)
F_3	Foam coalescence caused by oil saturation
F_4	Increase of foam for gas velocity (Shear thinning effect)
F_5	Shear-thinning effect in low quality regime
F_6	Critical capillary number effect
fmob	Normalized resistance to flow of a minimum-size bubble, in the absence of factors increasing bubble size. Surguchev approach according with Rossen *et al.* (2003)

All these factors were analyzed in different degrees during this research, but emphasis was focused in F_2, F_4, F_5, F_6 and *fmob*. Details of the dependence of F_1 can be found elsewhere Ma (2012).

Rossen *et al.* (2003) presented the form of the different functions that could be used to estimate the contribution of the mobility reduction factor. These correlations “usually” may take the following analytical forms:

$$F_1 = \left(\frac{C_s}{C_{s\max}} \right)^{eps}$$

(Equation 7-8) Contribution for surfactant concentration.

$$F_2 = \frac{1}{2} + \frac{1}{\pi} \arctan\left[epdry\left(S_w - fmdry \right) \right]$$

(Equation 7-9) Contribution for water saturation.

$$F_3 = \left(\frac{S_{o\max} - S_o}{S_{o\max}} \right)^{epo}$$

(Equation 7-10) Coalescence of foam for the presence of oil.

$$F_4 = \left(\frac{u_g}{u_{gref}} \right)^{epv}$$ **(Equation 7-11) Shear thinning effect for gas velocity.**

$$F_5 = \left(\frac{fmcap}{N_{Ca}} \right)^{epcap}$$ **(Equation 7-12)**

$$F_6 = \left(\frac{N_{Ca} - N_{Caref}}{N_{Caref}} \right)^{epn}$$ **(Equation 7-13)**

The forms presented here will be taken to simplify the analysis, but physical interpretation of the parameters may not necessarily represent the actual physical phenomena (*). In fact Zanganeh *et al*. (2011) presented different modifications of F_2 to overcome the different influence that brine saturation has on the mobility reduction. The use of equation (7-9) may not be applicable to any system, but it has the advantage of being a continuous function.

Previous equations are not unique, they may have different forms. In the expressions for F_5 and F_6 the capillary number was suggested by Cheng *et al.* (2000) in terms of absolute permeability and pressure gradient.

$$N_{Ca} = \left(\frac{k \nabla p}{\sigma_{wg}} \right)$$ **(Equation 7-14)**

Cheng *et al.* (2000) suggested using a different form of equation 7-11, where σ is the conventional power law exponent taking the form:

$$F_4 = \left(\frac{u_g}{u_{gref}} \right)^{\sigma - 1}$$

(Equation 7-15) here σ takes values of $\sigma < 1$ for shear thinning fluid.

Also Cheng *et al*. (2000), proposed a relationship between "σ" and "*epcap*" of the form:

$$\sigma = \frac{1}{1 + epcap} \qquad \textbf{(Equation 7-16)}$$

To simplify the algorithm and to give more eclectic approach to the fitting process, the capillary number used in the equation 7-14 was modified to the capillary number using the total velocity and a reference viscosity instead of the absolute permeability and pressure gradient.

$$N_{Ca} = \left(\frac{k \nabla p}{\sigma_{wg}} \right) \approx b_1 \left(\frac{U \, \mu_{ref}}{\sigma_{wg}} \right) \qquad \textbf{(Equation 7-17)}$$

7.3.1 Algorithm to fit parameters of the model.

The algorithm was obtained using the simplest approach with the measured data, and critical analysis of previous reports. Nevertheless results should be inspected before its use because this algorithm makes the assumptions that the measured apparent viscosities are correct and the error sources are minimal.

- Flowing fractions and pressure gradients are calculated from flows and pressure drop measurements.

- Apparent viscosity is calculated using absolute permeability and pressure gradient and equation 7-18 if there are several internal taps, viscosity and pressure gradient per section are calculated).

$$\mu_{app} = \frac{-k\,A\nabla p}{\left(q_w + q_g\right)} \qquad \textbf{(Equation 7-18)}$$

- Relative permeabilities are calculated with viscosity and volumetric flow rate of each phase assuming negligible capillary pressure gradient. (If capillary pressure gradient is going to be considered, calculate only relative permeability for wetting phase assuming the pressure gradient measured corresponds to wetting phase).

  Assuming: $\nabla p_c = \nabla p_g - \nabla p_w = 0$ and $\nabla p = \nabla p_w = \nabla p_g$

  (Equation 7-19a and 7-19b)

$$k_{rw} = \frac{\mu_w\, q_w}{\left(-k\,A\nabla p_w\right)} \qquad k_{rg}^{f} = \frac{\mu_g\, q_g}{\left(-k\,A\nabla p_g\right)} \qquad \textbf{(Equation 7-20a and 7-20 b)}$$

- Water saturation is estimated using the relationship between water saturation and water relative permeability (Equation 7-21). If there are several internal taps, it is possible to estimate capillary pressure gradient, using water saturation calculated for each section and knowing the

relationship between the capillary pressure and saturation and equations 7-22 to 7-23).

$$k_{rw} = k_{rw}^{0}\left(\frac{S_w - S_{wc}}{1 - S_{gr} - S_{wc}}\right)^{nw} \qquad \textbf{(Equation 7-21)}$$

If capillary pressure gradient is considered

$$\nabla p_c = \nabla p_g - \nabla p_w = \frac{dp_c}{d\tilde{S}_w}\nabla\tilde{S}_w = -\frac{p_c}{\lambda\tilde{S}_w}\nabla\tilde{S}_w \qquad \textbf{(Equation 7-22)}$$

$$\tilde{S}_w = \frac{S_w - S_{wc}}{1 - S_{gr} - S_{wc}} \qquad \textbf{(Equation 7-23)}$$

$$\frac{p_c}{\sigma Cos\theta}\sqrt{\frac{k}{\phi}} = \frac{\alpha_{BC}}{\left(\frac{S_w - S_{wc}}{1 - S_{gr} - S_{wc}}\right)^{1/\lambda}} \qquad \textbf{(Equation 7-24)}$$

- Relative permeability for the gas as a foam can be calculated using the pressure gradient for the gas phase obtained with the wetting phase saturation gradient previously calculated, and the relationship between capillary pressure and wetting phase saturation.

- Theoretical relative permeability of the gas as a foam is calculated using initial guess of the parameters in the mathematical model for gas relative permeability as a foam (i.e. including mobility reduction factor). The parameters for numerator must be known, e.g., S_{wc}, S_{gr}, k_{rg}^{0} and *ng*. and equations from 7-6 to 7-13.

- An objective function is generated as the sum of absolute values or relative errors for gas relative permeability calculated with measurements (i.e. using equation 7-20 b) and gas relative permeability theoretical (i.e. using 7-6).

$$f_{obj} = \sum \left| \frac{k_{rg T,i}^{f} - k_{rg,i}^{f}}{k_{rg,i}^{f}} \right| \qquad \textbf{(Equation 7-25)}$$

- The parameters of the mobility reduction factor model are found after minimizing the objective function using an appropriate algorithm (see Appendix 7F for details).

Some pertinent observations are that if Brooks and Corey (1964) approach is used, the value expected of "*nw*" is greater than 3; a value of 3 is consistent to the assumption of no capillary pressure gradient. A value less than 3 is inconsistent with the physics of the porous media with respect to capillary pressure dependence of saturation if the Brooks and Corey approach is used (i.e., this produces a positive slope of capillary pressure vs water saturation).

The values reported by Brooks and Corey (1964) for λ are 7.3 for glassbeads and 3.7 for sand pack, and the calculated value for α_{BC} in any of the sands they meassured has a value close to 0.165. The relation between λ and the exponent for the wetting relative-permeability function nw is:

$$nw = \frac{2 + 3\lambda}{\lambda} \qquad \textbf{(Equation 7-26)}$$

In our fitting process, selecting *nw*=3, 3.2 or 3.5 gave good results, which represent any of the scenarios described previously . For simplicity most of the results presented here are with a value of 3 for *nw*. Corey found that the exponent for the wetting phase in consolidated porous rock was 4, according to Brooks and Corey (1964).

7.3.2 Fitting process of foam model.

The figure 7-32 compares a few of the experiments conducted in the sand pack. Some tests are not included because they overlap with “LB+AOS” blend (e.g. overlaping for LB+AOS and CAPB+AOS included in figures 7-33 and 7-34). Some other blends “Zwitterionic+Anionic+Cationic” overlap with the curves from other experiments that showe weak foam at low flow rates. All the experimental results were used in the fitting, but the blend of interest “LB+AOS” was the one studied first.

The initial fitting process was done using the the steady state apparent viscosities reported in fig 7-33 and fig 7-34 for the blend Lauryl Betaine and C_{16-18}AOS. This blend was selected because it was strong in the range of flows studied. Initialy effects of anything besides water saturation and shear thinning were not considered (i.e. setting the product of “$F_1F_3F_5F_6$ “equal to one). After fitting the parameters the model was compared with a more extensive collection of data to see if the model can predict behavior of foams with blends of

surfactants in the with similar combinations (i.e. tests 14,15,16,17, 20, 21, 24, 25 and 26 of table 7-8), using the parameters resulting from the optimization search.

The default parameters for relative permeabilities without foam of nitrogen and aqueous phase were based in typical values reported by Apaydin and Kovscek (2000), and considerations discussed before, see table 7-12.

Table 7-12 Default parameters for relative permeability and capillary pressure

Parameter	Case I	Case II	Case II
nw	3	3.5	3.5
ng	1.8	1.8	1.8
k_{rw}^{0}	0.7	0.7	0.7
k_{rg}^{0}	1.0	1.0	1.0
S_{wc}	0.06	0.06	0.06
S_{gr}	0.05	0.05	0.05

Case 1 using values from Apaydin and Kovscek (2000), case 2 the value of "*nw"* was changed according to suggestion from Brooks and Corey (1964).

The viscosity of aqueous phase is close to the water viscosity at 94°C 0.3 cP, and for nitrogen the value is 0.02085 cP from Lemmon *et al.* (2004).

Table 7-13 Initial and final values during the search process.

	Initial	Final case I	Final Case II	**Final Case III**
epdry	(1000,500,100)	100 *	100 *	**56***
fmdry	0.3	0.6257	0.631	**0.0823**
fmmob	5000	2894.05	2695	**17.5**
epv	-0.8	-0.775	-0.781	**-0.78**
Ug ref	1	1.4214	1.4206	**1.4**

(*) "*epdry*" was fixed. Order of magnitude and values for "*epdry*" and initial for "*fmmob*" from Renkema and Rossen (2007)

Renkema and Rossen (2007) fixed the value of "*epdry*" to 500. This value of "*epdry*" gave good fit but a better fit was obtained with a value of 100 (See discussion Appendix 7-L). To see if this value is congruent with previous studies, figures 7-36a and 7-36b were prepared.

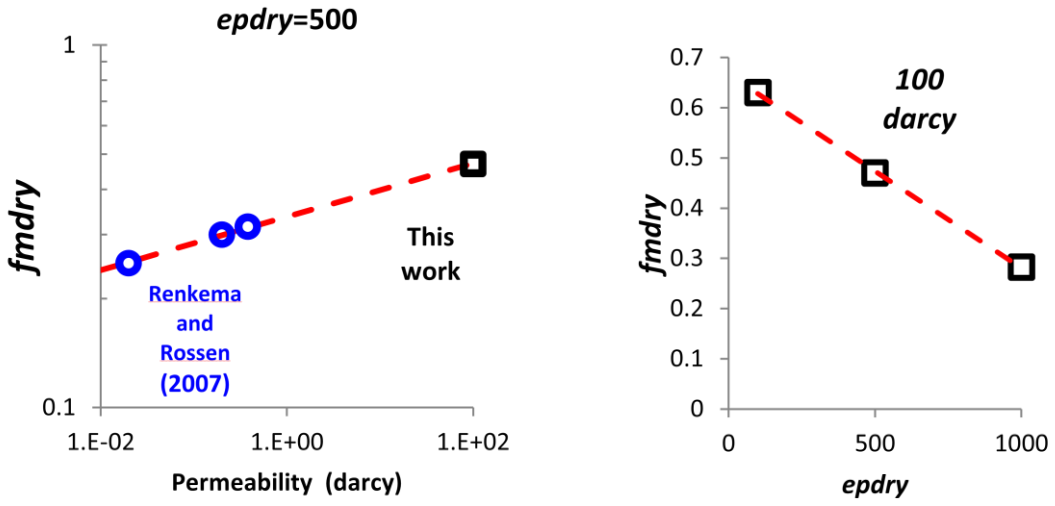

Figure 7-36 Values of "*fmdry*" after the fitting process using a default value of "*epdry*" of 500 in the left figure. The figure of the right shows values of "*fmdry*" for different values of epdry (See discussion in Appendix 7-L).

The plot on the left in fig 7-36, shows a trend in the value of "*fmdry*" as a function of permeability for a fixed value of "*epdry*"; this is not an indicator that the value necessarily is correct. Moreover, the plot on the right demonstrates that the value of "*epdry"* will depend of "*fmdry"*, indicating that to give a physical meaning "*fmdry*" in the equation 7-9 may require additional experimental information.

If additional constraints are imposed on the search, another solution can be obtained. The parameter for case III (table 7-13) was obtained adding the following criterion:

Fmdry< Sw* . Here Sw* is water saturation corresponding to the gas fractional flow when the the viscosity presents a maximum at constant total flow rate. This condition is required for unique solution for a given "epdry". (See appendix 7-L for details of this solution)

The resulting parameters listed in table 7-12, were used to model a surfactant blend that presented no foam coalescence in the range of flow rates studied. Comparison between experimental data and simulation are included in fig 7-37.

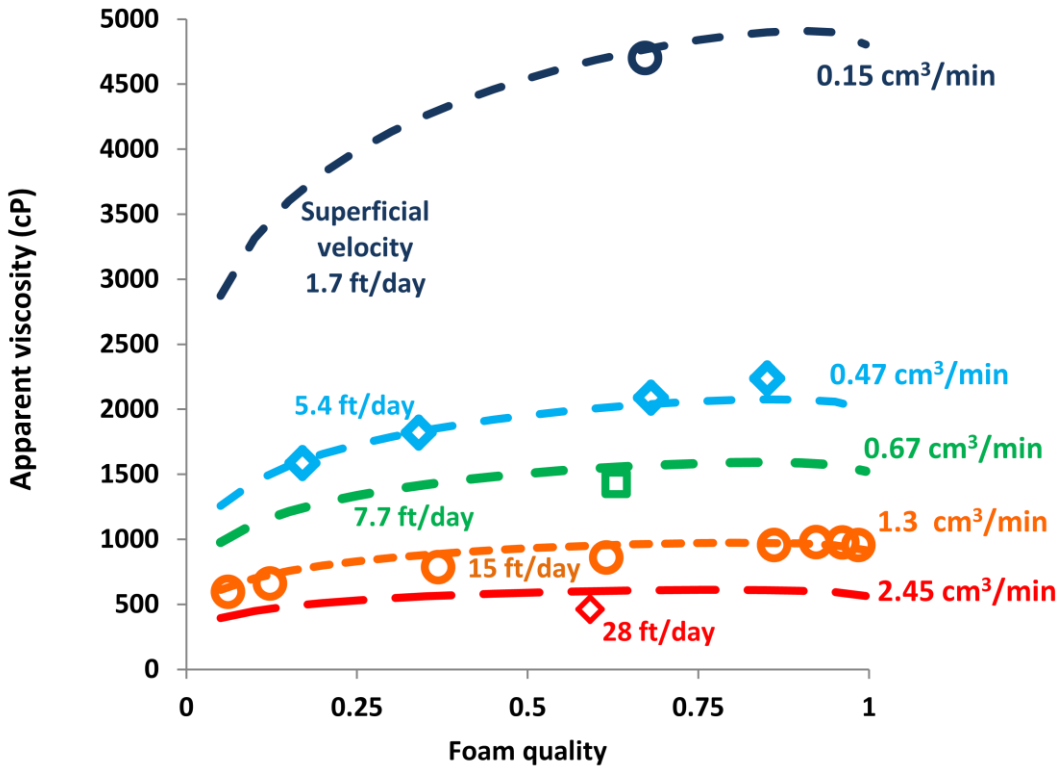

Figure 7-37 Apparent viscosity comparison, experimental values represented with symbols, and simulated values represented with dashed lines. The mobility reduction factor model and parameters of tables 7-11 and 7-12 for case I, were used in the calculations, and considering only water saturation effect and shear thinning effect.

The selected model seems to represent the trends observed with the surfactant blend called IMP. Of course, better prediction is obtained for “LB+AOS” surfactant blend and for “CAPB+AOS”. The comparison for the “CAPB+AOS” is not included in this report because, according to figures 7-33 and 7-34, the experimental values are very close to the values of “LB+AOS”, which was used in the fitting process. The comparison of the model predictions with “LB+AOS” results is presented in fig 7-39.

The next challenge is to see if the model can fit the lack of foam generation at low flow rates seen in fig 7-32 for those blends containing cationic surfactant, e.g., "LB+C_{14}AOS+BTC", "LB+$C_{16\text{-}18}$AOS+BTC" and "CTAB+NapTS". This behavior is not limited to these blends; it has been observed before in figs. 7-13 and 7-15.

Analyzing the form of correlations for F_5 and F_6 and assumptions discussed earlier, the functions for F_5 and F_6 can be grouped to simplify analysis and see if the lack of foam generation at low flow rates can be fitted.

$$F_5F_6 = \left(\frac{fmcap}{N_{Ca}}\right)^{epcap}\left(\frac{N_{Ca}-N_{Caref}}{N_{Caref}}\right)^{epn} \qquad \textbf{(Equation 7-27a)}$$

Re-arranging the product the equations take form:

$$F_5F_6 = \left(\frac{fmcap}{N_{Ca}}\right)^{epcap-epn}\left(\frac{fmcap}{N_{Ca}}\frac{N_{Ca}-N_{Caref}}{N_{Caref}}\right)^{epn} = \left(\frac{N_{Caref}}{N_{Ca}}\right)^{epcap-epn}\left(\frac{fmcap}{N_{Caref}}\right)^{epcap}\left(1-\frac{N_{Caref}}{N_{Ca}}\right)^{epn}$$

(Equation 7-27b)

Using the definition for capillary number given in equation 7-27, the product of two functions can be simplified as:

$$F_5F_6 \approx k_1\left(\frac{u}{u_{ref1}}\right)^{epcap-epn}\left(1-\frac{u_{ref}}{u}\right)^{epn} \qquad \textbf{(Equation 7-28)}$$

To incorporate these two functions in the mobility reduction factor the value of k_1 is set to 1 (or lumped with *fmmod*), *epcap* = *epn* is the first option to explore

during the fitting process, and the value of "*epcap*" was related to the value of "*epv*". This relation is evident after inspection of equations 7-14 and 7-16.

$$epcap = \frac{1}{1+epv} - 1 \qquad \textbf{(Equation 7-29)}$$

Then the only required parameter is u_{ref}. If this initial guess does not reproduce the behavior of the foam, then an additional parameter can be incorporated in the search (i.e. ***epcap*** ≠ ***epn***). Using a value for *epcap*=3, which is within the range of the value predicted by equation 7-29, gave good fit to experimental curves with lack of adequate foam generation in fig 7-38.

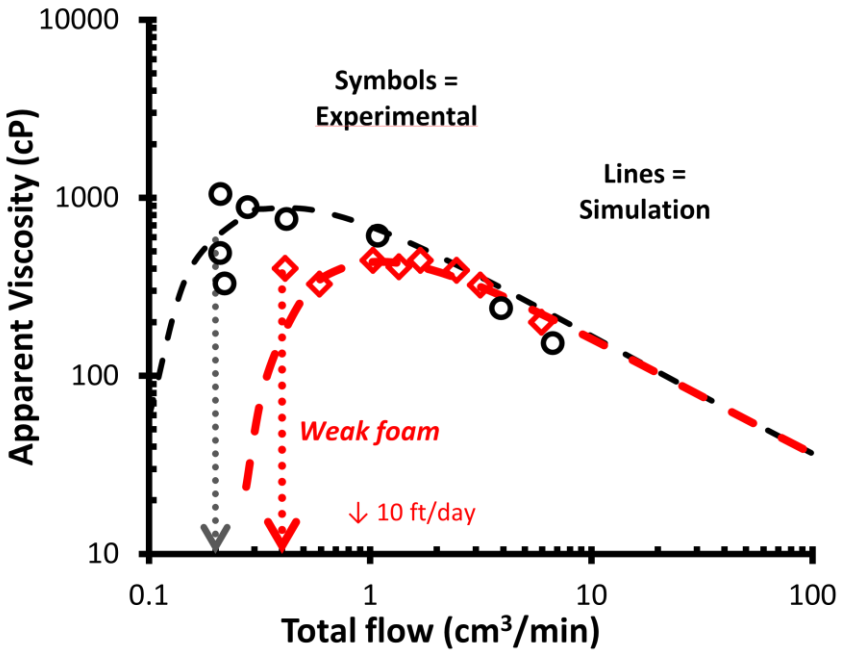

Figure 7-38 Apparent viscosity comparison, dashed lines obtained after fitting the value of u_{ref} in equation 7-28. This fitting was done to reproduce the falling in the foam strength at low flow rates. Black is for LB+C_{14}AOS+BTC, and red for CTAB+NapTS. The parameters are listed in table 7-13. The simulation was done with 70% of gas quality at 94°C.

Table 7-14 Parameters after fitting three different surfactant blends.

Parameters	LB+C_{16-18}AOS	LB+C_{14}AOS+BTC	CTAB+NapTS	CTAB+NapTS**
epdry (*)	100	100	100	1000
epcap = epn (*)	3	3	3	3
fmdry	0.625794	0.625794	0.625794	0.13
fmmob	2894.053	2158	2158	2490
epv	-0.77585	-0.7758	-0.7758	-0.775
u_{gref} *(m/s)*	1.421435	1.421435	1.421435	0.6
u_{ref} *(m/s)*	0	3.30E-06	9.10E-06	9.10E-06

(*) Parameters fixed during the fitting

(**) Parameters to fix the trend of decrease of foam strength with quality.

See appendix 7M, for another solution for CTAB+NapTS, with epdry=56

An additional figure to compare results from table 7-13 is included for further discussion. Table 7-14 gives two sets of parameters for the blend "CTAB+NapTS", the first column was able to reproduce weak foam at low flow rates and shear thinning effect, but not the trend of decreasing strength with quality observed in fig 7-35. So for this case extrapolation worked partially. To fit all the characteristics observed in experiments is required to adjust the parameters with experimental data to capture the dependence of quality, which seems to be strongly dependent of the surfactant used (for comparison see fig 7-35, 7-34, 7-31, 7-26 and 7-15). The last column of for "CTAB+NapTS" should be used.

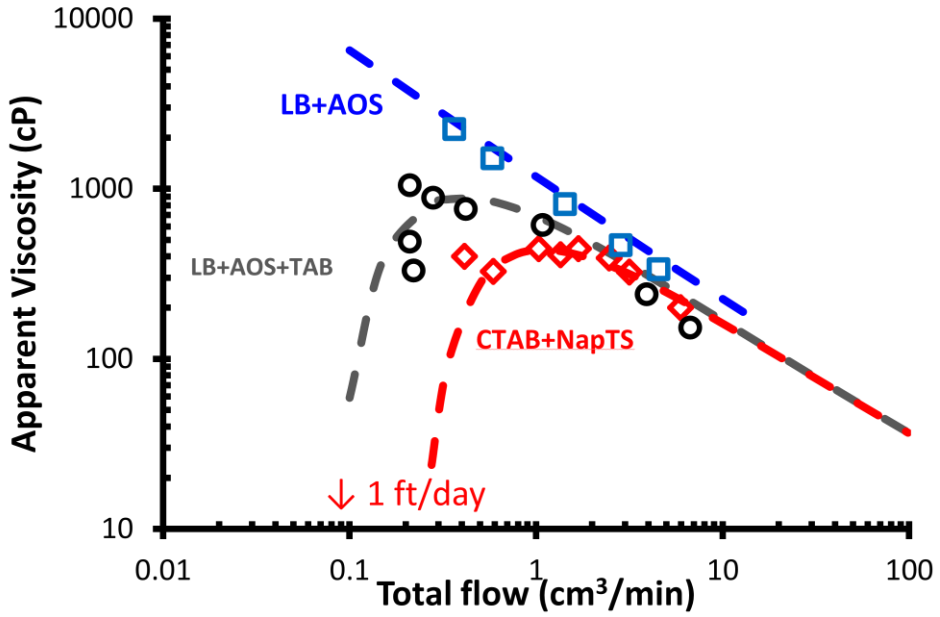

Figure 7-39 Simulation of the foam viscosity using the mobility reduction factor approach, equations from 7-6 to 7-22, and parameters from table 7-11 and 7-13 case I. The symbols are experimental data at gas quality close to that used in the simulation of 70%.

The selected model is able to reproduce most of the behaviors presented by the foaming systems studied in this work. The effect of oil was not included in this model, the effect of surfactant concentration was not a variable of this research, because the main objective of this research was focused in evaluating different formulations, but this work complements the research done by Ma (2012), which considered the effect of surfactant concentration.

Most of the formulations were tested at 1% total surfactant concentration, and for CTAB+NapTS the concentration used was 0.33% because the solution at 1% surfactant concentration at room temperature, was highly viscoelastic, and difficult to inject in the system with the existing filtration system.

The IMP formulation was tested at 1% in seawater, and 0.1% in formation brine, The foam strength at 0.1% surfactant concentration in formation brine decreased 25% respect to the foam at 1% surfactant concentration in seawater.

The shear thinning effect remains and the trend of viscosity with velocity and quality remains the same and the parameters of the mathematical model predicted the behavior even in this range of variation of concentration. Nevertheless this almost invariant change in viscosity at lower concentration may be compensating the effect of the increment in salinity. The experimental data and simulation are compared in fig 7-40

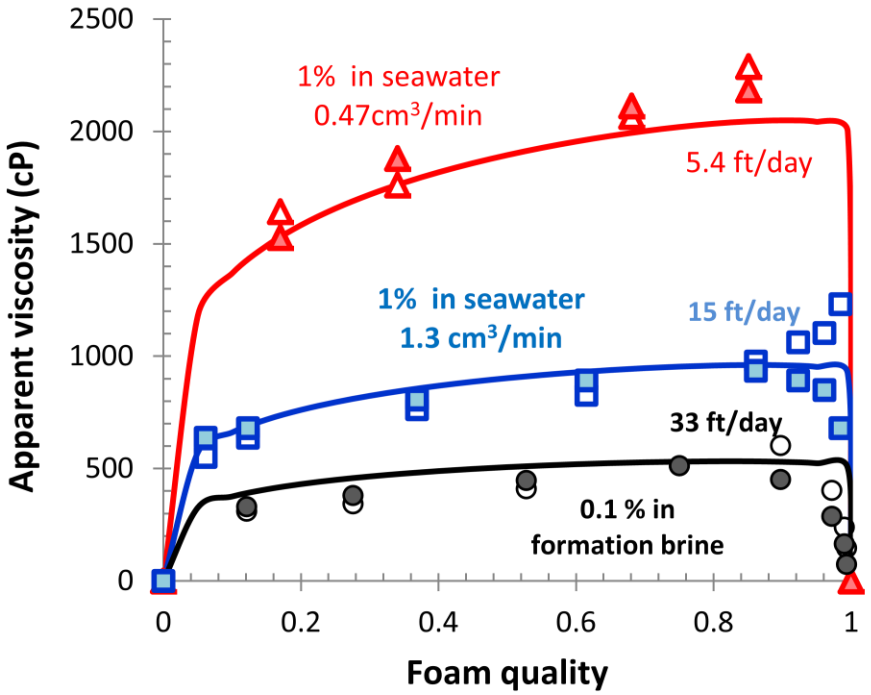

Figure 7-40 Apparent viscosity comparison for IMP formulation, simulation and experiments. Filled symbols are for downstream section of the sand pack, and non filled symbols for the upstream section. Blue and red are for 1% total surfactant concentration in seawater, black symbols are for 0.1% in formation brine at a flow rate of 2.9 cm^3/min. Continuous lines are results from simulation. Parameters from table 7-14 column 1

7.4 Gravity Drainage - Imbibition experiments

Surfactant formulations have been evaluated in previous sections from the foaming point of view. The blend C_{15-18}IOS+ $C_{28}PO_{25}EO_{25}CO_2Na$ presented weak foaming capacity, but was expected to have potential of oil recovery according with phase behavior, at least with the simulated live crude oil with

close to 30% of cyclohexane. Nevertheless in this research the simulated live crude oil has only 16% of cyclohexane.

The formulations studied have to be evaluated from the recovery point of view, and some imbibition/gravity drainage experiments were designed with this purpose.

The first formulation to be tested was the C_{15-18}IOS+ $C_{28}PO_{25}EO_{25}CO_2Na$. A special imbibition cell was designed to verify the recovery in a foaming environment at 94°C. This test was conducted with actual formation rock with maximum permeability of 40 mdarcy.

Formulations evaluated with potential to foam were studied in autoclavable imbibition cells. The blends used were LB+C_{16-18}AOS, LB+C_{14}AOS and LB+C_{14}AOS+BTC 8358. The main objective was not only to see their performance during Imbibition-Gravity Drainage process, but to analyze the role of using BTC 8358, which has been reported to alter wettability of carbonate rocks, as discussed by Pelia and Mohanty (2012) using benzalkonium chloride at high temperature, and to increase recovery by imbibition. The three different formulations were compared using the oil recovery index from rock samples saturated with simulated live crude oil. Silurian Dolomite outcrop cores with 300 mdarcy permeability were used for this study, after being treated, saturated and aged presumably restoring oil-wet condition, (See chapter 3 for wettability of rocks).

7.4.1 Imbibition in the special designed foaming-imbibition cell.

Formation rock cores were prepared using the following procedure:

- Cleaned with THF, then $CHCl_3$ and CH_3OH
- Dried at 95°C.
- Vacuum for 24 h.
- Permeability and porosity measured when inside Hassler coreholder.
- Dried at 95° C
- Two layers of Solvent resistant shrinking tape were used to prevent breaking during centrifugation.
- Vacuum for 24 h
- Saturated with formation brine and stored under pressure for 24 h.
- Placed in centrifuge with crude oil, and water displaced measured (24 h at 20000 RPM, between 27100 g and 38500 g)(*)
- Aged at 94° C for 6 months and 1 week at 120° C.
- Shrinking sleeve removed for placing plug inside “cell”. Plug was left for a few seconds for dripping excess of oil; surface was very oily when inserted in “cell.

(*) Radius to the bottom of the core 8.6 cm, radius to the top of the core 6.06 cm

The centrifuge worked in the range from 27100 g and 38500 g, which is equivalent to a capillary pressure of 8 atm = 810.624 kPa = 117.5 psi. For a core with porosity of 10% and 40 md of absolute permeability, and interfacial tension of 30 mN/m for crude-brine interface gives a minimun value of Leverett-J

function of 5.404, This value of Leverett – J function corresponds to a oil saturation of 95% in dolomite in accord of figures of Leverett – J functions reported by Amyx *et al.* (1960).

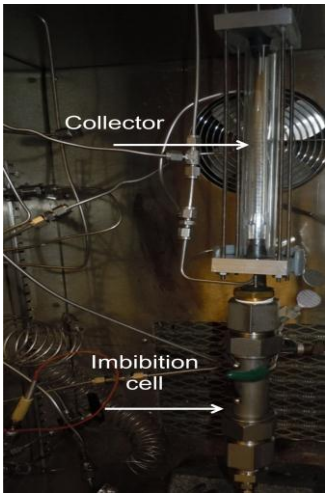

(a) Foam imbibitions cell

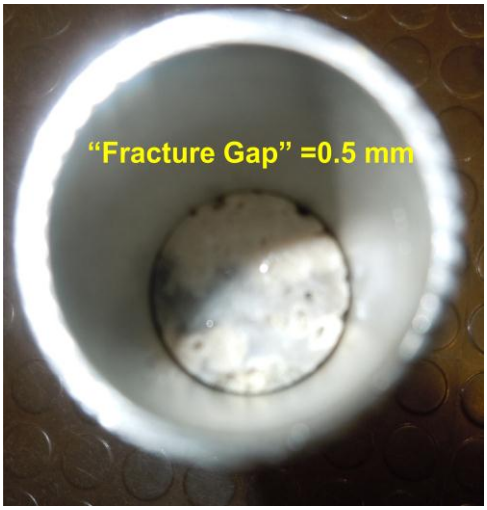

(b) Internal view of imbibitions cell

Figure 7-41 Apparatus to test formulation. Imbibition cell with renewing surfactant solution injected as foam.

The cell shown in fig7-41 and components described in fig 7-42 were designed to mimick reservoir conditions where oil is in the matrix surrounded by fractures. Fractures being the channels where surfacatnt can be transported as foam.

The apparatus in fig 7-41 resides in the interior of a temperature controlled oven (94°C). The injection of renewing surfactant solution as co-injection of nitrogen and surfactant solution is done in the base of the cell after being heated at 94°C. The cell is mantained at a pressure not less than 30 psig using a relief valve.

7.4.2 Procedure during imbibition experiment in foaming environment

Plugs were soaked in special UT Brine brine for 24 hours at test conditions.

- Surfactant and Nitrogen co-Injected at intervals of ~ 24 hours
- Core samples soaked overnight or days for production, without injection
- Repeated the process in cycles for 11 days.

The imbibition was done in 8 stages described in the table 7-15

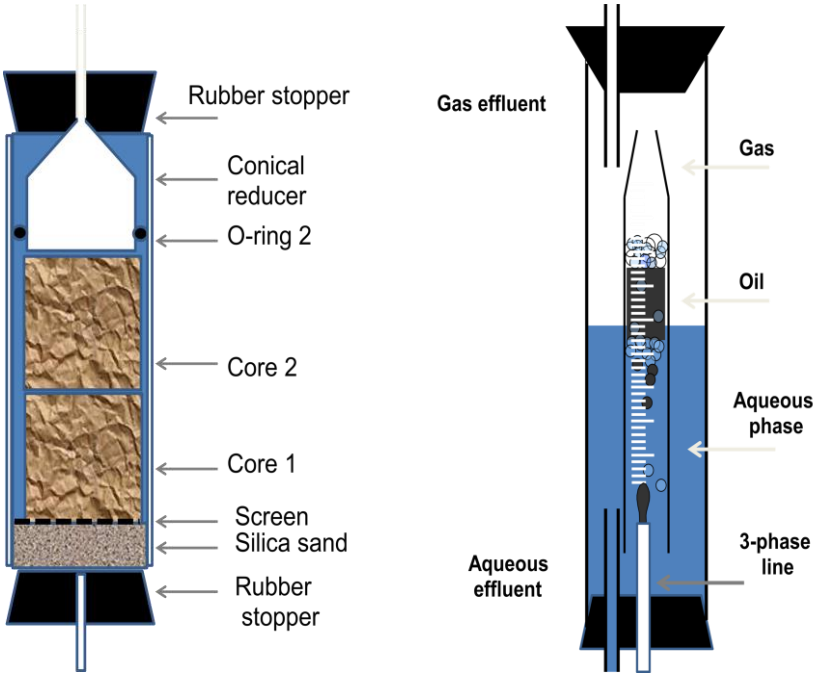

Figure 7-42 Components of Apparatus for imbibitions experiment in foaming environment. (See fig 7-43)

Table 7-15. Description of steps during imbibition.

Stage	Description
1	Co-injection of surfactant and nitrogen, no foam was observed, most of the crude oil was recovered during the first hours. Surfactant was injected at 1 cm^3/min in UT blend. Gas quality of the foam was 60%. Total volume of injected surfactant 80 cm^3
2	2 days injection shut in.
3	No significant additional free oil recovered. Different flow ratios were used to try to produce foam, foam was weak all the time. Total volume of liquid injected 125 cm^3. 80% of the co- injection surfactant and nitrogen was at the same flow conditions as stage 1.
4	4 days injection shut in.
5	UT Blend on was injected in synthetic seawater. Overnight no additional free crude oil was recovered, foam was not observed at different flow ratios and flow rates. 40 cm^3 of surfactant injected.
6	3 days injection shut in.
7	Avanel S70 and IOS 20-24 were injected in sea water to verify presence of foam. Strong foam created, but no additional crude oil was produced
8	2 days shut in. No additional oil observed.

The history of the oil recovery during the imbibition is plotted for analysis in figure 7-43

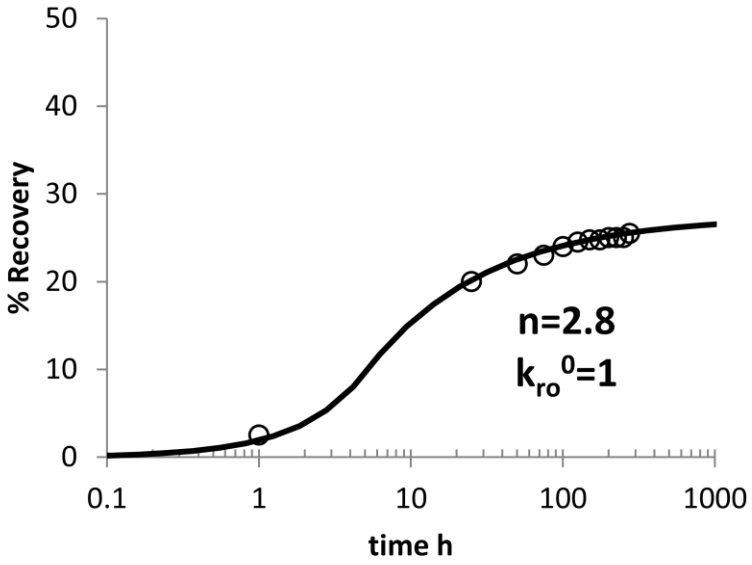

Figure 7-43 Oil recovery from a 40 mD formation core saturated with simulated live crude oil. The continuous line is a model fit. (See fig 7-48)

Discussion of this experiment will be presented after the description of the other imbibition experiments.

7.4.3 Oil recovery in the autoclavable-imbibition cell using 300 mD Silurian dolomite outcrop cores.

Because of the promising previous test results on foam generation, it is necessary to evaluate oil recovery during imbibition tests with Silurian Plugs that are somewhat mineralogically similar to formation rock.

It was decided to conduct imbibition tests in a “homogeneous” rock where surfactant formulations could be solely ranked by their interfacial activities.

The Silurian rock of 300-md permeability was selected for a rapid assessment of the test results. As it is well known, oil recovery by imbibition is a function of permeability and test duration in, for example, 20-mD permeability would be too long for screening many formulations.

These tests are being conducted with imbibition cells specially designed for particular requirements at UT Austin by professor **Kishore Mohanty**, which were kindly loaned to Rice University.

7.4.4 Procedure for imbibitions experiments

The cells were pre-tested with water for checking losses by evaporation. It was determined that in every test for proper seal, (1) a new O-ring most be inserted at the top and (2) at the flanged-open bottom, where plugs are inserted, a torque of 60 in-Lb_f should be applied on the nine bolts pressing against a brass, brand-new gasket.

A Silurian core, 1-inch OD x 12-inch, was cut into several, one-inch-long, pieces. Six of these pieces were assembled in a core holder, evacuated and saturated with sea water, consequently displaced by force with synthetic Pemex oil composed by mass ratio 84/16 dead crude oil and cyclohexane (Rice simulated live oil).

The plugs were aged inside the holder at 94°C for 8 days aiming for oil-wet wettability alteration. The pressure in the effluent of the core holder was maintained at a pressure no less than 30 psig using a relief valve.

Plugs from disassembled holder were individually immersed in Pemex oil to be ready for imbibition tests.

For speeding screening tests, only one of the six plugs was tested for 8 days immersed in seawater. It was assumed, as practically no oil was produced, that all plugs will behave similarly and plugs were immersed only in test formulation.

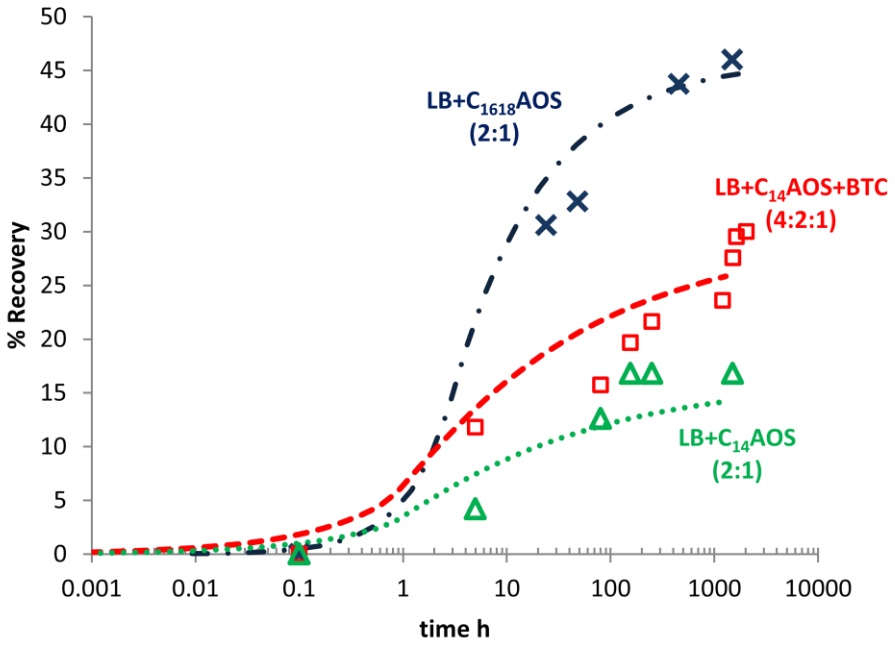

Figure 7-44 Imbibition test results for 3 similar plugs of Silurian core saturated with synthetic Pemex oil _84/16 wt crude /Cyclo-C6_and seawater. All surfactant solution were 0.5% wt/vol in seawater

Two important previous test results were initially considered for conducting imbibition tests:

- Formulation **"X** = LB + C_{16-18}AOS" has the potential to (a) produce low water-oil interfacial tension (IFT) from phase behavior test results at WOR~1 at 94°C and (b) make strong foam from flow tests in silica sand at 94°C.
- BTC, from UT oil-recovery imbibition test results, has great potential to "alter" wettability toward water wet. But BTC by itself failed to generate foam

It was decided to test first the BTC effect by adding it to formulation **"X** = LB + C_{16-18}AOS", appearing to be optimal for lowering IFT near formation brine. However test results were discouraging because adding BTC, within reasonable concentrations, produced only cloudy, non-injectable solutions in seawater. Thus, to be able to determine BTC effect, the AOS_{C16-18} in **"X** = LB + C_{16-18}AOS" was ad hoc substituted by a more hydrophilic C_{14}AOS, which helped to produce a clear, injectable solution.

The imbibition test for "Δ = LB + C_{14}AOS" was terminated because of its poor oil recovery performance. This result should not be surprising because "Δ = LB + C_{14}AOS" is more hydrophilic than **"X** = LB + C_{16-18}AOS"

Comparing test results of "Δ = LB + C_{14}AOS" with "□ = LB + C_{14}AOS + BTC" ,

it is clear that BTC improves performance; however is unclear if wettability alteration is the only cause because, from phase behavior test results, addition of BTC makes the system more lipophilic, shifting water-oil interfacial tension to lower values.

The formulation **"X** = LB + C_{16-18}AOS" is promising and appears to be recovering OOIP faster, but longer time of data collection is required for a firm conclusion.

After contact with the water-oil saturated Silurian plugs, all initially similar-looking surfactant-test solutions had different appearances that will be discussed next.

1 week 10 weeks

Figure 7-45 Appearance overtime of "LB + C_{14}AOS + BTC" solution.

Moderate oil recovery but solution appearance changed over time from slightly amber-colored to as clear as the original. This could be happening because one of the surfactants is preferencialy absorbed in the rock. Thus, at the beginning a lot of solubilitation occurred in aqueous phase, but after months the aqueous solution is crystal clear. Emerging big drops of oil never deataching from the rock was an indication of no ultralow IFT.

30 h
LB+C_{16-18}AOS

3000 h
LB+C_{14}AOS+BTC

Drop diameter **0.2**-**0.3** mm
corresponding to IFT
ca. 0.036 dyne/cm

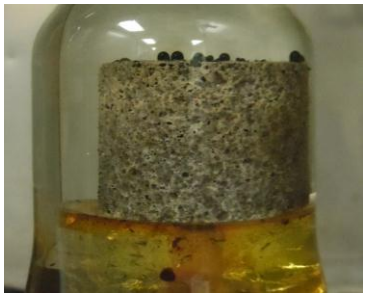

Drop diameter **1.0-1.37** mm
corresponding to IFT
ca. 0.9 dyne/cm

Figure 7-46 Comparison % OOIP recovery for two systems. Upper core in the upper right correspond to "LB + C_{16-18}AOS" and the core lower right is for "LB + C_{14}AOS + BTC" .

The values of IFT are approximate values, calculated by solving Laplace equation for emerging drop, measuring diameter and shape (see chapter 3). After capturing images, the shapes corresponded to values of "B", between 0.5 and 0.75, "B" being defined as the ratio between radius of curvature at the apex of the drop and capillary length. $B= r_{apex}/L_c$, $L_c= (\sigma / g\ \Delta\rho)^{1/2}$.

7.4.5 Analysis from Imbibition experiments.

Schechter *et al.* (1994) studied systems under imbibition in a wide range of conditions (e.g. IFT values, density differences and permeabilities), with wetting and non-wetting systems and they were able to identify different mechanisms of recovery. This is discussed as well by Adibhatla and Mohanty (2008).

They defined an “Imbibition Porous Media Bond Number” using the characteristic length as the geometric mean between height and the Leverett pore size defined by Civan (2011).

$$N_B = \frac{\Delta\rho\, g\, L_{Sh}^2}{\sigma_{ow}} \qquad \textbf{(Equation 7-30)}$$

$$L_{Sh}^2 = \frac{5\,h}{2}\sqrt{\frac{k}{\phi}} \qquad \textbf{(Equation 7-31)}$$

The 5/2 constant is needed to convert the Leverett pore size to the hydraulic radius of the porous media using Blake-Kozeny equation. Al-Lawati (1996) used a constant of 0.4 for capillary tube model.

They defined three mechanisms depending on the value of the inverse of Bond number:

(1) Imbibition process at high value of N_B^{-1} ($N_B^{-1} > 5$) is dominated by capillary forces, and the rate of imbibition is limited by the counter-current flow of the wetting and the non-wetting phase. This applies for water-wet system

(2) Imbibition at low values of N_B^{-1}($N_B^{-1} < 1$) is dominated by vertical flow driven by gravity forces.

(3) For water wet systems and for intermediate values of N_B^{-1}, the combined effects of gravity segregation and capillary-driven imbibition are important. If the IFT is reduced in the process there is a transition from counter-current capillary-dominated flow to co-current gravity-driven flow.

$$N_B^{-1} = \frac{2\,\sigma_{ow}\sqrt{\frac{\phi}{K}}}{5\;\Delta\rho\;\;g\;\;h} \qquad \textbf{(Equation 7-32)}$$

In the experiment using LB+AOSC$_{16\text{-}18}$ (2:1) the IFT was less 0.036 dyne/cm estimated with the size of drops emerging from the core (see fig 7-46). This IFT gives an inverse of Bond number of 0.5, then gravity forces dominates the oil recovery. If the value of the IFT were close to 0.1 dyne/cm, then the initial inverse of Porous Media Bond number will be 1.4, and both mechanisms will be present.

For the formulation LB+AOSC$_{14}$ +BTC (4:2:1) the IFT was never less than 0.1 dyne/cm.

Table 7-16 Some values of properties for calculations during imbibitions experiments LB+AOSC$_{16\text{-}18}$ (2:1)

Parameter	LB+AOSC$_{16\text{-}18}$ (2:1)	$C_{15\text{-}18}$IOS+ $C_{28}PO_{25}EO_{25}CO_2Na$ (1:1)	units
k	**300**	**< 40**	**mD**
kro	0.8	1.0	
$\Delta\rho$	100	100	kg/m^3
g	9.80665	9.8	m/s^2
S_{oi}-S_{or}	0.45	0.27	
L	0.0254	0.0254	m
μ_o	**3.00E-03**	3.0E-3	kg/m-s
ϕ	0.23	0.1	
σ_{ow}	0.036	0.1	mN/m
Rock	Silurian	Formation	

The inverse of bond number using IFT of 0.036 mN/m is 0.506

Schechter *et al.* (1994) developed an analytical expression to relate the remaining wetting phase saturation (R_{WPS}) to the Imbibition Porous Media Bond Number, using information from the relationship between saturation and Leverett-J function.

$$R_{WPS} = \frac{1}{N_B}\left[1 + \int_1^{N_B} S(J)dJ\right] \qquad \textbf{(Equation 7-33)}$$

Taking data listed by Schechter *et al.* (1994), Hirasaki *et al.* (2004) and this work, and plotting using the product of recovery and Bond number in the ordinate, and the inverse of Bond number in the abscissa, fig 7-47 is generated. (*Note: Eq. 7-33 was the inspiration to plot the product of Bond number and remaining wetting phase saturation*)

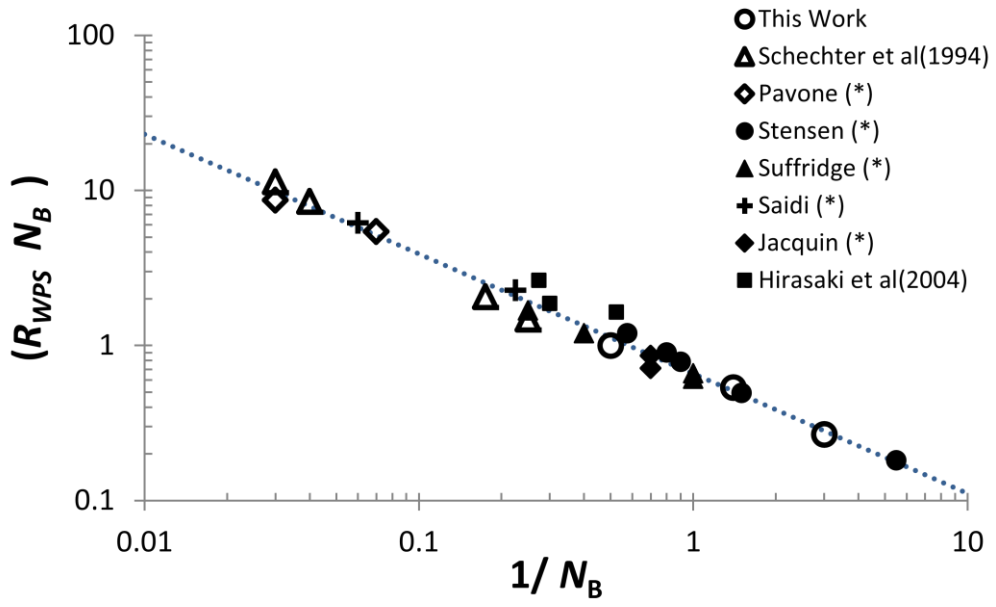

Figure 7-47 Relationship between inverse of Bond number, and the product of remaining wetting phase saturation by the Bond number.

(*) Experiments reported by Schechter *et al.* (1994).

The regression analysis from the previous plot gave:

$$R_{WPS} = 0.6579 \left(N_B^{-1}\right)^{0.22778} \qquad \textbf{(Equation 7-34)}$$

The previous equation can be used to estimate the remaining wetting phase saturation, when the wetting fluid will be displaced by another fluid in an imbibition cell.

Using Schechter's approach with the oil-saturated plugs contacted with LB+AOSC$_{16\text{-}18}$, for a 50% remaining wetting phase saturation corresponds to inverse of Bond number of 0.3, then the IFT has to be ca 0.02 mN/m (compare this with the estimated value of 0.036 mN/m listed in table 7-16). Then the imbibition is controlled by gravity drainage. If this is the case, the process can be simulated using approximate analytical solution given by Hagoort (1980) and

compared with experimental data. Results are included in fig 7-48 for both LB+AOSC$_{16-18}$ and UT Blend. Fitted values for end point relative permeabilities and Corey exponents are reasonable in both cases.

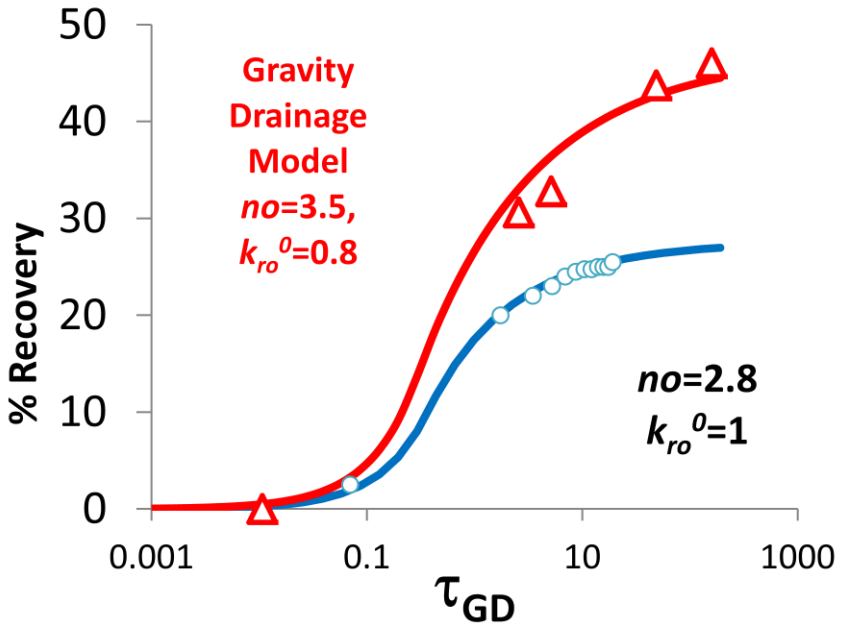

Figure 7-48 Analytical vs. experimental oil recovery. Blue circles are for " C_{15-18}IOS+ $C_{28}PO_{25}EO_{25}CO_2Na$ (1:1)" in 40mD formation cores. Red triangles are for "LB+AOSC$_{16-18}$ (2:1)" in 300mD Silurian cores.

The analytical expression for oil recovery has the form of equations 7-35 to 7-38 from Hagoort (1980), and Adibhatla and Mohanty (2007):

$$k_{ro} = k_{ro}^{0} S_o^{no}$$

(Equation 7-35) Relative permeability of oil as a wetting phase.

$$\tau_{GD} = \frac{\Delta\rho_{wo} g k k_{ro}^{0} t}{\mu_o \phi (1 - S_{or} - S_{iw}) L}$$

(Equation 7-36) Dimensionless gravity drainage time.

$$E_R = \begin{cases} 1-(1-1/no)\left(\dfrac{1}{no\, k_{ro}^{0}\, \tau_{GD}}\right)^{\frac{1}{no-1}} & \tau_{GD} > \tau_{BT} \\ k_{ro}^{0}\tau_{GD} & \tau_{GD} < \tau_{BT} \end{cases}$$

(Equation 7-37) Recovery

$$\tau_{BT} = \frac{1}{k_{ro}^{0} no}$$

(Equation 7-38) Break through

For the system LB+C_{14}AOS (2:1), the analysis is similar; but if the oil recovery is ca. 15%, it corresponds to an inverse of Bond number of 3. In this system no measurement of IFT is available, but using the Bond number of 3, the IFT should be ca. 0.165 dyne/cm. Curve fitting for this system indicates that the value of "*no*" for this blend is ca. 3.

For the LB + C_{14}AOS + BTC, the Bond number calculated from the estimation of the IFT using the sizes of drops is high, close to 17, then no oil recovery is possible by gravity drainage. However, recovery of approximately 30% was observed (fig. 7-44) as expected with BTC present.

If wettability is changed, then counter-current imbibition may occur with a maximum recovery of 30% if IFT is reduced to 0.1 dyne/cm (remaining non wetting phase saturation interpolated from Schechter's data from figure 7-50).

The theoretical recovery depends on the degree of wettability alteration. The experiment is compared with analytical solution proposed by Tavassoli *et al.*

(2005) for very strong water wet system (b), and with the empirical model by Morrow and Xie (2001) for very strongly water wet and intermediate wet (b).

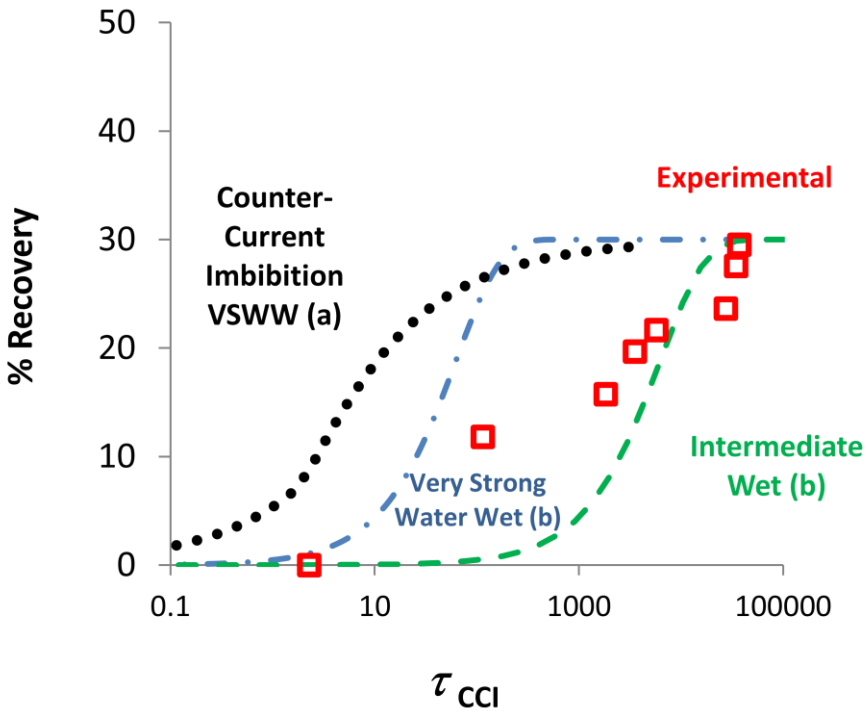

Figure 7-49 Comparison of analytical solution, empirical solution and experimental for "LB + C_{14}AOS + BTC"

To compare theoretical solution for a very strongly water wet system, a dimensionless time scale is needed. This counter-current imbibition dimensionless time is defined as:

$$\tau_{EIM} = \frac{t\sigma}{L_c^2\sqrt{(\mu_w\mu_o)}}\sqrt{\frac{k}{\phi}}$$

(Equation 7-39a) Dimensionless counter-current empirical imbibitions time by Morrow and Xie, (2001).

$$\tau_{CCI} = \frac{t\sigma}{L_c^2 \mu_o}\sqrt{\frac{k}{\phi}}$$

(Eq. 7-39b) Dimensionless countercurrent imbibitions time by Tavassoli *et al.* (2005).

And the imbibition's characteristic length is defined as:

$$L_c = \sqrt{\frac{V}{\sum \frac{A_i}{Li}}} \qquad \textbf{(Equation 7-40)}$$

Here: V= Volume of the rock sample, A_i= Surface area of the face "i", L_i = Distance from the open surface "i" to the non flow boundary.

The fig 7-49 Indicates that apparently the recovery by imbibition started as water wet, but it seems that as the process evolved, it changed to intermediate wet, requiring much time to reach the maximum recovery capacity. Then to study this kind of formulation longer and more permeable cores are recommended..

It is important to clarify that wettability changed during the process, and also the IFT; otherwise that recovery is not possible. Taking data from Orr *et al*. (1991), Schechter *et al*. (1994), the remaining non-wetting phase saturation (R_{NWPS}) is related to the inverse of Bond number as indicated in fig 7-50.

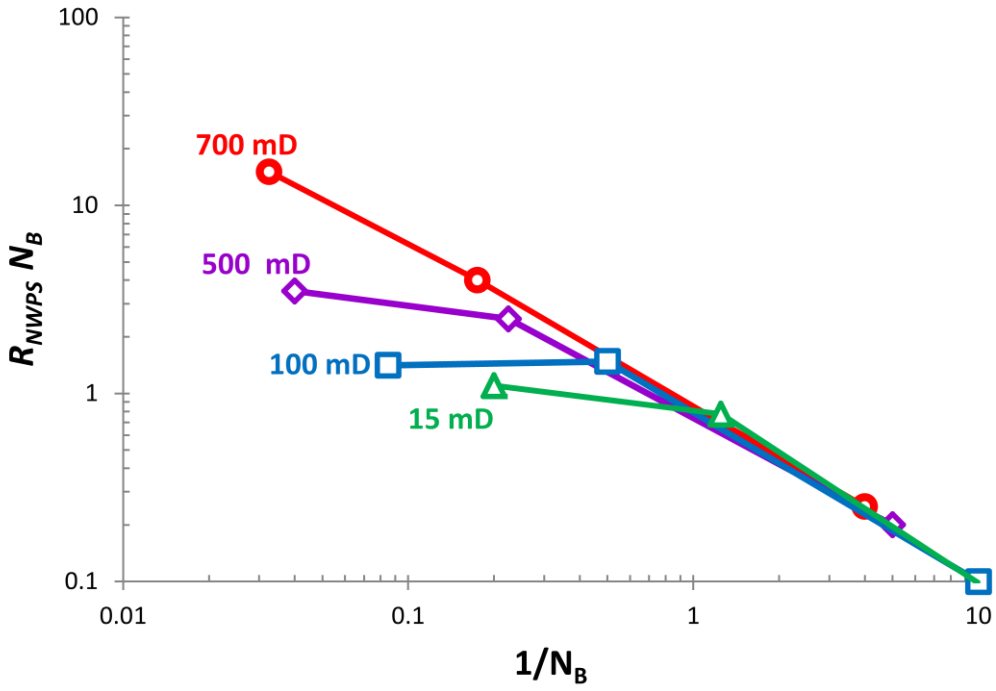

Figure 7-50 Remaining non-wetting phase saturation for different permeabilities, data adapted from Schechter *et al*. (1994)

Data from Al-Lawati *et al*. (1996) follow the same slope in log scale, but the effect of permeability in the range from 3 to 2000 mD presented almost no difference.

If it is assumed that the formulation "LB + C_{14}AOS + BTC" altered the wettability, then for a recovery of 30%, for a 300 mD rock, the inverse of Bond number has to be 0.55, corresponding to an IFT of 0.04 dyne/cm. Small droplets were never observed, only big droplets, that remained attached to the surface of the rock for long period of time. So the possibility of variations in the properties of the surfactant may explain early recovery and then the process stop after the IFT increased once the droplets were at the surface.

(See appendix 7H for analytical solution of counter current imbibitions for a strong water wet system.)

7.5 Experiments in capillaries to visualize oil recovery in gas cap.

Two groups of experiments were designed to visualize oil recovery from micro-capillaries (i.e. Borosilicate glass micro-channels filled with synthetic crude oil.):

- Immersed in aqueous surfactant solution, to verify the role of IFT and gravity in the process at 94°C.
- Placed within a glass beads packed bed aligned to the flowing foam at room temperature, to see the distribution of fluids during production using different configurations, i.e., flowing upward, downward and horizontally (*). ** flow direction kept more or less parallel to capillary*

Table 7-17 Dimensions of capillaries used

Capillary	Aperture (μm)	Width (μm)	Length (cm)
1	20	200	5
2	50	500	5
3	100	1000	5
4	200	4000	5

ε = Capillary aperture, W= Capillary width, L=Capillary length.

Within the gas cap, the rock is heterogeneous in properties, and the value of permeability can be used to classify the formation. The contrast of permeability

between fractures and matrix was used as basis for the experimental set up. The porous media represented the fractures and the micro-channels the matrix. Comparison of the permeability contrast is listed in Table 7-18.

The physical model representing the fractures and matrix was designed close to the extreme condition of permeability contrast according to figure 7-51. Using the glass beads with 23000 darcy permeability to represent the 10 darcy in the fracture, then the 100 μm, 50 μm and 20 μm micro-channels (see table 7-17), cover the three categories of matrix using the permeability contrast.

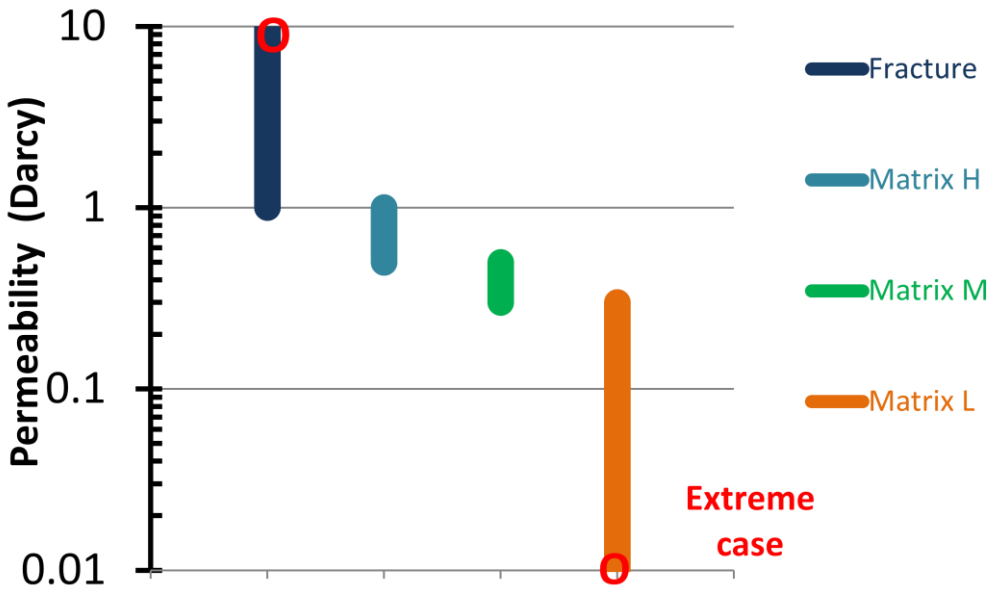

Figure 7-51 The matrix has three ranges of permeability. (Adapted from personal communication with Antonio Villavicencio, PEMEX)

Table 7-18 Comparison among permeability ratios for capillaries, glass beads and reservoir rock

Section	Permeability (darcy)			Contrast ratio
Porous media	Fracture	Matrix		
	Simulated	Simulated		
Glass beads (6 mm)	23000			
100 μm slit		690		33
50μm slit		170		135
20 μm slit		28		821
PEMEX	10		0.01	1000 *

7.5.1 Preparation of the capillary tubes

Capillaries as received were placed in vials contacting crude oil in one end and letting the crude oil fill the micro-channel by capillarity, then were aged.

Capillaries aged in crude oil before testing:

- 2 days in crude oil at 90°C, and for more than 2 weeks at room temperature.
- Then, in seawater or formation brine for one day; no crude oil was recovered at 90°C.

Note: Three 200μm capillaries were prepared. One capillary was treated with Si $(CH_3)_2Cl_2$, another with Si $(CH_3)_3Cl$, and the third without any chemical. After drying the capillaries in the oven, they were contacted and aged with simulated live oil at 120°C for a week. All of them were oil wet. No treatment was needed to warranty oil-wet capillaries for the particular simulated live oil used during the tests.

7.5.2 Oil recovery from oil filled micro-capillaries immersed in aqueous surfactant solution at 94°C

Few seconds after the half of the volume of seawater was replaced by 1% LB+$_{C16-18}$AOS in seawater surfactant solution the oil production started. Snapshots of the process are in fig. 7-52, and the curves of recovery and the theoretical expected are included in fig. 7-54

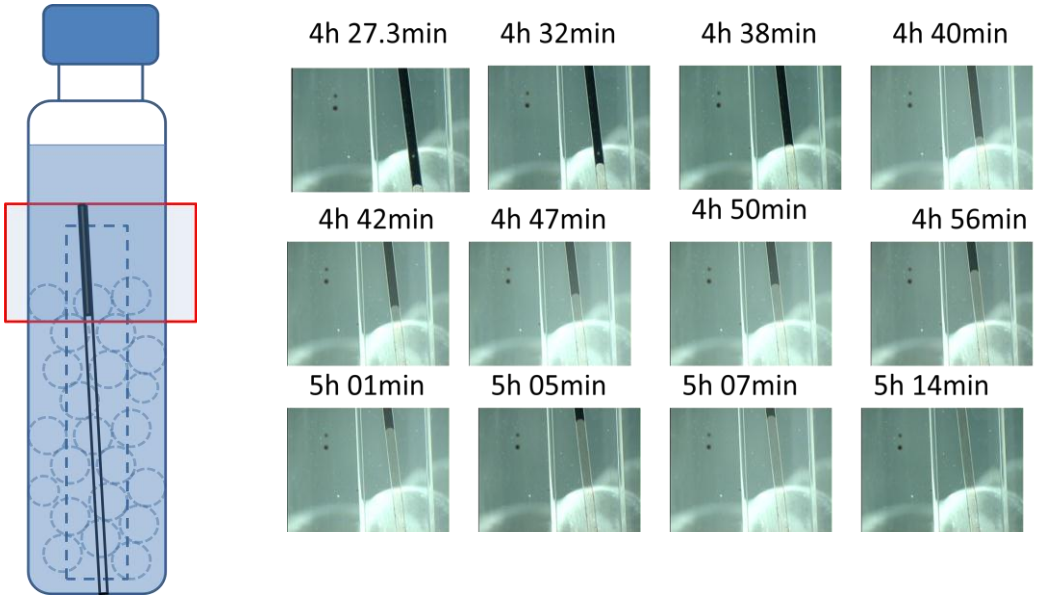

Figure 7-52 Snapshots during gravity drainage in micro-channels

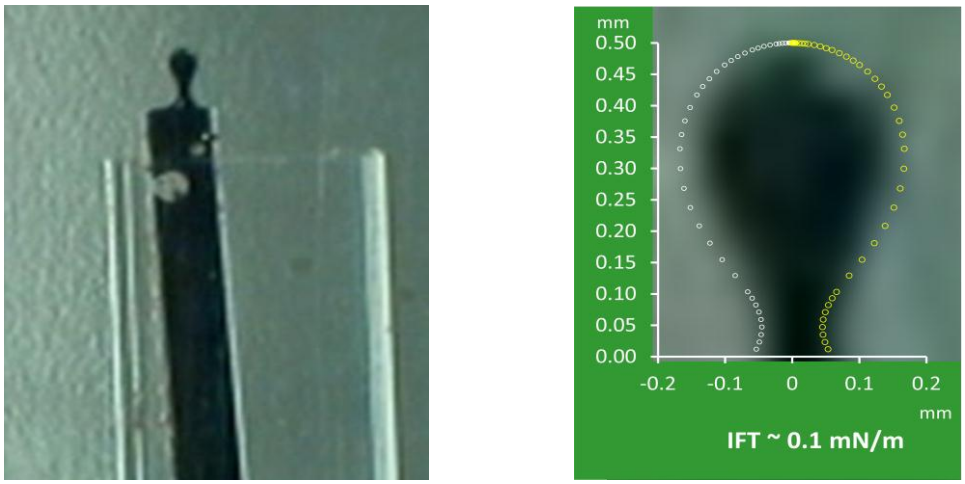

Figure 7-53 IFT Calculation by the shape of drops emerging from capillary immersed at 90°C in Rice Formulation for Pemex Gas Cap

The theoretical recovery history curve can be obtained if a reasonable IFT value is used and the proper boundary condition for the effluent is used. The production process at the outlet end has a renewing drop every time a drop detach., this can be used to measure the IFT value that has to be used for modeling the production.

In all the experiments conducted with capillaries immersed in aqueous surfactant solution the flow regime was in gravity drainage dominated regime according to the inverse of Bond number previously defined by eq. 7-30 or its equivalent for rectangular micro-channels eq. 7-41

$$N_B^{-1} = \frac{\sigma_{wo}}{\Delta\rho g L R_h} = \frac{\sigma_{wo}\left(1+\frac{\varepsilon}{W}\right)}{\Delta\rho g L(\varepsilon/2)} \qquad \textbf{(Equation 7-41)}$$

The value of IFT can be measured or estimated with the shape and size of emerging oil drops. This is not the equilibrium IFT value because the drops were detaching continually, but can be used as a reference value for the simulation.

Using the 50 μm and 100 μm capillary dimensions from table 7-16 and the IFT of 0.1 dyne/cm estimated from measurements fig. 7-53, the values for the inverse of Bond number are 0.09 and 0.045 respectively.

Using Schechter et al. (1994) approach the process corresponds to vertical flow driven by gravity forces.

Writing the quasi-steady state force balance for the flow within the capillary the governing equation is:

$$\Delta\rho \, \mathrm{g} \, \mathrm{z} - \sigma\left(\frac{1}{r_1}+\frac{1}{r_2}\right) - \sigma_o\left(\frac{1}{r_{1,o}}+\frac{1}{r_{2,o}}\right) - \frac{32\Psi\mu_o u}{D^2}\left[z+\frac{1}{M}(L-z)\right] = 0$$

(Equation 7-42a**)**

M=Viscosity ratio = μ_o/μ_w

D is the hydraulic diameter. For the capillary channel is given by:

$$D = \frac{2\varepsilon}{\left(1+\frac{\varepsilon}{W}\right)}$$

r_1,r_2 *are* curvature radii in the upstream interface, and $r_{1,o}$ $r_{2,o}$ are the curvature radii in the downstream interface between oil and brine, *g*=gravity, *z*= column of

oil, and *L*= length of capillary micro-channel, ε=aperture and *w* =width of the capillary.

The first term is the potential energy, the second and the third terms are the surface energy in the back and front ends of the crude oil, and the last term is viscous energy loss in the oil and brine filled sections. The previous equation can be written in dimensionless form to calculate the velocity of recovery, using the previously defined dimensionless numbers.

$$\zeta - \left(\frac{D}{2\varepsilon}\right) N_B^{-1} bCos\theta - \frac{\Psi}{2(1-\zeta_{\min})} \frac{d\zeta}{d\tau_{GD}} \left[\zeta + \frac{1}{M}(1-\zeta)\right] = 0$$

(Equation 7-42b**)**

$$\tau_{GD} = \frac{\Delta\rho_{wo} g D^2 t}{64\mu_o L(1-\zeta_{\min})}$$

Dimensionless time (Equation 7-43)

$$\zeta = \frac{z}{L}$$

Dimensionless length of oil column (Equation 7-44)

Here ε is the aperture, $\zeta_{\min}$ = is the remaining oil. θ = Is the angle between the capillary and the wetting fluid (in this case oil is wetting the surface. "θ" should not be confused with contact angle which is measured respect to the denser fluid in this case the aqueous phase, which is the complementary angle of θ.)

The dimensionless length of oil column represents the remaining oil saturation (or remaining wetting phase saturation "R_{WPS}", previously defined).

Recognizing that the minimum residual content is when velocity is zero, and defining normalized recovery, equation 7-42b is integrated to obtain oil recovery with equation 7-45.

$$\zeta_{\min} = \left(\frac{D}{2\varepsilon}\right) N_B^{-1} b Cos\theta$$

(Equation 7-45) Minimum remaining oil column trapped by capillary

$$E_R = \frac{1-\zeta}{1-\zeta_{\min}}$$

(Equation 7-46) Normalized oil recovery

$$E_R - \left(\frac{\frac{1}{M-1}+\zeta_{\min}}{1-\zeta_{\min}}\right)\ln\left(1-E_R\right) = \frac{2M}{\Psi\left(M-1\right)}\tau_{GD}$$

(Equation 7-47)

Equation 7-47 gives oil recovery by gravity drainage as function of gravity-drainage-dominated dimensionless time.

Normalized oil recovery equation 7-47 is implicit, but is an algebraic equation. The definition of dimensionless time used in this expression coincides with the equation 7-36 reported by Hagoort (1980).

"Ψ" is a geometric correction factor for viscous forces, 1.5 for rectangular slit and 1 for cylindrical capillary, " *b* " is the curvature correction factor 2 for rectangular slit and 4 for cylindrical geometry (see Appendix 7H for clarification) . " *D* " is the hydraulic diameter.

$$D = \frac{2\varepsilon}{\left(1+\frac{\varepsilon}{W}\right)}$$ **(Equation 7-48) for the slit**

Note that Equations 7-36 and 7-47, are equivalent after replacing diameter for hydraulic diameter for porous media.

$$D = \left(\sqrt{\frac{16b}{36}}\right)\left(\sqrt{\frac{k}{\phi}}\right)$$

(Equation 7-49) Hydraulic diameter for porous media (b=150), compare with Civian (2011)

The theoretical solution given by equation (7-47) can be plotted and compared with the experimental data using the estimated value of IFT.

The effective IFT can be estimated fitting the experimental data with the theoretical solution as indicated in figure 7-54. The resulting estimated IFT was 0.2 dyne/cm, close to the measured value of 0.1 dyne/ cm. (Note: For calculations 0º contact angle was assumed)

The product of the remaining wetting phase saturation in porous media by the Bond number is function of Bond number, but in the capillary channel the product is constant (Eq. 7-34 and 7-45).

$$R_{WPS}N_B = 2\left(\frac{D}{2\varepsilon}\right)Cos\theta \approx 1.818$$

(Equation 7-45b) Gravity drainage in capillary tubes

$$R_{WPS}N_B = \frac{0.6579}{\left(N_B^{-1}\right)^{0.772}}$$

(Equation 7-34b) Gravity drainage in porous media

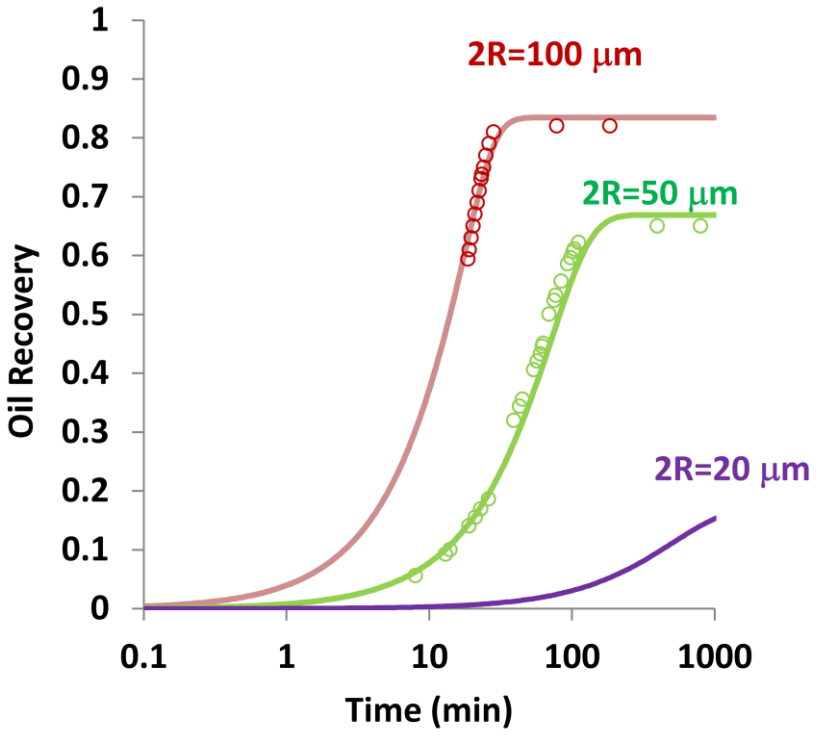

Figure 7-54 Oil recovery history curves from capillaries immersed in aqueous surfactant solution. Symbols are used for experimental data, and lines for theoretical calculations.

If a bundle of capillaries is used to model the gravity drainage of crude oil from a porous rock, it is inferred from fig 7-54 that the recovery is related with the inverse of Bond number, i.e. equation 7-45b or its equivalent for porous rock 7-34b. A comparison of normalized oil recovery is included in the Appendix 7K for porous rock and capillary channels.

From the previous experiments, it was concluded that capillaries have potential to visualize the oil recovery.

During experiment:

- Capillaries filled with crude oil.
- Capillaries aged at 90ºC for 2 weeks
- Capillaries left at room temperature for 2 days.
- No oil production when immersed for one day in synthetic seawater.
- No oil production when heated and aged for 2 days in seawater.
- Oil production started immediately after adding surfactant solution.
- As expected, the rate and final amount of oil recovery is a function of capillary dimensions.

.

7.5.3 Oil recovery from oil filled micro-capillaries immersed in foaming stream at room temperature.

The objective of the experiments in micro-channels is to visualize the distribution of phases when surrounded by foam. Two different setups were prepared (see fig 7-55); the first one is to screen potential formulations and is easy to assemble, the second one has a pressure difference between ends which can be modified by varying foam flow rate and quality. The equipment can be used to perform experiments flowing upward, downward or horizontally. (Appendix 7I)

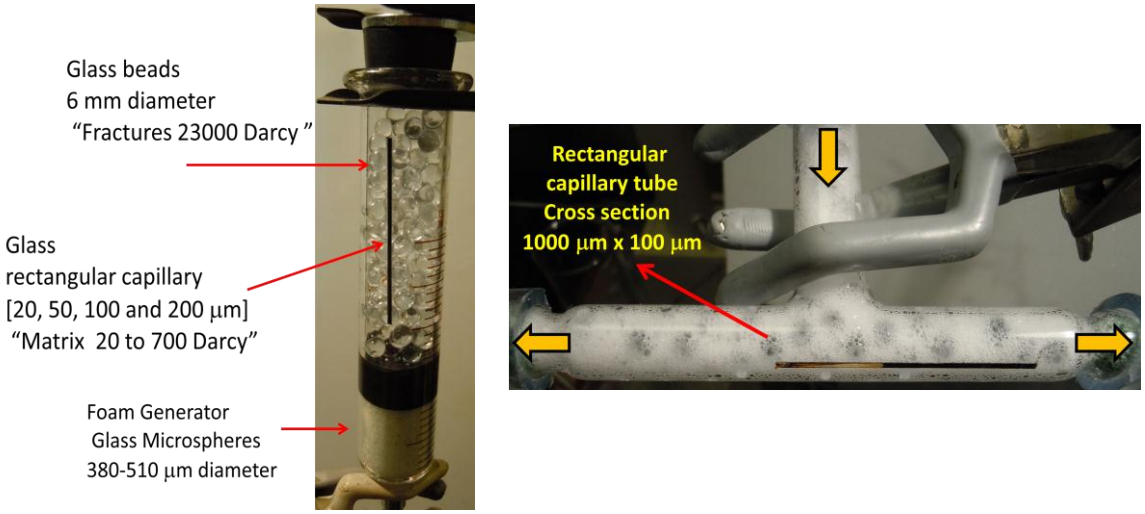

a) Setup for foam flowing upward

b) Setup to control pressure difference

Figure 7-55 Setup to study distribution of fluids within a system with contrasting permeability

Independently of the flow configuration the same pattern of distribution of fluids within the capillaries was observed in the upstream section of the rectangular capillary tube, as indicated in fig 7-56

Note: Don't confuse upstream of capillary with upstream of foaming stream.

Time between each frame	
30 sec	**10 sec**
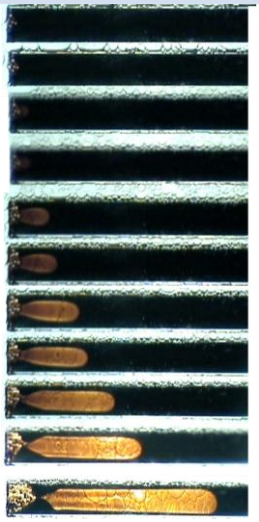	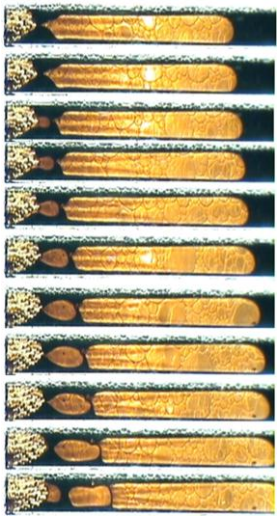

Figure 7-56 Frames taken during horizontal foam experiment, capillary and foam flows were parallels. Each frame was taken in the upstream section of the capillary. Capillary cross section is 1000 μm x 100 μm. Figure view is across the 1000 μm width.

During the oil production stage, the downstream flow was crude oil, the upstream section was predominantly aqueous surfactant solution. Close to the upstream end some foam was present, but it never propagated at rate comparable to the aqueous oil-interface. After oil-aqueous interface breakthrough, the foam started advancing at higher rate within the capillary tube. After inspection through the microscope, no sharp boundary was observed between aqueous phase and foam, see fig 7-57

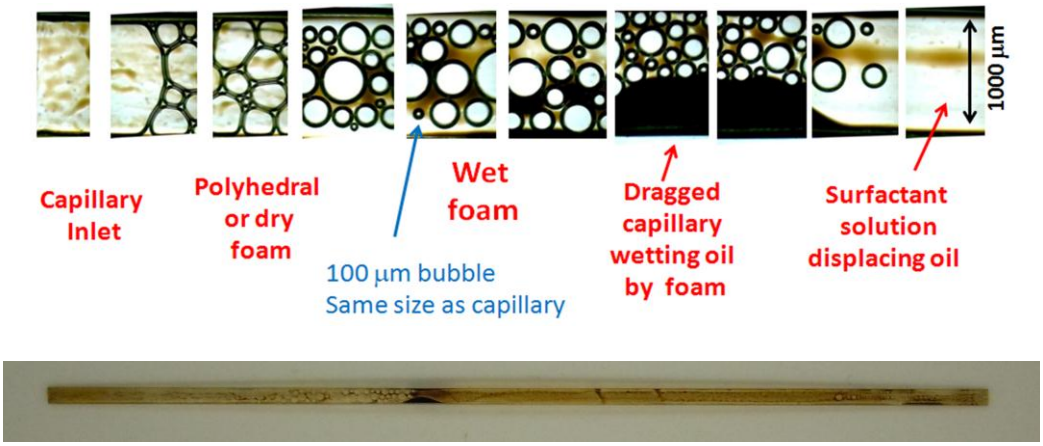

Figure 7-57 Pictures taken after foam test using 100 µm capillary. Upper frames correspond to the different sections of the capillary from upstream (left) to the downstream (right).

The theoretical recovery for the horizontal capillary can be estimated using some assumptions:

- Quasi steady state flow within the capillary tube.
- The fluid displacing oil is aqueous surfactant solution or wet foam.
- The oil and surfactant solution are Newtonian fluids.
- The pressure difference between ends of capillary tubes is close to the product of the capillary length times the pressure gradient produced by surrounding foam.

$$\left[-\frac{\nabla p_{\text{foam}}\, RL}{\sigma} - bCos\theta\right]\frac{2\sigma}{\varepsilon} - \frac{32\Psi\mu_o u}{D^2}\left[z + \frac{1}{M}(L-z)\right] = 0$$

(Equation 7-50a) Force balance

$$\frac{1}{\Psi}\left[-\frac{\nabla p_{\text{foam}}\, RL}{\sigma}-bCos\theta\right]+\left(\frac{2\varepsilon}{D}\right)\frac{d\zeta}{d\tau}\left[\zeta+\frac{1}{M}(1-\zeta)\right]=0$$

(Equation 7-50b) Dimensionless form

$$\tau=\frac{t\sigma\, D}{8L^2\mu_o}$$

(Equation 7-51)

Dimensionless time, for hydraulic diameter use eq. 7-48

Solution of equation 7-50b has the form:

$$\zeta=\sqrt{\left[1+\frac{1}{M-1}\right]^2-\tau\,\frac{2M}{\Psi}\left(\frac{D}{2\varepsilon}\right)\left[-\frac{\nabla p_{\text{foam}}RL}{\sigma}-bCos\theta\right]}-\left(\frac{1}{M-1}\right)$$

(Equation 7-52)

Ψ and b have the same values than equation 7-42b

Compare dimensionless time of eq. 7-39 with the used here, both expressions are equivalent if hydraulic diameter for porous media is used eq. 7-49

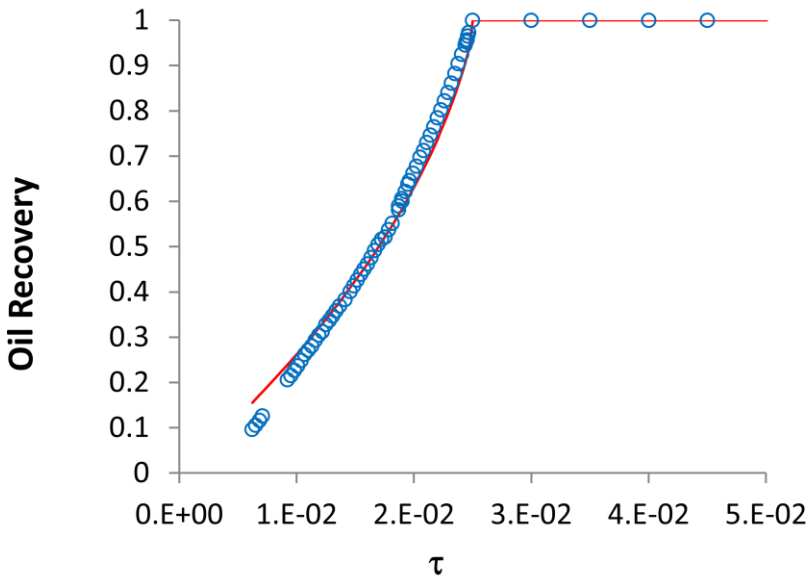

Figure 7-58 Oil recovery history curve from horizontal capillary filled with crude oil, immersed in flowing foam. Foam quality 78% and gas flow 3.5 sccm. Experimental data represented by circles, continuous line is the theoretical solution fitting the pressure gradient.

Using the dimensions of the 100 μm capillary, viscosities of 50 cP for crude oil, and 9 cP for surfactant solution, interfacial tension of 0.1dyne/cm, and via minimization of error the pressure gradient in the flowing foam was estimated close to 0.02 psi/ft. Theoretical and experimental data are included in fig 7-58

During experiments, oil production began immediately after the foam front reached the capillary end located in the upstream section of the oil within the capillary.

Foam Flowing Upward:

At test conditions for upward flow of foam, the oil production was delayed until the foam front reached the upper end of the capillary. Then oil was produced from the bottom of the capillary tube.

See figure 7-59 for video frames of the upper section during oil production.

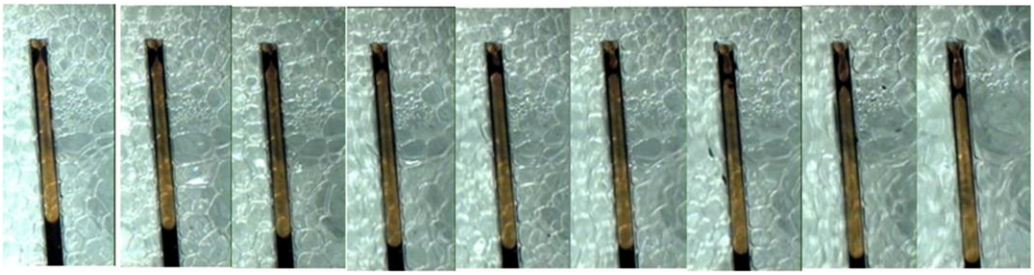

Figure 7-59 Frames of upper section of capillary every 12 s. Foam flowing upward. Capillary cross section 1000 μm x 100 μm.

The flow in vertical capillaries is similar to that of horizontal flow except that gravity and density must be taken into account.

$$\left[\frac{\Delta\rho_{wf}}{\Delta\rho_{wo}} - N_B^{-1}\left(\frac{D}{2\varepsilon}\right)bCos\theta + \frac{\nabla p_{foam}}{\Delta\rho_{wo}g} - \zeta\right] + \frac{\Psi}{2}\frac{d\zeta}{d\tau_{GD}}\left[\zeta + \frac{1}{M}(1-\zeta)\right] = 0$$

(Equation 7-53) Force balance in dimensionless form**.**

$$\alpha = \frac{\Delta\rho_{wf}}{\Delta\rho_{wo}} - N_B^{-1}\left(\frac{D}{2\varepsilon}\right)bCos\theta + \frac{\nabla p_{foam}}{\Delta\rho_{wo}g}$$

(Equation 7-54)

$$\frac{2M}{\Psi(M-1)}\tau_{GD} = \zeta - 1 + \left[\alpha + \frac{1}{M-1}\right]\ln\left(\frac{\alpha-\zeta}{\alpha-1}\right)$$

(Equation 7-55) Solution for oil recovery.

Foam flowing upward took almost double the time to recover oil, compared to the horizontal experiment, the pressure gradient estimated for the foam is 0.17 psi/ft.

Oil recovery is downward because the density difference drives the flow. The low density of foam outside the capillary compared of liquid inside has stronger effect than the pressure gradient caused by the flow of foam outside the capillary.

According to observations the possible mechanisms for oil recovery from matrix using the micro-channels as models are:

- Initially, foam transports surfactant solution, the surfactant from the Plateau borders of the foam flows into the capillary.
- Surfactant solution enters the capillary displacing oil;
- After a steady Surfactant-Oil front develops, foam starts invading the capillary

Note: By naked eye observation, during oil production no foam entered the capillary: only at the ends, some bubbles are observed as being trapped.

Foam Flowing Downward:

- Oil starts being produced immediately after the foam touches the upstream end of the capillary.
- Gravity and pressure difference, mobilize crude oil from capillary.
- The oil produced could travel within foam plateau channels and also as blobs.

These experiments in capillaries can be used to understand the mechanisms of oil recovery in the gas cap of a fractured reservoir that is oil wet.

Chapter 8

CONCLUSIONS AND RECOMMENDATIONS

The transport of surfactants in aqueous solution was studied and analyzed from two different points of view for EOR application (e.g., adsorption and mobility control as foam). Most of the surfactants used in this research are industrial surfactants, the exceptions being the alkyl polyethoxylate carboxylate, CTAB, DTAB and DDMA.

8.1 Adsorption

Adsorption / retention of surfactant blend of **$C_{28}H_{57}$ $(PO)_{25}(EO)_{25}CO_2Na$** and **$C_{15\text{-}18}$ IOS** in seawater at 94°C was measured in a dynamic process, injecting a continuous slug of surfactant. The use of two core materials of different sources was fundamental for understanding the importance of the flow conditions and rock properties (i.e. flowing fraction and surface area) during measurements. A 250 mD Silurian outcrop dolomite with high flowing fraction ca. 90% and a 3 mD formation rock with low flowing fraction ca. 27.3%, were used to represent different types of reservoir materials. For Silurian dolomite the adsorption was 0.44 mg/g of rock, and for the formation rock the adsorption was 2.09 mg/g of rock. The differences between them were directly related with the surface area. The surface areas were measured with BET technique and confirmed via NMR.

A mathematical model was proposed as a tool to study systematically results of this kind of experiment. The mathematical model allows conceptualizing the porous region in three different portions: the flowing fraction, the dendritic fraction, and the micro-porous space fraction.

The model was used and the parameters estimated with the aid of tracer experiments. Additional experimental work is recommended to guide in the prediction of the parameters for use of the model in future laboratory experiments and in extending the model for field applications.

A case study with information from literature of adsorption of betaines and anionic surfactants on dolomite by injection of a finite surfactant slug indicated that selective adsorption could be expected if blends of these surfactants were injected. Conducting dynamic adsorption experiments with such blends and simulating the results is needed to understand the behavior of EOR processes with selective adsorption.

The mathematical model and the case study, as well as the recent measurements of adsorption for a blend of $C_{16\text{-}18}$AOS and Lauryl betaine in formation rock (not presented in this dissertation, but in agreement with the case study presented) will guide in the study of adsorption in a process. That can be more complex to analyze if sacrificial agents are used to minimize the adsorption of blends that have been evaluated as good foaming and oil-displacing formulations.

The methodology to quantify surfactant concentrations in blends of carboxylate and IOS surfactants using two-phase titration at low and high pH was established. It has the advantage of being simple and inexpensive. The two-phase titrations, at low and high pH have already been adapted to analyze C_{16-18}AOS and Lauryl betaine blends. Static and dynamic adsorption measurements indicate that the adsorption occurs in selective fashion, which indicates that the ratio of the two surfactants in solution changes during transport through the formation.

Preliminary studies were done with the objective to reduce adsorption of anionic surfactant blends blend by the use of sacrificial agents. Sodium polyacrylate reduced adsorption by nearly 80%, but additional work is required for the C_{16-18}AOS and Lauryl betaine blend.

8.2 Foam

A systematic study of surfactant blends with the purpose of identify their foaming potential at 94°C in seawater in a silica sand pack permitted the selection of best candidates. This study gave additional information regarding to the behavior of surfactants in presence of oil, the behavior of foam at different fractional flows and different qualities of foam.

An existing mathematical model for foams was used to verify if by fitting parameters it was possible to predict trends observed during the different experimental tests. The model was able to reproduce experiments and predict observed behavior in steady state foam flow. However, non-uniqueness of the

parameters seems possible. Tuning of parameters will require additional foam tests at transient conditions. The experimental setup built to study foam under harsh conditions permitted collection of data with minimum noise or oscillation in the back pressure which is a challenging technical issue in this kind of experiment.

The mathematical model that uses the concept of mobility reduction factor permitted the matching of some characteristics observed in the laboratory tests, but the understanding of the physical meaning of some of the parameters will require more research.

The understanding of the rheology of foams in porous media is a subject that requires many variables to be taken into consideration and requires additional research. Studies of those good foaming candidates should be conducted using materials with permeabilities of different order of magnitude, different mineral composition, and porous media with heterogeneities in order to develop a more robust procedure to compare foams.

The developed experimental protocol to study and screen foaming formulations, will facilitate future evaluation of surfactants for foaming applications. The study should be conducted in parallel with developing a deep understanding of the physicochemical properties of the surfactants. In this initial stage some rheological properties of surfactants have been investigated, some trends were

observed, and some hypotheses were generated that will require more research to be able to better understand the relationship of properties of surfactants and foam behavior in porous media.

8.3 Corefloods

A new methodology to conduct core floods in sand packs using foaming surfactants guided by “surfactant blend ratio- salinity ratio maps” using equilibrium phase behavior to determine favorable conditions for oil recovery in such floods was presented. The methodology was applied to systems with potential to recover oil (according to reports from UT), but the systems turned out to have poor foaming potential.

Another system studied was a blend of C_9H_{19}-ϕ-$(OC_2H_4)_{8.6}SO_3Na$ + C_{20-24} IOS, which presented promising phase behavior to recover oil and better foaming characteristics than $C_{28}H_{57}(PO)_{25}(EO)_{25}CO_2Na$ blended with C_{15-18} IOS. However, the foam was not strong enough in presence of oil at low flow rates.

Using the “surfactant blend ratio- salinity ratio maps” to select favorable conditions for oil recovery during corefloods may require additional experimental data, to evaluate its advantage in the experimental and process design, using surfactant blends with potential to recover oil and potential to produce strong foams in unconsolidated and in consolidated rock.

8.4 Imbibition experiments

Imbibition experiments are important tests for the development of formulations for vuggy-fractured reservoirs. In this test the objective was to evaluate a surfactant blend that has low tension with oil and produces wettability alteration, and at the same time generates strong foam. In this case the imbibition test was done by injecting foam, then stopping flow and allowing foam to remain in contact with the rock for 2 days. Then foam injection was resumed to bring more surfactant solution into contact with the rock and recover oil produced from the matrix during the shutdown. This sequence of foam injection and shutdown was repeated several times. To conduct this experiment a cell was constructed to hold the core plug and surrounding foam and to enable separation of phases produced during every period of injection.

If foam is the fluid surrounding the matrix of rock during imbibition process, gravity may change the direction of the production as indicated in the study of mobilization of crude oil in micro-channels. Then the use of cells, where surfactant and gas can be co-injected for imbibition studies allows studying different scenarios of foaming systems for water invaded zones or gas invaded zones. The experimental set up was used to evaluate one of the surfactants under desirable foaming conditions, and results were presented for semi-batch process, co-injecting surfactant and nitrogen for short periods of time.

Additional standard (Amott) imbibition experiments were used to evaluate the role/influence of having cationic surfactants in formulations with blends with foaming potential. BTC 8358 (i.e. Benzalkonium chloride) was verified in marble rock to be a wettability alteration surfactant by itself in synthetic seawater brine. When studied as a component in a Lauryl betaine + AOS + BTC blend, it recovered less oil than LB/AOS blend itself at test conditions in the imbibition cell. No benefit was observed, but the poor performance can be because of an insufficient decrease of IFT. During this particular test with BTC added, big drops of oil were observed strongly retained on the surface of the rock, hardly detaching from the rock surface. These large drops are indicators of high IFT.

During the analysis of the performance of the different formulations, important trends in oil recovery as a function of the Bond number were observed. These trends were consistent with theoretical background, with observations done by other researchers, and with simplified tests of this work using micro-channels. The trends were generalized with a simple correlation in this research. This correlation will help in future not only to plan experiments but to predict performance of oil recovery during gravity drainage / imbibition experiments under oil wet conditions knowing the rock dimensions, porosity, permeability, phase behavior and IFT between fluids.

Initial analysis of literature experiments for water wet systems seems to follow a similar behavior, but with a strong dependence on permeability.

8.5 Studies for visualization of crude oil mobilization within micro-channels in an environment with foam

The conceptualization of how the phases will be distributed during EOR processes in heterogeneous porous media, such as in the fractures and matrix of fractured carbonate reservoirs, is a key component in the design of the process. To visualize oil recovery mechanism from matrix, a physical model constructed using micro-channels surrounded by glass beads to mimic matrix and fractures respectively was used. In this physical model the ratio of permeability between micro-channels and glass beads is approximately the same as the permeability ratio between fractures and matrix in the actual carbonate reservoir for the three zones identified.

An initial test with micro-channels completely filled with simulated live oil and treated to be oil-wet was conducted in which the micro-channels were immersed first in synthetic sea water and then in surfactant solution, both at 94°C, to determine oil recovery and characterize the mechanisms of recovery. Under test conditions, no oil was produced after immersion in sea water, but gravity mobilized the oil after IFT reduction resulting from replacing the synthetic seawater with 1% Lauryl betaine + C_{16-18} AOS 2:1 (w/w) surfactant solution. A mathematical model was presented to predict evolution of the process and the IFT was estimated. The IFT estimated coincided both with the IFT calculated

from the shape and size of drops formed during the oil production and with the value measured using the spinning drop apparatus.

Using the same concept of micro-channels filled with crude oil to represent the oil within the rock matrix, tests under different foaming conditions were performed at room temperature. Simplified mathematical models were presented for the different scenarios.

Observations in the different flow configurations indicated that at test conditions the crude oil was mobilized after reducing the IFT by contact with the aqueous surfactant solution in the upstream section of the micro-channel. The foam did not flow within the micro-channel during the oil production, but only after the breakthrough of surfactant production from the downstream section of the capillary.

Additional tests with foaming surfactants are recommended at high temperature because their viscoelastic properties are functions of temperature for the system under consideration. Studies where wettability can be altered and controlled during the recovery process should be investigated as well.

The physical model of capillary tubes was a useful tool to visualize the oil recovery and to understand the fundamental role of the gravity. In the case of foam flowing upward, the oil production at test conditions occurred at the lower

end of the capillary because the density of oil in the capillary exceeded the density of foam surrounding it.

8.6 Presence of anhydrite in the formation

The use of alkali in the formulations for EOR applications offers several benefits including lowering IFT by reaction of alkali with the acids in the crude oil to produce soaps in situ, and reducing surfactant adsorption by increasing the rock's surface negative charge. Alkali reacts with minerals in the rocks, especially strongly with anhydrite. As a result, the presence of anhydrite would produce detrimental effects on alkali/surfactant processes, even for anhydrite concentrations less than 0.1% by weight.

A methodology was presented to determine whether anhydrite is present in a formation and estimate its content. The method is based on brine software analysis of produced water compositions and inductively coupled plasma (ICP) analysis of core samples dissolved in acid. For the dolomite formation of interest the amount of anhydrite was estimated to be between 0.04 to 0.49%

Thermodynamic analysis of formation brines with existing brine software was used to calculate saturation index of minerals in a reservoir and, in particular, determine whether anhydrite is likely to be found in the formation. However, the analysis with software cannot determine the amount that is present.

The software selected for the study was compared and analyzed for reliability of the database using additional software and experimental values of solubility reported from literature for the minerals of interest under the spectrum of ionic strength studied.

X-ray powder diffraction (XRD) was used to verify the mineralogy of the rock. X-ray photoelectron spectroscopy (XPS) was used to obtain surface composition for comparison with bulk composition of the rock, XRD and XPS indicated that the formation was basically dolomite. The concentration of anhydrite in the different formation rocks analyzed by ICP was between 0.04 % and 0.49%. These concentrations are below the detection limits for the XRD and XPS.

The results obtained from the software for this project, which are strongly related with a representative chemical water analysis, seem to indicate that the methodology can be used as a tool. The methodology was successful in this case, but it is desirable to confirm its value by similar testing in other formations with different mineralogy.

NOMENCLATURE

Chapter 4

A	Debye-Hückel virial coefficient, specific for the solvent ($A=A_\gamma=3A_\phi$, Bradley and Pitzer, 1979)
A^{z-}	Anion and its charge
a_P	Activity of the ionic species p, $a_P = [P]\,\gamma_P$
B_P^{2-2}	*Second virial coefficient for 2:2 Electrolyte.(e.g. $CaSO_4$,* Lee, 2008*)*
b	b=1.2 with units of $(Im)^{-1/2}$
C^{z+}	Cation and its charge
C_P	$C_P = (3/2)\,C^\phi$ (Lee, 2008)
I_m	Molal ionic strength (gmol/ kg of water)
K^o_{SP}	Solubility product at atmospheric pressure. (i.e. equilibrium constant at 1 bar).
K_{SP}	Solubility product or equilibrium constant
m	Molality (gmol/ kg of water)
P	Pressure (Pa)
Po	Atmospheric pressure
$[P]$	Concentration of ionic species P (e.g. Na^+, K^+, Ca^{2+}, Mg^{2+}, Cl^-, SO_4^{2-}, CO_3^-, etc.)
R	Gas constant (8314.34 J /kmol-K)
SI	Saturation index

SR	Saturation ratio
T	Temperature (K)
z_+, z_-	charge of the cation (positive) and anion (negative) respectively, valences of ions.
α_1	α_1=1.4
α_2	α_2=12.0
α	α=2 (α_1=α and α_2=0 if the electrolyte is 1:1, 1:2 or 1:3)
β_0 ,β_1 ,β_2 and C^ϕ	are parameters specific to the ionic species
$\gamma_\pm$	Mean activity coefficient $\gamma_\pm = (\gamma_+^{\nu+}\gamma_-^{\nu-})^{1/\nu}$
ΔV^o_r	The change of the standard partial molal volume for the mineral dissolution
ΔK^0_r	The change of the standard compressibility of the dissolution reaction
ν_+ , ν_- ($C_{\nu+}A_{\nu-} = \nu_+ C^{z+} + \nu_- A^{z-}$) $\nu_+ z_+ + \nu_- z_- = 0$	Proportion of the cation and anion in the mineral or salt

Chapter 6

a	Parameter a in the mass transfer coefficient
a	$(L/R_{sph})^2$
A	Cross sectional area
a_{sph}	Surface area of clusters in shape of spheres containing the micropores
a_v	Surface area per unit volume
a_{v12}	Surface area per unit volume between porous fraction “i” and “j” for mass transfer exchange
a_{vij}	Surface area per unit volume between porous fraction “i” and “j”
a_{vis}	Surface area per unit volume between the flowing fraction “i” and its surrounding solid phase (i=1,2,3)
$A_{ij}^{(a)}$	First derivatives discretization matrix in axial direction. Discretization of point “i”
$A_{jk}^{(r)}$	First derivatives discretization matrix in radial direction. Discretization of point “j”
b	Dimenssionles weighting function in the advection term of the mass balance
b_1	Dimenssionles weighting function in the advection term of the mass balance for the flowing fraction
b_2	Dimenssionles weighting function in the advection term of the mass balance for the dendritic fraction
$B_{ij}^{(a)}$	Second derivatives discretization matrix in axial direction. Discretization of point “i”
$B_{jk}^{(r)}$	Laplacian operator discretization matrix in radial direction. Discretization of point “j”, Laplacian is the divergence of the gradient

C_i	All the concentrations used in the models are dimensionless concentration, i.e. actual concentration divided by the maximum concentration injected in the stream.
C_{so}	Concentration injected of surfactant.
C_i	Dimensionless concentration of tracer or surfactant in the porous fraction "i" (i=1,2,3). 1 is for flowing fraction, 2 for dendritic fraction and 3 for micro porosity
C_3^c	Dimensionless concentration of tracer or surfactant in the surface of the cluster of rock enclosing the micropores.
C_i^s	Dimensionless concentration of surfactant in the surface or rock contacting the porous fraction "i" (i=1,2,3). 1 is for flowing fraction, 2 for dendritic fraction and 3 for micro porosity
C_3^{surf}	Dimensionless concentration of surfactant in the surface of the grains composing the cluster of micropores.
C_{ki}	Concentration of tracer or surfactant in the porous fraction "k" (k=1,2,3) at the point "i" of axial discretization (i=1,2,3…,n)
C_{3ik}	Concentration of tracer or surfactant in the micro porous space in the point of axial discretization "i" (i=1,2,3,…,n) and in the radial discretization point k of the micro porous space (k=1,2,3,…,m)
D	Dispersion coefficient
D_1	Dispersion coefficient in the flowing fraction
D_2	Dispersion / Diffusion coefficient in the dendritic fraction
D_3	Diffusion coefficient in the micro porous fraction
$\underline{\underline{D}}_i$	Dispersion tensor in the porous fraction "i"
E	Electrode potential

E^o	Reference electrode potential
F	Faraday constant F = 96,485.3365 C/mol
f, f_1	Flowing fraction porous space ϕ_1/ϕ
f_2	Dendritic or meso fraction of porous space ϕ_2/ϕ
f_3	Micro porous space ϕ_3/ϕ
Fi or $F_i(C_i)$	Function, relating the concentration on the surface in equilibrium with the concentration in the surrounding medium $C_i^s = F_i(C_i)$
F_i'	Derivative of the Langmuir isotherm or any other isotherm relationship in the porous fraction "i"
$g_i(C_i^s)$	Relationship between the surface concentration to the apparent concentration adsorbed per unit volume of the fraction of rock in contact with the porous fraction "I". $g_i(C_i^s)=d\Gamma_i/d\,C_i^s$
h	Parameter in a double capacitance model weighting the dispersion
Ki,j	Nikolsky-Eisenman, selectivity coefficients
k_{cij}	Mass transfer coefficient between porous fraction "i" and "j"
k_1	Coefficient of dependence of dispersion respect to powered n1 velocity
k_2	Coefficient of dependence of the mass transfer coefficient respect to powered n2 velocity
k_c	Mass transfer coefficient
K	Langmuir adsorption constant
k_{cis}	Mass transfer coefficient between porous fraction "i" and its surrounding surface
ks	Saturation constant in Langmuir model
k_{perm}	Permeability (Only in this chapter)

L	Length of the porous core
n_1	exponent of the velocity in the dispersion coefficient
n_2	Exponent of the velocity in the mass transfer coefficient
ni	Number of moles of electrons in the electrode
N_{Pe}	Peclet number
N_{Pei}	Peclet number in the porous fraction “i”
N_{Peij}	Peclet number between fraction “i” and “j”
N_{St}	Stanton number o mass transfer dimensionless number
N_{Stij}	Stanton number o mass transfer dimensionless number between flowing fraction “i” and “j”
p_{ij}	Perimeter of surface perpendicular in axial direction of exchange surface between porous fraction “i” and “j”
R	Universal gas constant 8.3144621 j/(K-mol)
R	Equivalent radius of clusters of micro porous material
r	Radial distance from the center of the cluster of micro porous material
T	Absolute temperature
t	time
u_o	Superficial velocity
v_i	Velocity in the porous fraction “i”
$\underline{v}_i$	Velocity vector in the porous fraction “i”
V	Volume
zi	Valence of charge in an ion
γ_i	Activity coefficient of chemical component “i”
Γ_i	Surface concentration in the rock in contact with the porous region “i”

ϕI , φ_i	Void fraction of the porous region “i” (i=1,2,3)
Δx	Differential in axial direction
ψ	Laplace transform of concentration in the flowing fraction
Ξ	Laplace transform of concentration in the dendritic fraction of porous space
τ	Dimensionless time, or pore volumes
χ	Dimensionless axial direction, x/L
ζ	Dimensionless radial direction within the micro porous cluster r/R

Bodenstein or Péclet number:	$N_{Pe1} = \frac{u_0 L}{\varphi D_1}$	$N_{Pe23} = \frac{u_0 L}{\varphi D_3}$
Stanton number	$N_{St12} = \frac{k_{c12} a_{v12} L}{u_0}$	$N_{St23} = \frac{k_{c23} a_{v23} L}{u_0}$
Pore volumes number	$\tau = \frac{t\, u_0}{\varphi L}$	
Dimensionless distance and radius	$\chi = \frac{x}{L}$	$\zeta = \frac{r}{R_{sph}}$
Laplace transform:	$\mathbb{C}(s) = \int_0^\infty e^{-st} C(t)\, dt$	
Flowing, Dendritic and the Micro-porosity fractions respectively. (f_1,f_2 and f_3) $f_1 = \frac{\varphi_1}{\varphi}, f_2 = \frac{\varphi_2}{\varphi}, f_3 = \frac{\varphi_3}{\varphi}$		

Chapter 7

A	Heat exchanger are
A	Cross sectional area
Ai	Surface area of face “I” for imbibition
B	Capillary constant
b	Curvature correction factor
b1	Constant for equation 7-17
Cp	Specific heat capacity of the fluid.
C_s	Surfactant concentration
C_{smax}	Maximum surfactant concentration
D	Hydraulic diameter
epcap	exponent of the mobility reduction factor equation in low quality regime
epdry	Parameters for contribution for water saturation, in the mobility reduction factor model.
epn	Exponent of capillary number effect in foam strength
epo	Exponent for effect of oil in foam strength
epv	Exponent for effect of gas velocity in the mobility reduction factor model
E_R	Efficiency recovery
Fi	Contribution of mobility reduction factor (1 for surfactant, 2 for water saturation, 3 for oil, 4 gas velocity effect, 5 shear thinning in low quality regime and 6 critical capillary number)

fmcap	Parameter in shear thinning at low quality regime
fmdry	Parameters for contribution for water saturation, in the mobility reduction factor model.
fmmob	Parameter for relative permeability reduction factor equation
f_{obj}	Objective equation to minimize error in gas relative permeability
g	Gravity constant, 9.80665m/s^2
H , h	Height
ID	Internal diameter
J	Leverett J Function
K, k	Permeability
k^f_{rgT}	relative permeability of gas as foam
k_{rg}	Relative permeability of gas
k_{ri}	Relative permeability for component “i”
k_{ri}^0	Endpoint relative permeability for phase i, (i=1 for displacing fluid, 2 for displaced fluid, w for water, g for gas and o for oil)
k_{rw}	Relative permeability of water
k_{rw}^0	Endpoint relative permeability for water
L	Length
Lc	Effective Length or equivalent length for imbibition experiment
L_{Sh}	Schechter Characteristic Length
M^o	Mobility ratio defined by equation 7-4
M	Viscosity ratio between oil and surfactant
N_B	Imbibition Porous Bond number

N_{Bo}	Capillary Bond number by equation 7-2
N_{Ca}	Capillary number by equation 7-1
N_{Caref}	Capillary number of reference for effect in foam
n,no,nw,ng	Corey exponent for relative permeability for oil, water and gas
N_T	Trapping number
NTU	Number of transfer units (dimensionless) = $U A / (\rho q Cp)$
p	Pressure
P_c	Capillary pressure
q	volumetric flow rate
q_i	Volumetric flow for component i (i=1,2,w,o,g) 1 =displacing, 2 = displaced, w=water, g=gas, o=oil
R	Half of the path in the capillary channel
r_i	Radius of curvature
r_{apex}	Radius of curvature at the apex
R_h	Hydraulic radius.
R_{WPS}	Residual wetting phase saturation
S_o	Oil saturation
S_{iw}	Irreducible water saturation
S_{omax}	Oil saturation maximum to produce foam coalescence
S_{ro} S_{or}	Saturation of residual Oil
S_{row}	Saturation of residual oil after water flood
S_w	Water saturation

S_{wc}	Conate water saturation
S_{gr}	Residual gas saturation
Ti	Constants for saturation curves.
U	Heat transfer coefficient
u	Superficial velocityor Darcy velocity
u_g	Superficial velocity of gas
u_{gref}	Shear thinning reference gas velocity
$Ux= u$	Velocity for stability criterion
W,w	Width in the capillary channel
α	Dip angle respect to horizontal, dimensionless group from equation 7-54
α_{BC}	Brooks and Corey constant for capillary pressure equation
$\Delta\rho$	Density difference between water and oil
$\Delta\rho_{ij}$	Density difference between phase i and j (k=i,j,o,w,f,g)
ε	Aperture of capillary rectangular micro-channel
ζ	Dimensionless length (z/L or z/H)
ζ_{min}	Minimum dimensionless length
λ	Parameter for capillary pressure, Brooks and Corey
μ	Viscosity
μ_{app}	Apparent viscosity of foam
μ_i	Viscosity of phase i
μ_{ref}	Viscosity of reference

θ	Contact angle
ρ_i	Density of component I, (i=1,2,w,o,g,f) 1=displacing, 2 = displaced, w=water, g=gas, o=oil, f= foam)
σ	Interfacial tension, or exponent of shear thinning effect
σ_{wg}	Surface tension between water and gas
σ_{BT}	Break through dimensionless time
σ_{ow}	IFT between oil and water
τ_{EIM}	Dimensionless empirical imbibition time
τ_{GD}	Dimensionless time for gravity drainage dominated process
ϕ	Porosity
Ψ	Hydraulic correction factor for viscous flow, 1 for cylinder and 1.5 for thin slit
∇p	Pressure gradient

REFERENCES

Abboud, J.L.M and Notario, R. 1999. Critical Compilation of Scales of Solvent Parameters. Part I. Pure, Non-Hydrogen Bond Donor Solvents. *Pure Appl. Chem*., **71**(4): 645–718.

Acosta, E., Szekeres, E., Sabatini, D.A. and Harwell, J.H. 2003. Net-Average Curvature Model for Solubilization and Supersolubilization in Surfactant Microemulsions. *Langmuir,* **19**: 186-195.

Acosta, E., 2008. The HLD–NAC equation of state for microemulsions formulated with nonionic alcohol ethoxylate and alkylphenol ethoxylate surfactants. *Colloids and Surfaces A: Physicochem. Eng. Aspects* **320**: 193–204.

Adibhatla, B. and Mohanty, K.K. 2006. Oil Recovery from Fractured Carbonates by Surfactant-Aided Gravity Drainage: Laboratory Experiments and Mechanistic Simulations. *SPE/DOE Symposium on Improved Oil Recovery,* Tulsa, Oklahoma, USA.

Adibhatla, B. and Mohanty, K.K. 2007. Simulation of Surfactant-Aided Gravity Drainage in Fractured Carbonates. *SPE Reservoir Simulation Symposium.* Houston, Texas, U.S.A.

Adibhatla, B. and Mohanty, K.K. 2008. Oil Recovery from Fractured Carbonates by Surfactant-Aided Gravity Drainage: Laboratory Experiments and Mechanistic Simulations. *SPE Reservoir Evaluation & Engineering,* **11**(1): 119-130.

Adkins, S., Arachchilage, G.P., Solairaj, S., Lu, J., Weerasooriya, U. and Pope, G. A. 2012. Development of thermally and chemically stable large-hydrophobe alcoxy carboxylate surfactans. *SPE Improved Oil Recovery Symposium,* Tulsa, Oklahoma, USA.

Alai, M., Sutton, M. and Carroll, S. A. 2005. Evaporative Evolution of a Na-Cl-NO_3-K-Ca-SO_4-Mg-Si Brine at 95ºC: Experiments and Modeling relevant to Yucca Mountain, Nevada, USA. *Geochemical Transactions* **6**(2): 31-45.

Al-Ahmadi, H.A. and Wattenbarger, R.A. 2011. Triple-Porosity Models: One Further Step towards Capturing Fractured Reservoir Heterogeneity. *Saudi Aramco Journal of Technology* :52-65.

Al-Lawati, S.and Saleh, S. 1996. Oil Recovery in Fractured Oil Reservoirs by Low IFT Imbibition Process*. SPE Annual Technical Conference and Exhibition,* Denver, Colorado.

Alshehri, A. J., Sagatov, E. and Kovscek, A.R. 2009. Pore-Level Mechanics of Forced and Spontaneous Imbibition of Aqueous Surfactant Solutions in Fractured Porous Media. *SPE Annual Technical Conference and Exhibition*, New Orleans, Louisiana.

Alvarez, J.M. 1998. Foam flow behavior in porous media: effects of flow regime and porous-medium heterogeneity. UT Austin Thesis.

Amyx, J. W., Bass, Jnr. D. M., Whiting, R. L. : Petroleum Reservoir Engineering, McGraw-Hill, 1960

Anderson, Glen Allen. 2006. Simulation of Chemical Flood Enhanced Oil Recovery Processes Including the Effects of Reservoir Wettability. UT Austin Thesis.

Apaydin, O.G. and Kovscek, A.R. 2000. Transient Foam Flow in Homogeneous Porous Media: Surfactant Concentration and Capillary End Effects. S*PE/DOE Improved Oil Recovery Symposium* Tulsa, Oklahoma*.*

Aronofsky, J.S., Masse L. and Natanson, S.G. 1958. A Model for the Mechanism of Oil Recovery from Porous Matrix Due to Water Invasion in Fractured Reservoirs. Petroleum Transactions, AIME, 213: 17-19.

Arora, S. and F. Potůček, F. 2009. Modelling of Displacement Washing of Packed Bed of Fibers. *Brazilian Journal of Chemical Engineering* **26** (2): 385-393

Babadagli, T., Al-Bemani, A. and Boukadi, F. 1999. Analysis of Capillary Imbibition Recovery Considering the Simultaneous Effects of Gravity, Low IFT, and Boundary Conditions. SPE Asia Pacific Improved Oil Recovery Conference, Kuala Lumpur, Malaysia.

Bai, M., Elsworth, D. and Roegiers, J-C. 1993. Multiporosity/Multipermeability Approach to the simulation of Naturally Fractured Reservoirs. *Water Resources Research* **29**(6): 1621-1633.

Bai, M, and Elsworth, D. 1995. On the Modeling of Miscible Flow in Multi-Component Porous Media. *Transport in Porous Media* **21**(1): 19-46.

Bai, M., Elsworth, D., Inyang, H.I. and Roegiers, J.-C. 1997. Modeling Contaminant Migration with Linear Sorption in Strongly Heterogeneous Media. *Journal of Environmental Engineering* **123**(11): 1116-1125.

Bai, M., Shu, Z., Cao, J., Zaman, M. and Roegiers, J.-C. 1999. A semi-analytical solution for a two-dimensional capacitance model in solute transport. *Journal of Petroleum Science and Engineering* **22** (4): 275–295.

Bai, M. and Elsworth, D. *Coupled Processes in Subsurface Deformation, Flow, and Transport*. Asce Press. (2000). Chapter 4.

Bai, M. and Roegiers, J.-C. 1997. Triple-porosity analysis of solute transport. *Journal of Contaminant Hydrology* **28**(30): 247-266.

Baker, L.E. 1977. Effects of Dispersion and Dead-End Pore Volume in Miscible Flooding. *Society of Petroleum Engineers Journal* **17**(3): 219-227.

Bansal, V.K. and Shah, D.O. 1978. The Effect of Addition of Ethoxylated Sulfonate on Salt Tolerance, Optimal Salinity, and Impedence Characteristics of Petroleum Sulfonate Solutions. *Journal of Colloid and Interface Science* **65**(3): 451-459.

Bares, M. 1969. Two-phase Titration of Soap in Detergents. *Tenside* 6: 312-316.

Barnes, H.A., Hutton, J.F., Walters K. *An Introduction to Rheology*. Elsevier (1989). pp 38-54.

Bavière, M. *Basic Concepts in Enhanced Oil Recovery*, CRAC 33. Elsevier (1991).

Beerbower, A. and Hill, M. *McCutcheon's Detergents and Emulsifiers*, Allured Publishing Co. (1971).

Bernard, G. G. and Jacobs, W.L 1965. Effect of Foam on Trapped Gas Saturation and on Permeability of Porous Media to Water. *SPE Journal* **5**(4): 295-300.

Blaker, T. Celius, H.K. Lie, T. Martinsen, H.A. Rasmussen, L. and Vassenden, F. 1999. Foam for Gas Mobility Control in the Snorre Field: The FAWAG Project. *SPE Annual Technical Conference and Exhibition*, Houston, Texas.

Blount, C.W. and Dickson, F.W. 1973. Gypsum-Anhydrite Equilibria in Systems $CaSO_4$-H_2O and $CaSO_4$-NaCl-H_2O. *American Minerologist, **58**: 323-331*

Bouhroum, A. and Bal, M. 1996. Experimental and Numerical Simulation of Solute Transport in Heterogeneous Porous Media. *International Journal For Numerical And Analytical Methods In Geomechanics* **20**(3): 155- 171.

Bourrel, M. and Schechter, R.S. *Microemulsions and Related Systems, formulation, solvency, and physical properties*. Editions TECHNIP. (2010).

Brigham, W.E. 1974. Mixing Equations in Short Laboratory Cores. *Society of Petroleum Engineers Journal* **14**(1): 91-99.

Brigham, W.E., Reed, P.W. and Dew, J.N. 1961. Experiments of Mixing During Miscible Displacement in Porous Media. *Society of Petroleum Engineers Journal* **1**(1): 1-8.

Brooks, R.H. and Corey, A.T. Hydraulic Properties of Porous Media. *Hydrology Papers Colorado State University*. March, 1964.

Brunauer, S., Emmett, P.H. and Teller, E. 1938. Adsorption of Gases in Multimolecular Layers. *Journal of the American Chemical Society* **60**(2): 309-319.

Brusseau, M. L., Jessup, R. E. and Rao, P.S. 1989. Modeling the Transport of Solutes Influenced by Multiprocess Nonequilibrium. *Water Resources Research* **25**(9): 1971-1988.

Carmona, I., Schechter, R.S., Wade, W.H. and Weerasooriya, U. 1985. Ethoxylated Oleyl Sulfonates as Model Compounds for Enhanced Oil Recovery. *SPE Journal* **25**(3): 351-357.

Carreau, Pierre J., De Kee, Daniel and Chhabra, Raj P. *Rheology of Polymeric Systems*. Hanser, (1997).

Carta, G. 1988. Exact Analytic Solution of a Mathematical Model for Chromatographic Operations. *Chemical Engineering Science* **43**(10): 2877-2883.

Chen, P. and Mohanty, K. K. 2012. Surfactant-Mediated Spontaneous Imbibition in Carbonate Rocks at Harsh Reservoir Conditions. *SPE Improved Oil Recovery* held in Tulsa, Oklahoma.

Cheng, Liang. 2002. Modeling and Simulation Studies of Foam Processes in Improved Oil Recovery and Acid-Diversions. UT Austin Thesis.

Cheng, L., Reme, A.B., Shan, D., Coombe, D. A. and Rossen, W. R. 2000. Simulating Foam Processes at High and Low Foam Qualities. SPE Improved Oil Recovery Symposium, Tulsa, Oklahoma.

Chrysikopoulos, C.V., Roberts P.V. and Kitanidis, P.K. 1990. One-Dimensional Solute Transport in Porous Media With Partial Well-toWell Recirculation: Application to Field Experiments. *Water Resources Research* **26**(6): 1189-1195.

Civan, Faruk. Porous Media Transport Phenomena. John Wiley & Sons. (2011).

Coats, K.H. and Smith, B.D. 1964. Dead-End Pore Volume and Dispersion in Porous Media. *Society of Petroleum Engineers Journal* **4**(1): 73-84.

Cohen, L., Moreno, A. and Berna, J.L. 1997. Two phase titration of anionic surfactants – a new approach. *Tenside Surf. Det.* **34**:183-185.

Corapcioglu, M.Y.,Yoon, Sunhee and Chowdhury,S. 2009. Pore-Scale Analysis of NAPL Blob Dissolution and Mobilization in Porous Media. *Transp. Porous Med.,* 79: 419–442.

Corapcioglu, M.Y., Cihan, A. and Drazenovic, M. 2005. Hydrodynamics of an air bubble motion in porous media. *3rd Biot Conference on Poromechanics*, Norman, Oklahoma, USA.

Correa, A.C., Pande, K.K, Rayme, Jr.H.J. and Brigham, W.E. 1990. Computation and Interpretation of Miscible Displacement Performance in Heterogeneous Porous Media. *SPE Reservoir Engineering* **5**(1):69-78.

Croft, D.T., Friday, D.K. and Mahle, J.J. 1996. Evaluation of Post-Treatment Filter part 2: Modeling Laboratory-Scale Filter Breakthrough Data. ERDEC-TR-317: 1-25.

Delshad, M., Najafabadi, N.F., Anderson, G.A., Pope, G.A., and Sepehmoori, K. 2006. Modeling Wettability Alteration in Naturally Fractured Reservoirs. *Symposium on Improved Oil Recovery*. Tulsa, Oklahoma, USA

de Gennes, P-G., Brochard-Wyart, F. and Quéré, D. *Capillarity and Wetting Phenomena*. Springer. (2004).

deVries, J.E. 1998. Surface Characterization Methods—XPS, TOF-SIMS, and SAM A Complimentary Ensemble of Tools, *Journal of Materials Engineering and Performance,* **7**(3): 303-311.

Di Carlo, D.A. and Jessen, K. 2007. Simulation of Compositional Gravity Drainage Processes. *SPE Annual Technical Conference and Exhibition*, Anaheim, California, U.S.A.

DOE Handbook of methods for the analysis of the various parameters of the carbon dioxide systems in seawater; version 2, A.G. Dickson & C. Goyet, eds., ORNL/CDIAC-74 (1994)

Dombrowski, H.S. and Brownell, L.E. 1954. Residual Equilibrium Saturation of Porous Media. Industrial and Engineering Chemistry **46**(6): 1207-1218.

Du Prey, E. Lefebvre. 1978. Gravity and Capillarity Effects on Imbibition in Porous Media. *SPE Journal* **18**(3): 195-206.

Epton, S.R. 1947. A Rapid Method of Analysis for Certain Surface-Active Agents. *Nature*, 160: 795-796.

Exerowa, D. and Kruglyakov, P.M *Foam and Foam Films*. Elsevier (1998).

Falls, A.H., Musters, J.J. and Ratulowski, J. 1989. The Apparent Viscosity of Foams in Homogenous Bead Packs. *SPE Reservoir Engineering* **4**(2): 155-164.

Fanchi, John R. *Principles of Applied Reservoir Simulation.* 3rd edition. Elsevier, 2006.

Friedmann, F., Chen, W.H. and Gauglitz, P.A. 1991.Experimental and Simulation Study of High-Temperature Foam Displacement in Porous Media. *SPE Reservoir Engineering Journal* **6**(1): 37-45.

Ganjali, M.R. Norouzi, P., Golmohammadi, M., Rezapour, M. and Salavati-Niasari, M. 2004. Novel Bromide PVC-Based Membrane Sensor Based on Iron(III)-Salen. *Electroanalysis* **16**(11): 910-914.

Garnes, J.M., Mathisen, A.M., Scheie, A. and Skauge, A. 1990. Capillary Number Relations for Some North Sea Reservoir Sandstones. *Symposium on Enhanced Oil Recovery, Tulsa, Oklahoma.*

George, A.L. and White, G.F. 1999. Optimization of the methylene blue assay for anionic surfactants added to estuarine and marine water. *Environmental Toxicology and Chemistry,* **18**(10): 2232-2236.

Gerkea, H.H., and Kohne, J.M. 2004. Dual-permeability modeling of preferential bromide leaching from a tile-drained glacial till agricultural field. *Journal of Hydrology* **289**(1-4): 239–257.

Gottfied, B.S., Guilinger, W.H. and Snyder, R.W. 1966. Numerical Solutions of the Equations for One-Dimensional Multi-Phase Flow in Porous Media. *Society of Petroleum Engineers Journal.* **6**(1): 62-72.

Goudarzi, Ali. 2011. Modeling Wettability Alteration in Naturally Fractured Carbonate Reservoirs. UT Austin Thesis.

Guo, X., Rong, Z. and Ying, X. 2006. Calculation of hydrophile–lipophile balance for polyethoxylated surfactants by group contribution method. *Journal of Colloid and Interface Science* **298**(1): 441-450.

Gupta, S.P. and Trushenski, S. P. 1979. Micellar Flooding- Compositional Effects on Oil Displacement. *Society of Petroleum Engineers Journal* **19**(2):116-128.

Gwo, J.P, Jardine, P. M. and Sanford, W. 2005. Effect of Advective Mass Transfer on Field Scale Fluid and Solute Movement: Field and Modeling Studies At A Waste Disposal Site In Fractured Rock At Oak Ridge National Laboratory, Tennessee, USA . *Hydrogeology Journal* **13**(4): 565–583.

Gwo, J.P, Jardine, P. M. and Sanford, W.E. 2005. Modeling field-scale multiple tracer injection at a low-level waste disposal site in fractured rocks: Effect of multiscale heterogeneity and source term uncertainty on conceptual understanding of mass transfer processes. *Journal of Hydrology* **77**(1-2): 91-118.

Gwo, J.P, Jardine, P. M., Wilson, G.V. and Yeh, G.T. 1995. A Multiple-Pore Region Concept to Modeling Mass Transfer in Subsurface Media. *Journal of Hydrology* **164**(1-4): 217:237.

Gwo, J.P, Jardine, P. M., Wilson, G.V. and Yeh, G.T. 1996. Using a Multiregion Model to study the effects of advective and diffusive mass transfer on local physical nonequilibrium and solute mobility in a structured soil. *Water Resources Research* **32**(3): 561-570.

Haefliger, O.P. 2003. Universal Two-Dimensional HPLC Technique for the Chemical Analysis of Complex Surfactant Mixtures *Anal. Chem*. **75**(3): 371-378.

Hagoort, J. 1980. Oil Recovery by Gravity Drainage. *SPE Journal* **20**(3): 139-150.

Hall, D.G. 1996. Ion-Selective Membrane Electrodes: A General Limiting Treatment of Interference Effects. *J. Phys. Chem*. **100**: 7230-7236.

Hamon, G. and Vidal, J. 1986. Scaling-Up the Capillary Imbibition Process from Laboratory Experiments on Homogeneous and Heterogeneous Samples. SPE European Petroleum Conference , 20-22 October 1986, London, United Kingdom

Hayami, Y. 1996. The influence of asymmetry in drop shape on an interfacial tension measurement. *Colloid & Polymer Science* **274**(7): 643-647.

Hayashi, K. 1975. A Rapid Determination of Sodium Dodecyl Sulfate with Methylene Blue. *Analytical Biochemistry* **67**(2): 503-506

Hirasaki, G.J. and Lawson, J.B. 1985. Mechanisms of Foam Flow in Porous Media: Apparent Viscosity in Smooth Capillaries, *SPE Journal* **25**(2): 176-190.

Hirasaki, G.J. and Zhang, D.L. 2004. Surface Chemistry of Oil Recovery from Fractured, Oil-Wet, Carbonate Formations. *SPE Journal* **9**(2): 151-162.

Hirasaki, G.J., Miller, C.A. Szafranski, R., Lawson, J.B. and Akiya, N. 1997. Surfactant/Foam Process for Aquifer Remediation. *SPE International Symposium on Oilfield Chemistry*, Houston,Texas.

Hirasaki, G.J., Miller, C.A., Szafranski, R., Lawson, J.B., Tanzil, R.E, Jackson, Londergan, J. and Meinardus, H. 1997. Field Demonstration of the Surfactant/Foam Process for Aquifer Remediation. *SPE Ann. Tech. Conf. and Exhibition*, San Antonio,Texas.

Hirasaki, G.J, Miller, C.A and Pope, G.A. 2005. Surfactant Based Enhanced Oil Recovery and Foam Mobility Control. Semi Annual Technical Report.

Holmberg, K. Handbook of Applied Surface and Colloid Chemistry, Volumes 1-2 John Wiley, 2002.

Huber, H.F. and Curt, T.1970**.** Adsorption of Toluene-Soluble Polymers at the Toluene-Water Interface. *Journal of Polymer Science,* **8**(1): 71-80.

Im, S.H., Jeong, Y.H. and Ryoo, J.J. 2008. Simultaneous analysis of anionic, amphoteric, nonionic and cationic surfactant mixtures in shampoo and hair conditioner by RP-HPLC/ELSD and LC/MS *Analytica Chimica Acta* **619**(1): 129–136.

Israelachvili, J. *Intermolecular & Surface Forces*. Second edition. Academic Press. 1991

Jamshidnezhad, M., Shen, C., Kool P., Mojaddam Zadeh, A., and Rossen, W.R. 2010. Improving Injectivity To Fight Gravity Segregation in Gas Enhanced Oil Recovery. SPE Journal **15**(1): 91-104.

Jasti, J.K., Valdya, R.N. and Fogler, H.S. 1988. Capacitance Effects in Porous Media. SPE Reservoir Engeenering **3**(4): 1207-1214.

Jeong, Seung-Woo and Corapcioglu, M.Y. 2003.Physical Model Analysis of Foam–TCE Displacement in Porous Media. *AIChE Journal* **49**(3): 782-788.

Jiménez, A. I. and Radke, C. J. 1989. Dynamic Stability of Foam Lamellae Flowing Through a Periodically Constricted Pore. in *Oil-Field Chemistry: Enhanced Recovery and Production Stimulation*. J. K. Borchardt and T. F. Yen, eds., Washington, D.C., American Chemical Society. 396: 460-479

Kalur, G.C. and Raghavan, S.R. 2005, Anionic Wormlike Micellar Fluids that Display Cloud Points: Rheology and Phase Behavior *J. Phys. Chem. B* **109**(18): 8599-8604.

Kamath, J., Meyer, R.F. and Nakagawa, Frank M., 2001. Understanding Waterflood Residual Oil Saturation of Four Carbonate Rock Types. SPE Annual Technical Conference and Exhibition, New Orleans, Louisiana.

Karimaie, H. and Torsæter, O. 2008. Low IFT Gas-Oil Gravity Drainage in Fractured Carbonate Porous Media. Europec/EAGE Conference and Exhibition, 9-12 June. Rome, Italy.

Khatib, Z. I., Hirasaki, G. J. and Falls, A. H. 1988. Effects of Capillary Pressure on Coalescence and Phase Mobilities in Foams Flowing Through Porous Media. Soc. Pet. Eng. Res. Eng. **3**(3): 919-926.

Kovscek, A.R. 1998. Reservoir Simulation of Foam Displacement Processes. 7th UNITAR International Conference on Heavy Crude and Tar Sands, Beijing, China.

Kovscek, A.R. and Bertin, H.J. 2002. Estimation of Foam Mobility in Heterogeneous Porous Media. SPE/DOE Improved Oil Recovery Symposium, Tulsa, Oklahoma.

Kovscek, A.R. and Radke, C.J. 1993. A Comprehensive Description of Transient Foam Flow in Porous Media. D.O.E./NIPER Symposium on Field Application of Foams for Oil Production, Bakersfield, CA.

Kovscek, A.R., Patzek, T.W. and Radke, C.J. 1997. Mechanistic Form Flow Simulation in Heterogeneous and Multidimensional Porous Media. SPE Journal. 2: 511–517.

Kumar, R., Kalur, G.C., Ziserman, L., Danino, D. and Raghavan, S.R. 2007. Wormlike Micelles of a C22-Tailed Zwitterionic Betaine Surfactant: From Viscoelastic Solutions to Elastic Gels *Langmuir*, **23**(26): 12849-12856.

Kumar, P and K.L. Mittal. *Handbook of Microemulsion Science and Technology*. Marcel Deckker, Inc. 1999.

Kunieda, H., Hanno, K., Yamaguchi, S. and Shinoda, K. 1985. The Three-Phase Behavior of a Brine/Ionic Surfactant/Oil System: Evaluation of the Hydrophile-Lipophile Balance (HLB) of Ionic Surfactant. Journal of Colloid and Interface Science **107**(1): 129-137.

Kuryashov, D. A., Philippova, O. E., Molchanov, V. S. Bashkirtseva, N. Yu. and Diyarov, I. N. 2010. Temperature Effect on the Viscoelastic Properties of Solutions of Cylindrical fixed Micelles of Zwitterionic and Anionic Surfactants. *Colloid Journal* **72**(2): 230-235.

Lake, L.W. *Enhanced Oil Recovery*. Prentice Hall, (1989).

Lapidus L., and Amundson, N.R. 1952. Mathematics of Adsorption In Beds. Vi. The Effect of Longitudinal Diffusion in Ion Exchange and Chromatographic Columns. *J. Phys. Chem.* **56**(8): 984-988.

Larson, R.G. *The Structure and Rheology of Complex Fluids*. Oxford University Press, New York, 1998.

Lemmon E.W. and Jacobsen R.T 2004.*Viscosity* and Thermal Conductivity Equations for Nitrogen, Oxygen, Argon, and Air*. International Journal of Thermophysics,* **25(**1): 21-69.

Levy, B.S. and Chambers, R.M. 1987. Bromide as a Conservative Tracer for Soil-Water Studies. *Hydrological Processes* **1**(4): 385-389.

Leyu Cui Evaluation of Betaine as a foam booster.
http://www.owlnet.rice.edu/~gjh/Consortium/meeting_2011.html, 2011

Lee Lloyd, L. *Molecular Thermodynamics of Electrolyte Solutions*, 2008
Li, K. and Home, R. N. 2003. Prediction of Oil Production by Gravity Drainage. SPE Annual Technical Conference Denver, Colorado.

Li, B. Surfactant/Foam Enhanced Aquifer Contacting and modeling for Aquifer Remediation. Rice University. Thesis 2006.

Li, Y, Abriola, L. M., Phelan T.J., Ramsburg, C. A. and Pennell, K. D. 2007. Experimental and Numerical Validation of the Total Trapping Number for Prediction of DNAPL Mobilization. Environ. Sci. Technol. **41(**23): 8135–8141.

Lin, I. J. 1972. The Hydrophile-Lipophile Balance (hlb) of Fluorocarbon Surfactants and Its Relation to the Critical Micelle Concentration (cmc) *Journal of Physical Chemistry* **76**(14): 2019-2023.

Lin, I.J., Friend, J.P. and Zimmels, Y. 1973. The Effect of Structural Modifications on the Hydrophile-Lipophile Balance of Ionic Surfactants. *Journal of Colloid and Interface Science* **45**(2): 378-385.

Lin, I. J. and Marszall, L. 1978. Partition coefficient, HLB and effective chain length of surface-active agents. *Colloid & Polymer Sci* **63**: 99-104.

Lin, I. J. and Marszall, L. 1976. CMC, HLB, and Effective Chain Length of Surface-Active Anionic and Cationic Substances Containing Oxyethylene Groups. *Journal of Colloid and Interface Science* **57**(1): 85-93.

Lin, I.J. Moudgil, B.M. and Somasundaran, P. 1974. Estimation of the effective number of $–CH_2-$ groups in long-chain surface active agents. *Colloid & Polymer Sci*. 252:407-414.

Lin, I. J. and Somasundaran, P. 1971. Free-Energy Changes on Transfer of Surface-Active Agents between Various Colloidal and Interfacial States. *Journal of Colloid and Interface Science* **37**(4): 731-743.

Liu, B., Zeng, L., Mao J. and Ren, Q. 2010. Simulation of Levulinic Acid Adsorption in Packed Beds using Parallel Pore/Surface Diffusion Model. *Chem. Eng. Technol*. **33**(7): 1146–1152

Liu, S. Alkaline Surfactant Polymer Enhanced Oil Recovery Process, *Rice University,* Thesis 2008.

Liu, S., Li, R., Miller, C.A. and Hirasaki, G.J 2010**.** Alkaline/Surfactant/Polymer Processes: Wide Range of Conditions for Good Recovery *SPE J.* **15**(2): 282-293.

Liu, S., Li, R., Miller, C.A. and Hirasaki, G.J. 2008. ASP Processes: Wide Range of Conditions for Good Recovery, SPE/DOE Symposium on Improved Oil Recovery, Tulsa, Oklahoma.

Lopez-Diaz, D. and Castillo, R. 2010. The Wormlike Micellar Solution made of a Zwitterionic Surfactant (TDPS), an Anionic Surfactant (SDS), and Brine in the Semidilute Regime. *J Phys Chem*. **114**(27): 8917-8925.

López-Salinas, J.L., Hirasaki, G.J. and Miller, C.A. Internal communication PEMEX-RICE 2008. Report to PEMEX. (INTERFACIAL TENSIONS OF PEMEX CRUDE OILS).

Lopez-Salinas, J., Miller, C.A., Koh Yoo, K., Puerto, M. and Hirasaki, G.J. 2009. Viscometer for Opaque, Sealed Microemulsion Samples. *SPE International Symposium on Oilfield Chemistry,* The Woodlands, Texas.

López-Salinas, J.L., Hirasaki, G.J. and Miller, C.A. 2011. Determination of Anhydrite in Reservoirs for EOR. SPE International Symposium on Oilfield Chemistry, The Woodlands, Texas.

Lu, H., Kan, A.T., Zhang, P., Yu, J., Fang, C. and Tomson, M.B. 2010. Phase Stability of Calcium Sulfate in the System NaCl/monoethylene glycol/water. *SPE International Conference on Oilfield Scale*, 26-27 May 2010, Aberdeen, UK

Lu, J., Britton, C., Solairaj, S., Liyanage, P.J., Kim, D. H., Adkins, S., Arachchilage, G.P., Weerasooriya, U. and Pope, G. A. 2012. Novel large-hydrophobe alcoxy carboxylate surfactans for enhanced oil recovery. *SPE Improved Oil Recovery Symposium, Tulsa, Oklahoma, USA.*

Ma, K., Biswal, S.L. and Hirasaki, G.J., 2012. Estimation of parameters for simulation of steady state foam flow in porous media. *The 2012 AIChE Spring Meeting & 8th Global Congress on Process Safety*, Houston, U.S.A.

Ma, S., Morrow, N. R. and Zhang, X. 1997. Generalized Scaling of Spontaneous Imbibitions Data for Strong Water-Wet Systems. Journal of Petroleum Science and Engineering **18**(3-4): 165-178.

Macosko, C. W. *Rheology Principles, Measurements and Applications* Wiley-VCH, (1994).

Mandru, I. 1972. Surface-active Cationic Substances of the Type Alkyl Ether Trimethylammonium and Alkyl Ether Pyridinium Halides Micelle formation and Oxyethylene Groups Behavior. V. *Journal of Colloid and Interface Science* **41**(3): 430-436.

Mannhardt, K., Schramm, L. L. and Novosad, J.J. 1992. Adsorption of anionic and amphoteric foam-forming surfactants on different rock types. *Colloids and Surfaces* **68**(1-2): 37-53.

Mannhardt, K., Schramm, L. L. and Novosad, J.J. 1993. Effect of rock type and brine composition on adsorption of two foam-forming surfactants. *SPE Advanced Technology Series* **1**(1): 212-218.

Marquez, N. Anton, R. Graciaa, A., Lachaise,J. and Salager J.L. 1995. Partitioning of ethoxylated alkylphenol surfactants in microemulsion-oil-water systems. *Colloids and Surfaces A: Physicochemical and Engineering Aspects*, 100:225-231.

Mattax, C.C. and Kyte, J.R. 1962. Imbibition Oil Recovery from Fractured, Water-Drive Reservoir. SPE Journal **2**(2):177-184.

Mennella, A., Bryant, S.L. and Lockhart, T.P. 1999. Analysis of high-dispersion tracer tests in cores containing polymer gels. *Journal of Petroleum Science and Engineering* **23**(3-4): 201–212.

Miller, C.A. and Neogi, P. *Interfacial Phenomena Equilibrium And Dynamic Effects*. Second Edition. CRC. (2008).

Mohamadinejada, H., Knoxb, J. C. and Smith, J. E. 2010. Experimental and Numerical Investigation of Adsorption/Desorption in Packed Sorption Beds under Ideal and Non ideal Flows. *Separation Science and Technology* **35**(1): 1–22.

Mohanty, K.K. and Salter, S.J. 1982. Multiphase Flow in Porous Media: II. Pore-Level Modeling. *Society of Petroleum Engineers of AIME. SPE Annual Technical Conference and Exhibition,* New Orleans, Louisiana.

Mohanty, K.K. and Salter, S.J. 1983. Multiphase Flow in Porous Media: III. Oil Mobilization, Transverse Dispersation, and Wettability. *SPE Annual Technical Conference and Exhibition*, San Francisco, California.

Monnin, C. 1990. The influence of pressure on the activity coefficient of the solutes and on the solubility of minerals in systems Na-Ca-Cl-SO4-H2O to 200°C and 1 kbar, and high NaCl concentration. *Geochimica et Cosmochimica Acta* **54**(12): 3265-3283.

Morrison, I.D. and Ross, S. *Colloidal Dispersions. Suspensions, Emulsions, and Foams.* Wiley-Interscience. (2002).

Morrow, N.R. and Xie, X. 2001. Oil Recovery by Spontaneous Imbibition from Weakly Water-Wet Rocks. *Petrophysics* **42**(4): 1-10.

Myers, Drew. *Surfactant Science and Technology*. 3rd edition. Wiley, (2006).

Nelson, R.C. 1983. The Effect of Live Crude on Phase Behavior and Oil-Recovery Efficiency of Surfactant Flooding Systems. *SPE Journal* **23**(3): 501-510.

Nutting, P.G. 1925.Chemical Problems in the Water Driving of Petroleum from Oil Sands. *Journal of Petroleum Technology* **6**(5): 41-48.

Oli Systems
Support.olisystems.com/Documents/ValidationDataSets/PredSO4.xls,2011

Orr, F.M., Jr., Johns, R.T. and Dindoruk, B. 1991. Development of miscibility in four component vaporizing gas drives, *SPE Annual Tech. Conf. and Exhib.,* Dallas, TX.

Ott, J.B. and Boerio-Goates, J. *Chemical Thermodynamics: Advanced Applications*. Academic Press, (2000).

Özdural, A.R., Alkan, A. and Kerkhof, P. 2004. Modeling chromatographic columns Non-equilibrium packed-bed adsorption with non-linear adsorption isotherms. *Journal of Chromatography A* **1041**(1-2): 77–85.

Partridge, E.P. and White, A.H. 1929. The solubility of calcium sulfate from 0 to 200º *JACS* 51: 360-370.

Paulick H., Herzig, P. and Hoernes, S. 2005. 8.Data report: a comprehensive Geochemical, mineralogical, and Isotopic data set of variably altered Dacitic volcanic rocks from the Subsurface of the pacmanus Hydrothermal field (odp leg 193)

Pelia, Chen and Mohanty, K.K. 2012. Surfactant-Mediated Spontaneous Imbibition in Carbonate Rocks at Harsh Reservoir Conditions. SPE Improved Oil Recovery Symposium, Tulsa, Oklahoma.

Pennell, K.D., Pope, G.A., and Abriola, L. M. 1996. Influence of Viscous and Buoyancy Forces on the Mobilization of Residual Tetrachloroethylene during Surfactant Flushing. *Environ. Sci. Technol.*, **30**(4): 1328–1335

Piquemal, J. 1992. On the Modelling of Miscible Displacements in Porous Media with Stagnant Fluid. *Transport in Porous Media* **8**(3): 243-262.

Piquemal, J. 1993. On the Modelling Conditions of Mass Transfer in Porous Media Presenting Capacitance Effects by a Dispersion-Convection Equation for the Mobile Fluid and a Difussion Equation for the Stagnant Fluid. *Transport in Porous Media* **10**(3): 271-283.

Poling, B.E., Prausnitz, J.M. and O'Connell, J.P. *The Properties of Gases and Liquids.* McGraw-Hill. (2001). pp 9.77-9.79.

Pollack, S.R. and Petrov, N. 2000. A Triple Porosity Model of Stress Induced Fluid Flow in Cortical Bone. In the Proceedings of the International Conference on Biorheology, Sofia, Bulgaria.

Pomerantz, P., Clinton, W.C. and Zisman, W.A. 1967. Spreading Pressures and Coefficients, Interfacial Tensions, and Adhesion Energies of the Lower Alkanes, Alkenes, and Alkyl Benzenes on Water. *Journal of Colloid and Interface Science* **24**(1): 16-28.

Proverbio, Z.E., Bardavid, S.M., Arancibia, E.L. and Schulz, P.C. 2003. Hydrophile-lipophile balance and solubility parameter of cationic surfactants. *Colloids and Surfaces A: Physisochemical and Engineering Aspects* **214**(1-3): 167-171.

Puerto, M., Hirasaki, G.J., Miller, C.A. and Barnes, J.R. 2010 Surfactant Systems for EOR in High-Temperature, High-salinity Environments. *SPE Improved Oil Recovery Symposium,* Tulsa, Oklahoma, USA.

Puerto, M. and Reed, R.L. 1983. A three-parameter representation of surfactant/oil/brine interaction. *SPE Journal* **23(**4): 669-682.

Pulido, H., Samaniego, V., Rivera R., Galicia-Muñoz, G. and Vélez, C. 2008. Tracer Test Analysis with Triple Porosity Model for Naturally Fractured Reservoirs with Transient Transfer in Matrix-Fracture and Microfractures-Fractures. *Thirty-Third Workshop on Geothermal Reservoir Engineering Stanford University.* Stanford, California.

Racz, I. and Orban, E. 1965. Calorimetric Determination of the Hydrophile-Lipophile Balance of Surface-Active Substances. *Journal of Colloid Science* **20**(2): 99-103.

Radke, C.J., Gillis, J.V 1990. A Dual Gas Tracer Technique for Determining Trapped Gas Saturation During Steady Foam Flow in Porous Media *SPE Annual Technical Conference and Exhibition,* New Orleans, Louisiana.

Raghavan, N. S. and Ruthven, D. M. 1983. Numerical Simulation of a Fixed-Bed Adsorption Column by the Method of Orthogonal Collocation. *AIChE Journal* **29 (**6): 922-925.

Ransohoff, T.C. and Radke, C.J. 1998. Mechanisms of Foam Generation in Glass-Bead Packs. *SPE Reservoir Engineering* **3**(2): 573-585.

Rasmuson, A. and Neretnieks, W. 1980. Exact Solution of a Model for Diffusion in Particles and Longitudinal Dispersion in Packed Beds. *AIChE Journal* **26** (41): 686-690.

Reed, R.L. and Healy, R.N. 1984. Contact Angles for Equilibrated Microemulsion Systems. *SPE Journal* **24**(3): 342-350.

Reis, J.C. and Cil, M. 1993. A Model for Oil Expulsion by Counter-Current water Imbibition in Rocks: One-Dimensional Geometry. *Journal of Petroleum Science and Engineering* 10: 97-107.

Renkema, W.J. and Rossen, W.R. 2007. Success of Foam SAG Processes in Heterogeneous Reservoirs. *SPE Annual Technical Conference and Exhibition*, Anaheim, California, U.S.A.

Rezaveisi, M., Ayatollahi, S. and Rostami, B. 2012. Experimental Investigation of Matrix Wettability Effects on Water Imbibition in Fractured Artificial Porous Media. *Journal of Petroleum Science and Engineering* **86-87**: 165-171.

Richardson, J. G. and Blackwell, R. J. Use of Simple Mathematical Models for Predicting Reservoir Behavior. *Journal of Petroleum Technology* **23**(9): 1145-1154.

Rieger, M. M and Rhein, L. D. *Surfactants in cosmetics*, (Surfactant Science Series No. 68) 2nd edition. (1997).

Rosen, M.J., Zhao, F. and Murphy, D.S. 1987. Two-Phase Mixed Indicator Method for Determination of Zwitterionic Surfactants. *JAOCS*, **64**(3): 439-441.

Ross, S., Chen, E.S., Becher, P. and Ranauto H.J. 1959. Spreading Coefficients and Hydrophile-Lipophile Balance of Aqueous Solutions of Emulsifying Agents. *J. Phys. Chem.*, **63**(10): 1681–1683.

Rossen, W.R., Zeilenger, S.C. Shi, J.X. and Lim, M.T. 1994. Mechanistic Simulation of Foam Processes in Porous Media. 69th Ann. Tech. Conf. and Exhibition of the SPE, New Orleans, Louisiana.

Rossen, W.R., Johns, R.T. and Pope, G.A. 2003. Development of More-Efficient Gas Flooding Applicable to Shallow Reservoirs. Center for Petroleum and Geosystems Engineering. The University of Texas at Austin. Work Performed under DOE Award Number DE-AC26-99BC15208.

Rossen, W.R. Mechanistic Studies of Improved Foam EOR Processes. Center for Petroleum and Geosystems Engineering. The University of Texas at Austin. March, 2005.

Rossen, W.R. 2003. A critical review of Roof snap-off as a mechanism of steady-state foam generation in homogeneous porous media. *Physisochemical and Engineering Aspects* **225**(1-3): 1-24

Rossen, W.R., Zeilenger, S.C., Shi, J.X. and Lim, M.T. 1994. Mechanistic Simulation of Foam Processes in Porous Media. *SPE 28940, in Proceedings of the 69th Ann. Tech. Conf. and Exhibition of the SPE, New Orleans, Louisiana.*

Rowe**,** R. K**.** and Booker, J. R. 1990. Contaminant Migration In A Regular Two-Or Three-Dimensional Fractured Network: Reactive Contaminants. *International Journal for Numerical and Analytical Methods In Geomechanics* **14**(6): 401-425.

Rusanov, Prokhorov. *Interfacial Tensiometry*. Elsevier, (1996).

Sahimi, M. 1993. Flow phenomena in rocks: from continuum models to fractals, percolation, cellular automata, and simulated annealing. *Rev. Mod. Phys* **65**(4): 1393-1534.

Salager, J.L. 1996. Quantifying the concept of physic-chemical formulation in surfactant-oil-water system-State of the art. *Progr Colloid Polym Sci*. 100: 137-142.

Salager, J.L. 2002. Surfactants Types and Uses. *Firp booklet # E300-A.Teaching Aid in Surfactant Science & Engineering.*

Salager J.L. Microemulsions, in *Handbook of Detergents - part A: Properties***,** G. Broze Ed., Surfactant Science Series vol. **82**, Chapter 8, pp 253-302, Marcel Dekker New York (1999)

Salager J.L. 1979. Mixing Rules for Optimum Phase-Behavior Formulations of Surfactant/Oil/Water Systems. *SPE Journal* **19**(5): 271-278

Salter, S.J. and Mohanty, K.K. 1982. Multiphase Flow in Porous Media: I. Macroscopic Observations and Modeling. Society of Petroleum Engineers of AIME. SPE Annual Technical Conference and Exhibition, New Orleans, Louisiana

Sardin, M., Schweich, D., Leij, F. J. and Van Genuchten, M. T. 1991. Modeling the Nonequilibrium Transport of Linearly Interacting Solutes in Porous Media- A Review. *Water Resources Research* **27**(9): 287-230.

Schechter, D.S., Zhou, D. and Orr, F.M. 1994. Low IFT Drainage and Imbibition. *Journal of Petroleum Science and Engineering* **11**(4): 283-300.

Schwartz, R.C., Juob, A.S.R. and McInnesb, K.J. 2000. Estimating parameters for a dual-porosity model to describe nonequilbrium, reactive transport in a fine-textured soil. *Journal of Hydrology* **229**(3): 149-167.

Seethepalli, A., Adibhatla, B. and Mohanty, K. 2004. Wettability alteration during surfactant flooding of Carbonate Reservoirs. SPE/DOE Fourteenth Symposium on Improved Oil Recovery held in Tulsa, Oklahoma, U.S.A.

Shamsipur, M., Rouhanib, S., Mohajeri, A. Ganjali, M.R. and Rashidi-Ranjbar, P. 2000. A bromide ion-selective polymeric membrane electrode based on a benzo-derivative xanthenium bromide salt. *Analytica Chimica Acta* **418**(2): 197–203.

Sharma, G. and Mohanty, K.K., 2011. Wettability Alteration in High Temperature and High Salinity Carbonate Reservoirs. SPE *Annual Technical Conference and Exhibition,* Denver, Colorado, USA.

Sheng, James J. Modern Chemical Enhanced Oil Recovery. Elsevier. (2011).

Shinoda K. and Arai, H. 1964. The correlation between PIT in emulsion and cloud point in solution of nonionic emulsifier. *J. Phys. Chem*., **68**(12): 3485-3490.

Singh, G., Hirasaki, G.J, and Miller, C.A. 1997. Dynamics of Foams Films in Constricted Pores. *AIChe Journal* **43**(12): 3241-3252.

Solairaj, S., Britton, C., Lu, J., Kim, D.H. Weerasooriya, U. and Pope, G. A. 2012. New correlation to predict the optimum surfactant structure for EOR. *SPE Improved Oil Recovery Symposium,* Tulsa, Oklahoma, USA.

Stegemeier, George L. 1974. Relationship of Trapped Oil Saturation to Petrophysical Properties of Porous Media. *SPE Improved Oil Recovery Symposium*, Tulsa, Oklahoma

Stehfest, H. 1970. Numerical Inversion of Laplace Tranforms. *Communications of the ACM* **13**(1): 47-51.

Stokes, R.J. and Evans, D.F. *Fundamentals of Interfacial Engineering*. Wiley-VCH, (1997).

Stubenrauch, C. *Microemulsions - Background, New Concepts, Publications, Perspectives.* Oxford: Wiley-Blackwell. (2009).

Stumm, W. and Morgan, J. J. *Aquatic Chemistry* third edition, Wiley (1996).

Sudicky, E.A. and McLaren, R.G. 1992. The Laplace Transform Galerkint Technique for Large-Scale Simulation of Mass Transport in Discretely Fractured Porous Formations. *Water Resources Research* **28**(2): 499-514.

Taber, J.J. 1969. Dynamic and Static Forces Requires to Remove a Discontinous Oil Phase from Porous Media Containing Both Oil and Water. *Society of Petroleum Engineers Journal* **9**(1): 3-12.

Tadros, T.F. *Applied Surfactants*. Wiley. (2005).

Talley, Larry D. 1988. Hydrolytic Stability of Alkylethoxy Sulfates. *SPE Reservoir Engineering*, **3**(1): 235-242.

Tang, D. H., Frind, E. O. and Sudicky, E.A. 1981. Contaminant Transport in Fractured Porous Media: Analytical Solution for a Single Fracture. *Water Resources Research* **17**(3): 555-564.

Tavassoli, Z., R. W. Zimmerman, R. W. and Blunt, M. J. 2005. Analytic Analysis for Oil Recovery During Counter-Current Imbibition in Strongly Water-Wet Systems. *Transp. Porous Med.,* **58**: 173–189.

Tsubochi, M., Yamasaki, N. and K. Matsuoka, K. 1979. Determination of Anionic Surfactants by Two-Phase Titration with Tetrabromophenolphtalein Ethyl Ester as Indicator. *SD&C Technical* **171**: 921-923.

Umezawa, Y. Umezawa, K. and Sat, H. 1995. Selectivity Coefficients for Ion-Selective Electrodes: Methods For Reporting $K^{pot}_{A,B}$ Values. *Pure & Appl. Chern.* **67**(3): 507-518.

Van Genuchten, M.T. and Wlerenga, P. J. 1976. Mass Transfer Studies in Sorbing Porous Media I. Analytical Solutions. *Soil Science Society of America Journal* **40**(4): 473-480.

Van Genuchten, M.T. and Parker, J.C. 1994. Reply to Comments on Boundary Conditions for Displacement Experiments through Short Laboratory Soil Columns *Soil Sci. Soc. Am. J.* **58**(3): 991-993.

Varade, D., Rodriguez-Abreu, C., Shrestha, L.K., and Aramaki, K. 2007. Wormlike Micelles in Mixed Surfactant Systems: Effect of Cosolvents. *J. Phys. Chem. B*, **111**(35): 10438-10447.

Vold, R. D. and Mittal, K. L. 1972. Determination of Sodium Dodecyl Sulfate in the presence of Lauryl Alcohol, *Analytical Chemistry*, **44**(4): 849-850.

Von Rosenberg, D.U., R. P. Chambers, R. P. and Swan, G. A. 1977. Numerical Solution of Surface Controlled Fixed-Bed Adsorption. *Ind. Eng. Chem., Fundam.* **16**(1): 154-157.

Warren, J.E. and Root, P.J. 1963. The Behavior of Naturally Fractured Reservoirs. *Society of Petroleum Engineers* **3**(3): 245-255.

Winsor, P.A. *Solvent Properties of Amphiphilic Compounds*, Butterworth, London (1954).

Witthayapanyanon, A., Harwell, J.H., and Sabatini, D.A. 2008. Hydrophilic–lipophilic deviation (HLD) method for characterizing conventional and extended surfactants. *Journal of Colloid and Interface Science* **325**: 259-266.

Yan, Wei. Foam for Mobility Control in Alkaline/Surfactant Enhanced Oil Recovery Process. Rice University. Thesis 2006.

Yan, W. Miller, C.A. and Hirasaki, G.J. 2006. Foam Sweep in Fractures for Enhanced Oil Recovery. *Colloids and Surfaces A: Physicochem. Eng. Aspects* (282–283): 348–359.

Yildirim, O.E., Xu, Q. and Basaran, O.A. 2005. Analysis of the drop weight method. *Physics of Fluids*. **17**(6): 1-13.

Yusong, Li, Abriola, Linda M., Phelan, T.J., Andrewramsburg, C. and Pennel, K.D. 2007. Experimental and Numerical Validation of the Total Trapping Number for Prediction of DNAPL Mobilization. *Environ. Sci. Technol.* **41**: 8135–8141.

Zanganeh, M.N., Kam, S.I., LaForce, T.C. and Rossen, W.R., 2011. The Method of Characteristics Applied to Oil Displacement by Foam. *SPE Journal* **16**(1): 8-23.

Zhang, P., Tweheyo, M.T. and Austad, T. 2006. Wettability Alteration and Improved Oil Recovery in Chalk: The Effect of Calcium in the Presence of Sulfate. *Energy & Fuels*, **20**(5): 2056-2062.

Zhou, D. and Stenby, E. H. 1993. Displacement of Trapped Oil from Water-Wet Reservoir Rock. *Transport in Porous Media* **11**(1): 1-16.

Zhou, Z. and Rossen, W.R. 1995. Applying Fractional-Flow Theory to Foam Processes at the "Limiting Capillary Pressure. *SPE Advanced Technology Series* **3**(1): 154-162.

Zoller, Uri. Handbook of Detergents Part E: Applications. CRC Press. (2009).

APPENDICES

Appendix 3A Interfacial tension of contaminated oils

Fig 3A-1 shows the value of IFT for different crude oils measure in our lab, by Robert F. Li, Shunhua Liu, and Jose Lopez. Contaminated samples and samples in presence of alkali had IFT less than 15 dynes/cm. IFT for Ethyl acetate was measured as reference for comparison (6.8 dyne/cm consistent with reported by Morrison and Ross, 2002).

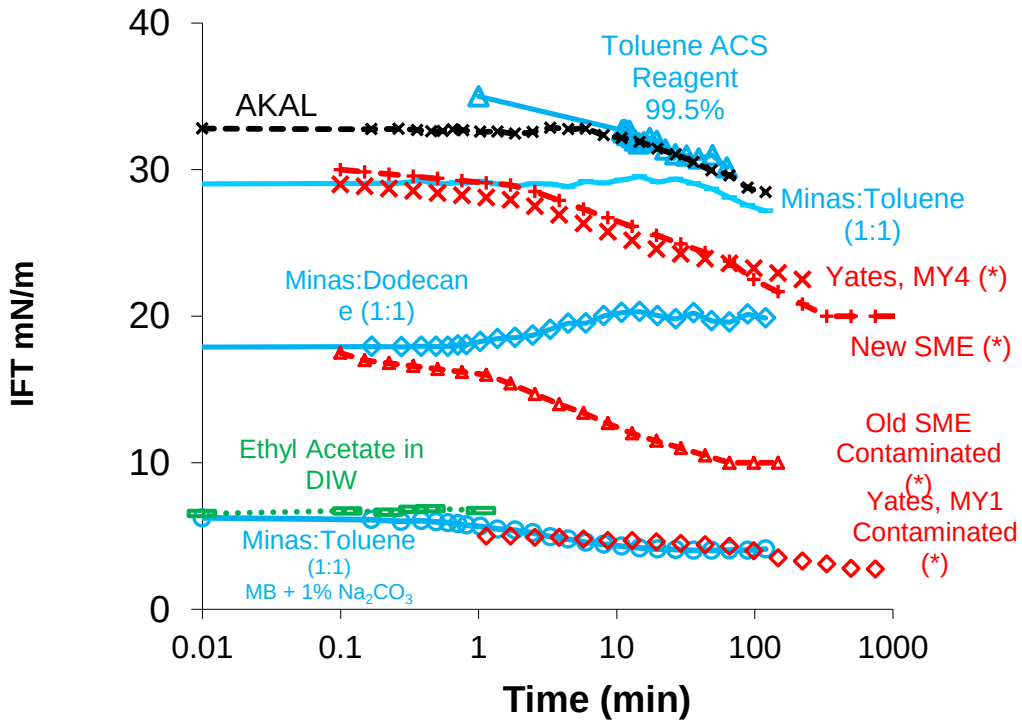

Figure 3A-1 Comparison of IFT for crude oils that presented contamination in measurements performed in the lab in previous years.

Appendix 3B Viscosity of Akal dead oil

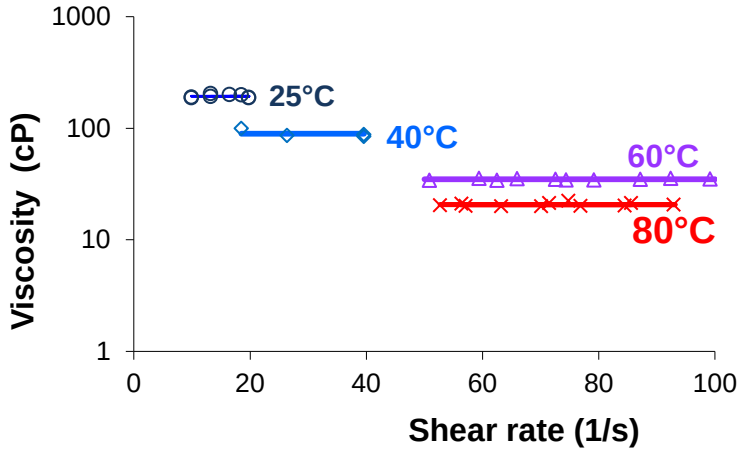

Figure 3B-1 Viscosity measured using Couette flow viscometer. Brookfield DV III+

Viscosity of the crude oil at different temperature at different shear rates for AKAL sample.

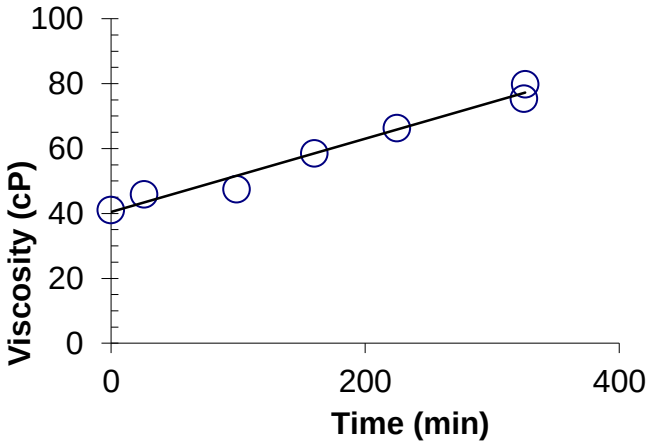

Figure 3B-2 Evolution of AKAL crude oil viscosity at 60°C exposed to atmosphere

The viscosity of the crude oil should be measured in a closed viscometer, or in short periods of time to prevent losing of volatiles. Figure 3B-2 indicates how viscosity increased if heated continuously in open viscometer.

Appendix 3C Rheology models to describe surfactant blends

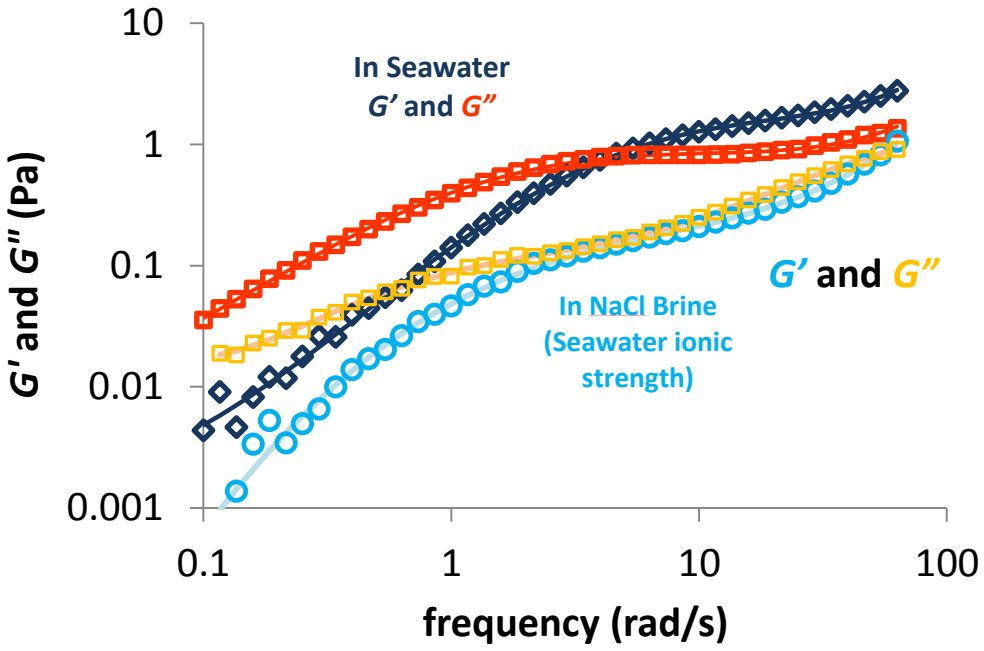

Figure 3C-1 C $_{16\text{-}18}$ AOS 1% Effect of divalent ions. The AOS in sea water produced viscous solution and is homogeneous while mixing, but if mixing stops the solution phase separates after 1 h. The continuous lines are the fit to the Jefffrey Model, and parameters are given in table 3C-1

Figure 3C-1 shows the storage and loss modulus for a 1% sample of $_{C16\text{-}18}$AOS in NaCl brine and seawater, and the fitted values using Jeffrey model reported by Carreau (1997) with a single relaxation and single retardation time.

Jeffrey model is described with equations 3C-1 and 3C-2

$$G' = \frac{G_0(\omega\tau_0)^2\left(1-\frac{\tau_2}{\tau_0}\right)}{[1+(\omega\tau_0)^2]} \qquad \textbf{(Equation 3C-1)}$$

$$G'' = \frac{G_0(\omega\tau_0)\left(1+(\omega\tau_0)^2\frac{\tau_2}{\tau_0}\right)}{[1+(\omega\tau_0)^2]} \qquad \textbf{(Equation 3C-2)}$$

The parameters after curve fitting are in table 3C-1

Table 3C-1 Parameters for Jeffrey Model for AOS

	Seawater		NaCl (Seawater ionic strength)	
i	0	2	0	2
G_i (Pa)	1.4995		0.20134	
τ_i (s)	0.29	0.0174	0.55	0.1

G' = Storage modulus or dynamic rigidity

G" = Loss modulus

τ_0 = Relaxation time

τ_2 =Retardation time

ω = frequency

A general mathematical expression for the behavior of viscoelastic materials is given by Barnes *et al.* (1989). The advantage of this expression is that can be

represented physically with an analogy of particular arrangements of springs and dashpots. In Maxwell $\alpha_1 = \tau_0$ and $\beta_1 = \eta$, In Jeffrey $\alpha_1 = \tau_0$, $\beta_1 = \eta$ and $\beta_2 = \tau_2\,\eta$.

$$\left[1 + \alpha_1 + \alpha_2\frac{\partial}{\partial t} + \alpha_3\frac{\partial^2}{\partial t^2} + \cdots + \alpha_n\frac{\partial^n}{\partial t^n}\right]\sigma$$

$$= \left[\beta_0 + \beta_1 + \beta_2\frac{\partial}{\partial t} + \beta_3\frac{\partial^2}{\partial t^2} + \cdots + \beta_m\frac{\partial^m}{\partial t^m}\right]\gamma$$

Jeffrey model can be represented as a dashpot and a spring in parallel with a dashpot in series, or a dashpot in parallel with a spring and a dashpot in series. If retardation time is set to zero then is equivalent to Maxwell model.

Appendix 3D Prediction of Rheology at 94°C

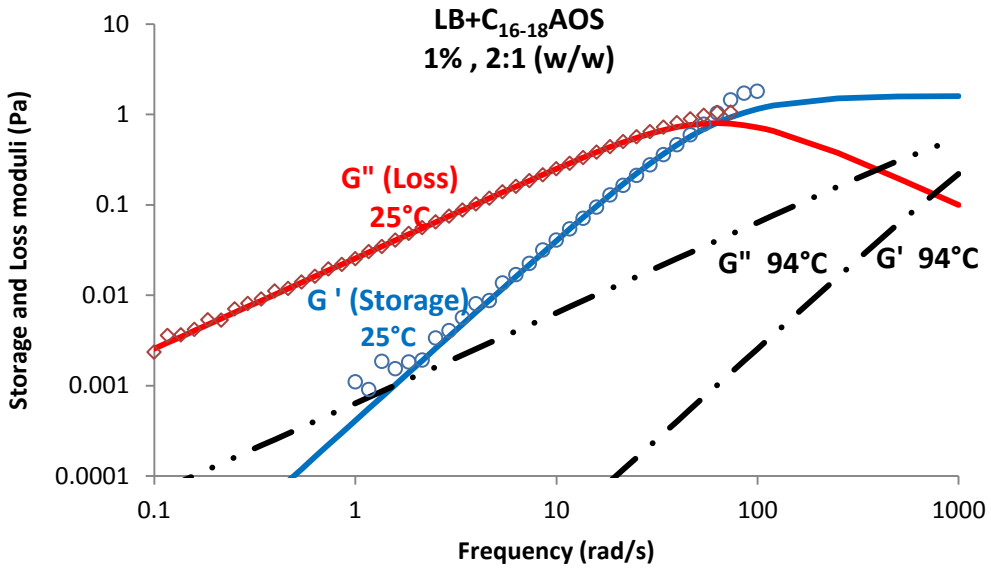

Figure 3D-1 Prediction of rheology at high temperature using Kuryashov approach. 1% LB+$C_{16\text{-}18}$AOS, 2:1 (w/w). Blue and red continuous lines are for the Maxwell model, circles and diamonds are experimental values. Dashed lines are predictions.

Kuryashov (2010) studied the viscoelastic properties of solutions of cylindrical mixed micelles of zwitterionic and anionic surfactants and for the system under study he realized that the activation energy describing the behavior of viscosity and relaxation time are equal. He got a value of activation energy of 48 kT or 120 kJ/mol, and reported that typical values for these systems were from 70 to 300 kJ/mol. They observed that the elastic modulus was independent of temperature.

Under the assumption that for high temperature the loss modulus dominates, the estimated value of activation energy for LB+AOS is 70.7 kJ/mol (E_η/R= 5815 K^{-1}), obtained from experimental data of fig 3-11. The value is close to the lower limit of 70 kJ/mol reported by Kuryashov (2010). The activation energy estimated was used to predict the viscoelasticity at 94°C. Assuming the same elastic modulus the fig 3D-1 is obtained.

The Cox-Merz relation states that the shear rate dependence of the steady state viscosity η is equal to the frequency dependence of the linear viscoelastic viscosity η^*, Macosko (1994).

That is:

$$\eta\,(\dot{\gamma}) = |\eta^*(\omega)|\; with\; \dot{\gamma} = \omega$$

$$|\eta^*| = \sqrt{\left(\frac{G''}{\omega}\right)^2 + \left(\frac{G'}{\omega}\right)^2}$$

See Appendix 3C for definition of the previous variables

With the Cox-Merz relation the viscosity predicted is ca. 0.6 cP at 94°C which is consistent with the experimental value.

$$\eta = \eta_{\infty} exp\left(\frac{E_{\eta}}{RT}\right) \qquad \textbf{(Equation 3D-1)}$$

$$\tau_R = \tau_{R\,\infty} exp\left(\frac{E_{\eta}}{RT}\right) \qquad \textbf{(Equation 3D-2)}$$

Appendix 3E Falling sphere viscometer designed by Jose Lopez and Kyu Hun.

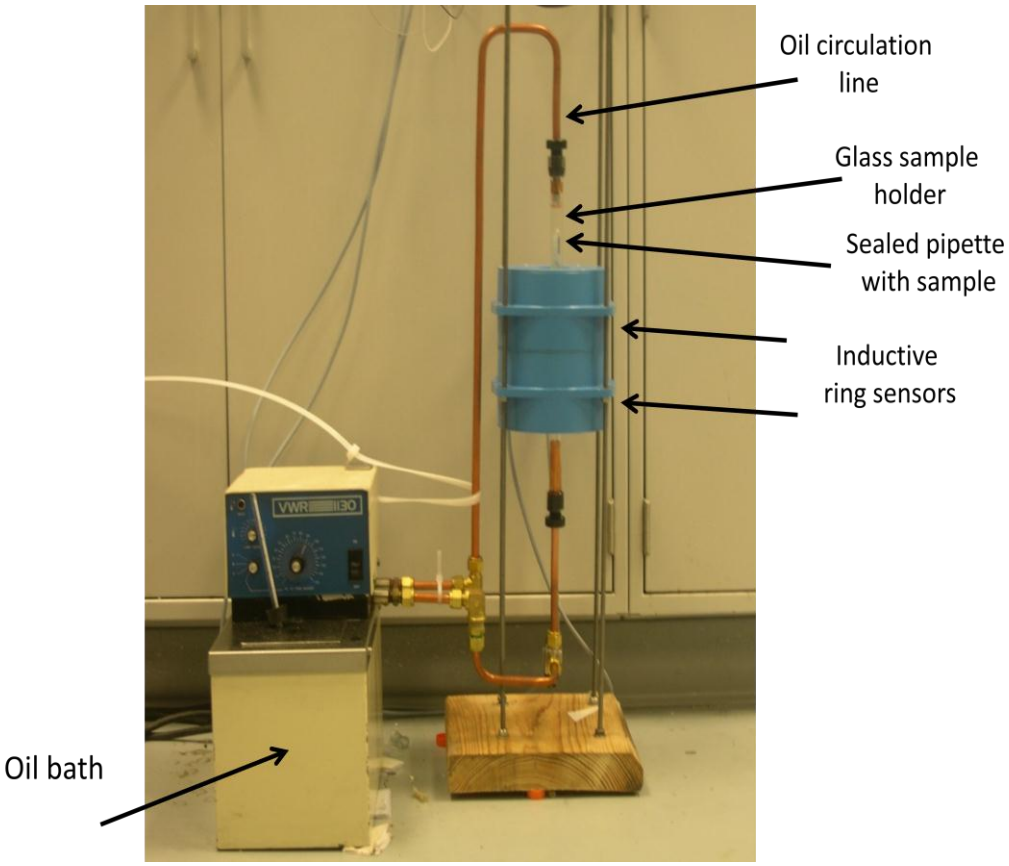

Figure 3E-1 High temperature falling sphere viscometer.

Viscometer on figure 3E-1, is an improved version of Viscometer for room temperature by Lopez *et al.* (2009)

Appendix 3F Contact angle determination.

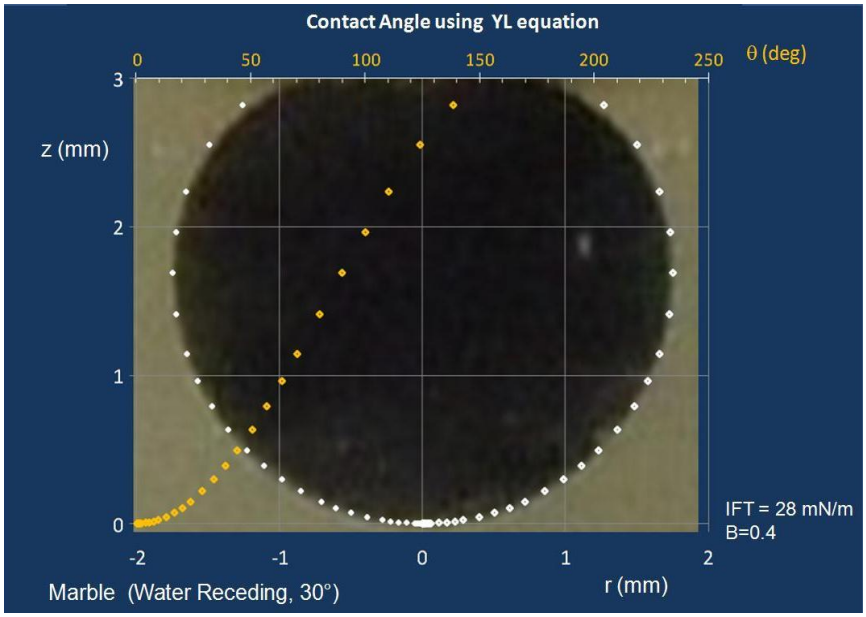

Figure 3F-1 Contact angle measurement. Solving the sessile drop equation (see Miller and Neogi 2008) contact angle can be measured.

IFT can be measured as well using this technique.

Appendix 3G Idealization of molecular interactions to explain Viscoelasticity, and some other observed phenomena.

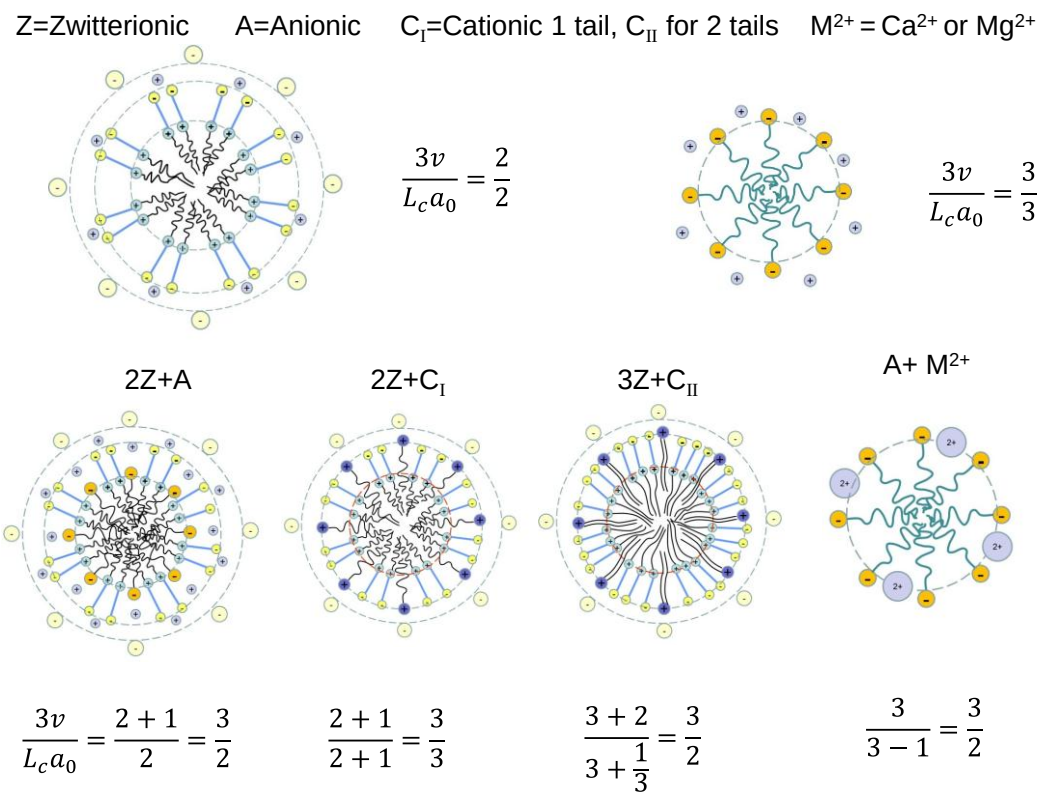

Figure 3G-1 Comparison of different surfactants and surfactant blends (Idealized analysis)

The base cases are Zwitterionic surfactant (e.g., betaine, amidopropylbetaine or sultaine) as a spherical micelle and anionic surfactant (i.e., AOS) as spherical micelle as well, the cartoon 3G-1 is used to visualize the next description of surfactant blends .

- **Case I:** Zwitterionic and anionic in molar ratio 2 to 1. Addition of anionic will increase the volume of the lipophilic chain from 2 to 3, and the hydrophilic repulsion area doesn't change too much because the affinity of the anionic surfactant with the positive portion of the zwitterionic and the

space left so counter-ion can pack as well, then the system will turn to worm-like micelle (WM).

- **Case II**: Zwitterionic and cationic in molar ratio 2 to 1. Addition of cationic will increase the volume of the lipophilic chain from 2 to 3, and the hydrophilic repulsion increases from 2 to 3, because the cationic surfactant with positive portion will pack in the external section of the micelle with the negative portion of the zwitterionic, no space available for counter-ion, then the system keeps its spherical shape.
- **Case III**: Zwitterionic and cationic in molar ratio 3 to 1, but cationic with double tail. Addition of cationic will increase the volume of the lipophilic chain from 3 to 5, and the hydrophilic repulsion increases from 3 to 31/3, because the cationic surfactant with positive portion will pack in the external section of the micelle with the negative portion of the zwitterionic, no space available for counter-ion, then critical packing parameter will allow WM.
- **Case IV:** Anionic originally as spherical micelle. Adding calcium or magnesium, will require less space to balance the charge of the head groups because they have double charge, then will result in less repulsion area from 3 to 2, then the value of CCP is within the range to form WM. If no divalent cations are added, the reduction of repulsion area can be done with higher concentration of salt.
- **Case V:** Cationic originally as spherical micelle. (This case is not included in the cartoon). Addition of internal salt or hydrotrope was required to

reduce the area of repulsion without increasing the volume of the lipophilic tail, is equivalent to case IV, and as like case IV if no hydrotrope added then will require higher concentration of salt to obtain WM.

Disclaimer: The numbers used to represent area of repulsion weren't measured, they are just guess values obtained from observation of viscoelasticity of the different surfactant blends used during experiments (see chapter 7 for details)

Excess of calcium in formulation of AOS will produce precipitation, the same phenomenon was observed with the blend LB+AOS if they are in a molar ratio close to1:1, so in presence of divalent ions the proportion of LB+AOS will be important not only for the rheology, but for aqueous stability, see figure 3G-2 (details of formulations and observations included in chapter 7).

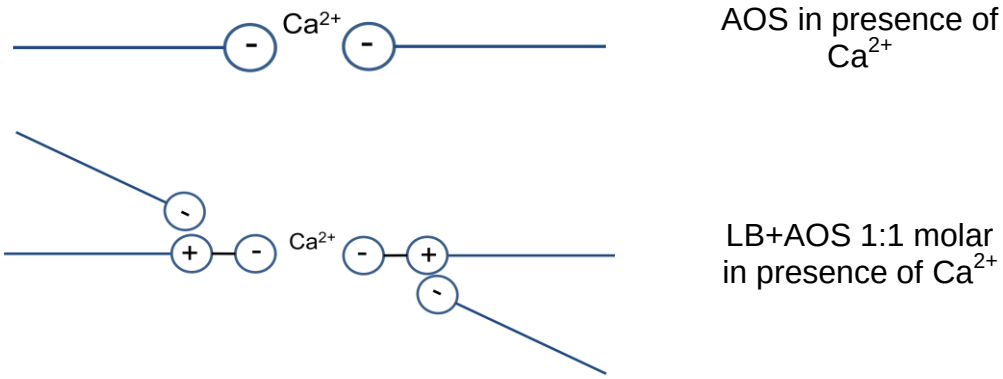

Figure 3G-2 Precipitate and/or aggregates observed in presence of high concentration of divalent cations in aqueous solutions (e.g. seawater of higher content of divalent cations).

Appendix 4A XRD results for Formation Rock

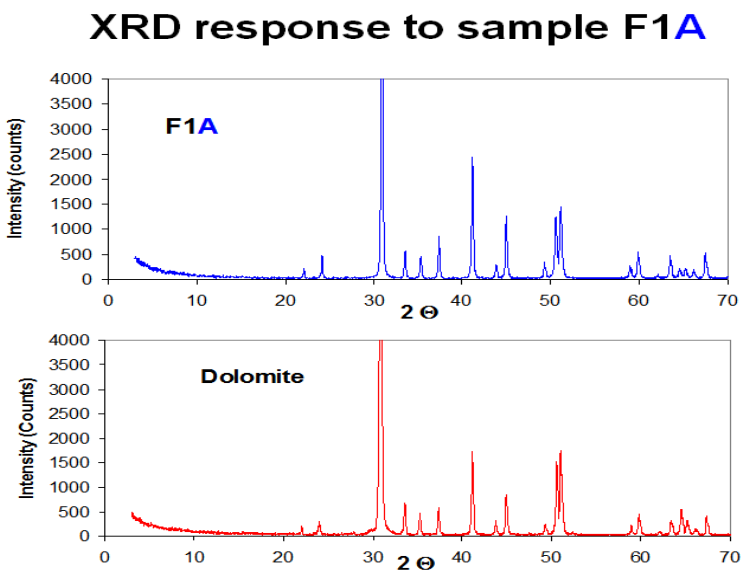

Figure 4A-1 Intensity response of the powder XRD from a rock sample (F1A, blue) and a sample of dolomite (red)

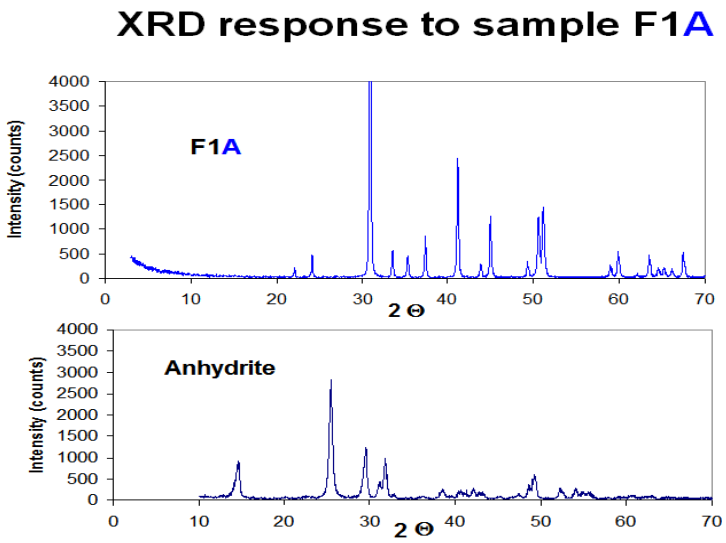

Figure 4A-2 Intensity response of the powder XRD from a rock sample (F1A, blue) and a sample of anhydrite (dark blue)

Examination of fig 4A-1 and fig 4A-2 helps to conclude that the content of anhydrite in the sample is too low to be detected using this technique. Using zooms of the zone where the maxima of the different components (dolomite and anhydrite) are located was not enough to confirm the presence of anhydrite peaks.

Appendix 4B Analytical methods

Solution phase or the dissolved rock in solution, the total Ca, Na, S, Fe Mg and K concentrations were measured by ICP (Perkin–Elmer Optima 4000 DV, Atlanta, GA, USA). Ca and Na were detected at 371.933 and 589.59 nm wavelengths, respectively, with ICP. ICP was calibrated at 0, 0.2, 1.0 and 5.0 ppm for Ca, 0, 2, 10 and 50 ppm for Na. Fe, Mg, K and S were detected at 238.204, 285.213, 766.49 and 181.975 nm wavelengths, respectively, with ICP. ICP was calibrated with 0, 1, 5 and 25 ppm for all of them (i.e. Fe, Mg, K and S). Yttrium (Y) was used as the international standard for ICP calibration. Excellent linear calibration was generally observed with a correlation coefficient higher than 0.9999. A quality control sample was analyzed every three samples to insure that the calibration was valid for the analysis. The detection limit was 0.01 mg/L for ICP and the relative standard deviation of three replicate analyses was generally below 3%.

Appendix 4C Water analysis

It is important to have reliable and complete information about the water from the reservoir. The pH and alkalinity are variables that affect the results of the saturation index for most of the minerals of interest. However, in the particular case of anhydrite, the effect of alkalinity and pH are almost negligible.

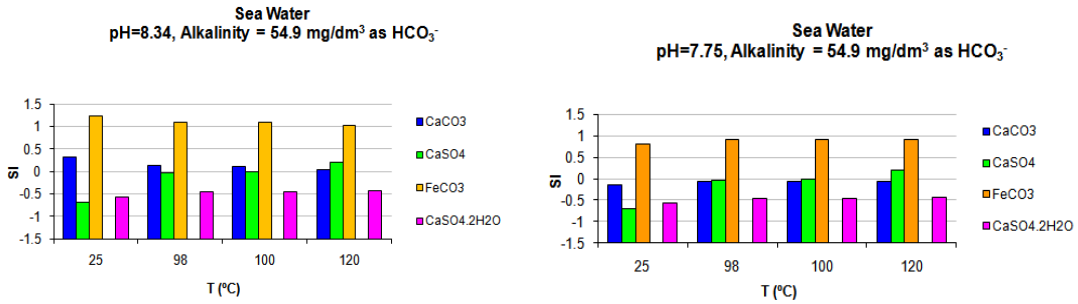

Figure 4C-3 Comparison of saturation index for a seawater with different pH. The saturation of anhydrite is not affected by the hydrogen potential, but the saturation of calcite at low temperature has a strong effect in saturation, this effect can be seen over siderite as well.

This behavior is shown in fig 4C-3, where it may be seen that at low temperature (25°C) the saturation index of calcium carbonate strongly depends on pH, but the saturation index of anhydrite stays about the same. Similar comments can be made for the higher temperatures. The effect of temperature on calcium carbonate saturation index changes from one pH to the other. For this seawater if the pH is 7.75, the brine is unsaturated in calcium carbonate, but it will be oversaturated if the pH is 8.34. Hence it is important to know with precision the values of the alkalinity and pH, or know the pH and the partial pressure of CO_2 in equilibrium with the brine, or know the partial pressure of CO_2 in the atmosphere in contact with the brine when the analysis was made.

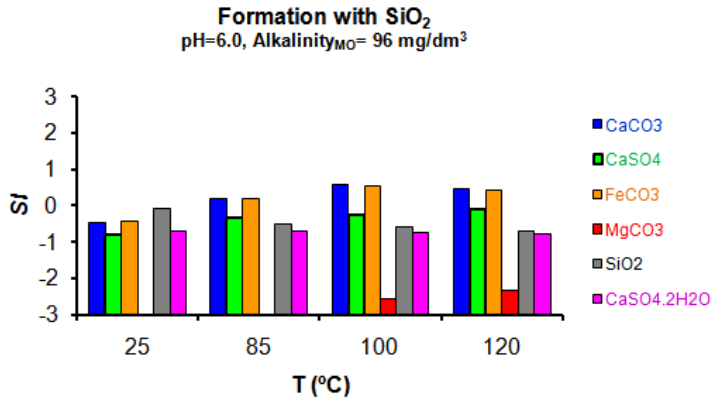

Figure 4C-4 Saturation index of formation brine with high content of silica. For this formation the saturation limit respect to anhydrite is 120C. For this case the temperature is important.

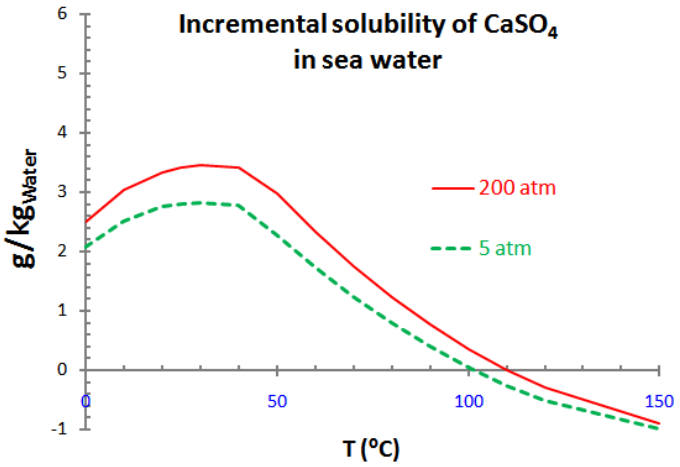

Figure 4C-5 Incremental solubility of anhydrite in seawater at low and high pressure. Incremental solubility is the additional calcium sulfate that can be added to the seawater. The seawater of this study already has 1.615 g of calcium sulfate per kilogram of water. Above the curve of incremental solubility the sample will be oversaturated.

Pressure is another variable that must be considered in the analysis, but little effect was found respect to anhydrite saturation index. Figure 4A-5 shows that by

increasing the pressure from 5 atm to 200 atm or approximately 3000 psi, an increment in saturation temperature of 4ºC is predicted. This small temperature increment is not enough to produce solubility of anhydrite in seawater at reservoir temperature. The actual reservoir pressure is only about 130 atm or 1900 psi.

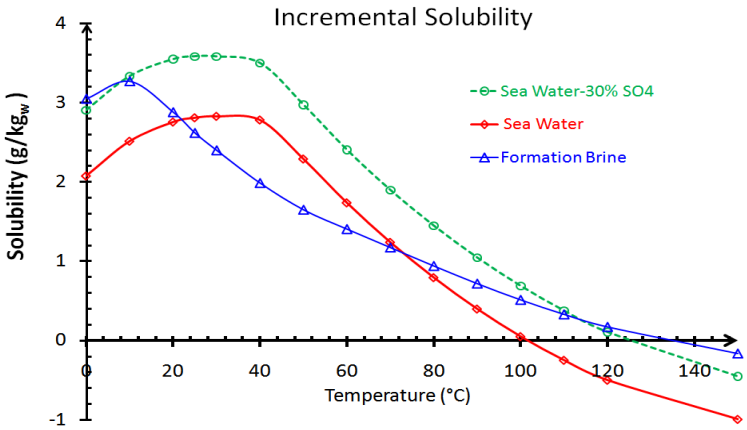

Figure 4C-6 Incremental solubility of the synthetic formation brine used in the experiments during core flooding. Incremental solubility in seawater, and the Incremental solubility in treated seawater (i.e. replacing 30% of sulfates)

For laboratory experiments the synthetic seawater cannot be used at temperatures higher than 100º C, in order to do that 30% of the sulfates need to be replaced, in this simulation 30% of sulfates were replaced by chlorine ions and its corresponding divalent ions (Ca and/or Magnesium) were replaced by sodium ion in the same proportion. The synthetic formation brine presented no problem of saturation respect to anhydrite.

For qualitative purposes any software can be used to see trends in the effects of the variables like, pressure, salinity, pH, alkalinity and even the effect of ions, but

for precision is required to have a software able to fit parameters to experimental data, and to be familiar with the activity models in order to select the one that will model your system. Software like ScaleSoftPitzer has features that will let you analyze the effect of using scale inhibitors, using the Pitzer activity model and was designed for special applications. PHREEQC is a free software and can be modified, but is recommended to verify the database for the salts and minerals of interest, and it limited by the activity model which is the extended version of Debye-Hückel that works at low salinity, it also has the database to use the Pitzer model, but its database is limited and can't predict the concentration of ion pairs with the Pitzer model.

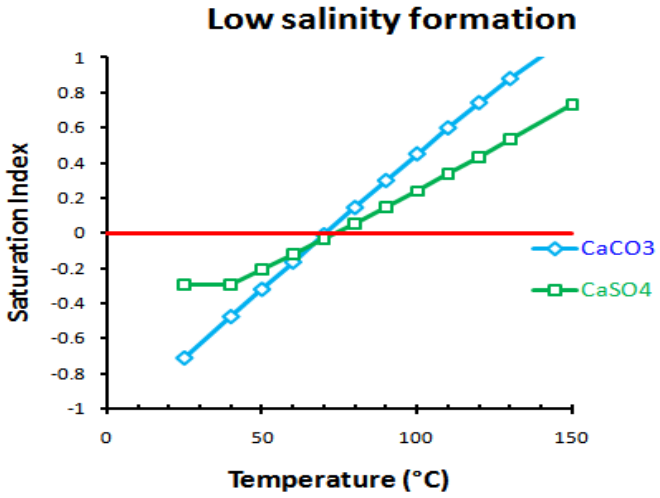

Figure 4C-7 Most of the formations at low salinities (i.e. less than 4% of TDS) may be oversaturated with anhydrite, if calcium content in the sample is high. For this case the concentration of the ions are: Na^{+} = 11638 mg/l, Ca^{2+} = 2800 mg/L, Mg^{2+} = 559 mg/L, Fe^{2+} =20 mg/L, Cl^{-} = 23660 mg/L, SO_4^{2-} = 1120 mg/L, HCO_3^{2-} = 120 mg/L, and pH=6. The red line is the saturation limit.

Appendix 5A Titration of blends using Low pH and High pH two-phase titration.

The two colorimetric two-phase titrations, methylene blue and bromocresol green, can be used to quantify the two surfactants in the new UT Blend of **C_{15-18} IOS + $C_{28}PO_{25}EO_{25}COONa$**.

- pH of a 1% solution of the new UT blend in seawater at 90°C decreases over time, possibly caused by hydrolysis of impurities in the IOS and carboxylate; this 1% solution remains clear and concentration is stable, which is not the case at low surfactant concentrations.
- Solutions of new UT carboxylate itself in DI water becomes cloudy and experiences decreases in pH and carboxylate concentration over time at 90°C. The cloudiness remains on cooling to room temperature.
- New UT formulation at 1% concentration exhibits about twice as much adsorption of carboxylate as IOS in mg/g. Solution after adsorption has higher mass fraction but lower mole fraction of IOS.
- There is less IOS 15-18 adsorption compared to IOS 19-23 adsorption with old formulation.
- Reported adsorption values are for powder dolomite. Scaling factor to Cantarell cores is between 0.1 to 0.2 (i.e. powder dolomite has higher surface area)

- Adding polyacrylate to old UT formulation provides clearer solutions for a longer time and slight decrease in IOS adsorption.

Adsorption and clear aqueous solutions

Appendix 5B Titration at low pH (Titration of anionic surfactant A^- using cationic titrant $TEGO^+$, and Cationic methylene blue as dye)

$$MB^+_{(aq,blue)} + A^-_{(aq)} \rightleftarrows MB^+ \circ A^-_{(org,blue)}$$

$$TEGO^+_{(aq)} + A^-_{(aq)} \rightleftarrows TEGO^+ \circ A^-_{(org)}$$

$$MB^+ \circ A^-_{(org,blue)} + TEGO^+_{(aq)} \rightleftarrows TEGO^+ \circ A^-_{(org)} + MB^+_{(aq,blue)}$$

Caution:

$$MB^+ \circ Cl^-_{(aq,blue)} \rightleftarrows MB^+_{(aq,blue)} + Cl^-_{(aq)}$$

$$MB^+ \circ Cl^-_{(aq,blue)} \rightleftarrows MB^+ \circ Cl^-_{(org,blue)}$$

Ionic strength must be kept as constant as possible, and the chlorine concentration high, so that end point is when the ion pairs of methylene blue cations form ion-pair with chlorinde and this ion-pair partitions equally in both phases. Then the end point is when both phases have the same blue hue. See figure 5B-1. Additional details about technique can be found in Epton (1947) and Cohen (1997).

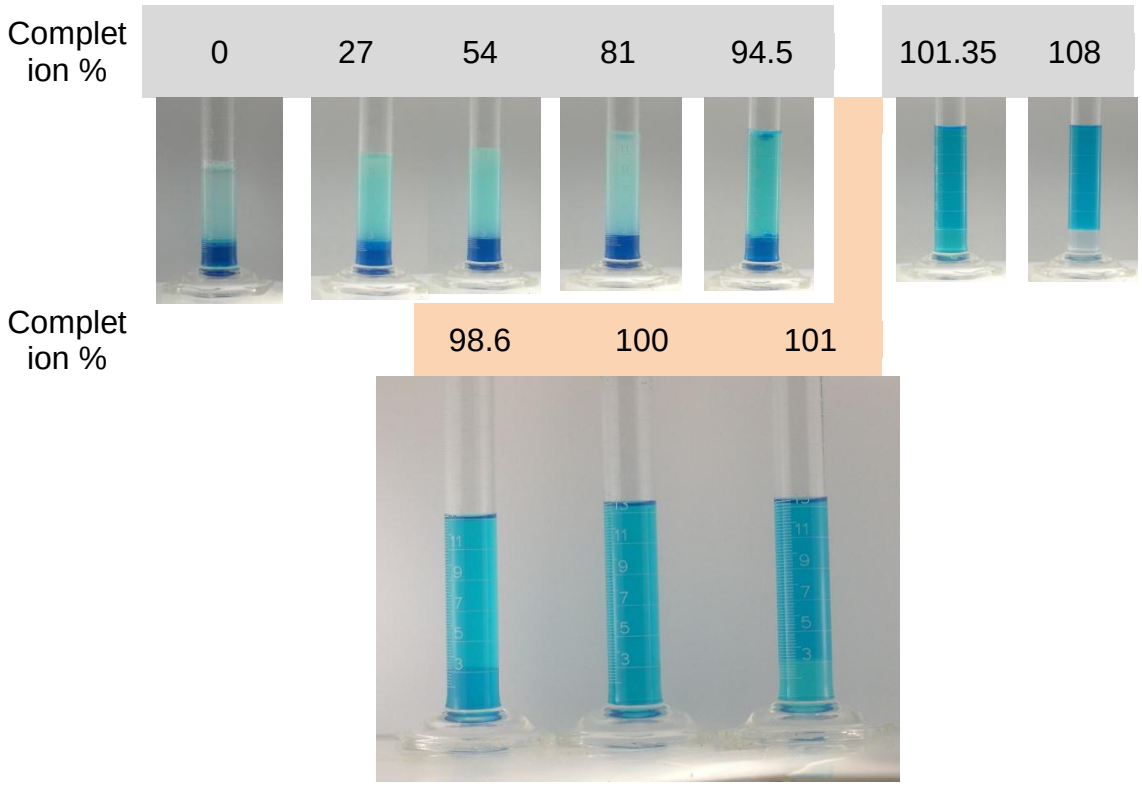

Figure 5B-1 Evolution of the titration at low pH.

Appendix 5C Titration at high pH (Titration of anionic surfactant A^- using cationic titrant $TEGO^+$, and Anionic bromocresol green as dye-indicator)

$$TEGO^+_{(aq)} + A^-_{(aq)} \rightleftarrows TEGO^+ \circ A^-_{(org)}$$

$$TEGO^+_{(aq)} + BG^-_{(aq,REB)} \rightleftarrows TEGO^+ \circ BG^-_{(org,REB)}$$

For this reaction bromocresol green will be used as dye, but its indicator characteristic is useful to make sure that the titration is performed under buffer conditions. The high pH buffer will keep the hue of the solution as robbin egg blue (REB), so the end point is when the upper phase turns colorless. In this technique the titration measures both the anionic surfactant (A^-) and the anionic

dye (BG^-), so the blank is always needed, or know the exact amount of bromocresol green used. See Bares (1969) and Cohen (1997) for details about the technique.

Appendix 5D Titration of blends containing zwitterionic, anionic and cationic surfactants.

If there is a blend with Anionic (A^-), Cationic (C^+), and Zwitterionic (Z^{+-}), and if the anionic is in higher molar proportion than the cationic during high pH titration, excess of anionic can be titrated with a cationic titrant (T^+).

Ion pairs formed with cationic surfactant with the anionic surfactant

$$\beta\left[C^+ + A^- \rightarrow C^+ \circ A^-\right]$$

Ion pairs formed with the excess of anionic and the titrant.

$$(1-\beta)\left[T^+ + A^- \rightarrow T^+ \circ A^-\right]$$

In this equation, β is the molar proportion of cationic with respect to the anionic. Then during titration the quantified amount is 1-β that represents the excess of anionic with respect to cationic. According to Rosen (1987), the zwitterionic (Z^{+-}), remains with both charges under alkaline conditions. Then during titration the quantification represents the excess of anionic respect to the cationic.

Under acid conditions, the sample can't be analyzed with this technique if the anionic surfactant is in lower molar proportion than the zwitterionic.

If the anionic mole fraction is higher than the sum of cationic and zwitterionic mole fractions, the low pH technique can be used as well.

$$\gamma\left[Z\,\mathrm{H}^{+}+A^{-}\rightarrow Z\,\mathrm{H}^{+}\circ A^{-}\right]$$

$$\beta\left[C^{+}+A^{-}\rightarrow C^{+}\circ A^{-}\right]$$

$$(1-\beta-\gamma)\left[T^{+}+A^{-}\rightarrow T^{+}\circ A^{-}\right]$$

Here γ is the molar ratio of zwitterionic to anionic, and β the molar proportion of cationic to anionic. For this third case the titrant will measure the excess of anionic with respect to cationic and zwitterionic.

If the anionic surfactant is in greater molar concentration than the sum of zwitterionic and cationic, then both techniques can be used to quantify how much excess of anionic respect to both surfactants, and respect to the cationic.

In the formulations proposed in the following chapters the zwitterionic is always in excess with respect to anionic and cationic, so the technique can only be used under basic conditions to measure the excess of anionic with respect to cationic surfactant.

As first approach to know the value of the adsorption of a blend composed of CAPB + AOS C14 + TTAC (Tallow trimethyl ammonium chloride), the high-pH, two phase titration method was used and the adsorption estimated assuming all components adsorbed in the same proportion, resulting in a high adsorption. Results are in fig 5-14

Appendix 5E Titration for zwitterionic.

To quantify the concentration of Zwitterionic for the new formulation different techniques can be used. If the zwitterionic surfactant is amphoteric and titration is implemented at low pH, we can convert the zwitterionic surfactant into cationic surfactant as suggested by Rosen (1987)

Two indicators are used, one is Patent Blue (V) (Food blue 5) Sulphane blue, which is anionic dye $C_{27}H_{31}N_2NaO_7S_2$ (DBV^-Na^+), and the other is dimidium Bromide, a cationic $C_{20}H_{18}BrN_3$ (D^+Br^-). The reactions are in the titration are:

$$Z^{+-}_{(aq)} + DBV^-_{(aq)} + H^+_{(aq)} \rightarrow ZH^+ \circ DBV^-_{(blue,organicphase)}$$

$$ZH^+ \circ DBV^-_{(blue,o)} + DS^-_{(aq)} \rightarrow ZH^+ \circ DS^-_{(colorless)} + DBV^-_{(aq)}$$

$$D^+_{(aq)} + DS^-_{(aq)} \rightarrow D^+ \circ DS^-_{(pink)}$$

Z^{+-}: Zwitterionic (Cocamido propyl betaine and or Lauryl Betaine)

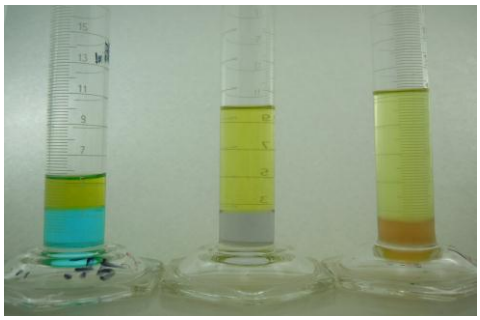

Figure 5E-1 Evolution of titration for CAPB

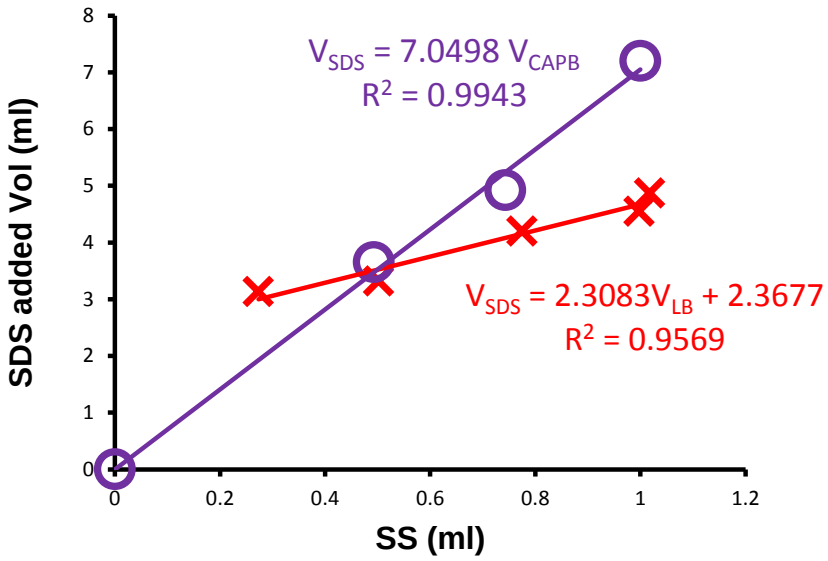

Figure 5E-2 Comparison of titration for CAPB and LB

During the titration we were able to determine the concentration of the 28 mM concentration of Cocamidopropylbetaine (CAPB) with an error less than 4% adding 2 drops of H_2SO_4 to maintain the pH<3 during the titration, but in the case of Lauryl betaine, the concentration measured is lower than theoretical. Then at low pH, not all the Lauryl betaine in the carboxylic group is in the acid form. Most of the amphoteric surfactants should behave as cationic surfactants at low pH, i.e. $Z^{+-} + H^+ = ZH^+$, but for the Lauryl betaine the one fraction of the surfactant is in Zwitterionic fiorm (Z^{+-}) and another in the cationic form (ZH^+)

Appendix 5F Sacrificial agents, titration reagents and indicators.

Table 5F-1 List of sacrificial agents

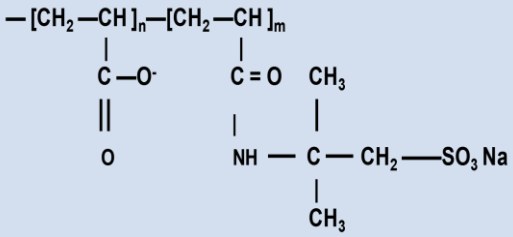	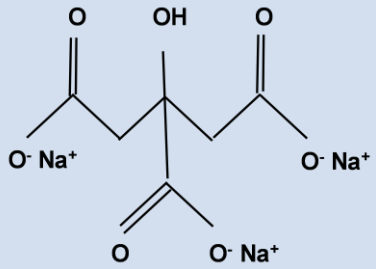
SPA(*), Sulfonated polyacrylic acid, MW=3500 Da	Tri sodium citrate MW=294.1 Da
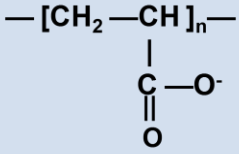	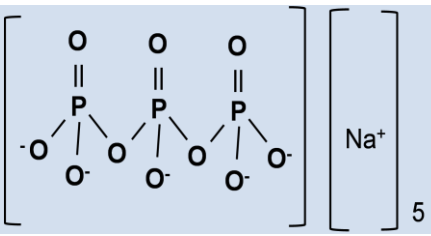
Sodium polyacrylate, MM= 2100 Da, n=30	Tripolyphosphate , MM= 367.864 Da
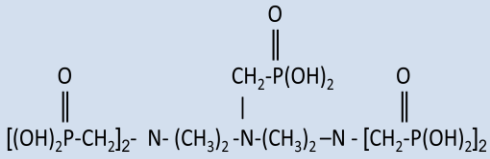	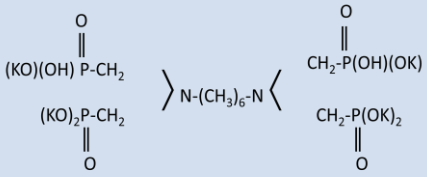
Diethylene triamine-penta (methylphosphoric) acid MW=573 Da , DTPMP(*)	Hexamethylene diamine-tetra (methylenephosphoric) acid MW=492 Da , HDTMP(*)

Additional additives were Sodium citrate that produced precipitation in formation brine, and Disodium EDTA (Na_2H_2Y) that precipitated in seawater. (*) Mason Tomson Lab

Figure 5F-1 Aqueous stability of surfactant solutions

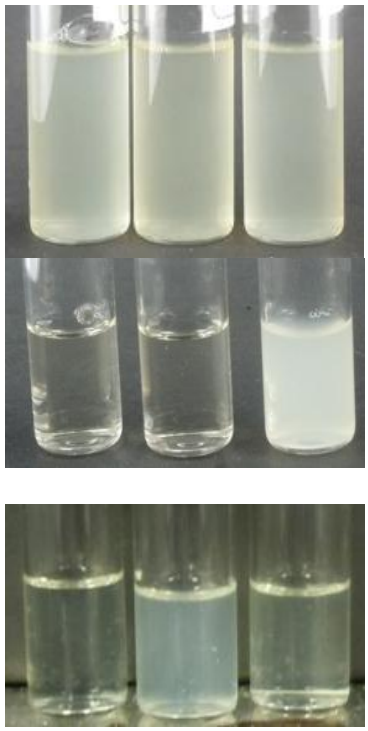

Addition of TPP increased the pH and did not produced clear solutions as the PA.

Aqueous stability of UT Blend adding Lauryl betaine or Lauryl hydroxyl sultaine.

The use of foam boosters is recommended when anionic surfactants are not capable of foam by themselves. The most common foam boosters are Alkyl amidopropyl betaines, alkyl betaines, and alkyl hydroxy sultaine.

The amidopropyl betaines may decompose at high temperature low and high pH, so Laurylbetaine and lauryl hydroxy sultaine were used instead, mixed with UT blend to verify aqueous stability. The foaming characteristics will be discussed in chapter 7.

Table 5F-2 List of titration reagents and indicators

Name	Symbol	formula
Methylene	**MB^+Cl^-**	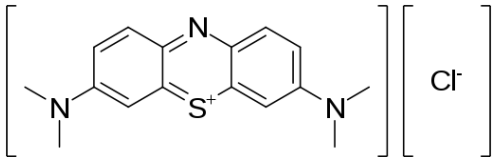
SDS	**Na^+DS^-**	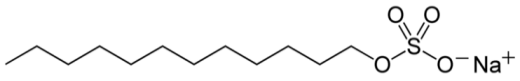
Bromocresol green	**BG^-Na^+**	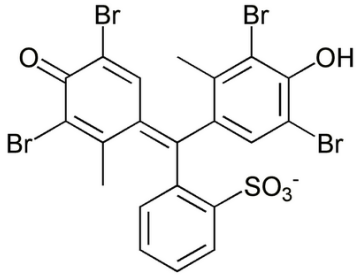
TEGOtrant A100	**$TEGO^+Cl^-$**	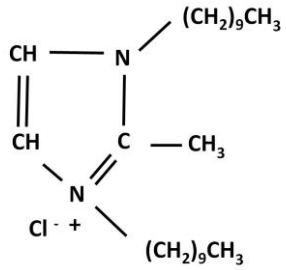
odium Disulphine Blue V	**Na^+DSV^-**	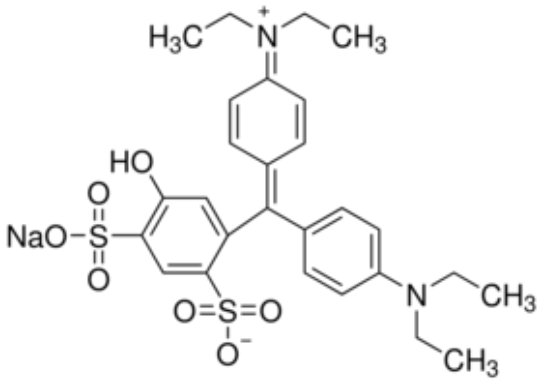
Dimidium Bromide	**D^+Br^-**	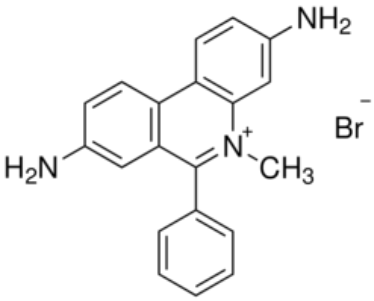

Appendix 6A Determination of adsorption using mass balance.

Using Eulerian approach and selecting as a system the core, and dead volume (i.e the lines, the fittings and heat exchangers), after integration the adsorption is calculated.

$$\frac{dm}{dt} = \dot{m}_{in} - \dot{m}_{out}$$

To calculate the integral, fig 6-11 is used.

$$\left(C_{sf} - C_{si}\right)\left(V_{PV} + V_{DV}\right) + m_{Rock}\Delta a = C_{so}V_{PV}\left[\int_0^{\infty}\left(1 - \frac{C_s}{C_{so}}\right)d\tau\right]$$

$$\left(10\,mg_{surf}/cm^3\right)\left(24\,cm^3 + 33.5\,cm^3\right) + \left(455.85 g_{Rock}\right)\Delta a = \left(10\,mg_{surf}/cm^3\right)\left(24 cm^3\right)\left(6.4\right)$$

This results as:

$$\Delta a = 2.11\frac{mg_{surf}}{g_{Rock}}$$

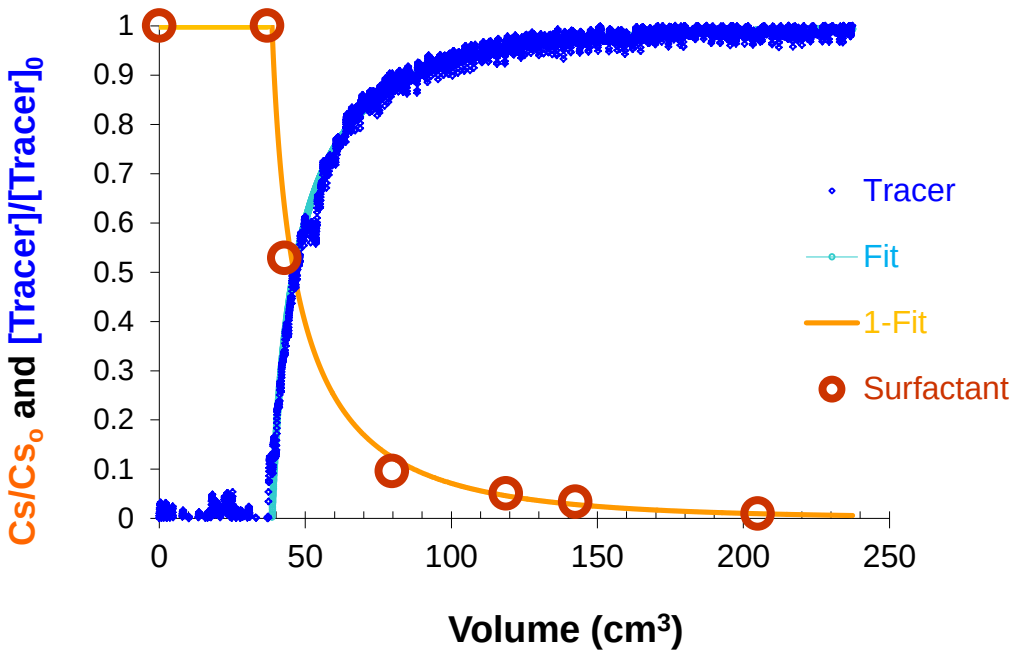

Figure 6A-1 Curve during the first stage of cleaning, while injecting aqueous brine with no surfactant.

The value of adsorption can be verified, regenerating or cleaning the core, first with brine, then followed by a solution of IPA in DI water and measuring the surfactant in both effluents.

At first glance, the response curve for the cleaning process indicates that the adsorption process is almost irreversible (Fig 6A-1). The curve of the surfactant concentration vs pore volumes injected is the complement of the tracer curve.

Verification of surfactant in pore volumes and dead volume. Injecting 10 PV of seawater brine eliminates ca. 88.3 % of the surfactant in the pore space and dead volume. The next step is try to recover the surfactant adsorbed by injecting IPA-DIW.

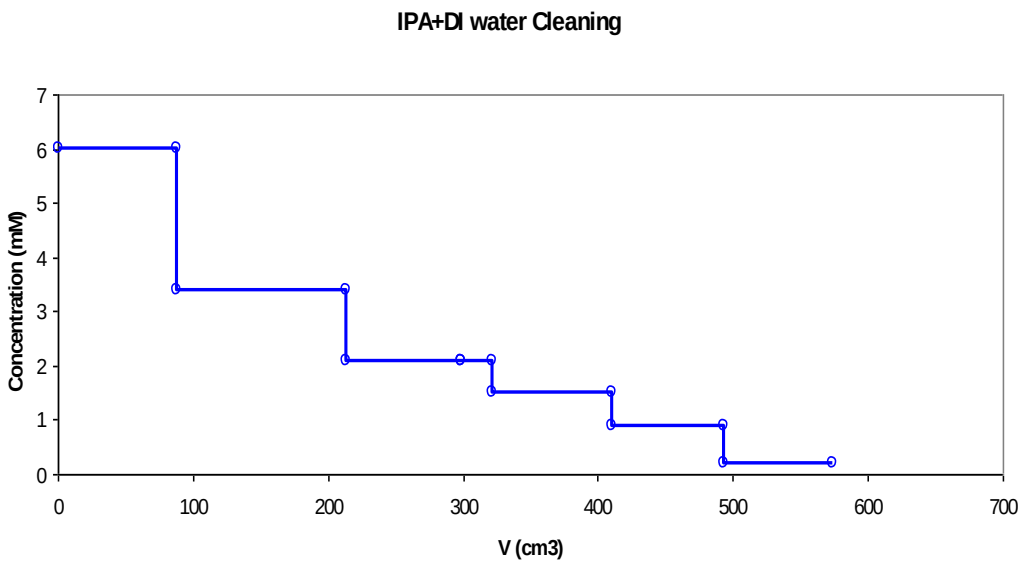

Figure 6A-2 The collected effluents after titration are used to estimate the total adsorption after mass balance during the cleaning.

After injecting 20 PV of sea water, the core material was cleaned by injecting IPA (IPA+DI water and Oxygen scavenger SO_3^{2-}). The removed surfactant was quantified. This methodology predicted an adsorption of 1.73 mg/g of rock.

Appendix 6B Cartoon or representation of the porous structure used in the mathematical model.

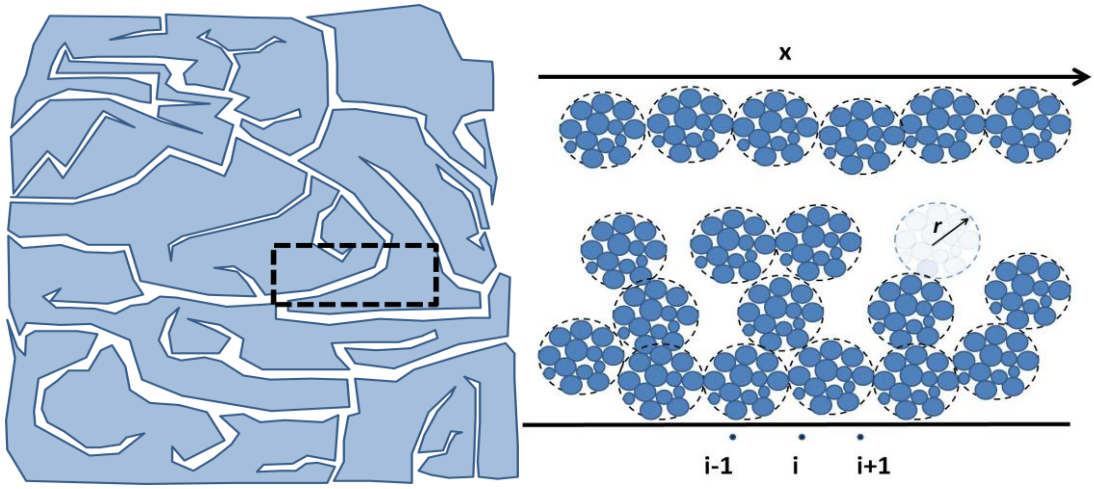

Figure 6B-1 Left cartoon represent a piece of core material with macro pores and dendritic pores. The Figure in the right indicates the zoom in the dashed rectangle of the figure in the left. The zoomed area indicates the discretization used in axial direction.

In the simulation results for this chapter 60 points were used in axial direction and for the radial direction in the cluster of micro pores three internal points are used in addition to the external point. The point in the center is not required because symmetrical orthogonal polynomials were used for the discretization.

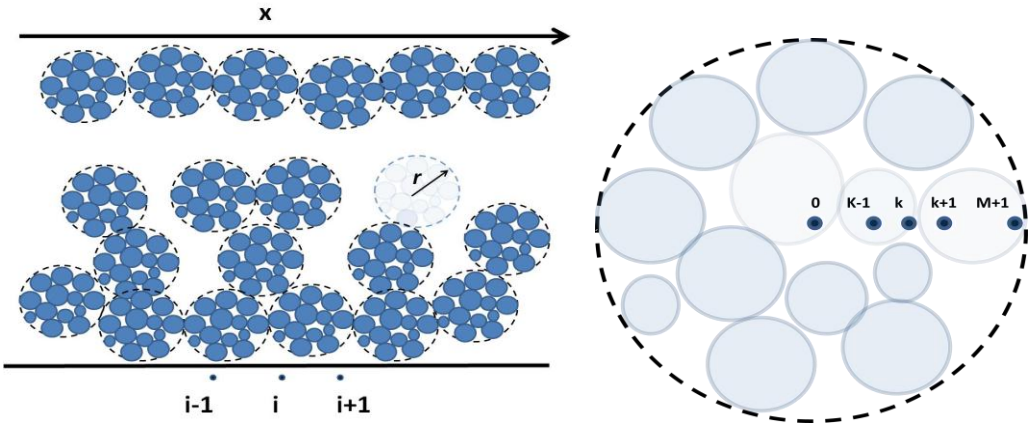

Figure 6B-2 Figure in the right indicates the zoom in the micro pore space.

The sketches represented here, can be extended to different physical meanings, for example what is called micro porous space in this chapter, can be another region where the transport mechanism is basically the diffusion, which is different from the dendritic pore space, where mass transfer can occur but in the capacitance pore model assumes that the diffusion process is fast, which not necessary be true in all the situations.

Appendix 7A Information about surfactants

Table 7A-1 Surfactants and Salts

Name	Names	Activity % **	Company	Lot No. or Date
C_{1618} AOS	AGENT X-3153-026, Sodium (C1618) Alpha Olefin Sulfonate	32.5	Stepan	July 2004
Lauryl Betaine	MACKAM LAB	30.1	Rhodia	Lot. 110403
NaCl	Sodium Chloride	99.98	Fisher Scientific	S671-500 LOT 108013
Na_2SO_4	Sodium Sulfate Anhydrous	99.97	EMD	SX0760-1 LOT 1690C118
$CaCl_2$ $2H_2O$	Calcium Chloride Dihydrate	99.9	EMD	CX0130-1 LOT A0141702 020
$MgCl_2$ $6H_2O$	Magnesium Chloride	99.88	Fisher Scientific	M33-500 Lot 028490
Na_2SO_3	Sodium Sulfite	98.2	Fisher Scientific	S430-500 Lot 041744

** Purity of salts or activity of the surfactants

Table 7A-2 Information of Surfactants

Surfactant	Name	Company
LHS	Laurylhydroxy sulfo betaine	**Rhodia**
LB	Lauryl betaine	**Rhodia**
CAPB	Cocamidopropyl beatine	**Rhodia**
C_{14}AOS	Alpha olefin sulfonate	**Stepan**
C_{16-18}AOS	Alpha olefin sulfonate	**Stepan**
C_{20-24}AOS	Alpha olefin sulfonate	**Stepan**
BTC 8358	Benzalkonium chloride	**Stepan**
DDAB	Didodecyldimethylammonium bromide	**Sigma-Aldrich**
CTAB	Cetyltrimethylammonium bromide	**Sigma-Aldrich**
DTAB	Dodecyltrimethylammonium bromide	**Sigma-Aldrich**

LB=dodecyl dimethyl ammonio acetate

Appendix 7B Foam equipment photograph.

Fig 7B-1 Pump and gas mass controller in the left, and foam apparatus in the right. See diagram of fig

Appendix 7C CDC Parameters and equations for capillary desaturation curves.

Table 7C-1 Parameters for capillary desaturation curve

System	*Model*	T_i	T_1	T_2
Non-wetting	1	-	14000	1.55
Wetting	1	-	120	1.8
Ottawa	**2**	**5345**	-	**-**

$$\breve{S} = \left[1 + \left(T_1 \; N_T\right)^{T_2}\right]^{\frac{1}{T_2}-1}$$ Model 1 from Li *et al.* (2007)

$$\breve{S} = \frac{1}{1 + T_i \; N_T}$$ Model 2 UTCHEM model

$\breve{S}$ = Normalized saturation, N_T=Trapping Number (Vectorial sum of Capillary and B and Number, Pennell *et.al.*1996)

Appendix 7D Aqueous stability of UTB formulations with zwitterionic added

%UTB	0	50	60	70	80	90	100
%LB	100	50	40	30	20	10	0

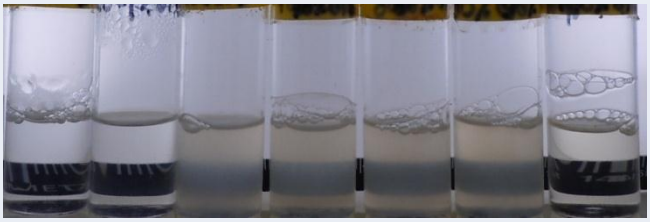

Fig 7D-1 Solutions of mixtures of the UT Blend and Lauryl Betaine in seawater at 1% of total surfactant concentration at 100°C for a week.

No clear solutions at low concentrations of LB, or LHS as indicated in fig 7D-1 and 7D-2

%UTB	0	20	50	70	75	85	95	100
%LHSB	100	80	50	30	25	15	5	0

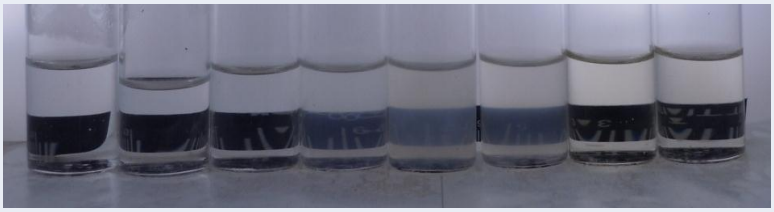

Fig 7D-2 Solutions of mixtures of the UT Blend and Lauryl Hydroxy Sultaine in sea water at 1% of total surfactant concentration at 100°C for a week.

%UTB	0	75	85	95	100	0
%LHSB	100	25	15	5	0	0

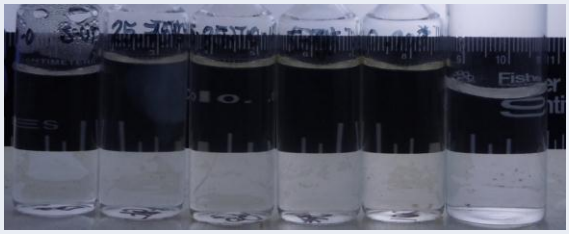

Fig 7D-3 Solutions of mixtures of the UT Blend and Lauryl Hydroxy Sultaine in 76/24 Sea water to formation water ratio at 1% of total surfactant concentration at 100°C for a week

Appendix 7E Oil in Plateau borders in foam experiments with crude oil.

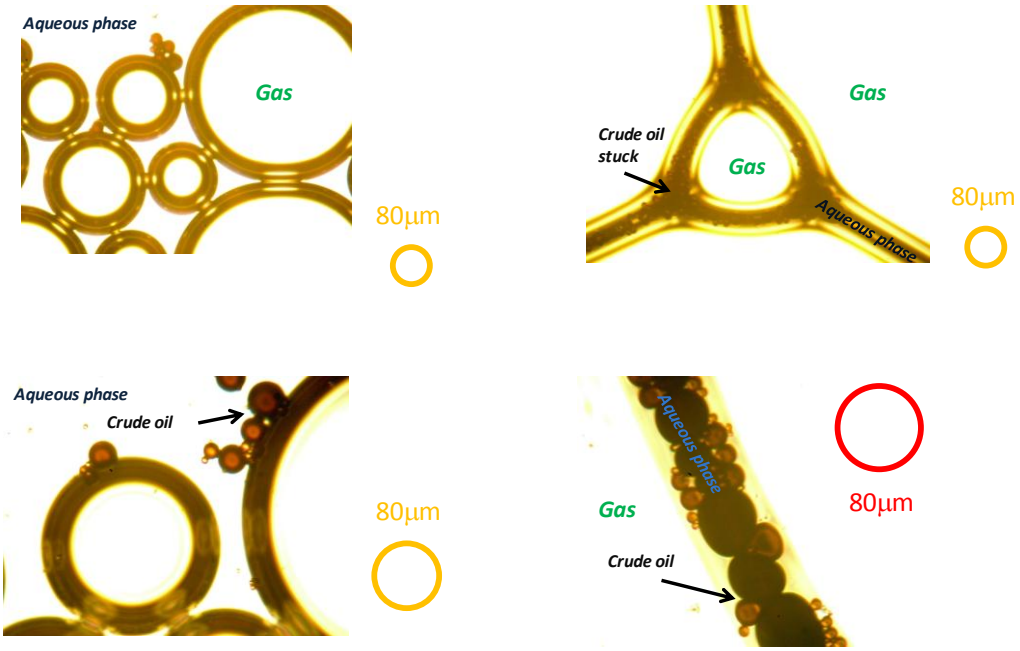

Figure 7E-1 Beads of oil traveling through the plateau borders. This is phenomenon is observed with the blends: IMP, LB+C_{16-18} AOS, 2:1(w/w) and LB+C_{16-18} AOS+BTC

Figures in the left is wet foam, and in the right is for wet foam. Oil beads remained in the aqueous phase all the time.

Appendix 7F Information about the algorithm to parameter estimation.

Excel Microsoft. Generalized Reduced Gradient Method.

Love, Jonathan. Process Automation Handbook. Spring 2007. 882-883.

Appendix 7G Brines comparison

Table 7G-1 Composition of synthetic seawater and Synthetic formation brine.

Component	Concentration mg/l	
	Seawater	Formation
Na^+	12174.86	41948.21
K^+	0.00	0.00
Ca^{2+}	469.45	3847.34
Mg^{2+}	1339.19	147.07
SO_4^{2-}	3246.03	500.43
Cl^-	21116.49	71557.08
Br^-	0.00	0.00

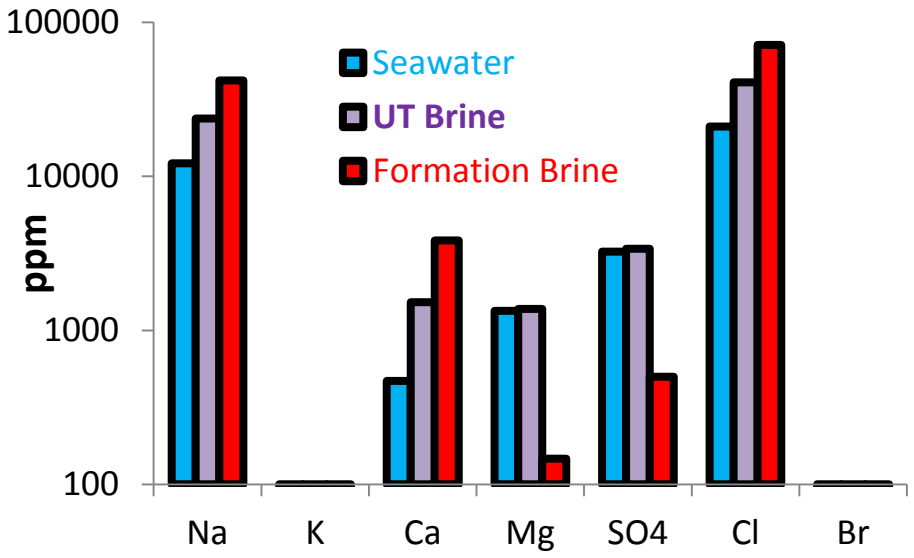

Figure 7G-1 Brines comparison

The brine should be a mixture between sea water and formation brine, the figure indicates that the brine proposed by UT requires addition of SO_4^{2-} and Mg^{2+}

Appendix 7H Analytical solution of counter current imbibitions for a strong water wet system (See nomenclature section)

t=time, σ= surface tension, *k*=absolute permeability, *L*=length, ϕ=porosity, μ_0= Oil viscosity, P_c=capillary pressure, nw =Corey exponent for water, no=corey exponent for crude oil, S_D = Saturation of water normalized, *J* = Leverett J Function. β,γ,κ = Functions defined below.

$$\tau_D = \frac{t\sigma}{\mu_o L^2}\sqrt{\frac{k}{\phi}}$$

$$\frac{P_c}{\sigma}\sqrt{\frac{k}{\phi}} = J(S_D)$$

$$k_{rw} = k_{ro}{}^{o}(1-S_D)^{no}$$

$$\beta = \frac{2(2+no)}{(1+no)}k_{ro}{}^{0}J'$$

$$\kappa = \left[\frac{2(2+no)}{3+2no}\right]\left[\frac{2(1+no)^2}{no(3+2no)}\right]^{no}k_{ro}{}^{0}J'$$

$$J' = \left.\frac{dJ}{dS_D}\right|_{S_D=1}$$

$$\gamma = \frac{2}{(1+no)(2+no)}k_{ro}{}^{0}J'$$

$$k_{rw} = k_{rw}{}^{o}S_D{}^{nw}$$

$$\tau_D \le \tau_{D1}$$

$$\bar{S}_D = 1 - \frac{1+no}{(2+no)(1+\kappa(\tau_D-\tau_{D1}))^{1/no}}$$

$$\bar{S}_D = \sqrt{\gamma\,\tau_D}$$

$$\gamma = \frac{\beta}{(2+no)^2}$$

$$\tau_{D1} = \frac{1}{\beta}$$

Tavassoli *et al.* (2005)

Appendix 7I Materials for experiments in micro-channels

Video Camera: Panasonic GP-KR222 (Industrial Color CCD Camera)

Lens:Computar Macro 10X

Micro channels

Microslides: Vitrto Dynamics Inc and VitroCom Inc.

- 200 μm x 4000 μm x 5 cm
- 100 μm x 1000 μm x 5 cm
- 50 μm x 500 μm x 5 cm
- 20 μm x 200 μm x 5 cm

Camera for Microscope: Minivue 3.1M (Aven, Inc.)

Microscope:

Nikon Polarizing Microscope. OPTIPHOT-POL

4p, 0.1, 160/-

TV Relay Lens 1x/16 (between microscope and camera)

Appendix 7J Solutions of mixtures of the UT Blend

Solutions of mixtures of the UT Blend and Lauryl Hydroxy Sultaine in 76/24 Sea water to formation water ratio at 1% of total surfactant concentration at 100°C for a week.

In an effort to scale the results for a similar porous media and assuming the foam as a bulk fluid, the Carreau (1997) approach is used. Carreau proposed a model to scale the behavior of polymeric fluids in a porous media and defined a pseudo-shear rate and a pseudo shear stress as:

Using the Kozeny-Carman equation to obtain the Leverett pore size factor defined by Civan (2011)

$$\frac{\phi\, d_p}{6(1-\phi)} = \left(\sqrt{\frac{k}{\phi}}\right)\left(\sqrt{\frac{b}{36}}\right) \qquad \textbf{Equation 7J-1}$$

$$\langle \dot{\gamma}_w \rangle = \frac{u}{\sqrt{\phi\, k}}\left(\sqrt{\frac{36(T\, k_o)^2}{150}}\right) \qquad \textbf{Equation 7J-2 for pseudo-shear rate}$$

$$\langle \tau_w \rangle = \frac{\Delta p\sqrt{k}}{L}\left(\sqrt{\frac{150}{36\,\phi\, T^2}}\right) \qquad \textbf{Equation 7J-3 for pseudo shear stress}$$

And using the following parameters:

Table 7J-1 Parameters of porous media

b	**150**	**Constant**
T	1.4142	Tortuosity
ko	2	Constant
ϕ	0.36	Void fraction
K	100 darcy	Permeability

u is superficial velocity and *Δp* is pressure drop

d_p is particle diameter, for unconsolidated porous media can be estimated with 7J-1

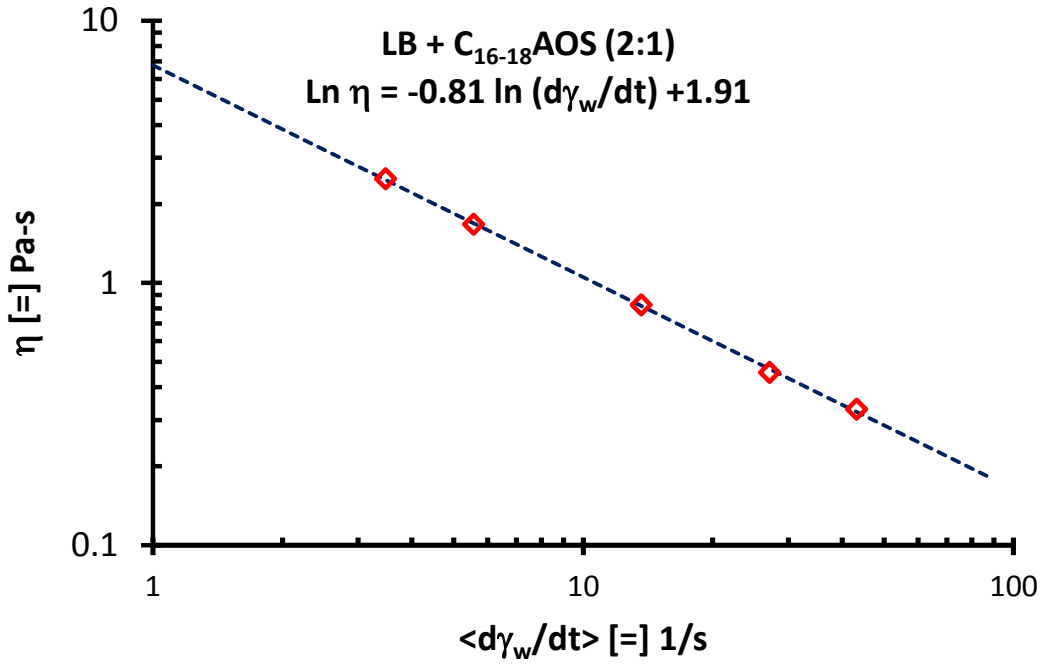

Figure 7J-1 Pseudo rheology for the foam of N2 in 1% Total surfactant concentration (LB + C_{16-18}AOS, 2:1) in synthetic seawater at 94°C

Appendix 7K IMP Transient foam

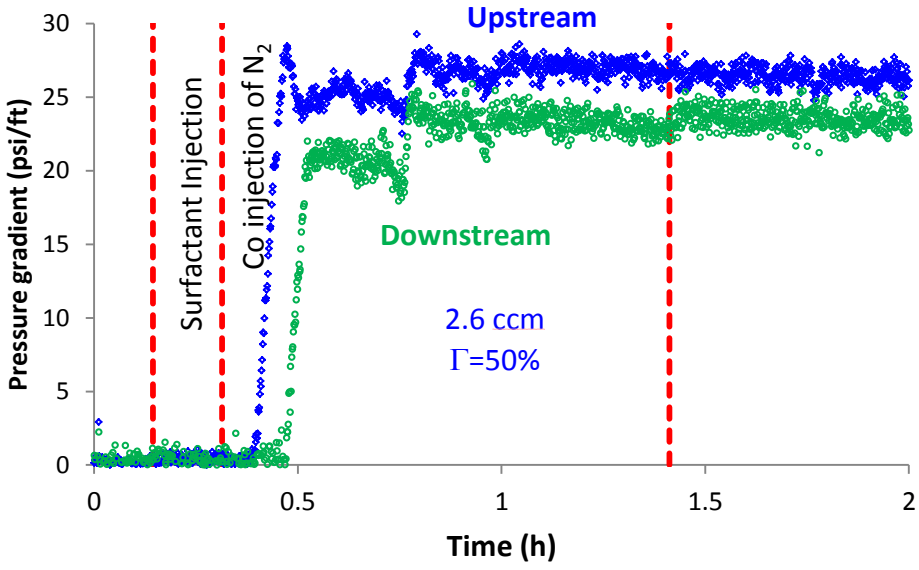

Figure 7K-1 Start up of 1% IMP formulation in seawater

1 h ~ 1 PV of liquid

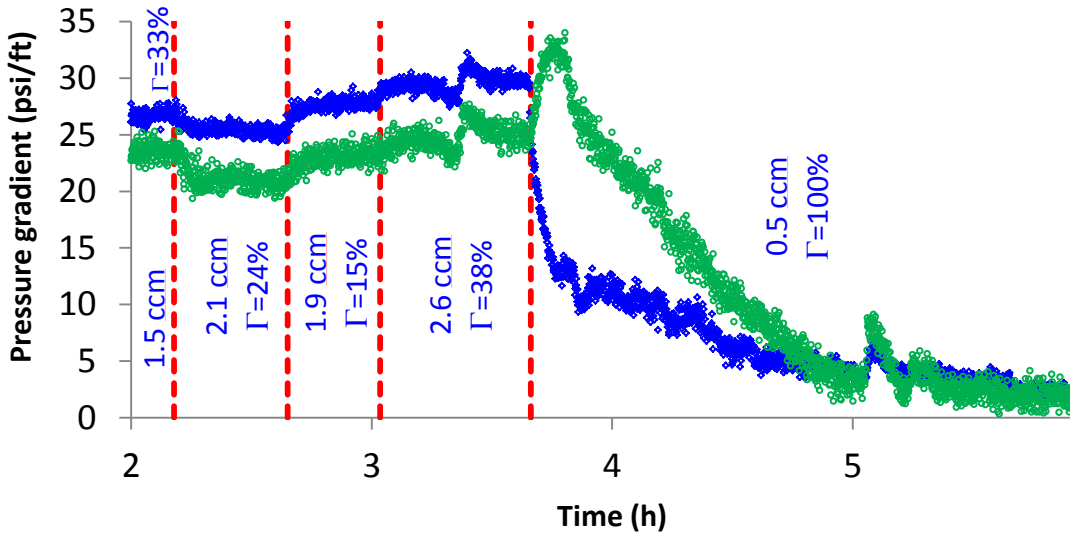

Figure 7K-2 Transient to see the effect of stopping liquid injection.

Foam kept strength when flow rate increased and quality changed. When liquid flow was cut the foam kept strength for more than an hour.

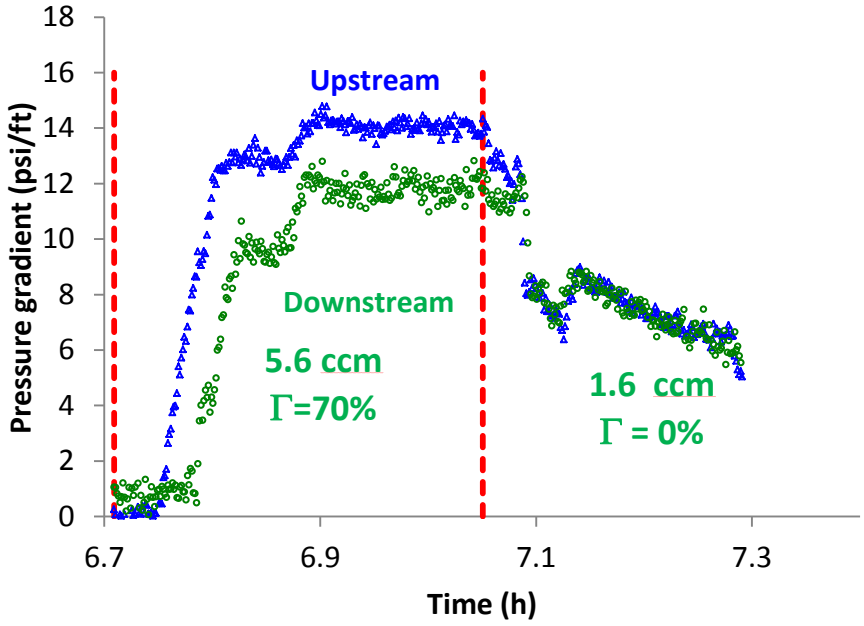

Figure 7K-3 Resume of foam, and transient after stopping gas injection. 1% IMP in seawater

When flow rates were resumed foam propagated from bottom to top taking close to 1 PV to fill the column. When gas injection was stopped, foam kept strength for ca. ½ h

Appendix L Oil recovery in rectangular capillaries, and oil recovery for a bunndle of rectandular capillaries.

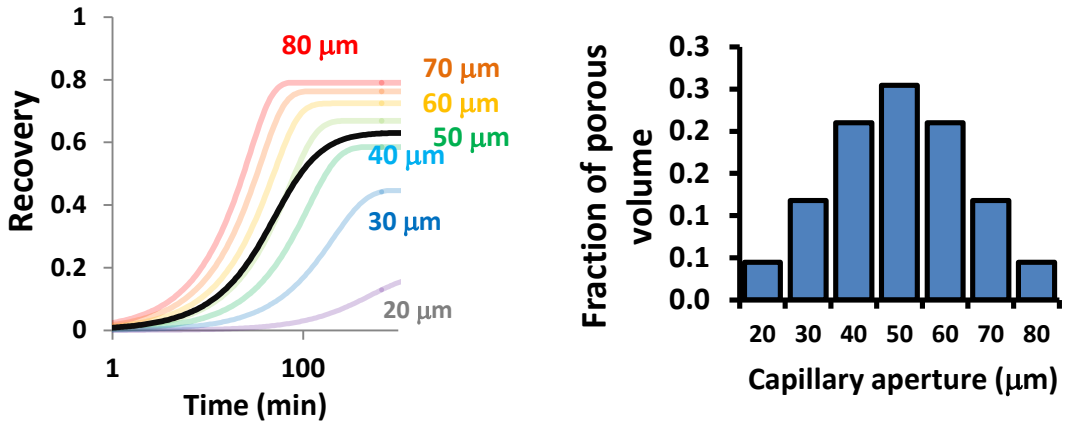

Table 7L-1 Oil recovery from a bundle of capillaries (i.e., rectangular micro-channels). Lines in color represent the recovery of individual capillaries. The distribution of sizes is indicated on the right figure..

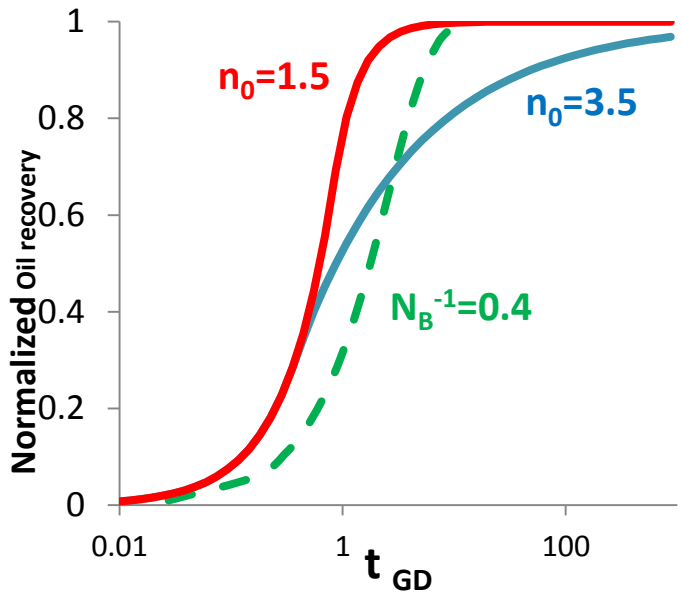

Figure 7L-2 Comparison of normalized oil recovery by gravity drainage. Curves constructed using two different values of Corey exponent for oil. The green dashed line is the solution for a rectangular micro-channel for inverse of Bond number of 0.4.

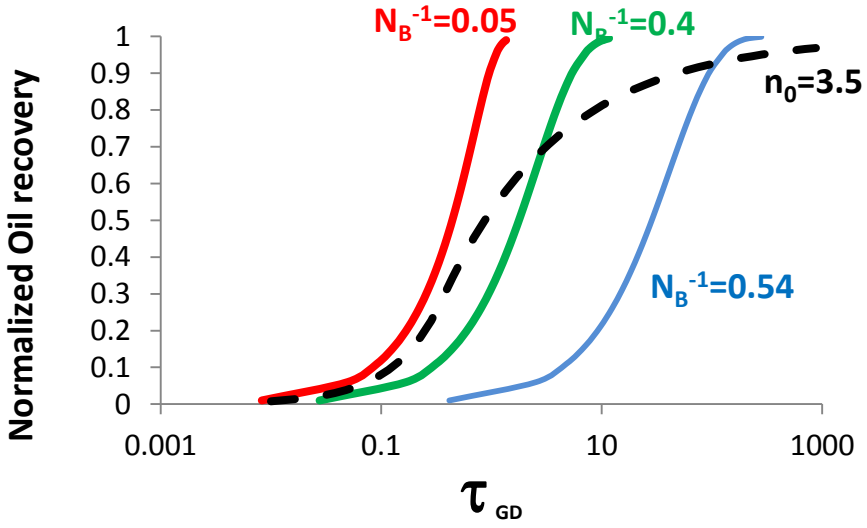

Table 7L-3 Normalized oil recovery from micro-channels. Three different values of Bond number are represented by continuous lines. The dashed line is the expected oil recovery by gravity drainage of a porous media with relative permeability represented by Corey model.

Appendix 7M Parameters for foam simulation / surfactants of different nature

Parameters	LB+C_{16-18}AOS	CTAB+NapTS	CTAB+NapTS **	CTAB+NapTS ***
epdry (*)	100	100	1000	56
epcap = epn (*)	3	3	3	204.75
fmdry	0.625794	0.625794	0.13	0.12
fmmob	2894.053	2158	2490	90
epv	-0.77585	-0.7758	-0.775	-0.77
u_{gref} *(m/s)*	1.421435	1.421435	0.6	0.6
u_{ref} *(m/s)*	0	9.10E-06	9.10E-06	9.1E-6
n_w	3.5	3.5	3.5	3

For the last column, to reproduce the experimental trend of viscosity vs quality a total flow rate, it was needed to change n_w.